MODELLING THE INITIAL SPRAY CHARACTERISTICS OF FIRE SPRINKLERS

by

Hamed Aghajani

BSc in Mechanical Engineering (Solid Mechanics), Guilan University, Rasht, Iran (2002)

MSc in Aerospace Engineering (Propulsion), Amirkabir University of Technology, Tehran, Iran (2007)

Submitted to the School of Mechanical Engineering

In Partial Fulfillment of the Requirements for the Degree of

DOCTOR OF PHILOSOPHY IN MECHANICAL ENGINEERING

at the

Kingston University London

SEPTEMBER 2013

Thesis committee:

Siaka Dembele

Senior Lecturer of Mechanical Engineering, Kingston University London

Jennifer X. Wen

Professor of Mechanical Engineering, University of Warwick

Title: Modelling the initial spray characteristics of fire sprinklers
Hamed Aghajani
Kingston University, 2013
Ethos persistent id: uk.bl.ethos.587413

Please do not digitise the following images:

Figure 1.1	p.2
Figure 1-4	p.9
Figure 1-5	p.10
Figure 1.6	p.10
Figure 2-1	p.22
Figure 2-2	p.25
Figure 2-4	p.27
Figure 2-5	p.31
Figure 2-6	p.34
Figure 2-10	p.41
Figure 2-11	p.43
Figure 2-12	p.43
Figure 2-13	p.44
Figure 2-14	p.44
Figure 2-15	p.45
Figure 2-16	p.45

Abstract

Sprinklers are automatically activated fixed installation suppression devices. They have found extensive applications due to minimum protection they provide for a wide range of applications including residential and warehouses. Modelling sprinkler atomization is a challenging task, due to the stochastic nature in impingement of water jets and the added complexity of sprinkler configuration.

In the literature, a spray initiation framework has been developed to address the multidimensional stochastic complexity associated with fire sprinklers. The initial sprinkler spray is completely characterized in terms of the following main parameters: droplet spatial location (radius, elevation angle and azimuthal angle), droplet velocity, droplet diameter and the spatial volume flux.

The present thesis aims to improve the prediction of the initial sprinkler spray characteristics through exploring different physics based modelling approaches. The sub-models for film flow and sheet trajectory adopted in the development of the fire sprinkler spray models are reviewed. Three new deterministic approaches for sprinkler atomization have been proposed by employing an existing film sub-model and a detailed water sheet trajectory sub-model which has never been used for fire sprinkler applications. The developed methods simulate the orthogonal impingement of water jet to a deflecting disk, with the potential to be adapted for tilted deflectors. A comparative analysis is carried out between the three introduced methods and a reference model in terms of their predictions for droplet median diameter and initial droplet location for a range of ambient temperatures and water injection pressures.

The developed methodologies have been further expanded by incorporating random behaviour to the spray formation procedure. The stochastically predicted mean velocity and volume median diameter have been compared against robust experimental data and empirical correlations. The improvements obtained by the developed methodologies are promising.

In further steps, a dimensionless formulation for predicting spray characteristics, sheet breakup distance and droplet sizes, in impinging atomizers have been

developed. The developed formulation is validated for impingements led the spray to occur in the rim breakup mode.

Building on the proposed methodologies, a semi empirical model has been developed capable of predicting the near field spray characteristics such as spatial distribution of droplet sizes, velocities and spray volume flux from local volume fraction measurements. The research outcome would benefit the computation fluid dynamic packages to initialize the spray in a more realistic manner. The study undertaken would lead to more efficient fire suppression and/or water and fire interaction studies. In addition to this, the methodology could reduce the cost of experiments in order to quantify new sprinkler sprays.

Acknowledgements

I wish to express my sincere gratitude and appreciation to my supervisors, Prof. Jennifer X Wen and Dr. Siaka Dembele. I am grateful that I had the opportunity of benefitting from their experience and guidance.

I gratefully acknowledge the financial support of FM Global and the technical guidance from Drs. Hong Zeng Yu, Yinbin Xin and Xiangyang Zhou of FM Global.

My endless gratitude goes to my wife, Noushin, for giving me the love that I needed while I was far from her.

My deepest thanks to my parents, sisters, brother and friends, Nima, Majid and Hassan, for their strong supports, appreciation of my willing to pursue toward end of PhD program, friendship and kind hearts.

List of Figures

List of Tables

Nomenclature

A	Amplitude [m]
a	Hydraulic radius – Water jet radius [m]
C	Coefficient of proportionality
C_d	Friction coefficient of the deflector surface
D_o	Sprinkler orifice diameter [m]
d	Diameter [m]
$d_{V_{50}}$	Volume Median Diameter [m]
f	Dimensionless total growth of the wave
f	Gas-liquid interfacial friction factor
Fr	Froud number
g	Gravitational acceleration [m/s^2]
H	Mean Curvature [m]
h	Film/sheet thickness [m]
I	Fluctuation Intensity
K	Sprinkler K-factor [$m^3/s.kPa^{-1/2}$]
$\dot{m}$	Mass flow rate [kg/s]
$\dot{m}''$	Mass water flux [kg/s/m^2]
N	Number of droplets per degree
Ń	Number density [m^{-3}]
n	Wave number [m^{-1}]
Oh	Ohnesorge number
Δp	Pressure difference at sprinkler orifice [Pa]
Q	Sprinkler's volumetric discharge [m^3/s]
$\dot{q}$	Volumetric flow rate [m^3/s)
$\dot{q}''$	Water volume flux [(m^3/s)/m^2] or [(liter/min)/m^2 ~ Lpm/m^2]
Re	Reynolds number
r	Radial location from sprinkler/Radius [m]
r_0	The distance where boundary layer interacts with free surface [m]
R	Radius [m]
S	Viscous force

T	Temperature [K]
t	Time [s]
U	Velocity [m/s]
$\breve{u}$	Terminal velocity [m/s]
V	Volume [m^3]
We	Weber Number
z	Vertical displacement below fire sprinkler angle [m]

Greek Symbols

α	Shape parameter
β	Scale parameter
γ	Volume fraction
θ	Elevation angle
δ	Boundary layer thickness [m]
ν	Kinematic viscosity [m^2/s]
ρ	Density [Kg/m^3]
ϕ	Azimuthal angle
Ψ	Sheet angle
λ	Wave length [m]
μ	Dynamic viscosity[Pa.s]
σ	Surface tension [N/m] and Standard deviation
σ^2	Variance

Subscripts

0	Jet
b	Break up
c	Curvature
d	Droplet

f	Fluid
g	Gas
h	Hydraulic jump condition
i	Deflector/Disc/Flat Plate
l	Ligament
P	Probe point/Measurement point
s	Sheet
ξ	Stream-wise coordinate/direction
η	Normal-wise coordinate/direction
ζ	Tangential coordinate/direction

List of Abbreviations

ADD	Actual Delivered Densities
CFD	Computational Fluid Dynamics
CMF	Cumulative Mass Fraction
DTM	Detailed Trajectory Model
EPA	Environmental Protection Agency
ESFR	Early Suppression Fast Response
FDS	Fire Dynamics Simulator
FMRC	Factory Mutual Research Corporation
gpm	Gallon Per Minute
H&S	Health and Safety
ILTD	Inversely Linear Thickness Decay
IMO	International Maritime Organization
K-H	Kelvin-Helmholtz
LHS	Left Hand Side
LNG	Liquefied Natural Gas
LPC	Loss Prevention Council
MMD	Mass Median Diameter
NFPA	National Fire Protection Association
NFSA	National Fire Sprinkler Association
PDF	Probability Density Function
PDI	Phase Doppler Interferometer
PIV	Particle Image Velocimetry
PMT	Photomultiplier Tube

PTVI	Particle Tracking Velocimetry and Imaging
PMS	Particle Measuring Systems
R-P	Rayleigh-Plateau
RHS	Right Hand Side
SMD	Sauter Mean Diameter
T-S	Tollmmien-Schlichting
VMD	Volume Median Diameter
US	United States

1 INTRODUCTION

The current chapter briefly reviews the most popular methods in use for fire protection and suppression/extinguishment. These methods include halon (§1.1.1), carbon dioxide (§1.1.2), foams and chemical (§1.1.3), and water based fire suppression systems (§1.1.5). The selected methods have been investigated in terms of their prospective applications, mechanisms through which they suppress the fire and their main advantages and disadvantages. In the past two decade extensive attention has been given to water (as an agent) in suppression systems. The effectiveness of water is primarily due to its high thermal capacity. It is noteworthy that water sprinklers are also part of the water based fire suppression systems, and they are the subject of current dissertation, hence they are exclusively reviewed in §1.2 with more details. In the current chapter sprinklers have been investigated in terms of their head construction and configuration, water feeding systems, and the sprinklers temperature rating. After reviewing the fire suppression methods and an introduction to fire sprinkler technology, the objectives of the current research are outlined in §1.3 followed by the structure of the thesis in §1.4.

1.1 Background of Fire Suppression Methods

There are a wide variety of different methods in use to suppress different class of fires. Conceptually, these methods operate by removing one of the elements of the 'fire tetrahedron'. Fire tetrahedron, Figure 1-1 is comprised of fuel, oxidizing agent, heat and the chain of chemical reaction.

Figure 1-1: The fire tetrahedron. [1]

The installation of fixed fire suppression systems in some buildings and spaces is often mandatory by health and safety (H&S) legislation, the local fire authority, insurers or other regulators. A summary of the selected types of fire suppression system is provided below. Each system has unique advantages and dis-advantages particularly concerning the type (or class) of fires they are effective against. The systems below are available in use in portable hand-held fire extinguishers and/or as a total flooding agent [2], [3].

1.1.1 Halon

Halon was in use as both hand-held fire extinguishers and as a total flooding agent in enclosures where a rapid quenching is desirable, or where other systems such as water were unsuitable. Two compounds of Halogen such as Halon-1211 [4] and Halon-1301 [5] are very effective fire suppression agents. The suppression mechanism of the Halon is due to its interference in the fire chemical reaction rather than diluting the oxygen/fuel or attempting to cool the fire. They can be used on many classes of fires, with the main exception being metal fires [6]. At high temperatures, the Halons decompose into radicals that promptly combine with the hydrogen radicals [7]. It is noteworthy that the free-radicals are able to

react with ozone and deteriorate the ozone layer. Due to this property the restrictive policies [8] phased out the usage of Halon.

1.1.2 Carbon Dioxide

In response to the halon phase-out, the fire protection industry proposed a number of alternative technologies which include carbon dioxide (CO_2) systems. CO_2 requires much higher concentrations compared to Halon to be effective, typically higher than 23% by volume [9] as demonstrated in Figure 1-2.

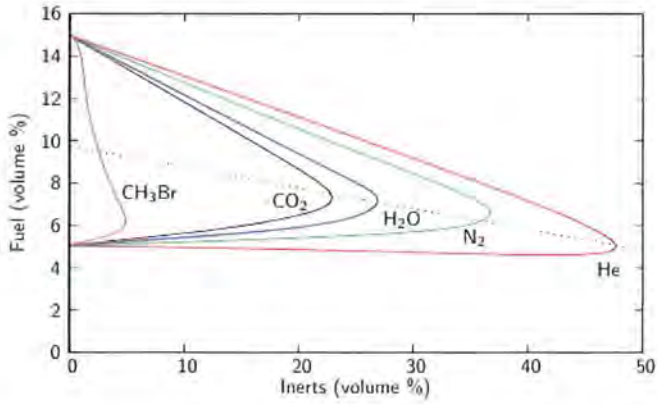

Figure 1-2: Flammability limits of various methane/air/inert gas mixtures at atmosphere pressure and 26 °C [10]

At these levels it can cause death by respiratory paralysis, and so is not suitable for occupied spaces [6]. Carbon dioxide is not suitable in areas that may contain an explosive atmosphere because it is known to produce electrostatic charges [9], however is not conductive. CO_2 penetrates to the hazard area within seconds and has no environmental impact. CO_2 systems are being used in power generation plants, metal protection and, marine systems, research facilities, etc.

Flame extinguishment by CO_2 is predominantly by a thermo-physical mechanism in which reacting gases are prevented from achieving a temperature high enough to maintain the free radical population necessary for sustaining the flame chemistry. CO_2 also dilutes the concentration of the reacting species in the flame, hence reducing collision rate of the reacting molecular species and slowing the heat release rate [11]. A CO_2 fire suppression system consists of one or more banks of cylinder storage containers. Flexible discharge hoses connect the cylinders into a piping manifold and nozzles regulate the flow of CO_2 into the protected area. [12]

1.1.3 Foams/Chemical

Powder and Foam systems operate by coating the burning object in a blanket (forming a barrier on the fuel surface) of the powder or foam and hence contribute to smothering of the flame/fire (producing inert vapor within the combustion within the combustion environment) [6].

They are effective against liquid fires or large solids, and unlike Halon or CO_2 do not require an enclosure to be effective [13], as foam will mix with water and then expand over the liquid that is on fire, cool the fire, and will finally suffocate it [14]. They are often used in Liquefied Natural Gas (LNG) storage, marine applications and warehouses.

Foam Fire Sprinkler Systems offer a proven technology for the control of burning flammable liquids. They operate by mixing a foam concentrate at specific proportions with water to create a foam blanket that smothers a fire. [14]

1.1.4 Heptafluoropropane

Heptafluoropropane (DuPont™ FM-200®), an alternative to Halon 1301, came under attention as the fastest fire protection available as reaches extinguishing levels in 10 sec [15]. It is a waterless fire suppression system which provides a non-toxic product, zero ozone depletion potential, leaves no residue or deposits upon discharge, and can be used for the protection of data processing and telecommunication facilities due to its non-conductive and non-corrosive property [16].

FM-200 requires a concentration range of between 6.25% and 9.0% for effective fire extinguishment. The upper limit of 9% concentration is the maximum allowable by the Environmental Protection Agency (EPA) without the need for a mandated egress time [17]. The FM-200 fire extinguishment is a physically acting suppression agent that absorbs heat energy from fire.

1.1.5 Water Based Fire Suppression

The effectiveness of water as a suppression agent is primarily due to its high thermal capacity and latent heat of vaporization. According to Grant et al. [3] the basic suppression mechanisms for water based fire suppression are combination of

followings: (i) wetting of adjacent combustible surfaces, (ii) cooling the fuel surface, (iii) cooling the flame zone, (iv) flame smothering (volumetric displacement of the oxidant), (v) radiation attenuation, (vi) and fuel blanketing. The characteristics of the initial spray determine the effectiveness of these mechanisms. For example, small droplets have higher surface to volume ratios, resulting in better cooling, oxygen depletion, and radiation attenuation performance. However the momentum of the smaller drops may be insufficient to penetrate the fire plume, (a gas-dynamic barrier).

Three main water-based suppression systems are employed nowadays: (i) sprinkler systems, (ii) water mist and (iii) water hose systems. The sprinkler system which is the subject of this study will be further discussed in §1.2. The spectrum of droplet sizes is shown in Figure 1-3. The average size range from 100 to 1000 μm was reported to be of most interest in fire suppression [3].

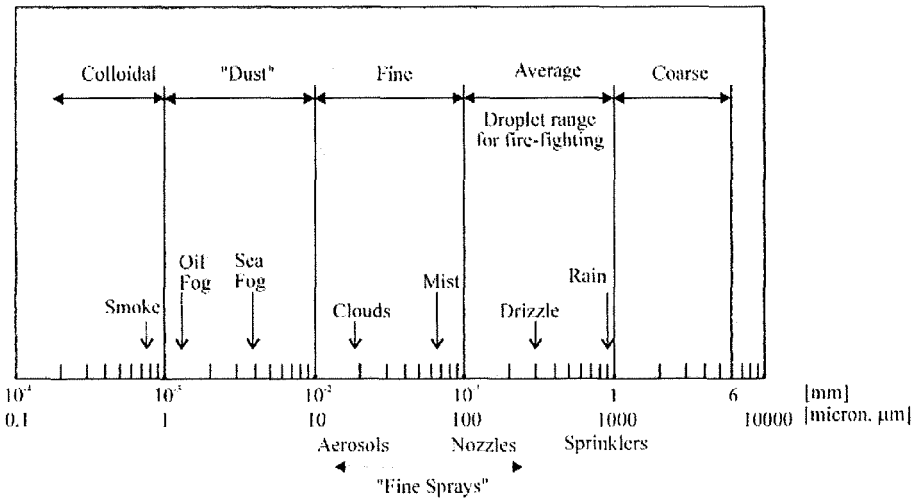

Figure 1-3: Spectrum of droplet diameters [18]

Water Mist Systems

The interest in water mist as a firefighting technology has been driven by its potential as a replacement for environmentally harmful halon-based systems. Hence, water mist systems have become popular in recent decades.

Much of the research that has been carried out over the last decade concentrates on nautical applications (e.g [19], [20]). This is due to a strong interest from the US Navy, US Army, International Maritime Organization (IMO) and the US Coastguard, in particular for engine rooms and on submarines where minimal

water usage is essential. There are other areas of interest including historic buildings and museums [21], Chinese restaurants [22], and aircraft engine nacelles [23].

The major suppression mechanism of water mist is to cool the fire plume. The tiny droplets that have a large surface to volume ratio evaporate very fast and absorb a large amount of heat reducing the plume and flame temperature. Meanwhile, a large amount of vapor is also generated, reducing the oxygen concentration, especially in a confined compartment. Without enough oxygen, the fire would be easier to control. Also, the water mist system requires a low flow rate, which means less water damage compared to sprinkler systems. The disadvantages of the water mist system are the high injection pressure it requires and the high cost relative to the sprinkler system. [24]

A general design method is not yet recognized for water mist protection systems [25], and any formal guidelines, such as NFPA-750 [26], tend to refer designers to manufacturers' information.

Victaulic Vortex Fire Suppression System

The Victaulic Vortex Fire Suppression System is the newest of the fire extinguishing systems available on the market. It is a unique combination of mist fire suppression and clean agent [Nitrogen (N_2)] Fire Suppression technologies. This technology uses a fine water drop that will absorb more heat while the nitrogen will reduce the oxygen feeding the fire. [27]

The pressurized N_2 atomizes water droplets to an average size of 10μm. Furthermore, N_2 lowers the oxygen (O_2) content below 16% (minimum threshold to support combustion), where human life support can be sustained in O_2 concentrations as low as 12%. A typical Vortex system will target the depletion of oxygen in a room to 14% which is low enough to eliminate combustion yet high enough to sustain human occupancy. N_2 supply is the greenest of the fire extinguishing mediums, as the atmosphere is made up of 79% N_2 it has a zero ozone depletion rating. Water is expelled at a rate of 0.227 m^3/h [~1 US gallon per min (gpm)] so that the residual effects of water in the hazard are minimal. The unit, US gpm have been quoted often in this text, as it is extensively common in the literature. This unit is different from Imperial gpm, 1 Imp gpm = 0.272 m^3/h.

Water Hose Systems

The water hose system is mostly used by fire fighters to extinguish fires because of the large amount of water they can deliver. Nowadays, new technologies for water hose systems are being developed. One new system is called water cannon that can automatically search for the location of a fire. The computer can automatically calculate and control the injection pressure needed to deliver the water to the fire. This system is more effective than sprinklers and water mist when the fire is in an early stage and is easier to control. These systems are still under development and their performance still needs to be evaluated. [3] & [24]

1.2 Water Sprinklers

Water sprinklers are one of the most commonly used fixed-installation fire suppression systems which maintain minimum fire protection to buildings. They have been in use for over a hundred years. The purpose of the sprinkler was expanded not only to prevent fire spread, but also control and suppress the fire.

One of the main disadvantages of water sprinklers is the large quantity of water used. This can lead to extensive damage beyond that caused by the fire itself. According to Hart [6], when sprinklers fail to operate, the reason most often given (53% of failures) is shutoff of the system before fire began.

The design of a sprinkler installation will depend on many factors such as the amount of stored flammable materials, risk to human personnel and the presence of items such as hot oil baths, exposed electrical systems etc., which in combination with a sprinkler systems are hazardous [28]. Design standards such as British & EN Standards ([29]&[30]), Loss Prevention Council Rules (LPC rules), National Fire Sprinkler Association (NFSA), FM Global Standards and Residential & Domestic Sprinkler Systems [31] give detailed requirements for the design and installation of sprinkler systems for various different classes of building.

As the fire sprinklers are the subject of the current dissertation, they are discussed in more detail in the following subsections.

1.2.1 Water Sprinklers Head Construction

Sprinkler concept started by pipes with a series of holes where the water would pumped in the system manually and would eject out in an upward direction. The holes were approximately 3.2 mm and spaced at intervals between 75 mm to 255 mm. The activation of this system was time consuming, despite that the water could have directed into the building and directly over the burning commodity. By the time that water is released the fire would gain a significant headway and the holes would have clogged resulting in deficiency of water distribution pattern. [32]

The perforated pipes have been sealed by coating the holes with tar and pitch. The tar would melt letting the holes located above the fire activate directly in a fire scenario. The major disadvantage of the system is that the delayed system activation could cause melting much of the tar, leading to the activation of more holes than desirable.

The early open sprinkler heads had metal bulbs with numerous perforations which provided better water distributions. This has been followed by the first automatic heat actuated sprinkler (1870s), whose head consisted of a spinning cup. In the successive years solder sealed sprinkler head, tined deflector and three piece fusible elements were developed.

In 1890, Frederick Grinnell patented an upright sprinkler head, which had a glass valve seat. In those days the sprinklers were designed in a way to spray 60% of water below the sprinkler, and 40% of the water continued in an upward direction to wet the timbers at the ceiling. Grinnell 1907 and 1915 sprinklers are shown in Figure 1-4-(a&b). The small tined deflector allowed water to be directed downward, while also permitting water to spray upward to wet the ceiling. Figure 1-4-(c) shows an early day Rockwood sprinkler which is identifiable by its distinctive four-piece fusible element [32].

Figure 1-4: a) Grinnell 1907 and b) 1915 sprinklers c) Rockwood 1912 [32]

Since the first sprinkler (an upright sprinkler), aimed at delivering the spray to the ceiling to prevent fire spread upstairs, the design of the sprinkler did not change until 1950, when improvements of the sprinkler performance were better understood.

In the typical modern day sprinkler head still consists of the heat sensitive operating element (Figure 1-5). Two trigger mechanisms are commonly used:

- A vacuum sealed glass tube filled with a glycerin-based liquid which has an air bubble trapped, shown in Figure 1-5-(a), so that the bubble expands as heated and shatters the glass. In the average sized room, a 5 mm diameter glass tube will usually break in about 60 to 90 sec from contact with a heat source. Glasses as thin as 1 mm are manufactured for a faster response time. Activation temperatures correspond to the type of hazard against which the sprinkler system protects. Residential occupancies are provided with a special type of fast response sprinkler with the unique goal of life safety that often activates at about 57 °C.
- The solder plate, Figure 1-5-(b), which melts at elevated temperatures, and has similar role as the aforementioned three to four piece fusible elements.

The plug is forced out, Figure 1-6, by the pressurized water behind it and deflected away by a beveled edge. The immediate cooling of the heat source usually prevents other sprinkler heads from activating. Often, one or two sprinkler heads are sufficient to control a fire.

Figure 1-5: Schematic view of a pendant sprinkler with a) glass and bulb b) solder plate. [33]

Figure 1-6:Sprinkler automatic activation mechanisms in (a) bulb break up mechanism and (b) triggering mechanism [33]

1.2.2 Sprinkler Heads

Configurations

Sprinkler heads are classified in three configurations, namely Upright, Pendant and Horizontal sidewall sprinklers.

- **Upright Sprinklers** are installed with the deflector above flow pipe, so that flow directs upward from sprinkler orifice, striking the deflector and discharging water in an upward pattern (example Figure 1-7-(a)).
- **Pendant Sprinklers** are installed with the deflector below the frame so that flow downwards from the orifice, striking the deflector and

discharging water in and umbrella-shaped pattern, similar to upright sprinklers (example Figure 1-7-(b)).

- **Horizontal Sidewall Sprinklers** are installed near the wall and near the ceiling. The axis of sprinkler is oriented parallel with ceiling and provides a water spray pattern outward in a quarter-spherical pattern (example Figure 1-7-(c)).

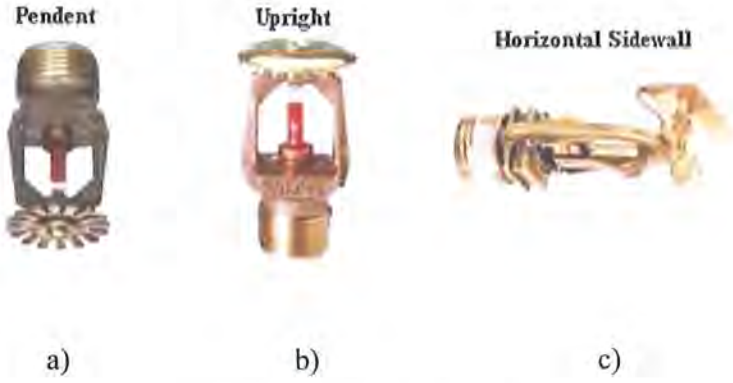

Figure 1-7: Sprinkler head configurations

Sprinkler Head Types

Different ranges of sprinkler heads have been developed to generate droplets with different sizes and spatial locations. To maintain penetrating in the fire plume, the droplet diameters has to be large enough to have higher velocity than upward plume velocity. In other term the droplet initial momentum has to be high enough to penetrate the fire plume and wet the surface of burning commodity.

Quick Response Sprinklers are designed with a fast-acting heat actuating element and considered a special purpose sprinkler. More information on the dynamics of spray could be found in [34], [35] and [36].

Extended Coverage Sprinklers are specially designed to discharge water over a greater area than conventional sprinklers. They are used in light hazard occupancies with smooth level ceiling.

Quick Response/Extended Coverage Sprinkler heads are limited to light hazard occupancies and combine the attributes of the two sprinkler heads listed in above.

Large Drop Sprinklers are designed to discharge water in a downward umbrella shaped pattern. Large drops have a higher mass, hence they are effective in

penetrating sever fires. The high challenge fires produce strong plumes and convective currents which will deflect away standard water droplets before they can reach the fire seat.

Early Suppression Fast Response (ESFR) Fire Sprinkler Systems:

Most sprinklers are intended to control the growth of a fire, but an ESFR sprinkler system is designed to suppress a fire. To suppress a fire does not necessarily mean it will extinguish the fire but rather to extinct the fire back down to smaller sizes. ESFR sprinklers are predominantly used for protection of high piled storage in place of in-rack fire sprinkler systems (see below) [37]. These fire sprinklers use large volumes of water (nearly 100 gpm ~ 22.7 m^3/h) per sprinkler and incorporate very large high volume, high-pressure heads to provide the necessary protection. Accordingly these systems require large water supplies and often require the installation of fire pumps. [38]

In-Rack Fire Sprinkler Systems:

Warehouse fires are extremely challenging due to their quick spread and immense increases in heat release rate over a short period of time. In-rack fire sprinkler systems are specifically designed for the protection of racked storage areas in warehouses. In-rack fire sprinklers prevent the spread of fire to other areas and will extinguish it. While ESFR Sprinkler Systems will sometimes eliminate the need for In-Rack sprinklers, the later typically are used when the storage of certain commodities exceeds 12 m in height where ESFR sprinklers cannot be employed as a protection scheme. [39]

1.2.3 Terminologies and Conventions

Nomenclature

Essential terminologies in fire sprinkler studies are shown in the Figure 1-8.

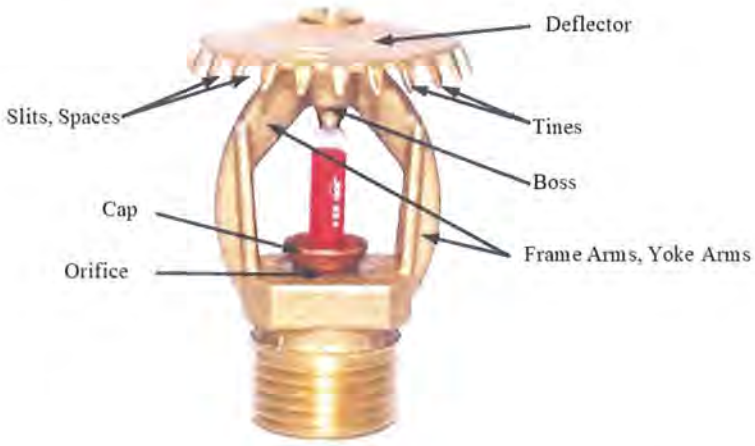

Figure 1-8: Essential nomenclature of fire sprinklers

The components which may affect the spray pattern in the sprinkler atomization process are listed as following:

- Number of slits,
- configuration of the tines (width, depth, number, tilt angle),
- diameter of the deflector,
- Deflector rise to center (tilt angle)
- diameter of the orifice,
- the shape of yoke arms (thickness and widths)
- the shape of boss (height, angle)

Sprinkler K-factor

The sprinkler orifice is designed to provide a known water flow rate at a given water pressure. The numerical designation given to represent the hydraulic characteristic of a sprinkler is called the *K*-factor. Sprinkler orifices conform to Bernoulli's equation, which states that square of the velocity of the water through the orifice is proportional to the water pressure, P [40]. For sprinkler design applications the volumetric flow rate, Q in [m^3/s] or [Lpm (Liter per minute)], is more relevant than the velocity. Therefore for design applications, Bernoulli's equation is written as:

$$Q = K\Delta p^{1/2} \tag{1-1}$$

The K-factor is nearly constant for the range of operating pressures used in sprinkler applications. It is common to describe flow characteristic by sprinkler K-

factor, rather than its diameter. The K-factor is nominally proportional to the square of the orifice diameter. This factor is usually expressed in $m^3s^{-1}kPa^{-1/2}$ or $gal.min^{-1}.psi^{-1/2}$. The K-factor for sprinklers may range from 5.6 $gal.min^{-1}.psi^{-1/2}$ (standard ½" orifice) to 14 $gal.min^{-1}.psi^{-1/2}$ for ESFR sprinklers. The conversion to other units, including SI, can be achieved using Table 1-1.

Table 1-1: Common K-factor units' conversion rates

K-(gpm-psi$^{0.5}$)		**K-(liter/min-kPa$^{0.5}$)**		**K-(lit/min-bar$^{0.5}$)**	
1	gpm	3.7854	liter/min	3.7854	liter/min
1	psi	6.8948	kPa	0.068948	bar
1	K-gpm/psi	1.44	liter/min /kPa$^{0.5}$	14.4	liter/min /bar$^{0.5}$

An increase in the K-factor of a sprinkler yields a higher flow and lower pressure. Conversely, the decrease in the K-factor yields a lower flow rate and higher pressure. The pressure at the sprinkler head affects the droplet size and spray pattern. These parameters are crucial spray characteristics in studying the suppression and extinguishment performance of sprinklers. [41]

Conventions

The initial spray is generated in about a semi-sphere below the sprinkler and can be characterized the same as its nature. Therefore, the spatial locations are expressed in spherical coordinate throughout this dissertation. In Figure 1-9 the origin of the coordinate is the sprinkler location. The r-r' plane is orthogonal to the downward water jet. In current reference system the r-r' planar angle, Φ, is called azimuthal angle and the θ is known as elevation angle.

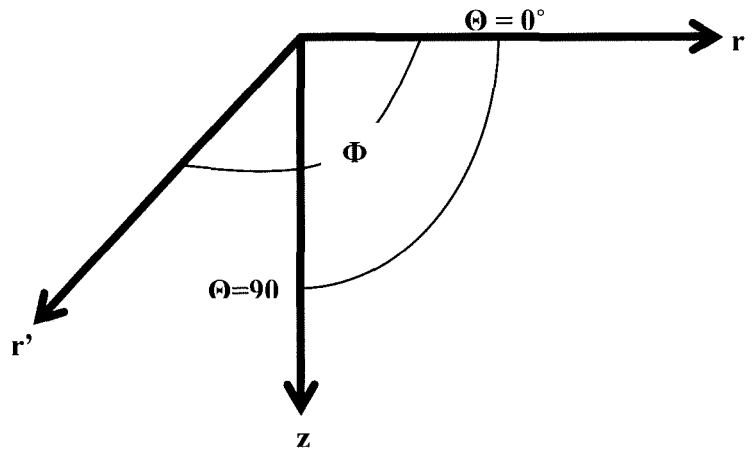

Figure 1-9: Graphical representations of elevation angle (θ) and azimuthal angle (Φ)

1.2.4 Water Sprinkler Systems

Different types of sprinkler systems have been designed for a broad range of fire scenarios. In some industrial buildings a manually activated system may be preferred. This is known as a deluge system, because all sprinkler heads on the same water supply circuit activate simultaneously. Some of the most widely used systems are Wet Pipe, Dry Pipe, Deluge and Recycling [42], Quell [43] and Pre-action [44] Fire Sprinkler Systems.

Wet Pipe Fire Sprinkler Systems are the most common fire sprinkler system. In a wet pipe system water is constantly maintained within the sprinkler piping. When a sprinkler activates this water is immediately discharged onto the fire. The main drawback of wet pipe systems is that they are not suited for sub-freezing environments. There may also be a concern where piping is subject to severe impact damage and could consequently leak [45].

Dry Pipe Fire Sprinkler Systems are filled with pressurized air or nitrogen, rather than water. This air holds a remote valve, known as a dry pipe valve, in a closed position. At elevated ambient temperatures the dry-pipe valve prevents water from entering the pipe until a fire causes one or more sprinklers to operate, where the air escapes and the dry pipe valve releases. Water then enters the pipe, flowing through open sprinklers onto the fire. They provide automatic fire protection in spaces where freezing is possible, however they have increased complexity, higher installation and maintenance costs, increased fire response time and increased corrosion potential compared to wet pipe systems [46].

1.2.5 Sprinkler Temperature Ratings

As discussed in section (§1.2.1), sprinkler heads activate either shattering the glass bulb or melting a metal alloy. NFPA-13 has recommendation for the temperature classification of sprinklers depending on the environment, as shown in Table 1-2.

Table 1-2: NFPA Temperature classification [40]

Temperature Rating	Temperature Classification	Color Code (with Fusible Link)	Glass Bulb color
57-77°C	Ordinary	Uncolored or Black	Orange (57°C) or Red (67°C)
79-107°C	Intermediate	White	Yellow (79°C) or Green (93°C)
121-149°C	High	Blue	Blue
163-191°C	Extra High	Red	Purple
204-246°C	Very Extra High	Green	Black
260°C-Above	Ultra High	Orange	Black

1.3 Motivation, Aims and Objective of the Thesis

1.3.1 Motivation of the Research

Among the present fire suppression systems the sprinklers are cheap, reliable and easy to install maintain and operate, hence are widely used in residential and warehouse applications. Depending on their applications and expected performances, the design of sprinklers would change in terms of configuration parameters listed in §1.2.3.

The performance of these suppression systems is primarily evaluated through both full-scale spray dispersion tests (without fire) and actual fire suppression tests. It is difficult to extrapolate the spray dispersion test performance to real fire scenarios because of the potential of strong coupling between the fire and the spray. Moreover, these spray dispersion tests are expensive to conduct, making it difficult to test all sprinkler sprays. The characteristics of the initial spray formed by sprinkler are more challenging to determine not only experimentally but also theoretically. These initial distributions are very difficult to obtain experimentally for every sprinkler due to the high spray density in the atomization region.

Predictive models are needed to evaluate the initial spray characteristics of sprinklers for coupling with fire models to predict the suppression performance.

Developments in Computational Fluid Dynamics (CFD) modelling make it possible to simulate fires with a high degree of fidelity. However, before CFD tools can be employed for fire suppression, the detailed physics involved in spray atomization and spray dispersion must be clearly understood. Then the descriptive models for the spray would be implemented into CFD codes to predict the performance of water based fire suppression systems. Droplets dispersion models are well defined for tracking the drops after the initial spray formation, and they have already been included into some CFD models. But there is no general model to predict the initial spray properties for deflecting injectors. As a result, the initial atomization model is a critical missing link in the modelling of sprinkler/fire suppression.

1.3.2 Aims and Objectives of the Research

Aims:

The main goal of the present PhD study is to develop the sprinkler spray atomization models to predict the initial spray characteristics taking into account the configuration aspects of real sprinklers and the ambient temperature.

Objectives:

The spray characteristics to be predicted are the initial droplet diameter, velocity, initial droplet location and spray volume flux.

Methodology:

Theoretical models have been developed which resembles the constituent physics of the spray. The research validated the proposed models and improved the overall modelling capability for initial sprinkler spray.

1.4 Layout of the Thesis

The rest of the thesis content below are presented in four chapters.

Chapter two explains the physics of spray for jets, films and sheets. State of the art literature for sub-physics would be summarized. Different class of atomizers would be explained and the fire sprinklers are addressed to be similar to impinging jet atomizer class. In addition to this a range of experimental and theoretical literature dedicated to sprinklers spray quantification has been studied in depth.

Chapter three reviews and presents the mathematical approach developed in the present study for sprinkler spray modelling.

Chapter four verifies and validates all the sub models and approaches developed and introduced in chapter three.

The main findings of this dissertation have been summarized in chapter five and final conclusions are made. In addition to this, suggestions are provided for further studies.

2 LITERATURE REVIEW

This chapter discusses the state of the art methodologies available to quantify the initial sprinkler spray characteristics. Sprinklers are regarded as the devices which produce sprays and could be categorized as a class of atomizers. Extensive literature is available on the sprays formed from classical atomizers types such as airblast, pressure-swirl, diesel and impinging atomizers. The term airblast atomizers are used primarily to describe operating condition (a high speed gas contributing to the atomization process) and are classified to two main geometrical subtypes (pre-filming and nonprefilming). Pressure-swirl atomizers describe the upstream geometry prior to the atomization, where a swirling annular sheet is formed following the tangential injection of liquid into a nozzle. Diesel atomizers describe both operational and upstream condition and generally represent a multi-hole injector and often imply that the liquid is pulsed. A good overview of a multitude of traditional atomizer types is given in [47]. The impinging atomizers and the pertinent literatures have been investigated in the course of this chapter as the sprinklers show a great resemblance to this category of atomizers.

The current chapter starts with a brief introduction to the instabilities lead to the fluid disintegration §2.1. Three main physics can be identified in the sprinkler spray formation process, i.e. jets, films and sheets. The underlying physics involved in atomization of jets (§2.2.1), sheets (§2.2.2) and films (§2.2.3) would be summarized. The researches which quantified the sprinkler spray

experimentally have been reviewed in §2.5. The theoretical studies undertaken relevant to sprinkler sprays are presented in §2.7. The technical specification of the fire sprinklers which have been referenced in the course of this dissertation will be explained in §2.6 dedicated to definitions and conventions.

2.1 Instabilities

Spray formation is due to the presence of disturbances in the structure of the flow. The most common disturbance is hydrodynamics instabilities. Many type of instabilities have been identified, i.e. Rayleigh, Kelvin-Helmholtz (K-H) and Tollmien-Schlichting (T-S). These instabilities lead to the creation of waves. The waves may cause either a large section of the bulk liquid to separate or a small fraction of the liquid to break down. The driving forces of instabilities include surface tension, aerodynamics shear, air turbulence and/or viscous stratification and the relative values of the forces acting in the liquid dictates the type of instability [48]. The Rayleigh mechanism is known to be responsible for the breakdown of ligaments on sheets and films for many operating conditions. K-H instabilities are driven by aerodynamics shear and T-S instabilities arise due to effects of gas phase turbulence. These instabilities would be further discussed in the course of this dissertation where appropriate.

2.2 Atomization

In this section a brief literature of jet, sheet and film atomization is provided.

2.2.1 Jet Atomization

The literature on jet atomization is quite extensive [47]. Articles of Chigier and Reitz [49] or Lin and Reitz [50] discussed jets in quiescent atmospheres, Lasheras and Hopfinger [51] studied jets in co-flow and Faeth [52] investigated jets atomization mechanisms in cross-flow. Whether or not the gas phase is moving, it plays an important role in atomization since it affects the forces on the jet and, consequently, the formation, growth and breakdown of disturbances on its surface. Traditionally, jets are broken into types based on the gas-phase environment –

quiescent, co-flow [49], [50], [51], [52], [53] and cross-flow [52], [53], [54], [55], [56], [57], [58].

Quiescent Environment

Jets exiting into quiescent environments are traditionally divided into four main regimes: (i) Rayleigh breakup, (ii) first wind-induced or non-axisymmetric Rayleigh breakup, (iii) second wind-induced or wind stress, and (iv) prompt atomization [49]. Both the Rayleigh mode [54], Figure 2-1-(a), and the first wind-induced mode, Figure 2-1-(b), are characterized by disturbances on the jet surface which are of the order of the jet diameter, $\eta_0 \cong (D_0)$. These disturbances grow until the column becomes so narrow that the interface meets and a droplet is formed. This droplet is of the same order as the characteristic jet dimension. In the first wind-induced mode the breakup occur many nozzle diameters downstream of the nozzle.

In certain circumstances small satellite droplets will also be formed. The disturbances on the surface are caused by hydrodynamic instabilities. In the Rayleigh mode the instabilities are purely driven by surface tension forces; in the first wind-induced mode aerodynamic effects are important and enhance disturbance growth and may alter the instabilities.

Disturbances and droplets are much smaller than the jet diameter in the second wind induced regime. In this regime, aerodynamic effects dominate surface tension effects and a large number of small disturbances appear on the surface of the jet. These small disturbances are enhanced due to the relative velocity between the jet and the environment and eventually break up into small droplets at some distance downstream of nozzle. Perturbations may be caused by liquid turbulence [52], hydrodynamic instabilities [56] or the interaction of gas-phase vortices and the interface [59].

In the final regime, prompt atomization, the jet disintegrates immediately upon exiting the nozzle with no observable intact length (Figure 2-1-d). Reitz and Bracco [60] performed a thorough analysis of this regime and suggested that the atomization is not actually instantaneous, but that some intact length exists on which disturbances quickly form, grow and breakdown.

Figure 2-1: Jet breakup regimes (a) Rayleigh, (b) First wind-induced, (c) Second wind-induced and (d) Prompt atomization. [50]

2.2.2 Sheet Atomization

Liquid sheets are produced by a wide variety of spray nozzles, e.g. fan-spray nozzles, swirl spray nozzles, spinning cups and impinging jet atomizers. Sheets are characterized by a liquid with two characteristic dimensions and multiple interfaces in contact. The most notable difference in liquid jets and sheets breakup mechanisms is that the surface tension is stabilizing in sheets with Weber numbers greater than a critical value, which is dependent on fluid properties and flow conditions [61].

Two different configurations are commonly encountered in sheet atomization: flat and annular. Most of the breakup phenomena are similar [62], however the main

focus of this section would be flat sheets because of the similarities they share with the physics relevant to sprinkler sprays.

The major regimes cited for the flat sheets are as following:

Surface mode: Small disturbances exist throughout the surface of the sheet and produce small droplets [63], where the surface perturbations may arise from liquid turbulence. [64]

Wavy sheet mode: where hydrodynamic instabilities grow and cause a section of the sheet to separate from the bulk [65]. This section extends over the span-wise dimension of the sheet and further breaks up into droplets following separation. Since surface tension is generally stabilizing in sheets [61], the instabilities are usually considered a result of the velocity difference between the liquid and gas. The wavy sheet regime is sometimes broken into three sub-regimes depending on the type of waves present – sinusoidal, dilatational or both. This regime has received the most attention in the sheet atomization literature and is implemented in numerous numerical calculations, i.e. [48], [66], [67].

Stretched-streamwise ligament & cellular regimes: involve the formation of cell-like structures bounded by thicker rims [63-64, 67]. Due to sheet flapping and aerodynamic effects the membranes of the cells may be stretched. The stretched-streamwise ligament regime strongly resembles a series of bag-breakup events where a number of cell membranes rupture leaving a network of small ligaments which break up into droplets. Similar cellular structures may occur at lower gas velocities when streamwise ligaments are less obvious or nonexistent; in that situation, the regime is generally titled perforated [68]; the holes in the sheet grow until they produce a random network of ligaments and some small droplets. In these regimes, the bulk of the discrete parcel volume comes from the ligaments, but membrane rupture or the collision of the rims produced by growth of the hole produce a series of smaller droplets. The cellular regime is characterized by a cell-like structure with much less pronounced streamwise ligaments than the stretched-streamwise ligament regime. When the cell membranes rupture they may again be bag-like, but they produce a single, span-wise ligament instead of a network of ligaments [65].

2.2.3 Film Atomization

The literature on film atomization mechanisms generally considers a surface mode where small disturbances on the film surface evolve into droplets e.g. [69].

Bulk fluid mode: In this mode a span-wise disturbance would grow until a large, span-wise ligament separate from the film. In some instances this ligament might be air borne, but it is more likely that it would occur when the disturbance reached a size where part of the interface contacted the wall. In this case, the ligament would be bounded by the wall and less likely to produce droplets than a free ligament due to the additional solid-liquid-gas surface tension.

Perforation-controlled breakup might also occur with the film rupturing into a series of ligaments or, since likely to be wall-bounded, rivulets. Despite holes occurring more commonly in films than sheets due to wall unevenness and spontaneous de-wetting [48], the extra surface tension created by the wall contact would slow any breakdown of perforations into droplets thus creating no or larger droplets than in the jet or sheet bag-breakup case.

Rivulet breakdown would also differ from ligament breakdown and might not produce droplets. A mixed mode based on perforations is therefore possible, but unlikely in films; the less wetting a liquid-wall combination is, the more likely this mode would occur. One final regime implied by the literature is a prompt regime [48].

2.3 Impinging Jet Atomizers

This type of atomizers is very similar to the fire sprinklers, hence have been investigated separately.

2.3.1 Early Studies

Savarat [70], [71], [72], [73] studied the experimental results of several open problems involving liquid jets. A cylindrical water jet of diameter D_0 impinges with velocity U_0 on a flat disc of diameter D_i. The water physical properties are defined by its density ρ_f, dynamic viscosity μ, kinematic viscosity ν and surface tension σ. The initial state of the jet is characterized with dimensionless numbers,

i.e. Reynolds, $Re_0 \equiv \rho_f U_0 D_0/\mu$, and Weber, $We_0 \equiv \rho_f D_0 U_0^2/\sigma$, that compare inertial to viscosity and surface tension respectively. Depending on the geometrical diameter ratio $X \equiv D_i/D_0$, different scenarios could occur.

The singular limit $X = 0$, shown in Figure 2-2-(b) is characterized by capillary instability of cylindrical liquid jets [70] and [74].

Savarat studied the impact of liquid jet on a circular solid surface with limits $X \sim 1$ [71], [72] and $X \gg 1$ [73]. In the $X \sim 1$ condition the liquid film is ejected from the deflector with the angle Ψ_0 and symmetrical water bell could be observed as shown in Figure 2-2-(c) [71], [72]. The dynamics and stability of water bells have been extensively investigated by Clanet [75]. The $X \gg 1$ condition, Figure 2-2-(d), leads to so-called hydraulic jump phenomenon, where a thick and quiescent layer of fluid is connected to the jet through a thin and rapid layer. The size of this stationary connecting region critically depends on both the injection parameters and the limit conditions at infinity. This has been explained in more depth in chapter three.

Figure 2-2: Structure of liquid jets impinging on a flat disc from Savarat: (a) sketch of the experiment; (b) Capillary water jet instability [70], (c) water bell [71], [72], (d) hydraulic jump [73].

2.3.2 Classification of Impinging Atomizers

Impinging jet atomizers can be classified as (i) two-impinging jets where two jets in opposing directions collide, and (ii) single jet hitting a surface as classified in Figure 2-3. Two similar configurations for a single jet hitting a flat disc are reported in the literature: a splash plate and jet impingement on a wall. In a splash plate geometry a jet impacts a disc and spreads to form a sheet. Splash plates are in between that of impinging jets and a jet impacting a wall [48] and share similar physics with fire sprinklers. In general four mechanisms have been reported based on the type of impingement and the velocity of the jet.

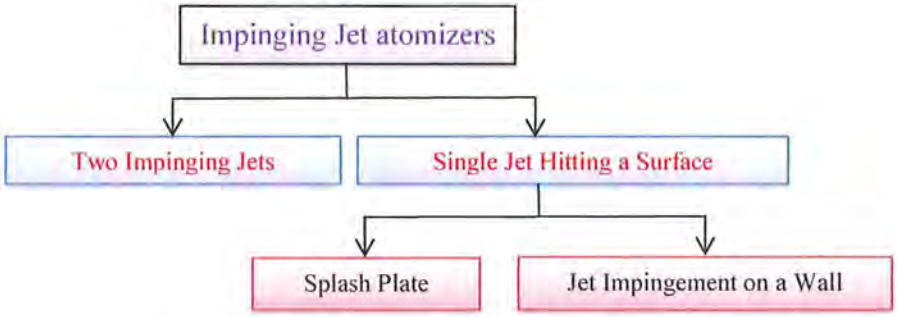

Figure 2-3: Impinging jet atomizers classification.

At low jet velocities the jet will conform to sheet after impingement. The sheet will falls into a jet subsequently. Atomization occurs after the sheet has transformed into jet.

The second reported mechanism is the so called rim atomization regime and characterized by periodic or random shedding from the edge of the sheet. Three modes are identified where sheet is thinned substantially at the periphery and undergo a disintegration [24], [76]:

i) Ligament: where ring like ligaments are formed at the breakup point. This mode is dominated by K-H breakup.

ii) Rim: where drops are formed directly at the edge of sheet. This mode is a result of Rayleigh-Plateau (R-P) breakup.

iii) Perforations: where irregular ligaments are formed at the location of sheet breakup. This mode is a transitional from K-H to R-P breakup.

In scenarios where two turbulent jets collide, a periodic regime is often reported, where droplets shedding from the edge of the sheet occur in a regularly spaced type.

The last regime to be mentioned in this section has been reported for the impingement jet with very high velocity, where catastrophic breakup takes place. This regime may be known as fully developed regime in the literature. The characteristic of this regime is that periodic waves of droplets is expelled from the point of impingement and no sheet is evident [67, 77].

2.4 Sprinkler Spray

Modeling atomization in fire sprinklers is a challenging task because of the complexity and stochastic behavior of the breakup process, which is influenced by sprinkler geometry, injection pressure drop, surrounding flow gas phase and liquid properties. It has been mentioned that sprinklers could be classified as impinging jet atomizers. Impinging atomizers are mainly discussed from view point of two impinging jets in the literature, but the outcomes apply equally to a single jet hitting a splash plate.

Essential features of the atomization process relevant to fire sprinklers are shown in Figure 2-4 where a liquid jet is orthogonally injected onto a flat disk. After impact, the jet is transformed into a thin film, moving radially outwards on the deflector surface. This film formation is the first stage of the atomization process.

Figure 2-4: Simplified sprinkler atomization physics. [77]

The film is transformed into an unconfined sheet as it expands beyond the deflector edge. A sinuous wave grows on the decaying thickness sheet due to existing inertia, viscous and surface tension forces as well as pressure difference between the sheet upper and lower surfaces [78]. At critical wave amplitude, the sheet breaks up into ligaments. As they expand outwards, aerodynamic forces cause dilatational waves to grow along the ligament. When these dilatational waves reach their critical amplitude, the ligaments break into smaller fragments. Due to surface tension, these fragments contract to form drops.

2.5 Experimental Studies on Sprinkler Spray Characterization

Most of the present knowledge on fire sprinkler spray quantification has been gathered through experimental measurements reviewed in the present section. Experimental measurements have been carried out to characterize the droplet size distribution, range of velocities and spray flux for different types of sprinklers.

2.5.1 Droplet Length Scale

Sprinkler sprays are composed of droplets ranging in diameter by over two orders of magnitude. The number of droplets of each size depends on the sprinkler head configuration (§1.2.1), operating conditions and spatial location in the spray.

The quantitative measure of a spherical droplet size is uniquely addressed by its diameter when discussing attributes of spray. For a comprehensive picture of the spray it is usual to quote an average diameter and to provide an idea of the distribution of the droplets in various size ranges, either in terms of histogram or a cumulative distribution curve [18]. Several different average diameters are defined in the literature, which makes it sometimes confusing. These possible equivalent diameters are divided in two categories by Lefebvre [47], namely mean diameters and representative diameters. Examples of common mean diameters and representative diameters used in droplet analysis are listed in Table 2-1.

In spray analysis, the mean diameters are used as a primary indicator of the spray characteristics. For example, when the intended use of the droplet size information

is to determine the mass of transported water, the mean diameter calculated from the volume, d_3, would be appropriate.

The equivalent mean diameters D_{10}, D_{20}, D_{30} for sprays with different size droplets are calculated as ensemble averages as shown in equations (2-1), (2-2) and (2-3) and D_{32} is calculated from the volume diameter and the surface diameter as shown in (2-4).

$$D_{10} = \frac{1}{N}\sum_{i=1}^{N} d_i \tag{2-1}$$

$$D_{20} = \sqrt{\frac{1}{N}\sum_{i=1}^{N} d_i^2} \tag{2-2}$$

$$D_{30} = \sqrt[3]{\frac{1}{N}\sum_{i=1}^{N} d_i^3} \tag{2-3}$$

$$D_{32} = \frac{D_{30}^3}{D_{20}^2} \tag{2-4}$$

Where N is the number of droplets in a sample of spray.

Table 2-1: Equivalent diameters (mean and representative) defining droplet sizes [18], [41]

Symbol	*Name*	*Definition*
$\boldsymbol{D_{10}}$	Diameter	Length Diameter of sphere
$\boldsymbol{D_{20}}$	Surface Diameter	Diameter of a sphere having the surface to volume ratios as a droplet
$\boldsymbol{D_{30}}$	Volume Diameter	Diameter of sphere having same volume as a droplet
$\boldsymbol{D_{32}}$	Surface Volume Diameter	Diameter of a sphere having the volume to surface ratio as a droplet, known also as Sauter Mean Diameter (SMD)
$\boldsymbol{D_{V_{50}}}$	Volume Median Diameter (VMD)	A statistical measure of the average droplet size in a spray cloud, such that fifty percent of the volume of sprayed material is composed of droplets smaller in diameter than the VMD

Representative diameters are conceptually different from mean values and are related to mass (or volume) distribution. Some common ones are $D_{V_{10}}$, $D_{V_{50}}$ and $D_{V_{99}}$, which means diameters below which 10%, 50% and 99% of spray mass (or Volume) resides, respectively. In effect, these diameters are mass (or volume) percentile and can be read off cumulative distribution curves. For sprinkler water

distribution analysis, $D_{V_{50}}$, (sometimes donated as d_m) is the key droplet length scale. It is often named the Volume Median Diameter (VMD) or the Mass Median Diameter (MMD). The calculation method of VMD is further discussed in Appendix-B.

2.5.2 Water Volume Flux

The water flux defines how much water is transported to each location around the sprinkler. From the standpoint of fire suppression, water flux is often considered the most important of sprinkler spray information. The water flux changes as a function of both elevation angle and azimuthal location. A single global value for the water flux of a sprinkler could not fully demonstrate the efficiency of sprinklers in suppressing the fire, and measurements at many locations in the spray are required. [41]

The mass water flux is the mass flow rate of the water through a surface. In simplest terms the mass water flux, $\dot{m}''$, can be quantified as

$$\dot{m}'' = \dot{m}/A \qquad (2\text{-}5)$$

Where $\dot{m}$ is the mass flow rate, A is the area through which the water is flowing.

For Sprinkler applications, the volumetric water flux is a better parameter to report than the mass water flux because the quantity of interest is amount of water coverage. The volumetric water flux is the volumetric flow rate, $\dot{q}$ of the water through a surface. The volumetric water flux, $\dot{q}''$, can be quantified as [79]

$$\dot{q}'' = \dot{q}/A \qquad (2\text{-}6)$$

In practice volume fluxes are quantified by either linearly arranged water panes at far distances, Figure 2-5-(a), or within a spherical coordinate setting at near field, Figure 2-5-(b).

Figure 2-5: Illustration of the overall test setup to measure volume flux (a) measuring pan and (b) spherical coordinate setting. [80]

Following previous researchers [80], [81], the characterization of fire sprinkler initial spray is established on an initiation sphere in this research. The impact of this choice of coordinate systems is that the areas are of different size depending on the elevation angle θ. For a spherical differential area element, $dA = r^2 sin\theta d\theta d\phi$, where r is the radius of the sphere and ϕ and θ are the azimuthal angle and elevation angle. [82]

Two techniques are usually considered for calculating the water volume fraction in sprays from laser sheet images; (i) Calculating the area of the visible droplets in an image and assuming that the sum of volumes is proportional to the water volume fraction, (ii) Counting the number of droplets in a region and assuming the count of droplets is proportional to the volume fraction of water. [41], [83]

Based on the count method of estimating water density, the differential volume of water, dq, in a differential measurement volume, dV is

$$dq = \frac{1}{6}\pi D^3 N' dV \qquad (2\text{-}7)$$

Where D is the average droplet diameter, and N' is the number density of droplets in a unit volume, dV. The differential volumetric flow rate, $d\dot{q}$, through area of, dA can be quantified as [81]

$$d\dot{q}(\theta, \phi) = \acute{N}.\left(\frac{1}{6}\pi d^3\right).U_r(\theta, \phi) \qquad (2\text{-}8)$$

2.5.3 Measurement Techniques

A number of direct (intrusive) and indirect (non-intrusive) methods are available for spray characterization. Experimental works conducted since 1970's to characterize the details of the sprinkler spray, droplet sizes and velocity have improved with advances in optical and laser technology. The methods vary from drop frizzing method [84] and photographic techniques [85] to more sophisticated techniques such as laser-light shadowing method [86], [87], [88], [89], [90], [91], Light diffraction method [92] and light scattering methods including Phase Doppler Interferometer (PDI) [79], [93], [94] and Particle Image Velocimetry (PIV) [41], [95].

2.5.4 Droplet and Velocity Characteristics

The droplet characteristics which are mainly of interest in this section include droplet size and droplet velocity. The droplet size will usually remain the same after initial formation. This is because the droplets would not undergo a second breakup. When referring to the spray velocity one means the initial droplet velocity at the location where the droplet is initially formed. The velocity of spray was reported by several researchers. Unlike the drop size, the droplet velocity changes with measurement location. Velocities may be reported either by their transient radial velocities or by terminal velocities. Terminal velocity is the constant speed a droplet can find when summation of the drag and buoyancy forces is in balance with gravity force. Detailed discussion on relationship between droplet diameter and terminal velocity has being performed by Grant et al. [3] and also being adopted as part of analyses required through the course of current dissertation in the next two chapters.

During the past decades the measurement distances have also been changing in addition to imaging techniques. It has started at far fields and from about 4m below the sprinkler and is reached to near fields at distances about less than 1m.

The early days sprinkler tests were mainly focused to answer; (i) where the water drops will go after they have been discharged from a sprinkler over fire, (ii) whether extinguishment of the fire is by wetting the burning surface or by pre-wetting the nearby unburned fuels. Yao and Kalelkar [84] carried out one of the

first scientific studies on spray formed from sprinklers in 1970. They found that the largest stable droplet is about 6 mm in diameter with a terminal velocity of 10 m/s. The corresponding Weber number for this droplet is about 9. This result is in accordance with theory of Pilch and Erdman [86], who found a droplet with Weber number greater than 12 is not stable and has a tendency to breakup in smaller droplets.

Dundas [85] at Factory Mutual Research Corporation (FMRC) correlated drop size measurements for several sprinkler geometries along in form of Equation *(2-9)* with a review of drop size data obtained in a variety of injectors, based on an expression first proposed by Heskestad [87].

$$D_{V_{50}}/D_0 = C\,.\,We_0^{-1/3} \qquad (2\text{-}9)$$

The drop size compiled data demonstrates that the coefficient of proportionality, *C*, depends on the sprinkler geometry. The coefficient varies in the range of 1.74 < C < 3.21.

Yu's [96] spray measurements show that the coefficient C increases with increasing injection orifice diameter for upright sprinklers and also very little change in drop size at different elevations below the sprinkler suggesting that secondary atomization does not occur in sprinkler sprays. The range of C in his measurements has been reported within a range of 2.33 < C < 4.48. The gross droplet-size distributions of the tested sprinklers have been represented by a combination of the log-normal and Rosin-Rammler distributions. Yu's results have been confirmed by Chan [37]. The drop sizes by Walmsley and Yule [97] are slightly different i.e. $D_{v50}/D_0 = 7.05\,We^{-0.3682}$. In experiments reported by Chan [37], the approximate velocities have been measured at 2.85 m below the two ESFR sprinklers for two water discharge pressures, 1.72 bar and 3.45 bar with a Particle Measuring Systems (PMS). At that level the droplet velocity was comparable with terminal velocity for different pressures.

Widmann and coworkers [88], [93], [98] used PDI technique to characterize velocities (axial and radial components) and drop sizes (D_{10}, D_{30} , D_{32}) in four residential pendant sprinklers, whose K-factor were ranging from 7.2×10^{-5} $m^3s^{-1}kPa^{-1/2}$ – 1.33×10^{-4} $m^3s^{-1}kPa^{-1/2}$. Widmann reported on the proportionality of

mean drop size (flux-averaged volume diameter, $\overline{D_{30}}$) to $p^{-1/3}$ for water pressures over the range 93 kPa$\leq$ p $\leq$200 kPa. Widmann performed his measurements at a horizontal level between 1.12-3.7 m below the sprinkler deflector. In general the velocity of droplets was higher than corresponding terminal velocity. This means that most of droplets leave deflector with greater momentum, hence has not reached to terminal velocity at the measurement plane after deceleration. The mean axial velocities peaked at 2.5 $m.s^{-1}$.

Sheppard [41] used a PIV technique to carry out measurements on nine pendant sprinkler and seven upright sprinklers, which are shown in Figure 2-6. The size of orifices in this set of sprinklers was ranging from 9.5 to 25.4 mm, with pressures ranging from 0.345-5.52 bar which represents flow coefficients from 40 to 363 l/min/bar$^{1/2}$, respectively. This research has been cited for validations purposes throughout this dissertation.

Figure 2-6: Overview of sprinklers tested by Sheppard [41]

The variation of radial velocity with polar angle at various azimuthally angles was investigated in [41]. Sheppard provided a rough approximation of the radial velocity close to the sprinkler which is described by Equation (2-10),

$$\bar{u}_d \approx 0.6(p/\rho_f)^{1/2} \qquad (2\text{-}10)$$

The author measured the initial spray velocity for a verity of commercial fire sprinklers in near field about 780 mm from the sprinkler head. A sample of the data obtained is given in Figure 2-7 [41]. The radial velocities shown strong dependency to the elevation angle and less dependency on the azimuthal angle and are a function of the specific sprinkler model, therefore a general description of the radial velocity independent of sprinkler model is not very accurate. The shape of the velocity profile varied widely from sprinkler to sprinkler with no differences between upright and pendant sprinklers. The origin of the spray velocity is along the axis of the sprinkler between the orifice and the deflector for pendant sprinklers and between the orifice and 50 cm above the deflector for upright sprinklers. The notation and value allocation to the elevation angle in the Figure 2-7 are different from the conventions used in this dissertation.

(a) (b)

Figure 2-7: Near field spray velocity, $p = 1.31\ bar$; (a) Velocity Vector; (b) average velocity in elevation direction [41]

As the PIV technique doesn't provide information on the droplet size distribution or size-velocity correlations, Sheppard utilized PDI to characterize the droplet size distribution for the set of commercial sprinklers shown in Figure 2-6.

Putorti [83] developed Particle Tracking Velocimetry and Imaging (PTVI) technique and found that in some Weber numbers, the drop size decrease follows a -2/3 power law. This indicates a faster decrease in comparison to equation *(2-9)*.

Sprinkler measurements conducted by Blum [92], Ren [82], [90], [99] and Do [100] explored the impacts of sprinkler components by using three different types of nozzle configurations, i.e. Basis Nozzle, Tined Nozzle and a standard Tyco D3

spray nozzle. Blum [92] found that characteristic drop sizes, for the Basis and Tined nozzles did not change significantly with respect to jet Weber number. On the other hand he Blum [92] reported on the droplet size decay of $We_0^{-1/6}$ from the spray produced by a flat disk. The reason to this behavior may be related to different sheet breakup mode.

2.5.5 Spray Volume Flux

The spray pattern formed in any type of sprinklers is unique to that type as shown in Figure 2-8. Characterizing the overall spray experimentally has been always prohibitive because of the number of measurements points required to map out the spray distribution. The most commonly cited techniques are (i) collecting water at areas of interest using pans, (ii) counting the droplets in laser sheet images and (iii) PDI flux measurements where the size and number of droplets through a small probe volume (detection volume) is recorded over time. The latter technique has drawn an enormous attention in the recent years, where due to the interference pattern, a droplet passing through the probe volume scatters light exhibiting an angular and temporal intensity distribution which is characteristic of the size, refractive index, and velocity of the droplet [93]. In addition to this, a broad range of technical issues have been reported in the literature for the precise measurements of the spray volume fluxes. The measurements being used in this dissertation for verification purpose have been employing PDI technique. As the associated sources of error for PDI technique quantifying dimensions of the probe volume, the effects of the photomultiplier tube (PMT) gain and burst splitting have received the most attention in the literature.

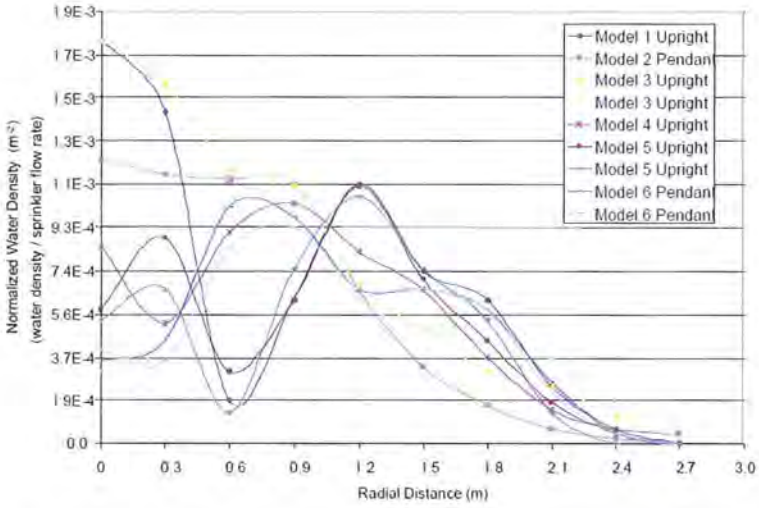

Figure 2-8: Delivered water flux as a function of radial distance from the fire [41]

Water density distributions measured for a sprinkler under fire and no fire conditions are quite different [84]. Sheppard [81] also showed that water flux is strongly dependent on the elevation angle and on the azimuthal angle. Chan [37] observed the water density distributions were roughly symmetrical to the plane containing the two deflector supporting arms (Yoke arms) for the two investigated ESFR sprinklers, and decreases with increasing radial distance from the sprinkler axis. In addition to this each gross water density distribution curve is well correlated with the Rosin-Rammler equation.

Zhou et al. [80], have measured both the near and far field spray patterns, including spatial distribution of water volume flux, drop size and velocity of sprinkler spray, of two warehouse in-rack fire sprinklers. These authors concluded that the spray pattern in the near field of the pendant sprinkler is strongly influenced by the sprinkler frame arms and the configuration of tines and slit, whereas it is more influenced by the frame arm than by the deflector's tines and slits in upright sprinkler. In the near field of the pendant sprinkler, large droplet sizes appeared at the spray center and in the region close to the deflector level, whereas for the upright sprinkler the large droplets appeared in middle elevation angle region. In the far field of the sprinkler, the droplet size increases with the radial distance. For both sprinklers, the droplet size decreases with the discharge pressures. The near-field measurements can be used to prescribe the spray starting condition for the modeling of spray transport through the fire plume. The far-field measurements can be used to evaluate the spray transport calculations. This

research has also been cited throughout this dissertation for validations purposes, hence the details of the sprinklers used by Zhou et al. [80] will be given in §2.6.

2.5.6 Sheet Breakup Distance

Sheet break up distance is also an impinging atomizer spray characteristics whose measurement has received attention in recent literature. As can be seen in the rest of this section stability sheet breakup distance is a function of jet Weber number, as shown by Equation (2-11), as demonstrated in (2-12) to (2-14)

$$\frac{2\mathrm{R}_b}{D_0} = f(We_0) \tag{2-11}$$

Where R_b is the breakup distance, D_0 is orifice diameter and the jet Weber number is $We_0 = \rho U_0^2 D_0/\sigma$.

Huang [91] provided insight into the stability of water sheets by expanded work of Taylor [101]. Huang found existence of a critical regime, where the sheet is stable, but sensitive to perturbations. As shown in Figure 2-9, this regime is characterized by the value of the weber number between 800 and 1000, containing the maximum water sheet break up radius. A semi-empirical correlation as Equation (2-12) is provided by [91]:

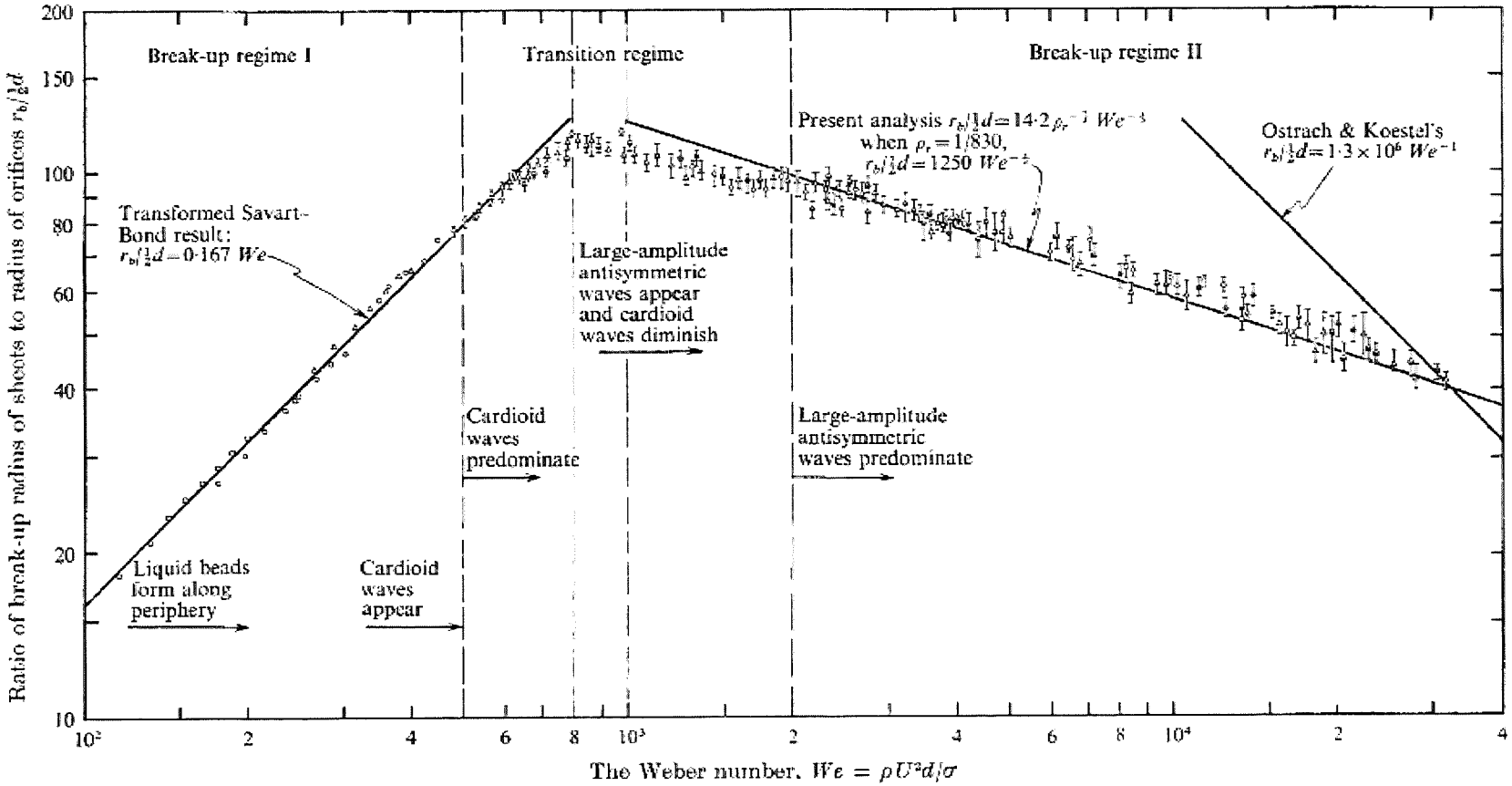

Figure 2-9: Relationship between the breakup radius of liquid sheets and Weber number [91]

$$R_b/D_0 = 625\, We_0^{-1/3} \tag{2-12}$$

Clanet and Villermaux [64], [102] studied smooth liquid sheet and flapping liquid sheet at two separate papers. The liquids forming the sheet were both water and ethanol. Transition from a smooth sheet to flapping regime occurred at $\tilde{\rho}^{1/2}\, We_0 = 40$, where $\tilde{\rho} = \rho_f/\rho_g$. For the smooth sheet, the breakup distance increased linearly with increase in We_0 and for the flapping sheet, they reported the same physics observed by Huang. In addition to this the authors studied variations of average drop size, D_{10}, and sheet breakup distance, R_b concluding that $D_{10}/D_0 \sim \tilde{\rho}^{-2/3}\, We_0^{-1}$ and $R_b/D_0 \sim \tilde{\rho}^{-2/3}\, We_0^{-1/3}$. The mean droplet diameter decreased with the Weber number. For Weber numbers less than 1200 decrease rate slowly follows $We_0^{-1/3}$ and for higher Weber number the decrease is stronger as We_0^{-1}.

Blum [92] found that break-up distances produced by three different types of nozzle configurations, i.e. Basis Nozzle, Tined Nozzle and a standard Tyco D3 spray nozzle, all follow a $We_0^{-1/3}$ scaling law. These results are consistent with those found in similar configurations by Huang [91] and Clanet and Villermaux [64], [102]. The empirical correlation for the basis nozzle has been reported to be,

$$R_b/D_0 = 482\, We_0^{-1/3} \tag{2-13}$$

Ren [89], [90], [99] quantified two different break-up modes, i.e. Rim break-up mode, occurring at $We_s < 150$, was described as drops detachment at the edge of the sheet, and ligament break-up mode, occurring at $We_s > 150$, consisting of the transformations from sheet to ligaments and from ligaments to drops. For standard nozzle configuration it was found that the sheet breakup distance is approximately one-half the distance of the basis nozzle, Equation (2-14). It is clear that the addition of the tines and spaces and the boss promotes the sheet instability, resulting in shorter disintegration distance.

$$R_b/D_0 = 248\, We_0^{-1/3} \tag{2-14}$$

Figure 2-10: Top view photographs of sheets. (a) $L_0 = 25.4\ mm$, We = 7000; (b) $L_0 = 25.4\ mm$, We = 15300; (c), $L_0 = 76.2\ mm$, We = 15300. [76]

Do [100] has quantified the flow split, sheet break-up, drop size, and velocity in the stream-wise discharge of nozzles having geometry similar to pendant sprinklers. Measurements also revealed that the drop size along the slit stream is smaller than the droplet size along the tine stream.

Ren [25, 77] discussed the importance of disturbance on jet surface on sheet breakup distance. The disturbance (i.e. turbulence) growth rate on the jet would reveal several regimes. For example, when the jet Weber number is small (We ~ 10^2), the turbulence is weakly developed on the jet which is very smooth. These smooth jets were experimentally observed at very small injection pressures. The experiments in this study (We > 10^3) were primarily conducted in the turbulence regime. The liquid turbulence is well developed and jet distortions are irregular.

2.6 Sprinklers Considered in the Validation Studies for this Thesis

In addition to the research based on sprinklers shown in Figure 2-6, there are other research studies which have been employed in the present thesis for verifications and validation purposes. As they will be referred in the rest of the text, more details of those experiments carried out at FM Global are provided in this section.

2.6.1 Study of Zhou et al. [80]

Zhou et al. [80] reported measurements on two fire sprinklers, a pendent fire sprinkler with a K-factor of 20.448 lpm/kPa$^{1/2}$ (205 lpm/bar$^{1/2}$,14.2 gpm/psi$^{1/2}$) and an upright sprinkler with a K-factor of 16.128 lpm/kPa$^{1/2}$ (161.4 lpm/bar$^{1/2}$, 11.2 gpm/psi$^{1/2}$) shown in Figure 2-11-(a) and Figure 2-12-(a) respectively. The measurements reported in Zhou et al. [80], are summarized in Appendix-C.

For the K-205 sprinkler, measurements were performed for water discharge pressures of 3.4 bar and 5.2 bar. The distance of the ceiling to the K-205 deflector was 0.46 m.

For the K-162 sprinkler, measurements were performed at 0.76 bar and 1.31 bar. The distance of the ceiling to the K-162 deflector was 0.17 m. The deflector diameter is 44.45 mm.

Figure 2-11b shows the geometrical structure of the deflector of the K-205 sprinkler. The azimuthal angle (Φ) was designated for each slit from one frame arm where $\Phi = 0^\circ$. If the sprinkler is symmetrical, the azimuthal distribution in each quadrant is expected to be comparable. Therefore, in their investigation the azimuthal distribution was measured in the 2nd quadrant. The selected azimuthal locations were 90° , 123° and 157° , corresponding to the tines, and 73° , 107° , 140° and 180° corresponding to the slits between the tines. [103], [104].

Figure 2-11: Azimuthal angle designations for each slit of the K-205 pendant sprinkler deflector [80]

Figure 2-12: (a) K-162 upright sprinkler (b) and its dimension on schematic view [80]

The K-162 sprinkler, Figure 2-12-(a), has 24 tines on the deflector. By checking different K-162 sprinkler samples, it was found that e position of the tines to the

frame arms varies. Therefore, the azimuthal distribution was measured at a constant angle increment of 15° starting from one of the sprinkler frame arms [80].

2.6.2 Study of Zhou and Yu [95]

Zhou and Yu [95] conducted series of experiments at low water discharge pressures to investigate the fire sprinkler spray formation as affected by sprinkler geometry. They measured water film thicknesses and sheet breakup distances for flat deflectors of three diameters, 25.4 mm, 38.1 mm and 50.8 mm, formed due to impingement of a jet with 9.5 mm diameter.

Figure 2-13 and Figure 2-14 show variety of slit deflectors and boss deflectors. Figure 2-15 shows slit spray discharge angle and slit stream being formed due to presence of slits on the deflector, and Figure 2-16 demonstrates detachment of water to arm and formation of vertical water sheets at two low pressures.

Figure 2-13: Three slit-sprinklers with the same disk diameter (25.4 mm), the same slit length (7.9 mm) but different slit widths of (a) 1.59 mm, (b) 3.18 mm and (c) 4.76 mm. [95]

Figure 2-14: Two conical boss-sprinklers with the same base radius (4.8 mm),disk diameter (25.4 mm) and slit width (1.59 mm), but different angles of (a)1271 and (b) 901. [95]

Figure 2-15: Slit stream from a 3.18 mm wide slit illustrated at pressure 0.034 bar. [95]

Figure 2-16: Vertical water sheet formed behind the sprinkler arm at discharge pressures of (a) 0.014 bar and (b) 0.034 bar. [95]

It is reported by them that deflector diameter and boss structure have little impact on drop size and sheet breakup distance. However, wider slits form larger drops. At constant operating pressure, the slit spray discharge angle is insensitive to the slit width, but sensitive to the boss that helps directing the slit spray toward the sprinkler centerline. The frame arm tends to produce a vertical spray sheet downstream of the frame arm, which increases the complexity of overall spray formation. An empirical correlation was also established to estimate the spray flux fraction discharging from a deflector slit. The above measurements and observations are useful for the development of a spray formation model for fire sprinklers.

2.7 Theoretical Modeling of Sprinklers and Implementation in CFD Codes for Fire Applications

As explained in the first chapter, the main aim of this research is to model the initial sprinkler spray based on the physics of sprays. The physics involved in the sprays formed from impinging jet atomizers has been explained in §2.4. The development of such an initial spray predictive model can help both designers and fire researchers. These models can be incorporated in CFD simulation packages to study the fire suppression performance of sprinklers in different fire scenarios. Once the initial spray is characterized, Lagrangian particles models could easily be employed in CFD packages to track the droplets. Without a robust modeling approach for the initial spray, modelers would have to rely on empirically-based correlations such as Rosin-Rammler (or Weibull) which are limited in their applications. This section is dedicated to review both the development of sprinkler spray models and the incorporation of spray models in numerical studies.

Fire researchers have employed room fire models for decades to understand the spread of fire and combustion products in structures. The most commonly used fire models are zone models. Zone models break the building compartments into hot upper level and cool lower level and are typically used to predict the movement of hot gases through the structure, i.e. height and temperature of the hot layer, and to predict the activation of fire sprinklers or detectors.

Computer models for sprinklers in fire protection have been continuously developing. Alpert [105] developed a sprinkler spray transport computer program called SPRAY in the 1980s, which was used to calculate the spray-plume interaction in the axi-symmetric configuration. Subsequently Bill [106] used the program to calculate drop size distribution, thrust force of the spray, water density in the horizontal plane and the Actual Delivered Densities (ADD). ADD measures sprinkler's suppression performance in a residential sprinkler. Later on, Nam and Bill [110] employed the GENTRA and PHOENICS codes to simulate the ADD results of a fire sprinkler. Then, Nam first studied both experimentally and numerically the superposition of a steady water spray on a steady thermal plume

(Nam and Bill, [107]) and Nam [108], [109], [110], and demonstrated that there is an optimal flow rate for a given sprinkler that gives the highest penetration ratio within a practical flow range [109] and increasing drop size is a much more effective way for obtaining a higher penetration ratio compared to increasing spray momentum [110]. The ALOFT model is available for downrange dispersion of pollutants in the environment [35], [83] and the Fire Dynamic Simulator (FDS) is available for fire flows in compartments [111]. FDS employs an empirical correlation for the initial spray distribution and predicts that once a sprinkler has activated and begins to discharge water, representative droplets are tracked. Drop size is randomly selected from a Probability Density Function (PDF) constructed from sprinkler data.

OpenFOAM is an open-source, an object-oriented code written in C++, which makes it reasonably straightforward to implement new models and fit spray models into the whole code structure. The code includes polyhedral mesh support, making it possible to create meshes using any form of cells, as long as the quality of the resulting mesh is high. Lagrangian parcels are tracked by face-to-face tracking, thus no parcels are lost when moving between cells as in Kiva-3V. Furthermore, models are implemented to be run-time-selectable, which makes it very easy for the user to switch between turbulence models, spray sub-models, numerical schemes etc. All solvers written in OpenFOAM can easily be run in parallel, since the code is parallelized at such a fundamental level, removing the need (in most cases) for the user to consider multiple processor simulations [112].

Theoretical research for investigating impinging liquid jet breakup and disintegration has focused on three general modeling approaches:

(i) Surface stability analysis, i.e. Dombrowski and Johns [78], Chang and Russell [113], Reitz and Bracco [60], Lian and Lin [114] and Liao et al [115].

(ii) Numerical solution with free surface dynamics, i.e. Watson [116], Ibrahim and Przekwas [117], Mao et al [118], Rizk and Mongia [119], and Hilbing and Heister [120].

(iii) Numerical solution with two phase flow coupling, i.e. (Liang and Ungewitter [121], Walmsley and Yule [97] and Chen et al.[122])

A useful model for predicting the film thickness and velocity along the deflector based on a free-surface similarity boundary layer concept [116] was adapted for sprinkler analysis by Wu [123] and Wu et al. [124].

The University of Maryland [82] [125], established a framework to compress the extensive initial spray data using compact analytical functions. The measured volume flux distributions, drop size distributions, and velocity distributions are used to generate the analytical functions describing the spatial variation of the droplet density, size, and velocity with elevation angle. Legendre polynomials and Gaussian functions were defined.

Numerically simulation the spray formed in the fire sprinkler, from first principle is quite expensive. Great amount of simulations is required to verify the reliability of the first principle modeling for a range of sprinkler configurations, at range of operational conditions and has been remained uncovered as yet. To reduce the computational cost, the problem can be simplified and reduced to the simulation of the jet interaction with sprinkler head components. Once the film characteristics have been evaluated, the sheet instability and disintegration can be analyzed through linear perturbation theory. The latter approach is under development in University of Maryland, but no official report has been published yet.

2.8 Summary

A comprehensive review of experimental and theoretical researches dedicated to quantify the spray characteristics for both sprinkler configurations and impinging jet atomizers is provided in this chapter.

Carrying out experimental measurements to quantify sprinkler spray dates back to four decade ago and the spray parameters quantification has benefited from advances in optic measurement techniques. Beside improvements in the accuracy of measurements, the spray quantifications have moved to near fields nowadays despite the far field measurements at the early stages. The results from early investigations provided sprinkler design guidance and valuable information for the development of atomization and spray models.

Empirical distributions as well as some other simple correlations which have been developed for estimating characteristic drop sizes based on the early experiments can be used as primitive predictive models; however, they are insensitive to many effects that are known to influence the initial spray behavior. The data in these correlations are obtained under quiescent cold flow conditions. In the experiments equivalent diameters are determined by measuring a size dependent property of an arbitrary property non-spherical droplet such as volume or surface area and relating it to the diameter of an equivalent spherical droplet.

Sprays are produced by a variety of sprinklers, generating large differences in data. In general sprinklers can be divided into two categories: high velocity sprinklers [9-15 $m.s^{-1}$] generating small-medium droplets and low velocity sprinklers [1-5 $m.s^{-1}$] generating medium-large droplets. The majority of water drops from sprinklers are relatively large [> 0.3 mm].

Even if the sheet breakup location can be predicted accurately, several uncertainties still remain in droplet size predictions. The primary uncertainty is how the sheet breaks up. The sheet can breakup into droplets directly, or into fragments or ring like ligaments. The second uncertainty is on how those ligaments and fragments will break up. So far, there are no accurate models to predict the ligament breakup.

The sheet breakup mechanism is attributed to a sheet instability resulting from interaction of the sheet with the surrounding medium, with inertial forces overcoming surface tension forces. At small Weber numbers and small density ratios, the disturbances in the sheet are damped, while at large Weber numbers and density ratios the sinusoidal disturbances in the sheet grow. The mean feature of the evolution is that the mean drop diameter decreases with Webber. For a given Webber number the mean drop diameter increases with surface tension.

The following chapter details the modeling approach adopted in the present thesis.

3 MODELLING SPRINKLER SPRAY CHARACTERISTICS

3.1 Introduction

The initial spray characteristics are described by the sheet breakup distance, droplet size, initial droplet formation location, droplet velocities and spray volume fluxes. This chapter will formulate and characterize the initial spray formation through series of theoretical and semi-empirical models mostly based on essential physics involved in an impinging jet atomizer. The main model developments introduced as part of this thesis will be highlighted throughout the chapter. The atomization process could be summarized in the following categories:

- Jet impingement,
- Film formation,
- Sheet formation,
- Development of instabilities on the sheet,
- Sheet breakup either to ligaments or to droplets due to growth of instabilities on the sheet surface.
- If ligaments are formed they will further disintegrate to droplets.

Formulations are presented for film formation (§3.2), sheet trajectory (§3.3) and the sheet breakup to ligaments and droplets (§3.4). The adopted numerical and modeling approaches in this thesis, based on the formulations explained in (§3.2) to (§3.4) are explained in (§3.5). At the next step a dimensionless formulation will be presented (§3.6) to evaluate the sheet thickness and the spray volume median diameter. A stochastic approach have been adopted to generalize some of the spray characteristics (§3.7). The development of a semi-empirical model will be presented in (§3.8) and the calculation of water volume fluxes and droplet trajectories are given in (§0) and (§3.10), respectively.

3.2 Mathematical Modeling of the Flow over a Deflector Disk

This section is devoted to the presentation and analysis of the models intended to improve sprinkler spray atomization. The base models in which modifications/developments were introduced as part of this thesis are presented in detail, together with the contributions of the PhD work.

3.2.1 Boundary Layer Model (BLM)

When a liquid jet of diameter D_0 and kinematic viscosity ν impacts with velocity U_0 a horizontal deflector (disc or impactor) of diameter D_i, it spreads radially as a film flow and its thickness and velocity are affected by the growth of the boundary layer on the deflector as presented in Figure 3-1 in its simplest form. A complete study of the radial film spread over the horizontal plane has been carried

out by Watson [116]. Four distinct regions denoted (i), (ii), (iii) and (iv) in Figure 3-1 are identifiable over the flat plane.

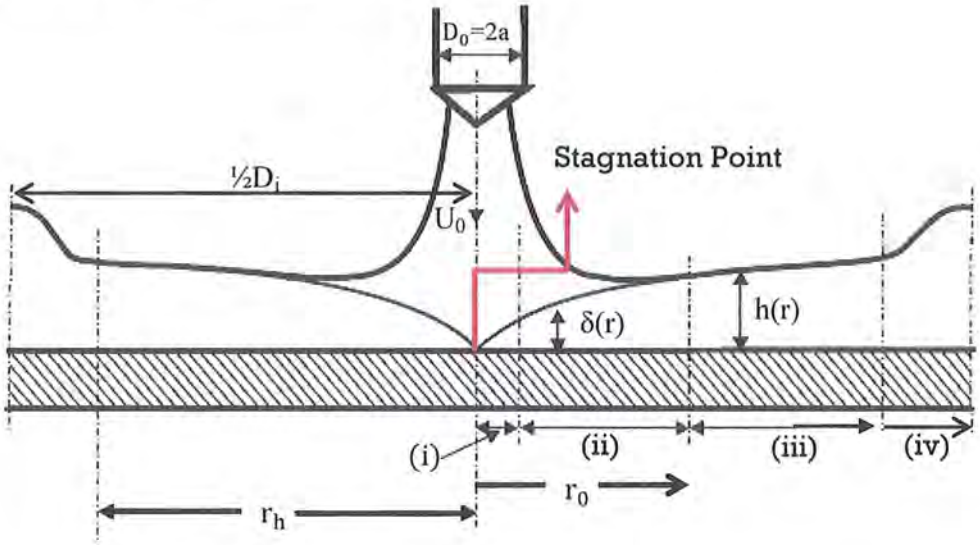

Figure 3-1: Impingement of a liquid jet on a flat surface and different flow regions.

Region (i)

An internal region (i), also called impinging or stagnation region, where the flow speed outside the boundary layer increases rapidly from 0 at the stagnation point to U_0, the speed with which the jet strikes the deflector and the boundary layer thickness, δ is $O\left(\sqrt{\frac{\nu_f D_0}{2U_0}}\right)$. In reality the stagnation point is not fixed. Region (i) is defined by radial distance from the axis of the jet, r, in the order of the radius of the impinging jet, $a = ½D_0$.The direction of the water jet is changed in this region from vertical to radial and a radial expanding film flow is formed.

Region (ii)

Region (ii) is also known as the boundary layer region [116] or developing region [75], and is distinguished by the boundary layer thickness $\delta(r)$ less than film thickness $h(r)$. The velocity outside the boundary layer region (ii) is still unaffected by the viscous stresses, hence is constant, $U(r) = U_0$, and the velocity inside the boundary layer of developing region has Blasius flat plate

profile. The boundary layer grows until the wall influences the entire thickness of the film.

Region (iii)

The external region (iii) is known as the transient region (fully developed region) where the whole film thickness corresponds to the boundary layer, $h(r) = \delta(r)$. The velocity in region (iii), $U(r)$ is less than U_0. The transition from (ii) to (iii) occurs at radial location r_0 defined by $h(r_0) = \delta(r_0)$. Regions (ii) and (iii) are defined by $r > D_0/2$, where streamlines remain nearly parallel.

Region (iv)

The region (iii) extends until the hydraulic jump occurs after r_h, where the region (iv) starts. The velocity profile in this region can be described by a non-Blasius similarity solution. A hydraulic jump occurs when the flow suddenly changes from supercritical (Fr > 1) to subcritical (Fr < 1), which is accompanied by a sudden increase in liquid film thickness. The Froud number, Fr, is the ratio of inertia to gravity, and is defined as $Fr = U_0^2/ga$. The phenomenon of hydraulic jump is very important for the process of heat transfer in the spreading film. After the jump in sub-critical region the slow moving liquid exhibits degraded heat transfer characteristics. Prediction and control of the jump location is important in thermal design. In modern sprinkler designs the radius of the deflector is not large enough for the hydraulic jump to occur [126].

Region Specific Modeling Equations

Regions specific equations are provided in the literature for the film thickness based on the radial location for laminar and turbulent flows. Regions (i) and (ii) are commonly encountered in sprinkler configurations. However, it was found that in some sprinkler scenarios, the film has persisted beyond Region (ii) and will be connected to sprinkler studies by evaluating some inputs from sprinkler's terminology [77].

Laminar motion in the layer

The formulations introduced below are mainly derived under laminar motion of the flow in the boundary layer. In region (ii), the boundary layer and sheet thicknesses obtained by Watson [116] can be respectively expressed as:

$$\delta(r) \approx 2.58690 \sqrt{\frac{\nu_f r}{U_0}} \tag{3-1}$$

$$h(r) \approx \frac{D_0^2}{4D_i} + 0.38482\, \delta(r) \tag{3-2}$$

Using equations (3-1) and (3-2), together with the definition of r_0, $h(r_0) = \delta(r_0)$, one can evaluate the location of transition between region (ii) to (iii) as follows:

$$r_0 \approx 0.183\, D_0\, Re^{\frac{1}{3}} \tag{3-3}$$

Where $Re = U_0 D_0 / \nu_f$ is the Reynolds number of the incident jet and the subscript f denotes fluid properties. For a typical value $Re = 6000$, the transition occurs at 3.3 times the jet diameters.

For the fully developed region, the film flow is characterized as [116]:

$$h(r) = \delta(r) = \frac{4.837}{Re} \frac{r^3 + l^3}{D_0 r} \tag{3-4}$$

$$U(r) \approx U_0 \frac{Re}{23.8} \frac{D_0^3}{r^3 + l^3} \tag{3-5}$$

The constant of integration, l, which appears in equations (3-4) and (3-5) is determined by the condition that the free surface velocity $U(r)$ in (3-5) must be equal to U_0 at $r = r_0$. This condition leads to:

$$l \approx 0.32955\, D_0 Re^{\frac{1}{3}} \tag{3-6}$$

Turbulent motion in the layer

The flow in the boundary layer may not always be laminar, especially if the liquid jet is unstable. The sheet thickness over a flat plate within region (ii) in turbulent cases is given by:

$$h_i = \frac{D_0^2}{4D_i} + C_1 \times \left(\frac{7\nu_f}{U_0}\right)^{1/5} \left(\frac{D_i}{2}\right)^{4/5} \tag{3-7}$$

Where $C_1 = 1.659 \times 10^{-2}$ is a coefficient determined from similarity analysis performed by Watson [116]. It is noteworthy that this coefficient will change with sprinkler injection geometry. Defining $\delta_0 = D_0^2/4D_i$, equation (3-7) can be normalized as:

$$\frac{h_i}{\delta_0} = 1 + 4\left(\frac{1}{2}\right)^{4/5} C_1 \left(\frac{7\nu_f}{U_0}\right)^{1/5} \left(\frac{D_i}{D_0}\right)^{4/5} \tag{3-8}$$

In region (iii) the sheet thickness for turbulent scenarios is found from:

$$h_i = C_2 \times \left(\frac{\nu_f}{Q}\right)^{\frac{1}{4}} \frac{r_i^{\frac{9}{4}} + l^{\frac{9}{4}}}{r_i} \tag{3-9}$$

Where $C_2 = 0.0211$, and l is an arbitrary constant length, which has to be determined by the conditions where the boundary layer reaches the free surface ($r = r_0$). Similar to previous section the expression for l is obtained by matching the sheet velocity at $r = r_0$ and is given by:

$$l = C_3 \times a\left(Q/\nu_f a\right)^{\frac{1}{9}} \tag{3-10}$$

where $C_3 = 4.126$.

At this point the full description of the radial spread of the jet over the flat disc in the different regions identified in Figure 3-1 is given. Now recalling that Q $[m^3 s^{-1}]$, equation (1-1), is the sprinkler volumetric discharge and can be expressed as equation (3-11) by mass conservation:

$$Q = K\Delta p^{1/2} = \frac{\pi D_0^2}{4} U_0 = 2\pi r_i h_i U_i \tag{3-11}$$

By rearranging equation (3-11) the average speed of the sheet when it leaves the deflector edge could be obtained as:

$$U_i = \frac{D_i^2}{8 r_i h_i} U_0 = \frac{Q}{2\pi r_i h_i} = \frac{K\Delta p^{1/2}}{2\pi r_i h_i} \tag{3-12}$$

The sprinklers hydraulic diameter (or radius) could be obtained from volumetric discharge as:

$$D_0 = 2\,a = \left(\frac{4Q}{\pi U_0}\right)^{1/2} \tag{3-13}$$

The sprinkler injection velocity could be found using Bernoulli's equation, $P_1 = P_0 + \frac{1}{2}\rho_f U_0^2$, assuming inviscid flow

$$U_0 = \sqrt{\frac{2\Delta p}{\rho_f}} \tag{3-14}$$

Substitution equation (3-14) into equation (3-13), the hydraulic radius of jet can be expressed in terms of sprinkler K-factor

$$a = \frac{1}{2}\sqrt{\frac{4Q}{\pi\sqrt{\frac{2\Delta p}{\rho_f}}}} = \sqrt{\frac{K}{\pi}}\sqrt[4]{\frac{\rho_f}{2}} \tag{3-15}$$

The sheet thickness is increased by the viscous effect, and this viscous effect is related to the disk radius and inversely to the initial jet speed (or discharge pressure).

In order to show the importance of the viscous effect, a non-dimensional thickening factor $\tilde{\boldsymbol{\delta}} \equiv h/\delta_0$ is defined in (3-17), i.e. the ratio of the actual thickness to the in-viscid sheet thickness, based on geometrical diameter ratio, i.e. equation (3-16). The detailed derivation is presented in Appendix A-1.

$$\boldsymbol{X} \equiv \frac{D_i}{D_0} \tag{3-16}$$

$$\tilde{\delta} = \begin{cases} 1 + 5.625 \times 10^{-2}\, \boldsymbol{Re}_0^{-1/5}\, \boldsymbol{X}^{9/5} & r_i < r_0 \\ 1.023 + 3.77 \times 10^{-2} \boldsymbol{Re}_0^{-1/4}\, \boldsymbol{X}^{9/4} & r_i > r_0 \end{cases} \tag{3-17}$$

For $\boldsymbol{Re}_0 = 10^5$ and $\boldsymbol{Re}_0 = 10^6$ the non-dimensional thickening factors are $\tilde{\boldsymbol{\delta}} = 1.041$ and $\tilde{\boldsymbol{\delta}} = 1.025$, respectively.

In sprinkler application studies it is required to check firstly if the release regime is laminar or turbulent. A stability criterion has been provided by Watson to determine whether the flow is laminar or turbulent. From similarity analysis it is derived a critical jet Reynolds number, $\boldsymbol{Re_0} = Q/\nu_f a = 27500$, above which the flow is turbulent. In the cases presented in the current study, the jet Reynolds number exceeds the criteria for the injection pressures above 5000 pa.

3.2.2 The Axisymmetric Film Model (AFM)

In addition to the method discussed in §3.2.1, an alternative model, for analyzing the development of the film thickness and velocity over the deflector is presented in this section. This model builds on the same principles as [95], [116] and presents formulations which enable characterizing the film flow over the deflector by ensuring mass flux conservation and describing the decrease of film momentum due to viscosity. This system of conservation equations are formulated in cylindrical coordinate for an axisymmetric film development, as sketched in Figure 3-2.

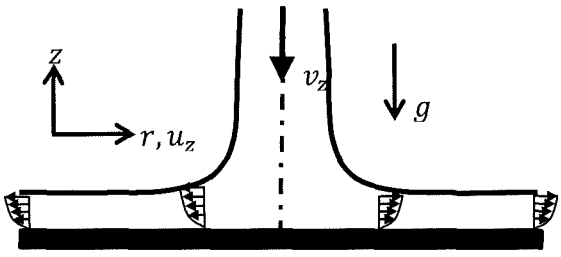

Figure 3-2: Film development on a flat plate upon orthogonal liquid jet impingement

The flow has been assumed incompressible and the formulation is developed in two dimensions. It is noteworthy is the flow above solid surface up to free surface.

It is assumed that liquid and ambient doesn't change throughout the film development process. Hence analyse of energy equation has been avoided.

Mass conservation

Equation (3-18) describes the mass conservation in cylindrical coordinate:

$$\frac{\partial \rho}{\partial t} + \frac{1}{r}\frac{\partial}{\partial r}(\rho r v_r) + \frac{1}{r}\frac{\partial}{\partial \theta}(\rho v_\theta) + \frac{\partial}{\partial z}(\rho v_z) = 0 \tag{3-18}$$

The mass conservation equation in axisymmetric coordinate will be reduced to (3-19), assuming steady state condition, $\partial/\partial t = 0$, in r-z plane, $\partial/\partial\theta = 0$:

$$\frac{\partial}{\partial r}(\rho r v_r) + r\frac{\partial}{\partial z}(\rho v_z) = 0 \tag{3-19}$$

Equation (3-19) can be expanded and re-written as:

$$\rho v_r + \rho r\frac{dv_r}{dr} + r v_r\frac{d\rho}{dr} + \rho r\frac{dv_z}{dz} + r v_z\frac{d\rho}{dz} = 0$$

and simplifies to equation (3-20),

$$\frac{\partial}{\partial r}(\rho r v_r) + \rho r\frac{dv_z}{dz} = 0 \tag{3-20}$$

From continuity equation, (3-18), v_z could be obtained. By rearranging (3-20), v_z could be found in the form presented in (3-21),

$$\frac{dv_z}{dz} = -\frac{1}{\rho r}\frac{\partial}{\partial r}(\rho r v_r)$$

$$v_z = -\frac{1}{\rho r}\frac{\partial}{\partial r}\int_0^z (\rho r v_r)\, dz \tag{3-21}$$

The equation (3-21) has been further expanded in the below section (Momentum equation).

Momentum equation

Momentum equation in r and z directions can be written as (3-22) and (3-23) respectively:

$$\rho\left(\frac{\partial v_r}{\partial t}+v_r\frac{\partial v_r}{\partial r}+\frac{v_\theta}{r}\frac{\partial v_r}{\partial \theta}+v_z\frac{\partial v_r}{\partial z}-\frac{v_\theta^2}{r}\right)=-\frac{\partial p}{\partial r}+$$
$$\mu\left[\frac{1}{r}\frac{\partial}{\partial r}\left(r\frac{\partial v_r}{\partial r}\right)+\frac{1}{r^2}\frac{\partial^2 v_r}{\partial \theta^2}+\frac{\partial^2 v_r}{\partial z^2}-\frac{v_r}{r^2}-\frac{2}{r^2}\frac{\partial v_\theta}{\partial \theta}\right]+\rho g_r \tag{3-22}$$

$$\rho\left(\frac{\partial v_z}{\partial t}+v_r\frac{\partial v_z}{\partial r}+\frac{v_\theta}{r}\frac{\partial v_z}{\partial \theta}+v_z\frac{\partial v_z}{\partial z}\right)$$
$$=-\frac{\partial p}{\partial z}+\mu\left[\frac{1}{r}\frac{\partial}{\partial r}\left(r\frac{\partial v_z}{\partial r}\right)+\frac{1}{r^2}\frac{\partial^2 v_z}{\partial \theta^2}+\frac{\partial^2 v_z}{\partial z^2}\right]+\rho g_z \tag{3-23}$$

Then the momentum in r –direction equation (3-22) would be reduced to equation (3-24) by eliminating the θ direction:

$$r:\ \rho\left(\underbrace{\frac{\partial v_r}{\partial t}}_{0}+v_r\frac{\partial v_r}{\partial r}+\frac{v_\theta}{r}\underbrace{\frac{\partial v_r}{\partial \theta}}_{0}+v_z\frac{\partial v_r}{\partial z}-\underbrace{\frac{v_\theta^2}{r}}_{0}\right)=-\frac{\partial p}{\partial r}+$$
$$\mu\left[\frac{1}{r}\frac{\partial}{\partial r}\left(r\frac{\partial v_r}{\partial r}\right)+\frac{1}{r^2}\underbrace{\frac{\partial^2 v_r}{\partial \theta^2}}_{0}+\frac{\partial^2 v_r}{\partial z^2}-\frac{v_r}{r^2}-\frac{2}{r^2}\underbrace{\frac{\partial v_\theta}{\partial \theta}}_{0}\right]+\rho\underbrace{g_r}_{0}$$

$$\rho\left(v_r\frac{\partial v_r}{\partial r}+v_z\frac{\partial v_r}{\partial z}\right)=-\frac{\partial p}{\partial r}+\mu\left[\frac{1}{r}\frac{\partial}{\partial r}\left(r\frac{\partial v_r}{\partial r}\right)+\frac{\partial^2 v_r}{\partial z^2}-\frac{v_r}{r^2}\right] \tag{3-24}$$

Taking into account constant uniform velocity profile in z -direction, the Momentum equation (3-23) would be reduced into:

$$\frac{\partial p}{\partial z}=\rho g_z \tag{3-25}$$

At this stage multiplying $\rho\frac{\partial v_r}{\partial z}$ on both sides momentum equation in r-direction (3-21) gives the second term in Left Hand Side (LHS) of (3-24). It has been obtained in (3-26), knowing that the derivation of an integral of the form $\int_{y_0}^{y_1} f(x,y)dy$ can be expressed as $\frac{d}{dx}\int_{y_0}^{y_1} f(x,y)dy=\int_{y_0}^{y_1}\frac{\partial}{\partial x}f(x,y)dy$. [127]

$$\rho v_z\frac{\partial v_r}{\partial z}=-\frac{1}{r}\frac{\partial v_r}{\partial z}\frac{\partial}{\partial r}\int_0^z(\rho r v_r)\,dz \tag{3-26}$$

The term $v_r\,\partial(\rho r v_r)/\,\partial r$ has been added and subtracted from RHS

$$= -\frac{1}{r}\left\{\frac{\partial v_r}{\partial z}\frac{\partial}{\partial r}\int_0^z (\rho r v_r)\,\partial z + v_r\frac{\partial}{\partial r}(\rho r v_r) - v_r\frac{\partial}{\partial r}(\rho r v_r)\right\} =$$

$$= -\frac{1}{r}\left\{\frac{\partial}{\partial z}\left[v_r\frac{\partial}{\partial r}\int_0^z (\rho r v_r)\,\partial z\right] - v_r\frac{\partial}{\partial r}(\rho r v_r)\right\}$$

Substituting equation (3-26) into equation (3-24), gives:

$$\rho v_r\frac{\partial v_r}{\partial r} - \frac{1}{r}\frac{\partial}{\partial z}\left[v_r\frac{\partial}{\partial r}\int_0^z (\rho r v_r)\,\partial z\right] + \frac{v_r}{r}\frac{\partial}{\partial r}(\rho r v_r)$$
$$= -\frac{\partial p}{\partial r} + \mu\left[\frac{1}{r}\frac{\partial}{\partial r}\left(r\frac{\partial v_r}{\partial r}\right) + \frac{\partial^2 v_r}{\partial z^2} - \frac{v_r}{r^2}\right] \tag{3-27}$$

Equation (3-27) is then integrated across the film layer, denoting the film thickness as, "h"

$$\int_0^h \rho v_r\frac{\partial v_r}{\partial r}\partial z - \frac{1}{r}\int_0^h \frac{\partial}{\partial z}\left[v_r\frac{\partial}{\partial r}\int_0^h (\rho r v_r)\,\partial z\right]\partial z + \frac{1}{r}\int_0^h v_r\frac{\partial}{\partial r}(\rho r v_r)\,\partial z$$
$$= -\int_0^h \frac{\partial p}{\partial r}\partial z + \mu\int_0^h \frac{\partial^2 v_r}{\partial z^2}\partial z + \int_0^h \frac{\mu}{r}\frac{\partial}{\partial r}\left(r\frac{\partial v_r}{\partial r}\right)\partial z - \mu\int_0^h \left[\frac{v_r}{r^2}\right]\partial z \tag{3-28}$$

Where the first and third terms on LHS of Equation (3-28) can be further written as:

$$\int_0^h \rho v_r\frac{\partial v_r}{\partial r}\partial z + \frac{1}{r}\int_0^h v_r\frac{\partial}{\partial r}(\rho r v_r)\,\partial z$$

$$= \int_0^h \rho v_r\frac{\partial v_r}{\partial r}\partial z + \frac{1}{r}\left[v_r\left(\rho v_r + \rho r\frac{\partial v_r}{\partial r}\right)\right]\partial z$$

$$= \int_0^h \rho v_r\frac{\partial v_r}{\partial r}\partial z + \frac{1}{r}\left(\rho v_r^2 + \rho r v_r\frac{\partial v_r}{\partial r}\right)\partial z \tag{3-29}$$

$$= \frac{1}{r}\int_0^h \left(\rho v_r^2 + 2\rho r v_r\frac{\partial v_r}{\partial r}\right)\partial z$$

$$= \frac{1}{r}\int_0^h \frac{\partial}{\partial r}(\rho r v_r^2)\partial z$$

As such equation (3-28) could be expressed in following form,

$$\underbrace{\int_0^h \frac{\partial}{\partial r}(\rho r v_r^2)\partial z}_{I} - \underbrace{\int_0^h \frac{\partial}{\partial z}\left[v_r \frac{\partial}{\partial r}\int_0^h (\rho r v_r)\,\partial z\right]\partial z}_{II}$$

$$= -r\underbrace{\int_0^h \frac{\partial p}{\partial r}\partial z}_{III} + \mu r\underbrace{\int_0^h \frac{\partial^2 v_r}{\partial z^2}\partial z}_{IV} + \mu\underbrace{\int_0^h \frac{\partial}{\partial r}\left(r\frac{\partial v_r}{\partial r}\right)\partial z}_{V} \tag{3-30}$$

$$-\mu r\underbrace{\int_0^h \left[\frac{v_r}{r^2}\right]\partial z}_{VI}$$

Some of the terms shown in (3-30) could be determined using Leibniz law. Leibniz integral rule gives a formula for differentiation of a definite integral whose limits are functions of the differential variable, [128]

$$\frac{\partial}{\partial z}\int_{a(z)}^{b(z)} f(x,z)dx = \int_{a(z)}^{b(z)} \frac{\partial f}{\partial z}dx + f(b(z),z)\frac{\partial b}{\partial z} - f(a(z),z)\frac{\partial a}{\partial z} \tag{3-31}$$

Hence the Leibniz rule has been applied to the terms, I, II and III;

$$I :: \int_0^h \frac{\partial}{\partial r}(\rho r v_r^2)\partial z = \frac{\partial}{\partial r}\int_0^h (\rho r v_r^2)dz - \rho r v_h^2 \frac{\partial \delta}{\partial r} \tag{3-32}$$

$$II :: \int_0^h \frac{\partial}{\partial z}\left[v_r \frac{\partial}{\partial r}\int_0^h (\rho r v_r)\,\partial z\right]\partial z$$

$$= \left[v_r \frac{\partial}{\partial r}\int_0^h (\rho r v_r)\,\partial z\right]\Bigg|_0^h = v_h \frac{\partial}{\partial r}\int_0^h (\rho r v_r)\,\partial z \tag{3-33}$$

$$III :: \int_0^h \frac{\partial p}{\partial r}\partial z = \frac{\partial}{\partial r}\int_0^h p dz - p_h \frac{\partial h}{\partial r} \tag{3-34}$$

At interface of sheet and air, the profile of radial velocity is assumed to be uniform or with negligible gradient, however the gradient at root is steep. The following expressions are obtained:

$$IV :: \int_0^h \frac{\partial^2 v_r}{\partial z^2}\partial z = \left.\frac{\partial v_r}{\partial z}\right|_0^h = \left(\frac{\partial v_r}{\partial z}\right)_{z=h} - \left(\frac{\partial v_r}{\partial z}\right)_{z=0} = -\left(\frac{\partial v_r}{\partial z}\right)_{z=0} \quad (3\text{-}35)$$

$$V :: \mu\int_0^h \frac{\partial}{\partial r}\left(r\frac{\partial v_r}{\partial r}\right)\partial z = \mu\int_0^h \left[r\frac{\partial^2 v_r}{\partial r^2} + \frac{\partial v_r}{\partial r}\right]\partial z = \mu\frac{\overline{v_r}}{r}h \quad (3\text{-}36)$$

$$VI :: \mu r\int_0^h \left[\frac{v_r}{r^2}\right]\partial z = \mu r\left[\frac{\overline{v_r}}{r^2}\right]h \quad (3\text{-}37)$$

If we assume that the plate is impermeable, we have that on the plate surface (z=0), $v_r = v_z = 0$ at the edge of layer $v_r = \overline{v}_r$, say. Substituting back equations (3-32) to (3-37) into equation (3-30), gives

$$\frac{d}{dr}\int_0^h (\rho r v_r^2)\,dz - \rho r v_h^2\frac{\partial h}{\partial r} - v_h\frac{\partial}{\partial r}\int_0^h (\rho r v_r)\,\partial z = -r\left[\frac{d}{dr}\int_0^h p dz - p_\delta\frac{\partial h}{\partial r}\right] - \mu r\left(\frac{\partial v_r}{\partial z}\right)_{z=0} \quad (3\text{-}38)$$

Further simplification can be introduced to the above formulation as shown below,

$$LHS = -r\frac{d}{dr}\int_0^h (p - p_h)dz - r\tau_w$$

$$LHS = -r\frac{d}{dr}\int_0^h \rho g(\delta - z)dz - r\tau_w$$

$$LHS = -r\frac{d}{dr}(½\rho g h^2) - r\tau_w$$

It should be noted that $\tau_w = \mu(\partial v_r/\partial z)_{z=0} = ½\rho C_c \overline{v}_r^2$, Where C_c is the average friction coefficient on the deflector surface [95]:

$$\frac{d}{dr}\int_0^h (\rho r v_r^2)\, dz - \rho r v_h^2 \frac{\partial h}{\partial r} - v_h \frac{\partial}{\partial r}\int_0^h (\rho r v_r)\, \partial z = -\tfrac{1}{2}\rho g r\, 2h\frac{dh}{dr} - \tfrac{1}{2}\rho r C_c \bar{v}_r{}^2 \tag{3-39}$$

The LHS of equation (3-39) can be expanded as following:

$$\begin{aligned} LHS &= \left[\frac{d}{dr}(\rho r v_r^2\, h)\right] - \rho r v_h^2 \frac{\partial h}{\partial r} - v_h \frac{\partial}{\partial r}(\rho r v_r\, h) \\ &= \rho v_r^2\, h + 2\rho r h v_r \frac{dv_r}{dr} + \rho r v_r^2 \frac{dh}{dr} \\ &\quad - \rho r v_h^2 \frac{\partial h}{\partial r} - \rho v_h \left(r v_r \frac{dh}{dr} + v_r h + r h \frac{dv_r}{dr}\right) \\ &= \rho r h v_r \frac{dv_r}{dr} - \rho r v_r^2 \frac{dh}{dr} \end{aligned} \tag{3-40}$$

Therefore, combination of equations (3-39) and (3-40) gives:

$$h v_r \frac{dv_r}{dr} + (gh - v_r^2)\frac{dh}{dr} = -\tfrac{1}{2} C_c v_r^2 \tag{3-41}$$

The system of non-linear first order differential equations given for AFM, (3-21) and (3-41), solve for the thickness and speed of the film over the deflector up to its edge and are subject to the following boundary conditions:

- It has been assumed that the film initiates at a radial distance equivalent to the jet diameter, $r = D_0$, and the starting thickness could be is $\delta_0 = D_0^2/4D_0$.
- The initial film average speed has been chosen based on the inviscid assumption and considered to be the same as the jet speed, U_0.

The system of equation summarized in (3-42) is solved using a fourth-order Runge-Kutta method to yield the solutions for h and v_r.

$$\begin{bmatrix} h & v_r \\ v_r h & gh - v_r^2 \end{bmatrix} \begin{bmatrix} \frac{dv_r}{dr} \\ \frac{dh}{dr} \end{bmatrix} = \begin{bmatrix} -\frac{h v_r}{r} \\ -\tfrac{1}{2} C_c v_r^2 \end{bmatrix} \tag{3-42}$$

3.3 Sheet Trajectory Model

In sprinkler applications the momentum of the water jet is sufficient to push most of the flow from film to sheet, however for part of the flow which sticks to the yoke arms, the momentum diminishes. Under these circumstances probably the film would not detach from the sprinkler and partial water bells, [75], will form. In this dissertation this flows have not been modeled.

It is crucial to precisely model the sheet trajectory. The inaccuracies in the sheet thickness, speed and location will influence to a great extend the favorable parameters in spray quantification, i.e. sheet breakup distance, initial droplet location, droplet velocity and even droplet size.

This section reviews an existing sheet trajectory model in (§3.3.1) and also presents the development of a novel sheet tracking model in (§3.3.2) undertaken in the present thesis.

3.3.1 Inversely Linear Thickness Decay

A popular hypothesis for predicting the characteristics of an attenuating sheet has been suggested by Taylor [101]. This model has been under attention of researchers studying the sheet formed by like-doublet impinging jets [129] and splash plates [130], [131]. The thickness of the sheet h at any arbitrary point is inversely proportional to its radial distance from the stagnation point (Figure 3-1)

$$h = \frac{h_i r_i}{r} \tag{3-43}$$

The initial thickness of the sheet is given by the film thickness at the perimeter of the deflector. This hypothesis is referred to as "Inversely Linear Thickness Decay (ILTD)" model.

In the sprinkler spray modeling [77], [124] the speed of the sheet $U_s$was assumed to be constant throughout the formation and destruction and equal to the speed of film at the deflector perimeter U_i.

3.3.2 Detailed Trajectory Model

This section introduces a more Detailed Trajectory Model (DTM) for investigating the characteristics of the radially expanding sheets available in the sprinkler studies and as an alternative to the ILTD. DTM builds on the approach developed by Mao et al. [118], Chuech [132] and Ibrahim and McKinney [133]. They studied the evolution of non-swirling and swirling liquid sheets from annular nozzle with formulation.

DTM calculates the radial change in speed, thickness, deflection angle, and vertical displacement of the sheet issuing from the deflector edge. This is the first time that a curvilinear model is formulated and being extensively used for impinging jet configuration. In the current system liquid stream-wise, ξ, tangential, ζ, and normal, η, to streamline directions are perpendicular to each other as displayed in Figure 3-3.

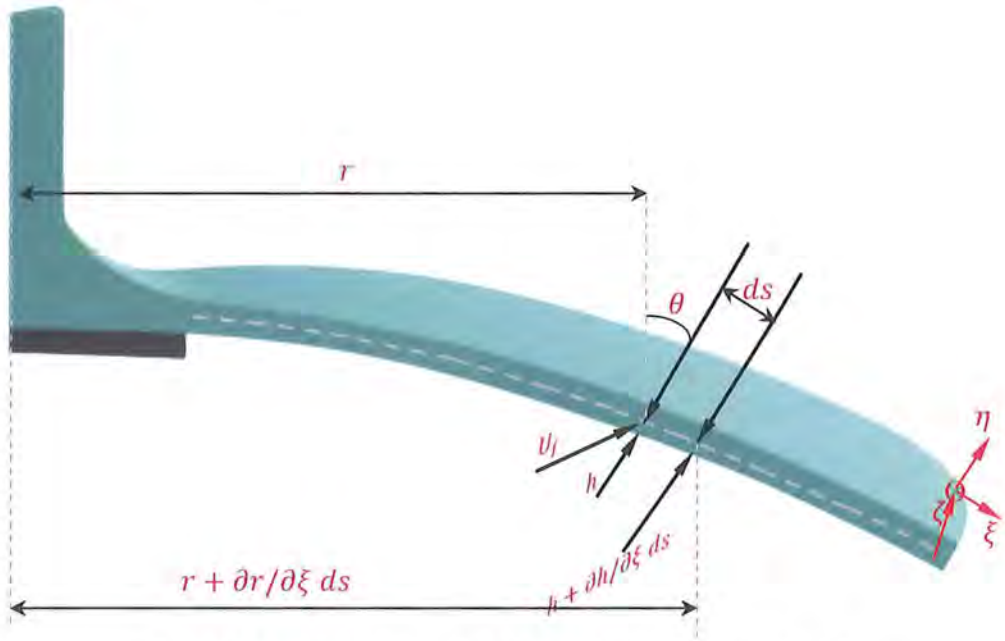

Figure 3-3: Schematic illustration of a radial expanding liquid sheet.

The system of ordinary differential equations can be expressed in the following simplified forms

Continuity:

$$\frac{\partial}{\partial \xi}\left(\rho_f u_f r h\right) = 0 \qquad (3\text{-}44)$$

Momentum in the stream-wise ξ-direction:

$$\rho_f u_f \frac{\partial u_f}{\partial \xi} - \rho_f u_f w_f \frac{\sin\theta}{r} = S_\xi + \rho_f g \cos\theta \qquad (3\text{-}45)$$

Momentum in the normal η-direction:

$$\rho_f u_f u_f \frac{\partial \theta}{\partial \xi} - \rho_f w_f w_f \frac{\cos\theta}{r} = -\frac{\partial p_f}{\partial \eta} - \rho_f g \sin\theta \qquad (3\text{-}46)$$

Momentum in the tangential ζ-direction:

$$\rho_f u_f u_f \frac{\partial w_f}{\partial \xi} + \rho_f w_f u_f \frac{\sin\theta}{r} = S_\zeta \qquad (3\text{-}47)$$

where the first term in equations (3-45) and (3-47) represents directional components of inertia forces in their respective directions, stream-wise and tangential. The second term in equations (3-45) and (3-47) and the first term in (3-46) denotes the directional components of centrifugal forces. The second term in equation (3-46) relates to Coriolis force. The terms $\rho_f g \cos\theta$ and $\rho_f g \sin\theta$ designate directional components of gravity force. The terms S_ξ and S_ζ account for the viscous forces in their respective directions.

Young-Laplace-Gauss equation is a non-linear partial differential equation that describes the capillary pressure difference sustained across the interface between two fluids. The pressure difference is due to the phenomenon of surface tension. This equation relates the pressure difference to the shape of the surface and it is fundamentally important in the study of capillary surfaces.

$$\Delta p = -\sigma \nabla . \hat{n} = 2\,\sigma\, H = \sigma\left(\frac{1}{R_1} + \frac{1}{R_2}\right) \qquad (3\text{-}48)$$

H is the mean curvature, and R_1 and R_2 are the principal radii of curvature.

The pressure gradient in the normal direction η can be approximated by its integrated form as a function of the gas pressure difference Δp_f between the upper and lower surfaces of the sheet and surface tension forces which can be related to capillary pressure and gas pressure differences Δp_g. The surface tension force is

proportional to the surface tension, σ, and inversely proportional to the radius of curvature R_c.

$$\Delta p_f = \Delta p_g - 2\sigma\left(\frac{\cos\theta}{r} \pm \frac{1}{R_c}\right) \tag{3-49}$$

The plus sign in front of $1/R$ is applied for negative $d\theta/d\xi$ case, and the minus sign is for positive $d\theta/d\xi$ case. In case of an sprinkler application it is modeled in form of *(3-50)*

$$\frac{\partial p_f}{\partial \eta} \cong \frac{\Delta p_g}{h} - \frac{2\sigma}{h}\left(\frac{\cos\theta}{r} - \frac{\partial\theta}{\partial\xi}\right) \tag{3-50}$$

Following Chuech and co-authors [132], [134] the viscous forces in the stream-wise and tangential momentum equations are accounted for through the interfacial friction forces acting on the inner and outer liquid-gas interfaces. Therefore, the viscous forces may be written respectively, in terms of gas-liquid interfacial friction factors representation [47] as

$$S_\xi = 0.5\,\frac{\rho_g\, f_\xi\,(u_g - u_f)|u_g - u_f|}{h}$$
$$S_\zeta = 0.5\,\frac{\rho_g f_\zeta\,(w_g - w_f)|w_g - w_f|}{h} \tag{3-51}$$

Where f_ξ and f_ζ in equation (3-51) are the gas-liquid interfacial friction factors.

$$f_\xi = 0.79(1 + 150\,h/r)(Re_\xi)^{-0.25}$$
$$f_\zeta = 0.79(1 + 150\,h/r)(Re_\zeta)^{-0.25} \tag{3-52}$$

Where the Reynolds numbers are:

$$Re_\xi = \frac{\rho_g h|u_g - u_f|}{\mu_g}$$
$$Re_\zeta = \frac{\rho_g h|w_g - w_f|}{\mu_g} \tag{3-53}$$

Owing to simplifying assumptions and use of conforming curvilinear coordinates in the present model, all the dependent variables have gradients only in the

stream-wise direction, ξ. Therefore the governing equations are given by the following equations:

$$u_f r\frac{dh}{d\xi} + u_f h\frac{dr}{d\xi} + rh\frac{du_f}{d\xi} = 0 \qquad (3\text{-}54)$$

$$\rho_f u_f \frac{du_f}{d\xi} - \rho_f w_f^2 \frac{\sin\theta}{r} = \rho_f g\cos\theta + S_\xi \qquad (3\text{-}55)$$

$$\rho_f u_f^2 \frac{d\theta}{d\xi} - \rho_f w_f^2 \frac{\cos\theta}{r} = -\frac{\Delta p_g}{h} + \frac{2\sigma}{h}\left(\frac{\cos\theta}{r} - \frac{d\theta}{d\xi}\right) - \rho_f g\sin\theta \qquad (3\text{-}56)$$

$$\rho_f u_f \frac{dw_f}{d\xi} + \rho_f u_f w_f \frac{\sin\theta}{r} = S_\zeta \qquad (3\text{-}57)$$

The system of equations (3-54) to (3-57) consists of four equations and five unknowns, w_f, u_f, h, θ, r an additional equation could be derived from geometrical considerations of the streamline as shown in Figure 3-3:

$$\frac{dr}{d\xi} = \sin\theta \qquad (3\text{-}58)$$

To track the sheet trajectory, its horizontal coordinate z is evaluated in reference with Figure 3-3 as:

$$\frac{dz}{d\xi} = \cos\theta \qquad (3\text{-}59)$$

The system of non-linear equations *(3-54)* to *(3-59)* is solved with a set of six initial conditions listed in equations *(3-60)* to *(3-65)* and provides numerical solution to the development of non-swirling planar sheet.

$$u_f\big|_{\xi=0} = u_i, \qquad (3\text{-}60)$$

$$w_f\big|_{\xi=0} = 0 \qquad (3\text{-}61)$$

$$h|_{\xi=0} = h_i, \qquad (3\text{-}62)$$

$$\theta|_{\xi=0} = \theta_0, \qquad (3\text{-}63)$$

$$r|_{\xi=0} = ½D_i \tag{3-64}$$

$$z|_{\xi=0} = 0 \tag{3-65}$$

The sheets developed in the sprinklers have complexities in the ability to impart swirl to either of gas flows and/or the liquid flow. The swirl can change the evolution of the sheet particularly the evolution of waves on its surface [135].

The system of non-linear first order differential equations given for DTM, *(3-66)*, subject to the boundary conditions explained as equations *(3-60)* to *(3-65)* is solved using a fourth-order Runge-Kutta method to yield the solutions for $u_f, w_f, h, \theta, r, z$.

$$\begin{bmatrix} rh & u_f h & u_f r & 0 & 0 \\ \rho_f u_f & 0 & 0 & 0 & 0 \\ 0 & 0 & 0 & \rho_f u_f^2 + 2\sigma/h & 0 \\ 0 & 1 & 0 & 0 & 0 \\ 0 & 0 & 0 & 0 & 1 \end{bmatrix} \times \begin{bmatrix} du_f/d\xi \\ dr/d\xi \\ dh/d\xi \\ d\theta/d\xi \\ dz/d\xi \end{bmatrix} = \begin{bmatrix} 0 \\ \rho_f g cos\theta + S_\xi \\ 2\sigma/h \times cos\theta/r - \rho_f g sin\theta \\ sin\theta \\ cos\theta \end{bmatrix} \tag{3-66}$$

3.4 Sheet Break-up and Droplet Formation

3.4.1 Sheet Breakup

According to Dombrowski [78], the growth of aerodynamic waves on a liquid inviscid sheet could be expressed in form of equation (3-67). The equation is a balance of four forces, namely, Pressure force, Surface tension force, Inertial force and Viscous force, by ignoring the 2nd derivative terms,

$$\rho_f h \left(\frac{\partial f}{\partial t}\right)^2 + \mu h n^2 \left(\frac{\partial f}{\partial t}\right) - 2\rho_g n\, u_f^2 + 2\sigma n^2 = 0 \tag{3-67}$$

Where f is defined as natural logarithm of the ratio of wave amplitude to amplitude of initial disturbance, $\ln(A/A_0)$, and is called the dimensionless total growth of the wave.

It is found by Dombrowski that the breakup of the liquid sheets due to the wave growth concept occurs as the total growth of the wave approaches a constant value of $f = 12$. The same value has been reported by Lin and Jiang [136], in their studies for a flapping sheet, when the jet Weber number is larger than 2000. However this value is not constant and increases with jet Weber number. For instance in a jet Weber number of 16000, the critical wave amplitude reach to 17 [76], [89]. This value is not only a function of jet characteristics, but also is affected by the deflector configuration. As a result of the presence of boss, space and yoke arms on the sprinklers, this value has to be significantly less than 12, due to increased disturbance and turbulence in the process where the water jet is transformed to sheet.

At this step solutions are required for equation *(3-67)* in order to incorporate the effect wave dispersion with sheet trajectory (models are explained in §3.3). This has been sought in the current dissertation by substituting $\partial f/\partial t = p$;

$$\rho_f h\, p^2 + \mu h n^2 p - 2\rho n u_f^2 + 2\sigma n^2 = 0 \qquad (3\text{-}68)$$

For an inviscid liquid $\mu = 0$ and equation (3-68) gives

$$\frac{\partial f}{\partial t} = p = \sqrt{\left[\frac{2}{\rho_f}\left(\rho_g\, u_f^2\, n - \sigma\, n^2\right)\right]}\; h^{-\frac{1}{2}} \qquad (3\text{-}69)$$

While equation (3-67) yields:

$$f = \sqrt{\left[\frac{2}{\rho_f}\left(\rho_g\, u_f^2\, n - \sigma n^2\right)\right]} \int_0^t h^{-\frac{1}{2}}\, dt \qquad (3\text{-}70)$$

Hydrodynamic-instability theories predict a most unstable wavelength as the one with the fastest (shortest) growth rate and suggest that this wavelength dominates and, hence, the droplet size is proportional to it. Differentiating equation (3-70)

with respect to n and equating to zero, $\partial(\partial f/\partial t)/\partial n = 0$, gives the wave with maximum growth. Thus,

$$n_{cr}^{sh} = \frac{\rho_g\, u_f^2}{2\sigma} \tag{3-71}$$

From Prahl and Wendt [137] the theoretical resonance frquency is obtained from their thoretical maximum wave growth number, which is:

$$n_{cr}^{sh} = \frac{\rho_g\, u_f^2}{2\sigma}\left(\frac{1}{2} - \frac{5}{We_h} + \left(\frac{1}{4} + \frac{5}{We_h} + \frac{1}{We_h^2}\right)^{1/2}\right) \tag{3-72}$$

Where We_h is the Weber number based on the sheet thickness at the edge deflector. In sprinkler applications, the spray velocity is on the order of 10 m/s, the sheet thickness at the edge of deflector is on the order of 1 mm. We_h will be on the order of 1000 and the effect of We_h can be neglected.Thus equation (3-72) is the same as equation (3-71).

The corresponding values of growth rate p and total growth f are obtained by substituting equation (3-71) in equations (3-69) and (3-70):

$$p = \frac{\rho_g\, u_f^2}{\sqrt{2h\rho_f\sigma}} \tag{3-73}$$

and

$$f = \int_0^t \frac{\rho_g\, u_f^2}{\sqrt{2h\rho_f\sigma}}.dt \tag{3-74}$$

For a parallel-sided sheet h is constant and equation (3-73) gives:

$$f = \frac{\rho_g\, u_f^2}{\sqrt{2h\rho_f\sigma}}\, t \tag{3-75}$$

As the sheet thickness varies with radial location in time and its breakup time value is not known, the following rearrangement is being made in the present work:

$$t = \frac{f\sqrt{2\rho_f\sigma}}{\rho_g u_f^2}\sqrt{h} \Rightarrow t^2 = \left(\frac{f\sqrt{2\rho_f\sigma}}{\rho_g u_f^2}\right)^2 h(t_b) \qquad (3\text{-}76)$$

Where t_b is the breakup time and the subscript b denotes the breakup characteristics.

ILTD

Where ILTD is employed, the speed of the sheet is assumed to be constant and the sheet thickness is expressed as:

$$h_b = \frac{h_i r_i}{r_b} \qquad (3\text{-}77)$$

Then break-up distance from stagnation point would be:

$$r_b = r_i + u_f\, t_b \qquad (3\text{-}78)$$

Or

$$r_b = r_i + \int_0^{t_b} u_f(t)\; dt$$

Substituting equations (3-78) and (3-77) in (3-76)

$$t_b^2 = \left(\frac{f\sqrt{2\,\rho_f\,\sigma}}{\rho_g\, u_f^2}\right)^2 \frac{h_i\, r_i}{r_i + u_f t_b} \qquad (3\text{-}79)$$

Further rearrangement would result to following equation:

$$u_f\, t_b^3 + r_i\, t_b^2 - h_i\, r_i \left(\frac{f\,\sqrt{2\,\rho_f\,\sigma}}{\rho_g\, u_f^2}\right)^2 = 0 \qquad (3\text{-}80)$$

The presently formulated equation (3-80), solves for sheet break-up time and consequently sheet break up radius would be found deterministically.

DTM

Where DTM is employed, *(3-74)* is solved by employing recursive adaptive Simpson quadrature method.

3.4.2 Ligament Formation

Thinning of sheet is caused by the growth of the harmonic wave, maximum thinning. According to the literature subsequent rupture occurs at positions corresponding to 3/8 and 7/8, of the length of the fundamental wave [78]. However in some other sheet breakup models, the sheet is assumed to breakup into ring-like structures (ligament) having radial width of one-half wavelength. As the 3/8 and ½ are close to each other, the latter has been preferred in part of this research, due to the simplicity it introduces. To get the diameter of ligaments, Figure 3-4, the volume of the ligament has been calculated by two methods:

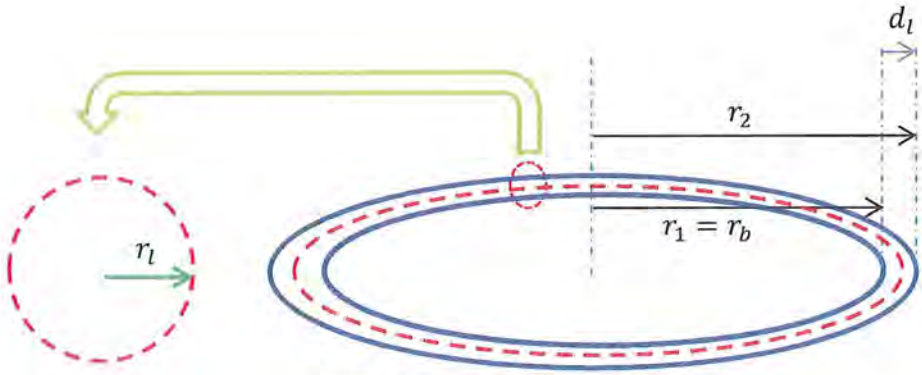

Figure 3-4: Nomenclature of ligaments

The first method calculates the volume of ligament from (i) the cross section of the ligament and (ii) the length of ligament. The latter is shown in dashed red on RHS of Figure 3-4,

$$V_1 = \pi r_l^2[2\pi(r_b + r_l)] = \frac{\pi}{4} d_l^2\, 2\pi \left[\frac{d_l}{2} + r_b\right] \tag{3-81}$$

In the second method, the area of torroid (bounded between two dashed circles in Figure 3-5) and the sheet thickness, h, have been used to obtain an approximate volume of ligament.

$$A = \pi(r_2^2 - r_1^2)$$

where $r_2 = r_1 + \frac{\pi}{n}$, then volume would become

$$V_2 = \pi\left[\left(r_1 + \frac{\pi}{n}\right)^2 - r_1^2\right]h \qquad (3\text{-}82)$$

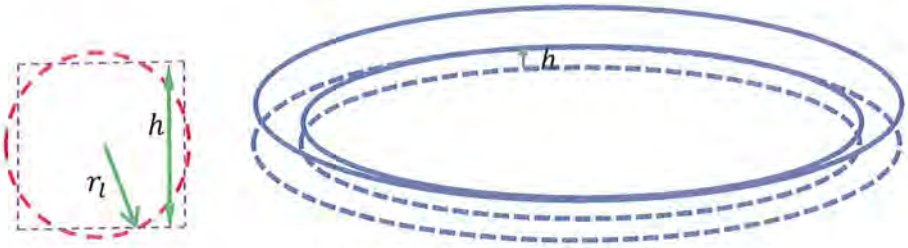

Figure 3-5: Nomenclature of ligaments.

Due to (small) size of sheet breakup distance, the assumption would not be of significant cause. Thus, the two volumes, (3-81) and *(3-82)*, have been considered to be equal, $V_1 = V_2$, hence,

$$\frac{\pi^2}{2} d_l^2 \left[\frac{d_l}{2} + r_b\right] = \pi\left[\left(r_b + \frac{\pi}{n}\right)^2 - r_b^2\right]h \qquad (3\text{-}83)$$

After substituting $\frac{\pi}{n} = \frac{\lambda}{2}$, and rearrangement, an equation for the ligament diameter is derived:

$$d_l^3 + 2\, r_b\, d_l^2 - \frac{4}{\pi}\, h\left[\left(r_b + \frac{1}{2}\lambda\right)^2 - r_b^2\right] = 0 \qquad (3\text{-}84)$$

Solving equation (3-84) would give the ligament diameter, d_l.

The mass of the ligament could then be determined:

$$m_l = \rho_f\, V_1 = \frac{1}{2}\pi^2 \rho_f\, d_l^2 \left[\frac{1}{2}\, d_l + r_b\right] \qquad (3\text{-}85)$$

Weber [138] provided an expression for the time that takes the ligament to breakup:

$$t_l^b = 24\left(\frac{2\,\rho_f}{\sigma}\right)^{1/2}\left(\frac{d_l}{2}\right)^{3/2} \qquad (3\text{-}86)$$

3.4.3 Droplet Formation

It has been observed by Dombrowski [78], [139] that ligaments produced from a liquid sheet break down through symmetrical (or dilatational) waves. In the present case the ligaments move transversely through the atmosphere. Under these conditions the surrounding atmosphere will have no effect on the wavelength and Weber's results for surface tension break down can be assumed to apply. That is,

$$n_l^{cr} d_l = \left[\frac{1}{2} + \frac{3\mu}{2\left(\rho_f\, \sigma\, d_l\right)^{1/2}}\right]^{-1/2} \qquad (3\text{-}87)$$

The above equation has been derived based on linear perturbation theory and is valid when the amplitude of the radial disturbances is small compared to ligament diameter. In and in-viscid flow, the critical ligament wave length for breakup $\lambda_l^{cr} = \pi\sqrt{2}\, d_l$

If it is assumed that the waves grow until they have amplitude equal to the radius of the ligament, one drop will be reduced per wave length. Thus by mass balance the relation between drop size and wave number is given by:

$$\frac{4}{3}\pi\left(\frac{d_d}{2}\right)^3 = \pi\left(\frac{d_l}{2}\right)^2 \lambda_l^{cr}$$

Or,

$$d_d^3 = 3\pi\, \frac{d_l^2}{n_l^{cr}} \qquad (3\text{-}88)$$

Which on combination with equation (3-87) gives;

$$d_d = \left(\frac{3\pi}{\sqrt{2}}\right)^{\frac{1}{3}} d_l \left[1 + \frac{3\mu}{\left(\rho_f \sigma d_l\right)^{\frac{1}{2}}}\right]^{\frac{1}{6}} = 1.881\, d_l\, (1 + 3Oh)^{\frac{1}{6}} \qquad (3\text{-}89)$$

Where $\left(3\pi/\sqrt{2}\right)^{1/3} = 1.881$, $Oh = \mu/\left(\rho_f \sigma d_l\right)^{1/2}$ is the Ohnesorge number and for in-viscid assumption $d_d = 1.88 d_l$. Equation (3-89) shows that the effect of viscosity on drop size is dependent on other operating conditions, being greater

for liquids of low density and surface tension. It should be noted that different droplet diameters could be generated from the same disturbances including the same wavelength of the disturbance. The one found in (3-89) is from the most unstable wavelength. Recent researches [140]&[141] suggest that not only wavelength, but other properties of the instability are important, for example amplitude and/or evolution time.

The number of droplets produced from each ligament, (3-90), is obtained from the mass of the ligament, equation *(3-85)*, and mass of droplet, $m_d = \frac{4}{3}\,\rho_f\,\left(\frac{1}{8}\pi d_d^3\right) = \frac{\pi}{6}\rho_f d_d^3$:

$$N = \frac{m_l}{m_d} \tag{3-90}$$

Dividing by ligament breakup time, would give, the number of particles per second.

The distance that it takes for the ligament to disintegrate into drops is calculated from the ligament velocity, u_l, and t_l^b. The initial drop location, which is the total distance the liquid travels until drop is formed, can be calculated from:

$$r_d = r_i + u_f\, t_s^b + u_l\, t_l^b \tag{3-91}$$

and where DTM is employed the initial droplet location would be:

$$r_d = r_i + \int_0^{t_s^b} u_f(t)\; dt + \int_0^{t_l^b} u_l(t)\; dt \tag{3-92}$$

Atomization relationships presented so far provide characteristic initial spray conditions for a given geometry, activation pressure, ambient condition, and liquid suppressant. The initial spray velocity has been considered to be U_0 in BLM and where ILTD is employed.

A brief investigation for the range of Ohnesorge number, obtained by the initial droplet diameter and their associated velocity revealed that this criterion was less than 0.01 for the current study. Taking into account that second breakup of droplets becomes significant as the Ohnesorge number exceeds 0.1 and droplet

Webber number greater than 6. Hence no further analysis of droplets has been carried out once their initial formation has been completed. From the literature [79], [81], [82], [83] secondary breakup mode is not important in sprinkler applications.

3.5 Deterministic Approaches

Four modeling approaches have been presented and are investigated in the present study. The approaches are developed based on the combination of sub-models presented from §3.2 to §3.4 in a deterministic framework. They are named Methods 1, 2, 3, 4 and their pertinent structures are shown in

Figure 3-6 to Figure 3-9. The constituent sub-models are as follow:

- Method-1, Figure 3-6: BLM-ILTD
- Method-2, Figure 3-7: AFM-ILTD
- Method-3, Figure 3-8: BLM-DTM
- Method-4, Figure 3-9: AFM-DTM

The ligament and instability analysis in all 4 methods has been carried out using the procedure explained in §3.4. The Method-1 has been treated as the basis approach in this dissertation and further development built on it. With the exception of Method-1 which has been previously studied [124], the other Methods have not been validated or verified for sprinkler applications. To the best knowledge of the author, it is the first time these methods are proposed and investigated for sprinkler applications.

The developed approaches provide the characteristic initial spray conditions for a given sprinkler geometry, i.e. K-factor, deflector diameter, pressure difference at sprinkler's orifice and orifice size, water injection condition, i.e. liquid density, dynamic viscosity, and surface tension, and surrounding medium temperature, the medium density and dynamic viscosity. The initial drop size, d_d, initial droplet speed, u_d, and initial droplet location, r_d, are the outputs of the modeling.

In the presented formulation the ambient gas velocity and turbulence have been neglected.

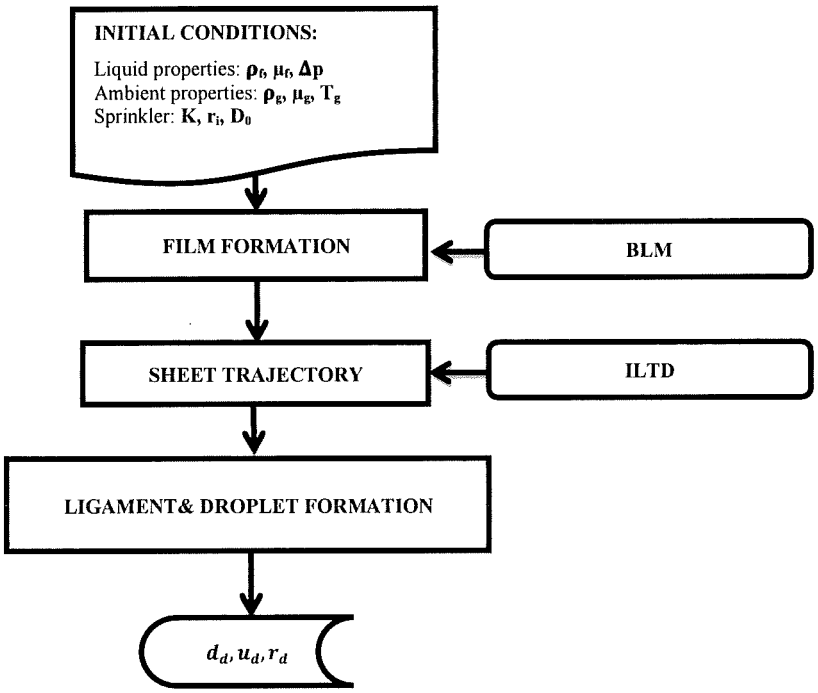

Figure 3-6: Layout of sub-models in Method-1

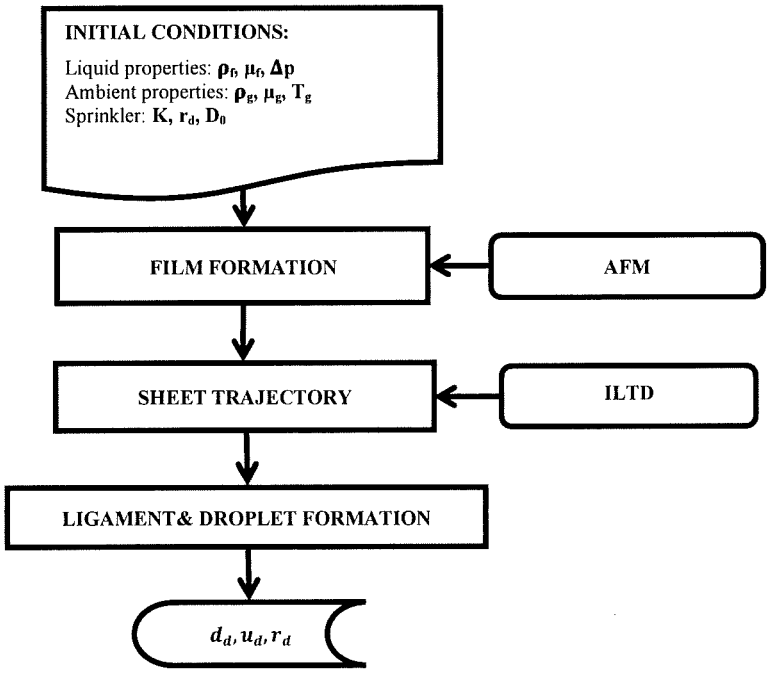

Figure 3-7: Layout of sub-models in Method-2

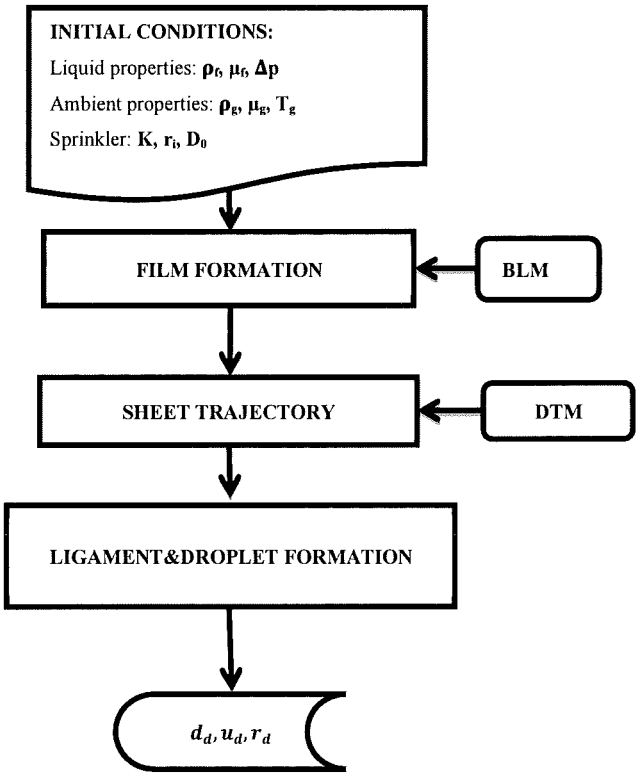

Figure 3-8: Layout of sub-models in Method-3

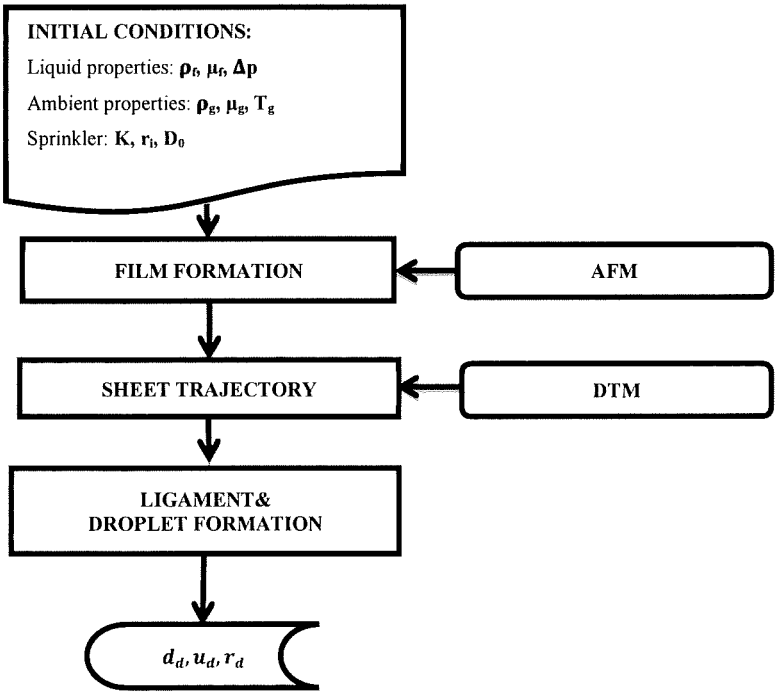

Figure 3-9: Layout of sub-models in Method-4

3.6 Non-dimensional Studies

Because of the inherent nonlinearity, most fluid-dynamical problems must be solved by either analytical approximations or by numerical computations. An essential first step of any analytical approximation is the art of scaling, which we shall emphasize repeatedly throughout thesis. In the present study, a scaling approach detailed hereafter, is proposed for the sprinkler important parameters.

Similarity studies have been performed in the current dissertation to drive equation which enables predicting sheet breakup distance and droplet diameter, straightaway. This has been completed by recalling geometrical diameter ratio $X \equiv D_i/D_0$ and density ratio that $\tilde{\rho} = \rho_g/\rho_f$, O ($10^{-3}$) the initial film thickness over the flat plate, δ_0, can be written as:

$$\delta_0 = \frac{D_0^2}{8r_i} = \frac{D_0^2}{4D_i} = \frac{D_0}{4\frac{D_i}{D_0}} = \frac{D_0}{4X}$$

The thickening factor of the film thickness can be determined by balancing the flow rates:

$$Q_0 = Q_i \rightarrow \frac{1}{4}D_0^2 U_0 = D_i h_i u_{f_i} \rightarrow \delta_0 U_0 = h_i u_{f_i} \rightarrow \tilde{\delta} = \frac{h_i}{\delta_0} = \frac{U_0}{u_{f_i}} \qquad (3\text{-}93)$$

The Weber number can be defined as $We_0 = \rho_f U_0^2 D_0/\sigma$, for a jet of hydraulic diameter D_0 coming out of the sprinkler's orifice. The sheet of initial thickness h_i at deflector edge being formed from jet impingement over flat plate has a Weber number defined by:

$$We_s = \frac{\rho_f \, u_{f_i}^2 \, h_i}{\sigma} \qquad (3\text{-}94)$$

The sheet Weber number based on the sheet thickness at the edge of deflector introduced in equation (3-94) contradicts the definition being used in [89], in the form, $We_s = \rho_f \, u_{f_i}^2 \, D_0/\sigma$, and is in agreement with [137]. Equation (3-94) reflects the impact of deflector's diameter on sheet characteristics. The ratio of the sheet to jet Weber numbers is:

$$\frac{We_0}{We_s} = \left(\frac{U_0}{u_{f_i}}\right)^2 \underbrace{\frac{D_0}{h_i}}_{?} \tag{3-95}$$

The part shown by question mark in equation (3-95) can be represented as:

$$\frac{D_0}{h_i} = \frac{D_0\, D_0/4D_i}{h_i\, D_0/4D_i} = 4\frac{D_i}{D_0}\frac{1}{\dfrac{h_0}{\dfrac{D_0^2}{4D_i}}} = \frac{4X}{\tilde{\delta}} \tag{3-96}$$

Substituting from (3-96) and (3-93) into equation (3-95), would give:

$$\frac{We_0}{We_s} = \left(\tilde{\delta}\right)^2 \frac{4X}{\tilde{\delta}} = 4X\tilde{\delta} \tag{3-97}$$

The sheet critical wave number can also be expressed in form of equation (3-98):

$$n_{cr}^{sh} = \frac{\rho_g u_{f_i}^2}{2\sigma} = \frac{1}{2}\frac{\rho_g}{\rho_f}\frac{\rho_f\, u_{f_i}^2\, h_i}{\sigma}\frac{1}{h_i} = \frac{\tilde{\rho} We_s}{2\delta_0\tilde{\delta}} = \frac{\tilde{\rho} We_0}{8X\delta_0\tilde{\delta}^2} = \frac{\tilde{\rho} We_0}{2D_0\tilde{\delta}^2} \tag{3-98}$$

The dimensionless wave growth rate is expressed as:

$$\frac{\partial f}{\partial t} = \sqrt{\frac{2\left(\rho_g\, u_{f_i}^2\, n - \sigma n^2\right)}{\rho_f h}}$$

Reminding that $h = D_i h_i/2r$, and substituting in $\partial f/\partial t$,

$$\frac{\partial f}{\partial t} = 2\sqrt{\frac{r\left(\rho_g u_{f_i}^2 n - \sigma n^2\right)}{\rho_f D_i h_i}}$$

$$\frac{\partial f}{\partial t} = 2u_{f_i}\left[\frac{r}{D_i}\left(\underbrace{\frac{\rho_g}{\rho_f}\frac{n}{h_i}}_{I} - \underbrace{\frac{\sigma n^2}{\rho_f u_{f_i}^2 h_i}}_{II}\right)\right]^{1/2} \tag{3-99}$$

In (3-99) the two parts marked by I and II can be further rearranged as:

$$I :: \frac{\rho_g}{\rho_f} \times \frac{n}{h_i} = \frac{\tilde{\rho}}{h_i}\frac{\tilde{\rho}\, We_0}{2D_0\,\tilde{\delta}^2} = \frac{\tilde{\rho}^2\, We_0}{2h_i D_0\tilde{\delta}^2} \tag{3-100}$$

$$2D_0h_i = \frac{2D_0^2h_i}{D_0} = \frac{2D_0^2}{D_0/h_i} = \frac{2D_0^2\tilde{\delta}}{4X} \tag{3-101}$$

Substituting equation (3-101) into (3-100)

$$I:: \frac{\rho_g}{\rho_f} \times \frac{n}{h_i} = \frac{2X\tilde{\rho}^2We_0}{D_0^2\tilde{\delta}^3} \tag{3-102}$$

Part (II) in equation (3-99) is

$$II:: \frac{\sigma n^2}{\rho_f\, u_{f_i}^2\, h_i} = \frac{n^2}{We_s} = \frac{4X\tilde{\delta}}{We_0}\left(\frac{\tilde{\rho}\, We_0}{2D_0\tilde{\delta}^2}\right)^2 = \frac{X\tilde{\rho}^2We_0}{D_0^2\tilde{\delta}^3} \tag{3-103}$$

Substituting equations (3-102) and (3-103) into equation (3-99),

$$\frac{\partial f}{\partial t} = 2u_{f_i}\left[\frac{r}{D_i}\left(\frac{2X\tilde{\rho}^2We_0}{D_0^2\tilde{\delta}^3} - \frac{X\tilde{\rho}^2We_0}{D_0^2\tilde{\delta}^3}\right)\right]^{1/2} = \frac{2\tilde{\rho}U_s}{\tilde{\delta}D_0}\left[\frac{XWe_0}{D_i\tilde{\delta}}\right]^{1/2} r^{1/2} \tag{3-104}$$

Knowing that $r = ½D_i + u_{f_i}cos\Psi t$, equation *(3-104)* could be rearranged as:

$$\frac{\partial f}{\partial t} = \frac{\partial f}{\partial r}\frac{dr}{dt} = \frac{\partial f}{\partial r}u_{f_i}cos\Psi = \frac{2\tilde{\rho}\, u_{f_i}}{\tilde{\delta}D_0}\left[\frac{XWe_0}{D_i\tilde{\delta}}\right]^{1/2} r^{1/2} \tag{3-105}$$

Then the wave growth equation can be expressed by equation (3-106),

$$\frac{\partial f}{\partial r} = f_r = \frac{2\tilde{\rho}}{\tilde{\delta}D_0cos\Psi}\left[\frac{XWe_0}{D_i\tilde{\delta}}\right]^{1/2} r^{1/2} \tag{3-106}$$

Integrating equation (3-106) with respect to r would result:

$$f_r^{cr} = \frac{4\tilde{\rho}}{3\sqrt{2}\tilde{\delta}D_0cos\Psi}\left[\frac{XWe_0}{\tilde{\delta}}\right]^{1/2}\frac{\left(r_b^{3/2} - r_i^{3/2}\right)}{r_i^{1/2}} \tag{3-107}$$

Rearranging

$$\frac{r_b^{3/2}}{r_i^{1/2}} - r_i = \frac{3\sqrt{2}\,\tilde{\delta}D_0cos\Psi_i\, f_r^{cr}}{4\tilde{\rho}\left[\frac{XWe_0}{\tilde{\delta}}\right]^{1/2}} \tag{3-108}$$

Dividing both sides of equation (3-108) by r_i and noting that the breakup radius r_b is non-dimensionalized with the deflector radius $½D_i$.

$$\frac{r_b^{3/2}}{r_i^{3/2}} = 1 + \frac{3\sqrt{2}\,\tilde{\delta} D_0 cos\Psi f_r^{cr}}{4 r_i \tilde{\rho}\left[\frac{X We_0}{\tilde{\delta}}\right]^{1/2}}$$

$$\frac{2r_b}{D_i} = \left[1 + \frac{3\sqrt{2}}{2} f_r^{cr} \frac{cos\Psi}{\tilde{\rho}\, We_0^{1/2}} \left(\frac{\tilde{\delta}}{X}\right)^{3/2}\right]^{2/3} \tag{3-109}$$

Or by dividing dominator and denominator of the right hand side by the jet diameter:

$$\tilde{r}_b = \frac{1}{2} X \left[1 + \frac{3\sqrt{2}}{2} f_r^{cr} \frac{cos\Psi}{\tilde{\rho}\, We_0^{1/2}} \left(\frac{\tilde{\delta}}{X}\right)^{3/2}\right]^{2/3} \tag{3-110}$$

Equation (3-109) shows that the non-dimensionalized breakup distance, $2r_b/D_i$, is a complex function of jet Weber number as well as other normalized parameters , X, $\tilde{\rho}$ and $\tilde{\delta}$. This equation can be simplified assuming:

$$3\sqrt{2}/2 \times f_r^{cr} cos\Psi / \tilde{\rho}\, We_0^{1/2} \left(\tilde{\delta}/X\right)^{3/2} \gg 1 \tag{3-111}$$

which means the sheet break-up distance is much larger than the radius of the sprinklers deflector. Under this circumstance, the dimensionless sheet break-up distance is reduced to:

$$\tilde{r}_b = \left(\frac{3\sqrt{2}}{2} \frac{cos\Psi_i}{\tilde{\rho}} f_r^{cr}\right)^{2/3} \tilde{\delta} We_0^{-1/3} X^{-1} \tag{3-112}$$

Sheet breakup distance shows a -1/3 power law relation with jet Weber number which has been reported by many researches for We_0 larger than 1000, however with regard to the density it appears to be -2/3 power law. The scaling laws show that the sheet breakup distance depends not only on the We_0, but also the critical dimensionless wave amplitude, f_0. This formulation different from the barely tested formulation reported by Marshall [125], presented in (3-113), and

$$\frac{r_b}{D_0} \sim \left[\frac{\rho_g}{\rho_f} f_r^{cr-2} We_0\right]^{-1/3} \tag{3-113}$$

The ligament diameter, d_l, could be found the same way as §3.4.2, hence ;

$$\pi\, \rho_f\, h_b \left[\left(r_b + \frac{\pi}{n}\right)^2 - r_b^2\right] \cong \frac{1}{2}\, \pi^2 \rho_f\, d_l^2\, r_b \tag{3-114}$$

$$d_l \cong 2\left(\frac{h_b}{n}\right)^{\frac{1}{2}}$$

Figure 3-10 shows a sketch of breakup radius versus radial distance of breakup point. Assuming asymptotic decay of sheet thickness with radial distance, $h_b = h_i\, D_i/2r$, equation (3-115) can be written in following form, where $r = \mathrm{r_b}/\cos(\Psi)$,

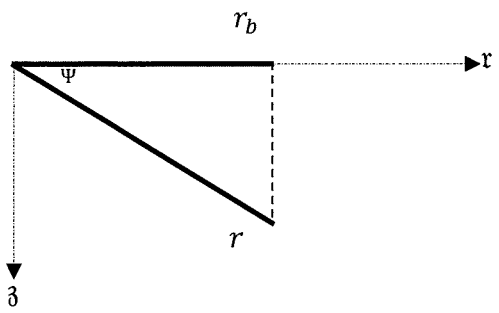

Figure 3-10: Schematic illustration of ejection angle and breakup radius

$$d_l = 2\left(\frac{\frac{h_i\, D_i}{2r}}{\frac{\tilde{\rho} We_0}{2D_0\tilde{\delta}^2}}\right)^{\frac{1}{2}} = 2\left(\frac{h_i D_i D_0 \tilde{\delta}^2 cos(\Psi)}{\tilde{\rho} We_0 r_b}\right)^{\frac{1}{2}} \tag{3-115}$$

It should be taken into account that the sheet breakup point may have an angle with deflector level. The droplet diameter, d_d, can be obtained from equation (3-89) by neglecting viscosity effect:

$$d_d = 1.88\, d_l = 1.88 \times 2\left(\frac{h_i D_i D_0 \tilde{\delta}^2 cos(\Psi)}{\tilde{\rho} We_0 r_b}\right)^{\frac{1}{2}} \tag{3-116}$$

Dimensionless sheet radial breakup distance is given by equation (3-109), and can be substituted in above relation of droplet diameter

$$d_d = 3.76\left(\frac{2h_i D_i D_0 \tilde{\delta}^2 cos(\Psi)}{\tilde{\rho} We_0\left[1+\frac{3\sqrt{2}}{2} f_r^{cr}\frac{cos\Psi}{\tilde{\rho} We_0^{1/2}}\left(\frac{\tilde{\delta}}{X}\right)^{3/2}\right]^{2/3} D_i}\right)^{\frac{1}{2}} \quad (3\text{-}117)$$

Rearranging the above expression gives:

$$d_d = 3.76\left(\frac{2^{5/3} h_i\, D_0\, \tilde{\delta}^2\, X cos(\Psi)}{\tilde{\rho}^{1/3} We_0^{2/3}\left[2\tilde{\rho}\, We_0^{1/2} X^{3/2} + 3\sqrt{2}\, f_r^{cr} cos(\Psi)\tilde{\delta}^{3/2}\right]^{2/3}}\right)^{\frac{1}{2}} \quad (3\text{-}118)$$

Droplet diameter can be further non-dimensionalized as follows:

$$\tilde{d} = \frac{d_d}{D_0} = \frac{3.76 \times \tilde{\delta}\left(2^{\frac{5}{3}} h_i\, X cos(\Psi)\right)^{1/2} D_0^{-1/2}}{\sqrt[3]{2\,\tilde{\rho}\, We_0^{1/2} X^{3/2} + 3\sqrt{2} cos(\Psi) f_r^{cr}\tilde{\delta}^{3/2}}}\,\tilde{\rho}^{-1/6}\, We_0^{-1/3} \quad (3\text{-}119)$$

If the sheet breakup distance is considerably larger than the radius of deflector, that is the condition listed in equation (3-111), the dimensionless droplet diameter is simplified to

$$\tilde{d} = 3.76\left(\frac{3\sqrt{2}}{2} f_r^{cr}\right)^{-1/3} D_0^{-1/2}\left(2h_i\tilde{\delta}X\right)^{1/2}(cos(\Psi))^{1/6}\,\tilde{\rho}^{-1/6} We_0^{-1/3} \quad (3\text{-}120)$$

Equation (3-120) demonstrates how sprinklers orifice size and physical parameters would affect droplet median diameter. This shows a $-1/3$ power law relation with Jet Weber number as well as a $-1/6$ power law for density. A decrease in the ambient air density will end to larger median droplet diameters. Reduction of ambient density is an outcome of fire scenario and consequent increase of temperature. Weber number is affected by jet diameter and working pressure. An increase in working pressure will increase the jet speed, and results larger droplet median diameters.

Later in §4 the presented dimensionless median droplet diameter in equation (3-120) derived as part of the present thesis, will be compared against prediction of diameter given in equation *(3-121)*. [89]

$$\tilde{d} = 3.5\,\tilde{\rho}^{-1/6} D_0^{-1/2} \left(\frac{h_i}{D_0}.\frac{r_i}{D_0}.\frac{\tilde{\delta}^2}{f_0}\right)^{1/3} (cos\Psi)^{1/6}\, We_0^{-1/3} \qquad (3\text{-}121)$$

The ratio between *(3-120)* and *(3-121)* is as below:

$$\frac{\left(3.76\left(\frac{3\sqrt{2}}{2} f_r^{cr}\right)^{-\frac{1}{3}} D_0^{-\frac{1}{2}} (2h_i\tilde{\delta}X)^{\frac{1}{2}} (\cos(\Psi))^{\frac{1}{6}}\, \tilde{\rho}^{-\frac{1}{6}} We_0^{-\frac{1}{3}}\right)}{3.5\,\tilde{\rho}^{-\frac{1}{6}} D_0^{-\frac{1}{2}} \left(\frac{h_i}{D_0}.\frac{r_i}{D_0}.\frac{\tilde{\delta}^2}{f_0}\right)^{\frac{1}{3}} (cos\Psi)^{\frac{1}{6}}\, We_0^{-\frac{1}{3}}}$$

$$= \frac{3.76\left(\frac{3\sqrt{2}}{2}\right)^{-\frac{1}{3}} 2^{\frac{1}{2}}}{3.5} \frac{h_i^{\frac{1}{2}} \tilde{\delta}^{\frac{1}{2}} X^{\frac{1}{2}}}{\left(\frac{h_i}{D_0}.\frac{D_i}{2D_0}.\tilde{\delta}^2\right)^{\frac{1}{3}}} \qquad (3\text{-}122)$$

$$= \frac{3.76\left(\frac{3\sqrt{2}}{2}\right)^{-\frac{1}{3}} 2^{\frac{1}{2}}}{3.5 \times 2^{-1/3}} h_i^{\frac{1}{2}-\frac{1}{3}} \tilde{\delta}^{\frac{1}{2}-\frac{2}{3}} D_i^{\frac{1}{2}-\frac{1}{3}} D_0^{-\frac{1}{2}-(-\frac{2}{3})}$$

$$= \frac{2 \times 3.76 \times 3^{-\frac{1}{3}}}{3.5} h_i^{\frac{1}{6}} \tilde{\delta}^{-\frac{1}{6}} D_i^{\frac{1}{6}} D_0^{\frac{1}{6}} = 1.4897 \left(\frac{h_i D_0 D_i}{\tilde{\delta}}\right)^{\frac{1}{6}}$$

3.7 Stochastic Modeling

In real sprays, a multitude number of drops with different sizes are created. In order to model this behavior, a stochastic analysis have been carried out in this research in a similar framework as Rizk and Mongia [119] and Wu et al [124]. This is an alternative to the deterministic approach presented in section 3.5

In the stochastic formulation, random behavior is added into the spray models with a physical basis to obtain the distributed spray characteristics. This physics-

based technique provides an alternative to specifying a distribution about a calculated characteristic size. The following parameters are treated stochastically:

(i) The liquid sheet critical breakup amplitude,

(ii) The liquid sheet breakup wavelength,

(iii) The ligament breakup wavelength,

Some deterministic modeling approaches have assumed the constant liquid sheet velocity throughout the spray atomization modeling process. However in a stochastic modeling approach a distribution could be considered for sheet velocity by defining turbulence intensity, I_u. The turbulence intensity is defined as [123]

$$I_u = \frac{\sqrt{\overline{u'^2}}}{\overline{U}} \qquad (3\text{-}123)$$

The velocity magnitude is the sum of the mean liquid velocity, $\overline{U}$, and the fluctuation zero-mean velocity magnitudes, u'. It can be assumed that liquid sheet velocity has a standard (Gaussian) probability density distribution. Thus the stochastic model creates a set of random sheet velocities, which satisfies the standard distribution based on the given turbulence intensity and the value of the mean liquid sheet velocity. The distribution of liquid sheet velocity would affect critical sheet breakup wavelength, sheet breakup time, sheet breakup and subsequent ligament and droplet characteristics.

3.7.1 The Liquid Sheet Critical Breakup Amplitude

In deterministic modeling a constant critical dimensionless breakup amplitude, f = 12, is assumed. However as discussed in §3.4.1 the initial disturbance amplitudes in sprinkler application are very variant, hence the critical conditions could become largely unknown. Therefore it is justified to treat the critical dimensionless breakup amplitude as a discrete random parameter.

In the present study the critical dimensionless breakup amplitude is defined over an n −element space to take in to account the assumed distribution of unknown initial disturbances, hence f [n]. A Gaussian normal distribution, appendix B, has been adopted for this parameter by mean critical dimensionless breakup amplitude

of 12 and a modeling parameter which is known as fluctuation intensity I_f. The fluctuation intensity is defined in form of turbulence intensity in equation (3-124)

$$I_f = \frac{\sigma_f}{\bar{f}} \qquad (3\text{-}124)$$

In the above equation σ_f is the standard derivation of f[m] . The random variable f[m] is used in the wave dispersion model resulting in m different critical sheet breakup wavelengths, sheet breakup times, and sheet breakup locations. Subsequently this perturbed variables will affect evaluations of ligament formation, droplet size and droplet location. The turbulence intensity is assumed to be chosen between $0.15 < I_f < 0.25$ in the format shown in *(3-125)*

$$I_f = (I_f)_{min} + \left\{(I_f)_{max} - (I_f)_{min}\right\} \times rand(1) \qquad (3\text{-}125)$$

To prevent the negative occurrences of variances, $\sigma_f = I_f \times \mu_f$, fluctuation intensities have been generated over a uniform probability distributed, appendix B, set of data.

Table 3-1 shows the minimum and maximum values for the critical sheet breakup wave lengths, obtained through stochastic analysis. The average values of (maxima-minima) from five attempts ranged from (8.98-14.62) to (6.43-1685) and (3.81-20.28) as the number of iterations increased from 10 to 100 and 1000, correspondingly. These synopses demonstrate the diversity of the values that the critical sheet breakup wave length can find in simulation with the explained setup.

Table 3-1: Minimum and maximum of normally distributed critical sheet breakup wavelengths calculated from uniformly distributed fluctuation dependency to the number of iteration.

Iteration no.		Attempt no.					Mean
		1	2	3	4	5	
10	Min	8.74	9.52	10.23	10.29	6.05	*8.98*
	Max	13.09	15.06	14.73	16.24	13.18	*14.62*
100	Min	6.28	5.98	6.11	6.36	7.4	*6.43*
	Max	17.27	17.82	16.38	15.80	16.97	*16.85*
1000	Min	5.17	4.41	4.01	4.74	0.71	*3.81*
	Max	20.21	20.59	19.97	20.84	19.81	*20.28*

Figure 3-11 presents the normal probability density function of critical sheet breakup wavelengths calculated from uniformly distributed fluctuation at 10 and 100 trials, which is built up around mean of 12.

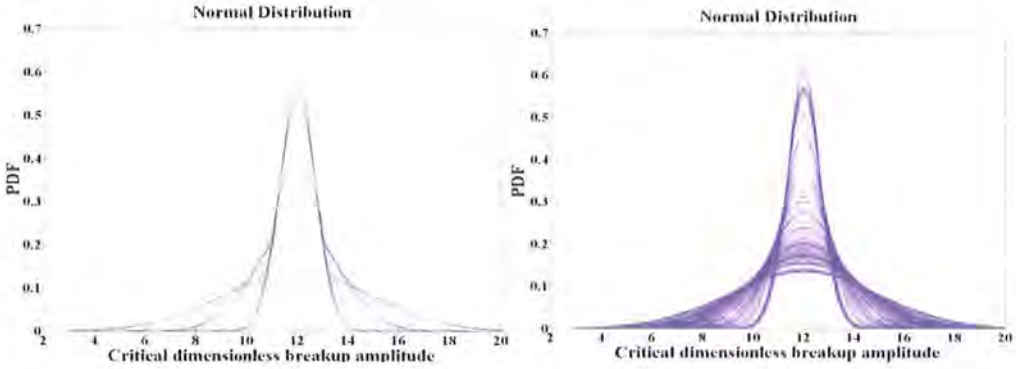

(a) (b)

Figure 3-11: Presentation of normal probability density function of critical sheet breakup wavelengths calculated from uniformly distributed fluctuation at a) 10 trials b) 100 trials

3.7.2 The Liquid Sheet Breakup Wavelength

It has been discussed, §3.4.2, that in the sheet breakup model, the sheet is assumed to break into toroidal ligaments having radial width of one-half wavelength. There is not any solid reason for the sheet breakup in one-half wavelength fragments as some literatures mentioned 3/8 of wavelength. In the stochastic model the liquid sheet breakup wavelength, $\overline{r_l}\,[n,p]$, presented in equation *(3-126)*, is treated as a discrete random variable for each of n sheet critical breakup amplitude over a p-element space.[124]

$$\overline{r_l}[n,p] = \frac{1}{2}\,\lambda_{sh}[n] \qquad (3\text{-}126)$$

The turbulence intensity for this parameter can be defined similar to critical sheet breakup wavelength as presented in *(3-127)*.

$$I_l = \frac{\sigma_l[n]}{\mu_l[n]} = \frac{\overline{r_l}'}{\overline{r_l}} \qquad (3\text{-}127)$$

Where the means, μ_l, are one-half wavelength fragments sizes, $\overline{r_l}$, and its standard deviation (disturbed values, $\overline{r_l}'$) could reach up to the mean values. Hence the fluctuation density is less than one. Distribution for ligament lengths has been obtained using Chi-squared distribution. The Chi-squared distribution is

a special case of Gamma distribution and both are explained in appendix B, and the rational of its preference to Gamma distribution was mainly to prevent the occurrence of negative ligament widths at high turbulence intensities and also to artificially imply the rosin-Rammler type of behavior in producing the spray charactistics.

The turbulence intensity for Chi-square distribution can be obtained

$$I_{\chi^2} = \frac{\sigma_{\chi^2}}{\mu_{\chi^2}} = \frac{\sqrt{2v}}{v} = \sqrt{\frac{2}{v}} \qquad (3\text{-}128)$$

As mentioned earlier the fluctuation intensity cannot exceed 1 due to physical constraints, thus v ≥ 2. From equation (3-128) can be rearranged to $v = 2/I_{\chi^2}$. In the simulation $25 \leq \mathrm{v} \leq 200$ has been chosen in order to ensure a turbulence intensity of $0.1 \leq I_l \leq 0.3$.

3.7.3 The Ligament Breakup Wavelength

Similar to the liquid sheet breakup wavelengths, the ligament breakup wavelengths $\mu_d\,[n,p,q]$, presented in equation *(3-129)* is treated as a discrete random variable for each of $n \times p$ sheet breakup wavelengths over an q-element space and are obtained by a chi-square distribution. The ligament breakup wavelength and the associated fluctuation intensity would be,

$$\mu_d\,[n,p,q] = \frac{1}{2}\,\lambda_l^{cr}\,[n,p] \qquad (3\text{-}129)$$

$$I_d = \frac{\sigma_d[n,p]}{\mu_d\,[n,p]} \qquad (3\text{-}130)$$

In overall $n \times p \times q$ droplets would be obtained in the stochastic analysis. This procedure have been applied to Method-1 to Method-4 and the results are presented and discussed in §4.5.

3.8 Semi-Empirical Modeling

As highlighted in the first two chapters, the actual number of droplets generated by sprinkler is still experimentally uncertain and it is estimated to be 10^5-10^8 particles/sec. These droplets which are formed below the sprinkler at different elevation angles and azimuthal locations have variant characteristic sizes, i.e. volume median diameters due to the periodic tine and space geometry of the sprinkler deflector. The difference between the minimum and maximum droplet diameters may reach even up to two orders of magnitude depending on operating pressures and ambient temperatures.

For a given set of working conditions the final outcome out of any of Method-1 to Method-4 was a single characteristic spray parameter representative of the whole spray. If Methods 1-4 are used in a deterministic frame, they hardly mimic what happens in real sprinkler spray and has not yet fulfilled the demands of industry. However, there have been some efforts to overcome these shortcomings in modeling, such as introducing the stochastic analysis. This approach however resulted in a range for predicted characteristics representative of the whole spray. The stochastic approach sheds more light to the overall spray distribution, but still does not picture a clear sprinkler spray, in the sense that volume flux or droplet characteristics at a specific spatial location (ϕ_j, θ_k) remains unidentified.

The semi-empirical atomization model, developed in the present thesis is built on the general understanding obtained from experimental measurements on a varied range of sprinklers. Measurements of volume flux for sprinklers of any configuration, any type and any working condition, [41] reveals that spray pattern at an Azimuthal location does not show uniform and homogeneous trend which is an evidence for sheet breakup and atomization in multiple elevation angles. In addition to this there is a higher possibility of formation of larger droplets at regions with higher fluxes. Therefore, this modeling approach uses experimentally evaluated volume fractions, as one of the inputs in the modeling approach, Figure 3-12, to tune the deterministic approach in such a manner to give different spray characteristics at specific spatial positions. Another rationale behind the semi-empirical approach is that to-date there is no sprinkler spray model that

includes in its formulation the effects of the arm, boss and tines which are extremely complex to model due to the wide variety of sprinkler head types. The measured volume fractions, which are relatively easy to obtain from spray manufacturers, would have taken implicitly into account these effects in a more realistic manner.

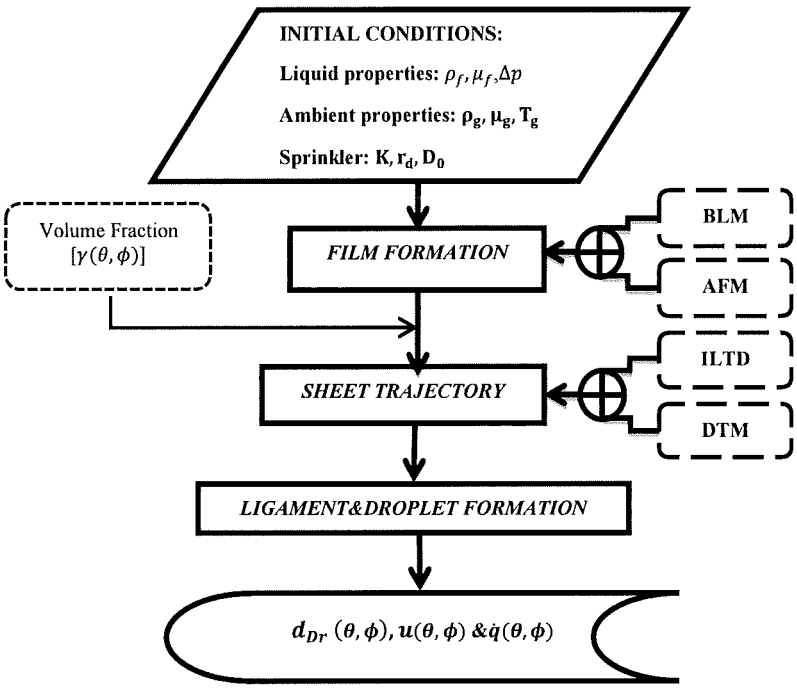

Figure 3-12: Structure of semi-empirical approaches.

In the semi-empirical approach an experimental volume fraction data is combined with physical sub-models to develop a semi-empirical model for the prediction of the spray characteristics at different local spatial locations in the sprinkler spray. This mainly implies that the spray characteristics are a function of spatial water flux for any sprinkler. The implication of volume fractions assumes that the water film leaving the deflector does not necessarily disintegrates at the same level as tine surface, $\theta \approx 0°$, but it forms spray at multiple elevation angles at any azimuthal location.

To estimate the spray characteristics at favorable azimuthal (ϕ_j) and elevation (θ_k) angles, the pertinent sheet's initial thickness at deflector's edge has been modified in the present study according to equation (3-131).

$$h_{jk_i} = \gamma_{jk} \times h_i \qquad (3\text{-}131)$$

Therefore the thickness of sheet facing an elevation angle is considered to be a fraction of film thickness at deflector edge. Each of these modified sheet thicknesses could be dealt as boundary condition in associated sheet trajectory modeling. In another word the essence of the method is to use the modified thickness (3.130) as an input into the earlier analyses.

The data which has been used to verify this concept is based on sprinklers explained in §2.6.1 where a series of experiments were carried out to quantify the spray. The total water volume flux analogous to each Azimuthal location has been approximated by integrating the partial volume fluxes over all elevation angles whose measurements were known. For most sprinklers, there is no significant flow before $\theta = 0°$.

$$\dot{q}(\phi_j) = \int_{\theta_k=\theta_{ini}}^{\theta_k=\theta_{final}} d\dot{q}(\theta_k, \phi_j) \qquad (3\text{-}132)$$

Having evaluated the corresponding water flux at each azimuthal location, the partial (regional) volume fraction at the elevation angles can be estimated by *(3-133)* as a number between 0 and 1.

$$\gamma_{jk} = \frac{d\dot{q}(\theta_k, \phi_j)}{\dot{q}(\phi_j)} \qquad (3\text{-}133)$$

One drawback of the presented semi-empirical model results from the fact that the volume fraction implies the distribution in elevation direction, but does not illustrates the distribution in azimuthal direction. Hence, for instance, for two azimuthal locations, the spray flux may be different; however, if the distribution in elevation direction is the same, γ_{ij} will be the same. Therefore, according to equation *(3-133)*, the same spray characteristics will be predicted for the two azimuthal locations. However, the reality may contradict with this.

To give a better picture on the value of evaluated volume fraction, they have been given in Appendix-D, for the pendant sprinkler working at 3.5 bar.

3.9 Water Volume Flux

Water volume flux has been well defined and explained in §2.5.2. This section explains how spatial water volume fluxes are evaluated numerically.

Number Density

Recalling from equation (2-8) that $\acute{N}$, is the number density of droplets in a probe volume of dV, it can be written as $\acute{N} = \widehat{N}/dV$, and $\widehat{N}$ is the number of droplets that enter the probe volume. In this study the differential azimuthal angle is assumed to be $d\phi_j = 1°$. Therefore the number of droplets per degree is obtained from equation (3-90)

$$\widehat{N} = N/360 \qquad (3\text{-}134)$$

Computational Volume

In the current analysis for fire sprinklers it is assumed that differential volumes, dV, and differential areas, dA, are located along or on the surfaces of a sphere around the sprinkler and this also is compatible with method undertaken in near field measurement whose data are being used for validation of theoretical predictions. Therefore, a spherical coordinate system seems to be the most appropriate one for the analysis. The impact of this choice is that the differential areas are of different size depending on the elevation angle, θ_k. A spherical differential area element at a given radial location can be presented in form of,

$$dA = (r \sin\theta \, d\phi)(r d\theta) \qquad (3\text{-}135)$$

where r is radius of the sphere. Consequently probe volumes at different elevation and azimuthal angles are not the same due to the fact that not only the initial droplet formation radius, r_d, will change for different locations around and below the sprinkler, but also the elevation angle itself has considerable change on, $sin\theta$.

In a given special location the probe volume is the region sweeps the region between the initial droplet formation location and the point at the same radial direction where the experimental measurements are being performed. Theoretically this sample volume would be the volume between two cones, as

shown in Figure 3-13 whose bases are the differential areas at the mentioned two radiuses, and its elevation angle. Based on this introduced methodology the probe volume is calculated as:

$$dV = \frac{1}{3} dA_p r_p - \frac{1}{3} dA_{Ini} r_d \tag{3-136}$$

Where $(r sin\, \theta d\phi\,)$ and $(r d\theta)$ will form the length and width of the base of the cone respectively. During the course of this study the width of probe domain $(r d\theta)$ has been replaced with d_d . During the droplets presence time in the probe volume, it has been assumed that droplets maintain their radial momentum dominance relative to the gravitational effect, thus the latter has been neglected.

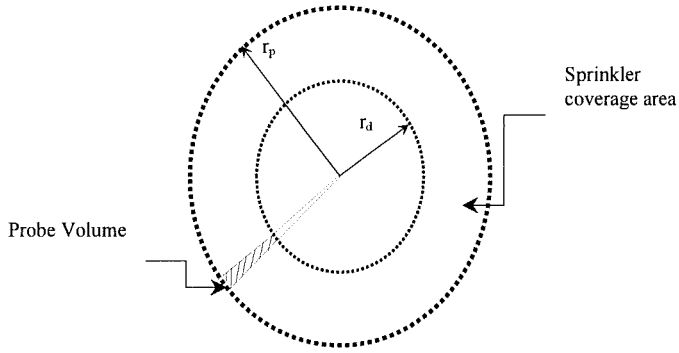

Figure 3-13: Top view and orientation of the initial droplet radius and the data collection location with respect to the sprinkler position in an arbitrary radial direction.

However in experiments, the minimum distance from sprinkler at which the volume flux measurements conducts, is approximately two to four times longer than initial droplet formation radius. As the droplet completes moving through the gap between formation point and measurement position, the surrounding air continuously exerts drag force on the droplets and results in reducing its stream-wise velocity. In the next section the formulation for calculating the effects of drag force on droplets are given.

Droplet velocity

The main goal of this study is to characterize the sprinkler spray. To validate the developed modeling approach, the predictions should be validated against the measurements which are always carried out at some distance away from the sprinkler as shown in Figure 3-13. Hence it is important to understand how the

droplet velocities will change as they leave their initial formation location and to determine how far the droplets will travel before they reach the terminal velocity. Therefore, the droplet velocity in the probe volume have been calculated rigorously in § 3.10.

3.10 Droplet Trajectories

Once droplets are formed, they will disperse in the surrounding medium due to their momentum. They will lose their momentum due to available drag. The formulation presented in this section, will enable studying the effect of the drag force on the droplets velocity from their initial formation point to any point of interest. The discussion presented in this section will be used in the next chapter.

The trajectory of droplets can be described with Newton's second law (3-137), [142]&[143].

$$\frac{d}{dt}(m_d u_d) - m_d g + \frac{1}{2}\rho_f C_c A_d (u_d - u_g)|u_d - u_g| = 0 \qquad (3\text{-}137)$$

In the above equation, the term, $d(m_d u_d)/dt$, represents the change in the momentum of the droplet. The term $m_d g$ is the force of gravity on the droplet. The term $\frac{1}{2}\rho_f C_c A_d (u_d - u_g)|u_d - u_g|$, is the drag force that surrounding air exerts on the droplet as it moves through the air [144]. The m_d is the mass of the droplet, g is the acceleration due to gravity, A_d is cross sectional area of the droplet, u_g is the velocity of the surrounding air and C_c is the drag coefficient and is described in equation (3-138).

$$C_c = \frac{F_{drag}}{\frac{1}{2}\rho_g A_d (u_d - u_g)^2} \qquad (3\text{-}138)$$

Where F_{drag} is the drag force. Figure 3-14 shows the relation of the drag coefficient to the Reynolds number for rigid spheres for the range of Reynolds Number. The data points represent experimental results. The solid curve represents an empirical correlation based upon the experimental data.

For flows around spheres where Re<1, the drag coefficient can be described using Stokes' sphere drag formula:

$$C_c = \frac{24}{Re} \quad Re < 1 \qquad (3\text{-}139)$$

For Reynolds numbers less than 10^5, White [128] suggests that a curve fit based upon empirical results to be used.

$$C_c = \frac{24}{Re} + \frac{6}{1+\sqrt{Re}} + 0.4 \quad 1 < Re < 10^5 \qquad (3\text{-}140)$$

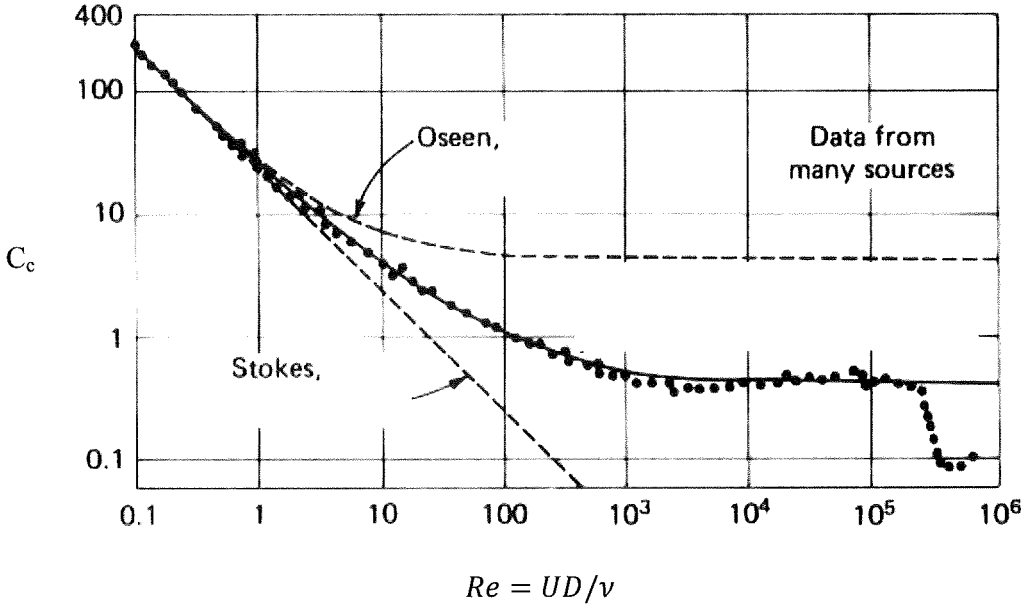

Figure 3-14: Drag coefficient for a solid sphere [41] and [128].

If the droplets are treated as solid spheres, the terminal velocity and the time to achieve the terminal velocity after leaving the initial formation location can be estimated. If the droplet size is assumed to be constant and the air velocity is assumed to be zero, equation (3-137) can be written as follows:

$$u_d \underbrace{\frac{dm_d}{dt}}_{=0} + m_d \frac{du_d}{dt} = m_d g - \frac{1}{2}\rho_g C_c \left(\frac{1}{4}\pi d_d^2\right) u_d^2$$

$$m_d = \rho_f V_d = \rho_f \left(\frac{1}{6}\pi d_d^3\right) \qquad (3\text{-}141)$$

$$\frac{du_d}{dt} = m_d g - \frac{\rho_g C_c \left(\frac{1}{4}\pi d_d^2\right) u_d^2}{2\rho_f \left(\frac{1}{6}\pi d_d^3\right)}$$

Hence,

$$\frac{du_d}{dt} = g - \frac{3}{4} C_c \frac{\rho_g}{\rho_f} \frac{u_d^2}{d_d} \qquad (3\text{-}142)$$

When stokes sphere drag formula is used for $Re < 1$, the terminal velocity, $\breve{u}_d$, can be found by solving equation (3-142) for the case when the droplet acceleration equals zero. When Stokes sphere drag formula is used for $Re < 1$, the terminal velocity, $\breve{u}_d$, can be found by solving equation (3-142) for the case when the droplet acceleration equals zero. Terminal speed is the constant vertical speed reached by the droplets after travelling a sufficient length of time in still air under the force of gravity.

$$\frac{du_d}{dt} = 0$$

$$g = \frac{3}{4}\left(\frac{24}{Re}\right)\frac{\rho_g}{\rho_f}\frac{u_d^2}{d_d} = \frac{3}{4}\frac{\rho_g}{\rho_f}\left(\frac{24}{\frac{u_d . d_d}{\nu}}\right)\frac{u_d^2}{d_d} \qquad (3\text{-}143)$$

$$\breve{u}_d = \frac{1}{18}\frac{\rho_f}{\rho_g}\frac{g}{\nu} d_d^2$$

For $Re < 1$, the velocity as a function of time can be found analytically by solving equation (3-142).

$$u_d(t) = \frac{1}{9\nu_f\rho_g}\left[\frac{1}{2}gd_d^2\rho_f + e^{-\frac{18\nu_f\rho_g}{\rho_f d_d^2}t}\left(-\frac{1}{2}gd_d^2\rho_f + 9u_0\nu_f\rho_g\right)\right] \qquad (3\text{-}144)$$

Where u_0 is the initial velocity of the droplet.

When the empirical drag formula is used for $Re \geq 1$, the equation for the terminal velocity is more complicated.

$$0 = g - \frac{3}{4}\frac{\rho_g}{\rho_f}\left(\frac{24\nu_f}{\breve{u}_d.d_d} + \frac{6}{1+\sqrt{\frac{\breve{u}_d.d_d}{\nu_f}}} + 0.4\right)\frac{u_d^2}{d_d} \qquad (3\text{-}145)$$

For $Re > 1$, equation (3-142) becomes

$$\frac{du_d}{dt} = g - \frac{3}{4}\frac{\rho_g}{\rho_f d_d}\left[\frac{24\nu_f}{d_d u_d} + \frac{6}{1+\sqrt{\frac{d_d u_d}{\nu_f}}} + 0.4\right]u_d^2 \qquad (3\text{-}146)$$

Equation *(3-146)* is solved numerically by 4th order Runge-Kutta.

However because the air is not quiescent while sprinklers are operating and there is a turbulence, the dissipation rate is higher and the theoretical models should over-predict the droplet velocities. According to Sheppard [41], in sprinkler applications, the droplets leave the sprinkler at an initial velocity on the order of 1-15 m/s. After their initial formation around sprinkler the droplet velocities approach their terminal velocities.

Figure 3-15 shows the time history of velocity change for a droplet of diameter 0.5mm, with an initial velocity of 20 m/s in horizontal direction. The vertical downward velocity, the horizontal velocity and the resultant velocity of the droplets are given in Figure 3-15 a-c, respectively. These figures show a glimpse of the way the formulation will help to simulate the droplet deceleration.

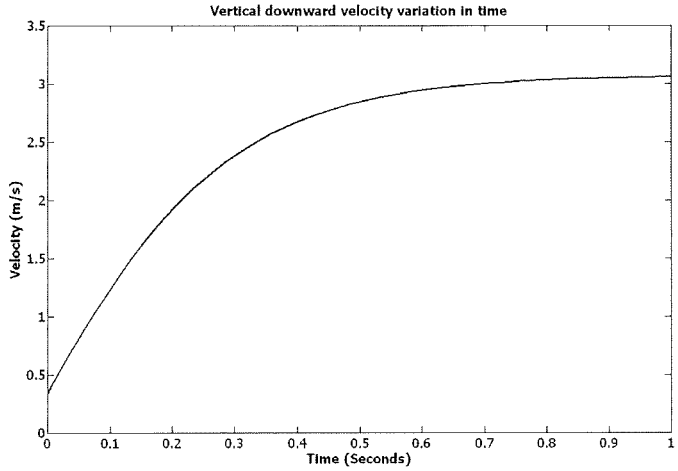

(a)

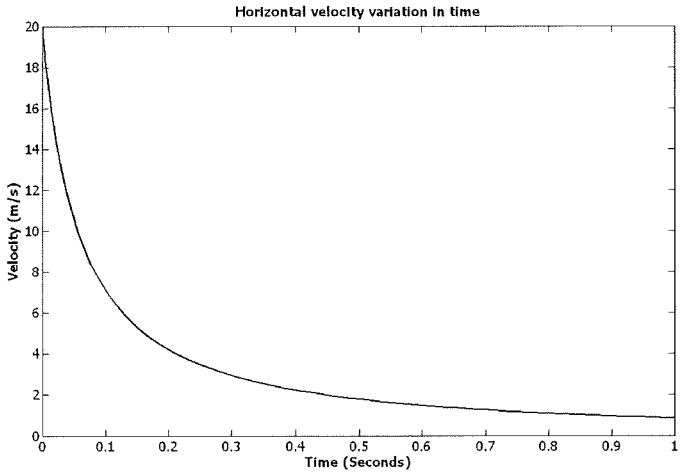

(b)

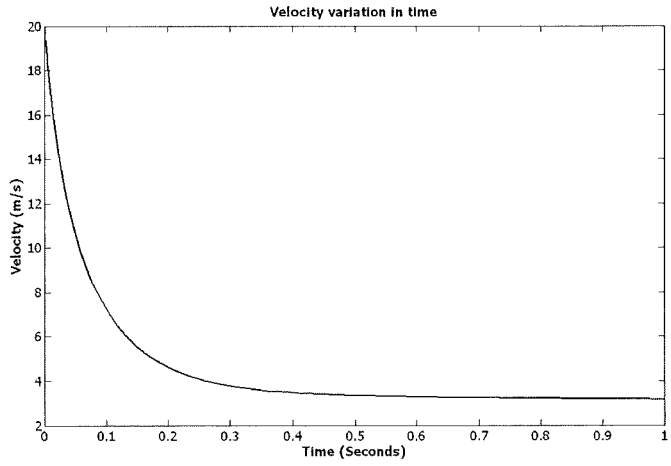

(c)

Figure 3-15: (a) Vertical, (b) horizontal, (c) resultant velocity change of a droplet with 0.5 mm diameter with initial horizontal velocity of 20 m/s

Figure 3-16 shows the time history of velocity of a 0.5mm diameter droplet for range of initial horizontal velocities from 1-18 m/s, and no downward vertical velocities. It shows the independency of terminal velocity to initial velocity as the 0.5mm diameter droplet will achieve the terminal velocity of 3.2 m/s after 0.6 seconds.

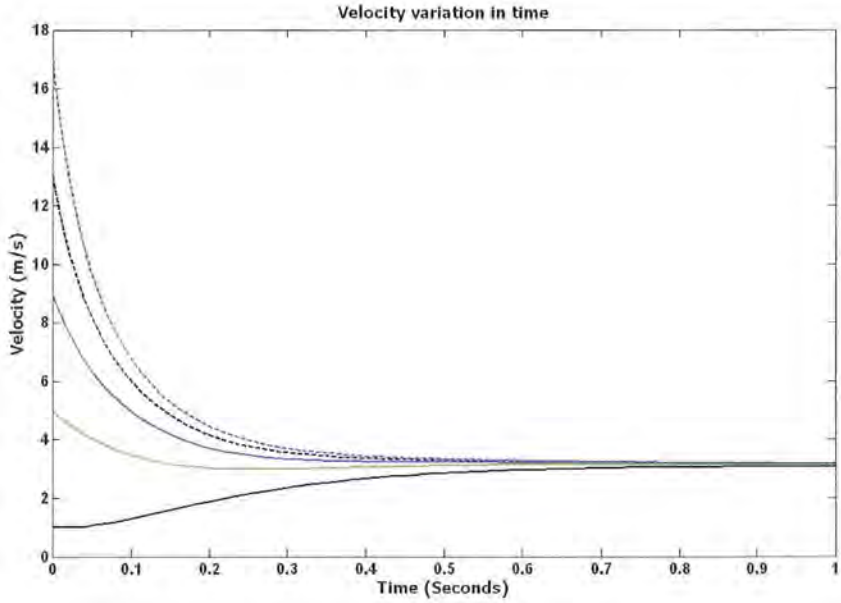

Figure 3-16: Velocity history of a 0.5 mm droplet at different initial horizontal velocities.

3.11 Summary

A series of mathematical models have been presented, discussed or modified for the main constituent physics of an axisymmetric impinging jet, i.e. film, sheet and ligament.

Furthermore, three new modeling approaches, which remain to the validated for sprinkler applications, have been introduced to deterministically evaluate spray characteristics, i.e. droplet size, velocity and initial location, by a given set of sprinkler data, injection and ambient conditions.

A stochastic approach has been applied to the developed deterministic models. These models ultimately provide distributions of initial spray characteristics.

A dimensionless formulation has been derived to estimate the sheet breakup distance and droplet diameter in an impinging jet atomizer. This facilitated

generalization over changes in operating conditions and nozzle and deflector geometries.

The effect of the frame arms and tine has been implicitly incorporated into the modeling by introducing a semi-empirical approach. The calculation method for volume flux has been presented and the trajectories of the droplets have been analyzed.

4 RESULTS AND DISCUSSION-VALIDATION STUDIES

4.1 Introduction

In this chapter the predictions of the sub models presented in previous chapter (theory) will be individually studied in depth for verification and validation purpose, and also for a better understanding of the spray atomization mechanism. The characteristics of flow over deflector and the sheet trajectory models will be studied in §4.2 and §4.3 respectively.

Furthermore the presently developed three deterministic models will be examined qualitatively and quantitatively in §4.4. The outcome of film models and sheet models will be used to verify their accuracy in predicting the sheet breakup distance and droplet median diameter. The stochastic approach (§3.7) has been applied to the all developed models and their accuracies have been investigated qualitatively and quantitatively in §4.5.

Two fire sprinklers have been fully quantified using the semi-empirical approach developed in the present thesis. The predictions for droplet size, droplet velocity and spray volume flux have been presented for one pendant sprinkler (§4.6) at two operational pressures and one upright sprinkler (§4.7) at two operational pressures. A sensitivity analysis has been performed in §4.8 to study the effect of approach to the lesser number of experimental data points. To minimize the dependency of the modeling to the experimentally evaluated volume fractions, uniform distribution assumption has been applied to the most efficient semi-

empirical approach in §4.9 and the spray characteristics has been reevaluated for the available sprinklers and operational conditions.

4.2 Characteristics of the Flow over Deflector Plates

The mathematical formulation of two film models are explained in §3.2.1 and §3.2.2. In this section the characteristics of these models will be explored in more depth for a better understanding of sprinkler spray atomization.

In the course of this chapter the investigations may be performed at a range of pressures and temperatures. This is either to depict the typical sprinkler's working condition or to match an available experimental set of data. Table 4-1 shows the injection pressures at their kpa and psi values and Table 4-2 summarizes ambient properties at different temperatures. They would be used to investigate characteristic behavior of atomization sub-models in this thesis. The initial conditions other than these have been addressed within the text where appropriate.

Table 4-1: Range of pressures used for characteristic studies

	P				
[kPa]	69	138	207	345	483
[psi]	10	20	30	50	70

Table 4-2: Ambient temperature, kinematic and dynamic viscosity of air

T [K]	300	400	500	700	900	1100
$\mu_g \times 10^5$ *[Pa . s]*	1.983	2.286	2.671	3.332	3.899	4.44
$\nu_g \times 10^6$ $[m^2/s]$	15.68	25.9	37.9	66.25	99.3	138.6

BLM vs. AFM

In Figure 4-1, the film thicknesses at the edge of deflector with diameter of $25\,mm$ for a sprinkler with K-factor of $7.7 \times 10^{-5}\ \mathrm{m^3/s.kPa^{-1/2}}$ are evaluated. This has been carried out using BLM over the pressures listed in Table 4-1. The maximum to minimum ratio of the considered pressures is 7. They will produce jet velocities, Equation (3-14), in the range of $12\,m/s - 31\,m/s$. For this range of pressures the film thickness shows an approximately 1% decrease as the pressure is increased. The axis of Figure 4-1, have been presented in non-dimensional form in the Figure 4-2. To do this, the film thickness is divided by hydraulic radius, a and injection velocity is converted to jet Reynolds number, Re_0.

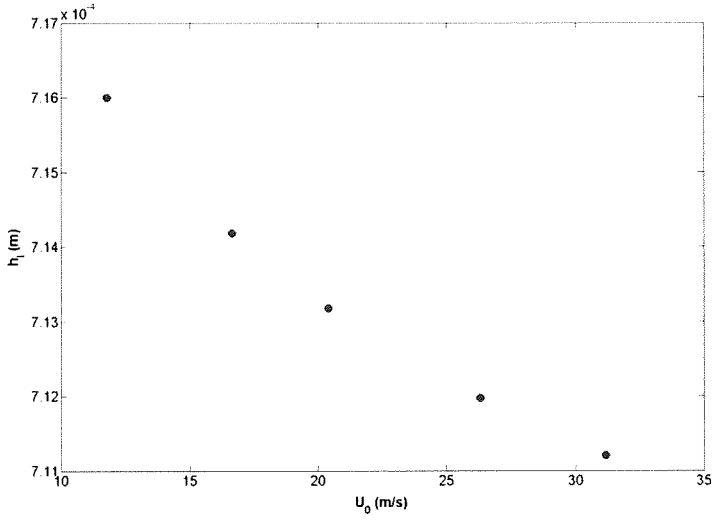

Figure 4-1: Resultant sheet thickness on edges of 25 mm deflector at different injection velocities

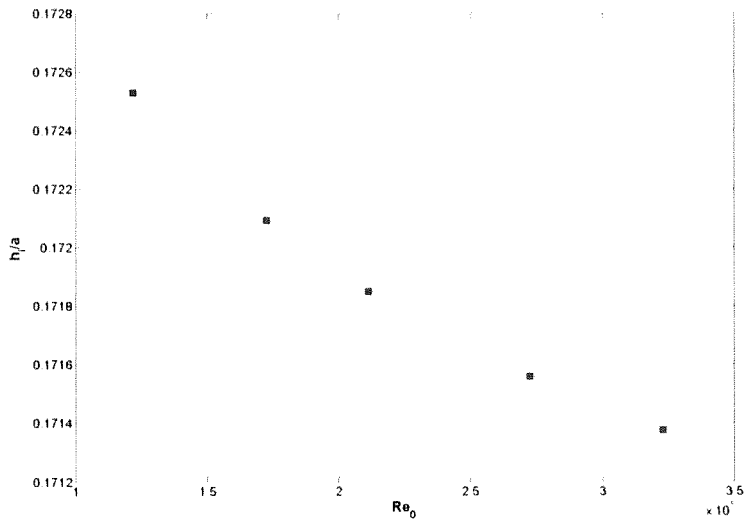

Figure 4-2: Non-dimensional sheet thickness versus jet Reynolds number

Figure 4-3 and Figure 4-4 show the predictions of film thickness calculated with AFM, BLM, and the equation (3-7) and compares them with the measurements [95]. The details of experiment are given in §2.6.2. The experiments were performed at two pressures of 3400 pa, Figure 4-3, and 6900 pa, Figure 4-4. Equation (3-7) is extensively employed in [75], where it is reported to underestimate the film thickness. The same observation is seen in the current analysis. However the BLM and AFM show improved predictions. They both showed an average mean error percentage of 15% against the four experimental data points in the two figures, however the AFM mainly tend to over-predict and the BLM slightly under predicts the film thickness. His analysis of the film

thickness is important as this parameter has an important effect on the spray characteristics after atomization.

Table 4-3: Film thickness measured at the disk edge [95]

	Film thickness (mm)	
	0.034 bar	0.069 bar
Disk (25.4 mm)	1.094±0.065	1.205±0.105
Disk (50.8 mm)	0.691±0.055	0.877±0.092

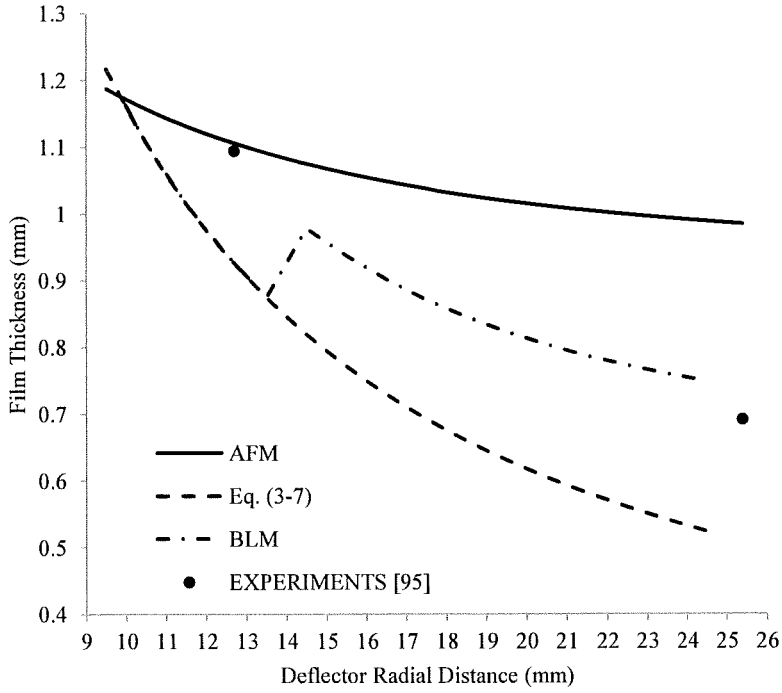

Figure 4-3: Comparison between calculated and measured film thickness over the deflector at 3400 pa, D_0 = 9.5 mm and D_i = 50.8 mm.

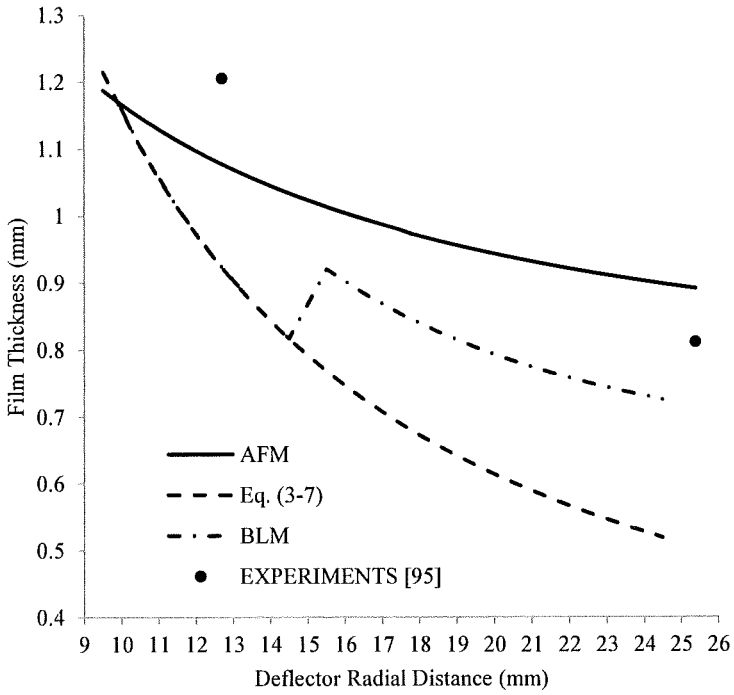

Figure 4-4: Comparison between calculated and measured film thickness over the deflector at 6900 pa, D_0 = 9.5 mm and D_i = 50.8 mm.

No measurements have been reported for the film speed decay over the deflector. Therefore the predictions of average speed of the film from AFM and BLM are compared against each other in Figure 4-5 and Figure 4-6 for the same set of configuration as above, at 3400 pa and 6900 pa, respectively.

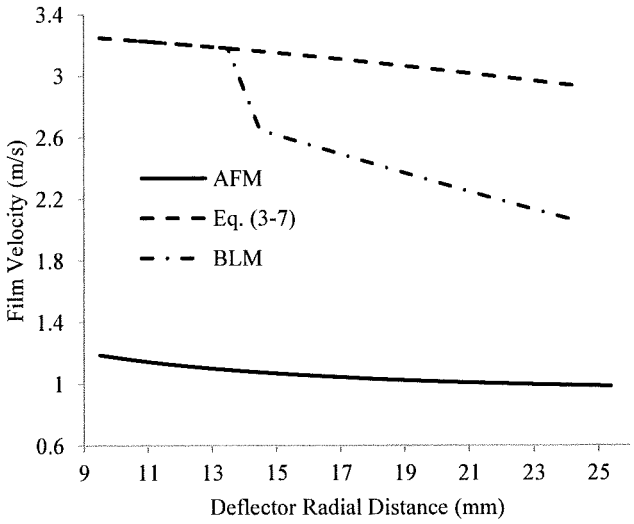

Figure 4-5: Comparison between calculated film velocity over the deflector at 3400 pa

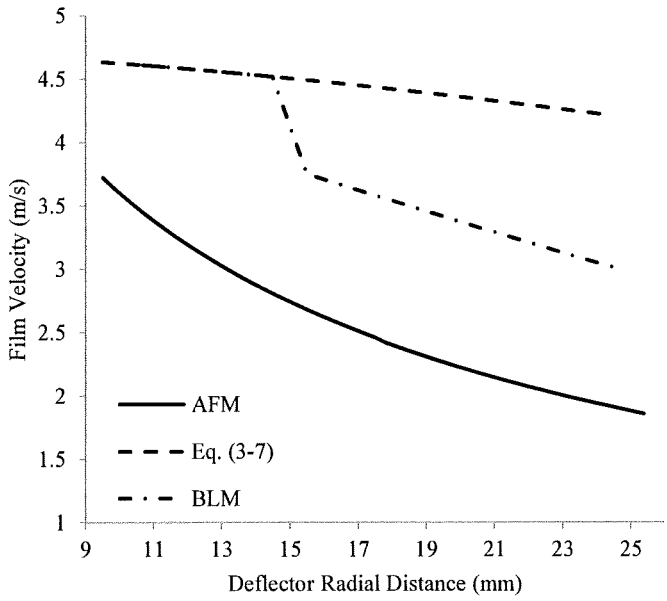

Figure 4-6: Comparison between calculated film velocity over the deflector at 6900 pa.

The AFM predicts smaller range of velocities compared to BLM.

Summary

There is a shortage of experimental measurements of film thickness for different working conditions in the literature, especially at high pressures which makes it difficult to fully validate film models independently of other models. Hence the prediction performance of film models could only be investigated in their overall capability to predict sprinkler spray characteristics when they are combined to other models. In addition to that, it should also be taken into account that the accurate film thicknesses and velocities play a crucial role in physic-based sprinkler spray modeling, as the available inaccuracies will cascade down to the evaluations of the sheet thickness, sheet breakup distance, ligament diameter, initial droplet size and initial droplet location.

4.3 Sheet Trajectory Model Analysis

As previously mentioned the only main approach in the literature that has been employed to calculate the sheet trajectory for sprinklers is the ILTD. In this thesis a new sheet trajectory model, DTM, has been built by extension from a base model and adopted for sprinkler atomization modeling applications. The

implementation of the DTM is verified and validated in section §4.3.1 and its characteristics at different ambient temperatures, injection pressures and sheet release angles are compared against ILTD (where appropriate) in §4.3.2. Such extensive verification of the DTM in sprinkler context has not been undertaken before, and will shed more light on its validity.

4.3.1 Sheet Trajectory Model – Verifications and Validations

The detailed sheet tracking model for sprinkler application has been presented in §3.3.2. Similar equations have been used by Ibrahim and McKinney [133] to study the evolution of non-swirling and swirling liquid sheets from annular nozzle. The solution of non-swirling liquid sheets in a quiescent surrounding medium has been reiterated based on the problem and initial conditions being followed by Chuech [132] and Ibrahim and McKinney[133] to validate the implemented formulations. The initial conditions for their studies are summarized in Figure 4-4.

Table 4-4: Properties of the annular sheet as been considered by Ibrahim and McKinney[133]

Variable	Value(s)
Nozzle orifice diameter	$12.41\ mm$
Initial water sheet thickness	$0.29\ mm$
Liquid flow rates	$13.09\ g/s$ $19.13\ g/s$ $25.50\ g/s$ $31.88\ g/s$
Surrounding surface tension	$0.025\ N/m$
Surrounding air density	$1.22\ kg/m^3$
Air dynamic viscosity	$17.9 \times 10^{-6}\ kg/ms$

In this case the swirl velocity, w_f, is set to zero, which eliminates the effect of both centrifugal and Coriolis forces from the presented model. Predictions of dimensionless radius, sheet angle, sheet thickness and stream-wise sheet velocity of a non-swirling hollow cone sheet with the axial distance from the nozzle are reproduced in Figure 4-7 to Figure 4-10 respectively. These four set of predictions all completely match well the data of Ibrahim and McKinney [133], hence the implementation of the sheet trajectory sub-model could be verified.

In the non-swirl annular liquid sheet, both the sheet radius, Figure 4-7, and sheet angle, Figure 4-8, always decrease as the sheet moves away from the nozzle – at a

constant liquid flow rate. The sheet angles are always negative; therefore the absolute values of angles increase in downstream direction.

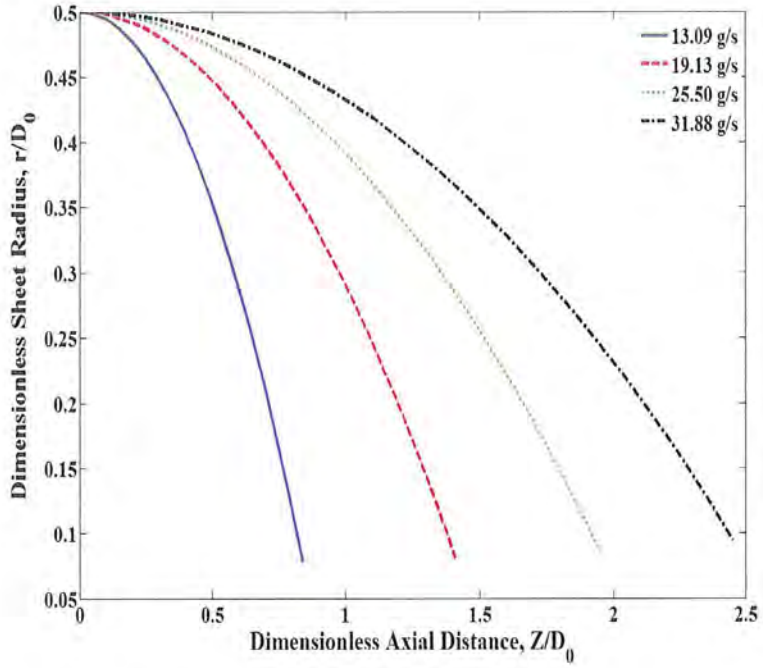

Figure 4-7: Axial variation of dimensionless radius for a non-swirling liquid sheet

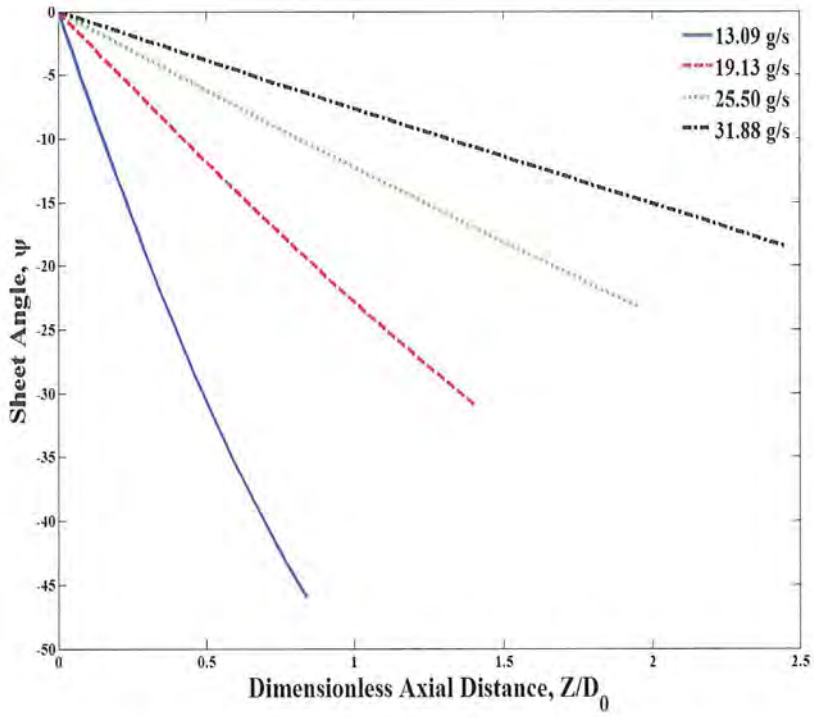

Figure 4-8: Axial variation of angle for a non-swirling liquid sheet

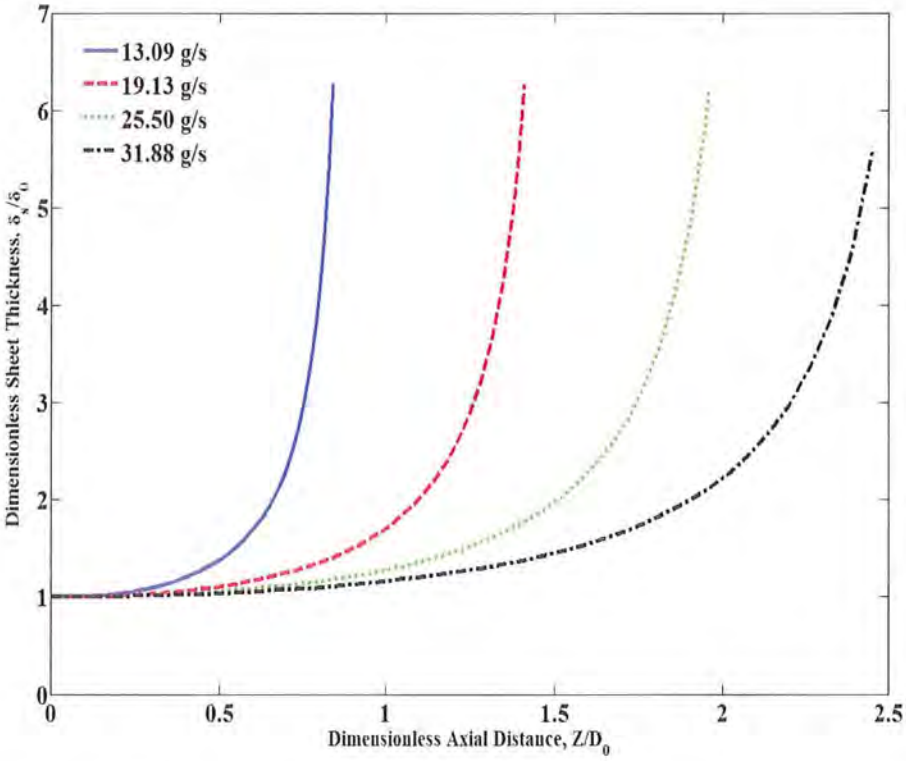

Figure 4-9: Axial variation of dimensionless thickness for a non-swirling liquid sheet

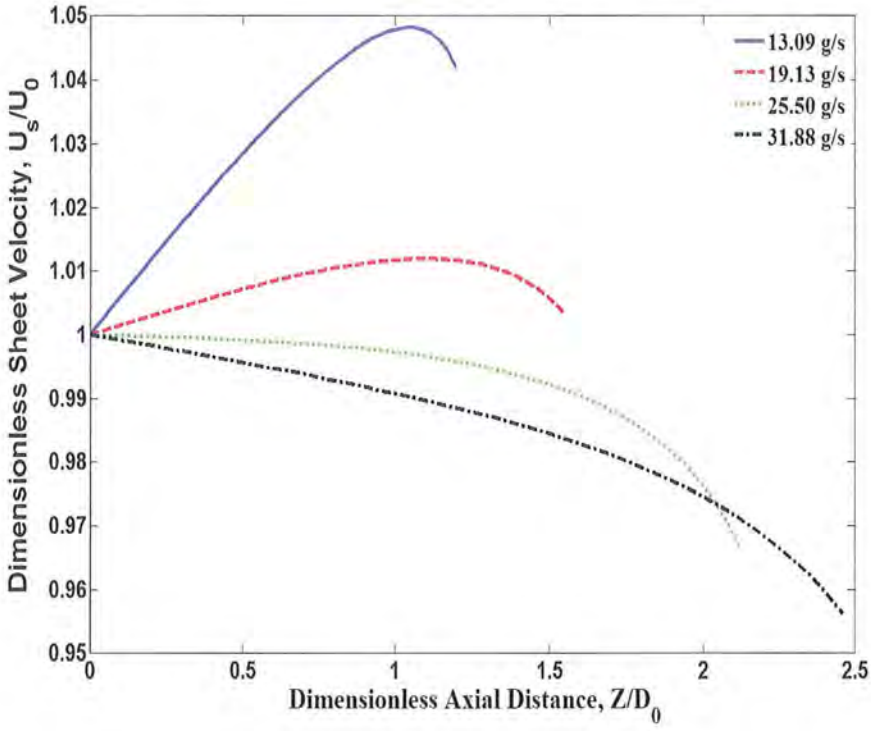

Figure 4-10: Axial variation of stream-wise velocity for a non-swirling liquid sheet

Figure 4-9 indicates that sheet thickness is reduced with an increase in liquid flow rates because of enlargement in its radius. At a given flow rate the sheet thickness

increase in the downstream direction due to the contraction of annular sheet, in accordance with requirements of conservation of mass.

The results in Figure 4-10 demonstrate that the dimensionless sheet streamwise velocity at variable flow rate exhibit a complex behavior. At small flow rates, the streamwise velocity first increases nearby the nozzle orifice and then decrease further downstream. The initial streamwise velocity in Figure 4-10 are calculated from corresponding mass flow rates in accordance with $U_0 = \dot{m}_f/(\pi\rho_f D_0 \delta_0)$.

4.3.2 Detailed Sheet Model Characteristics

In this section the characteristics of the sheet emanating from a disk, formed in an impinging jet configuration (similar to what happens in sprinklers and configured in Figure 3-3), has been investigated in depth. This has been achieved in three sections, by studying the effect of pressure, temperature, and ejection angle on the development of sheet characteristics. Predictions of the dimensionless streamwise velocity, u/u_i, dimensionless thickness, h/h_i, elevation angle, θ and vertical displacement, $Z/\frac{1}{2}D_i$, of a developing sheet at different jet release pressures, ambient gas temperatures and sheet ejection angles are presented in Figure 4-11, Figure 4-12 and Figure 4-13 respectively. The aforementioned physical parameters are normalized against the respective flow parameters at the edge of the deflector where appropriate. Hence their trend at different sheet release conditions is comparable. The variation of physical parameters is plotted against normalized radial displacement, $r/\frac{1}{2}D_i$. The sheet characteristics obtained from DTM are compared against ILTD where appropriate. In addition to the initial conditions being mentioned in §4.2, some of the extra information are listed in Table 4-5. The simulation terminated where radial displacement of the sheet approached *30* times of the deflector radius. In practice for both the smooth and flappy sheets would destruct prior this radius. Numerically it is tested to happen as ξ approaches *0.4*.

Table 4-5: Initial conditions for set up of the simulations

Variable	Value(s)
Initial water sheet thickness	$0.29\ mm$
Liquid kinematic viscosity	$0.798 \times 10^{-3}\ Pa.s$
Liquid dynamic viscosity	$0.801 \times 10^{-6}\ m^2/s$
Surrounding surface tension	$0.0728\ N/m$
Ambient air temperature	$300\ K$

Effects of Pressure

The predictions are undertaken at three jet release pressures, 69 kpa, 207 kpa and 483 kpa. The release pressures represent the lower and higher margin of pressure in which conventional sprinklers operate. These pressures correspond to jet Reynolds numbers of 1.2×10^5, 2.0×10^5 and 3.1×10^5. In sprinklers the jet Reynolds number and jet Webber number are a function of sprinkler operational (jet release) pressure due to consequent increase in jet velocity. Moreover, it has been assumed that the consequent water sheet leaves the deflector at $\psi = 0°$ (parallel to tine on the deflector surface). The ambient air temperature is assumed to be 300K.

Figure 4-11 shows that how the sheet speed, thickness and elevation angle always decreases as the sheet moves away from sprinkler. With an increase in the sprinkler injection pressure both the sheet streamwise speed, Figure 4-11-(a), and the sheet elevation angle, Figure 4-11-(c), show smooth and gradual decline in both their magnitude and rate. Besides that water sheets with greater radial momentum will be produced consequently. Therefore, the sheet radius will be amplified and less sheet deflection will be observed, Figure 4-11-(d).

At a given pressure, the sheet thickness decreases, Figure 4-11-(b), in the downstream direction. This decrease in radial direction is owing to expansion and in compliance with the requirements of conservation of mass. One distinguished point should be noted is that the decreasing trend is not inversely linear with radial location and deviates from ILTD. This conclusion might be described by looking for, $dh/d\xi$, into set of partial differential equations given for detailed sheet tracking model, where this only appears in mass conservation equation, *(3-54)*, and rearranging and integration of this equation over the liquid sheet domain will give, $h/h_i = r_i u_i/(ru)$.

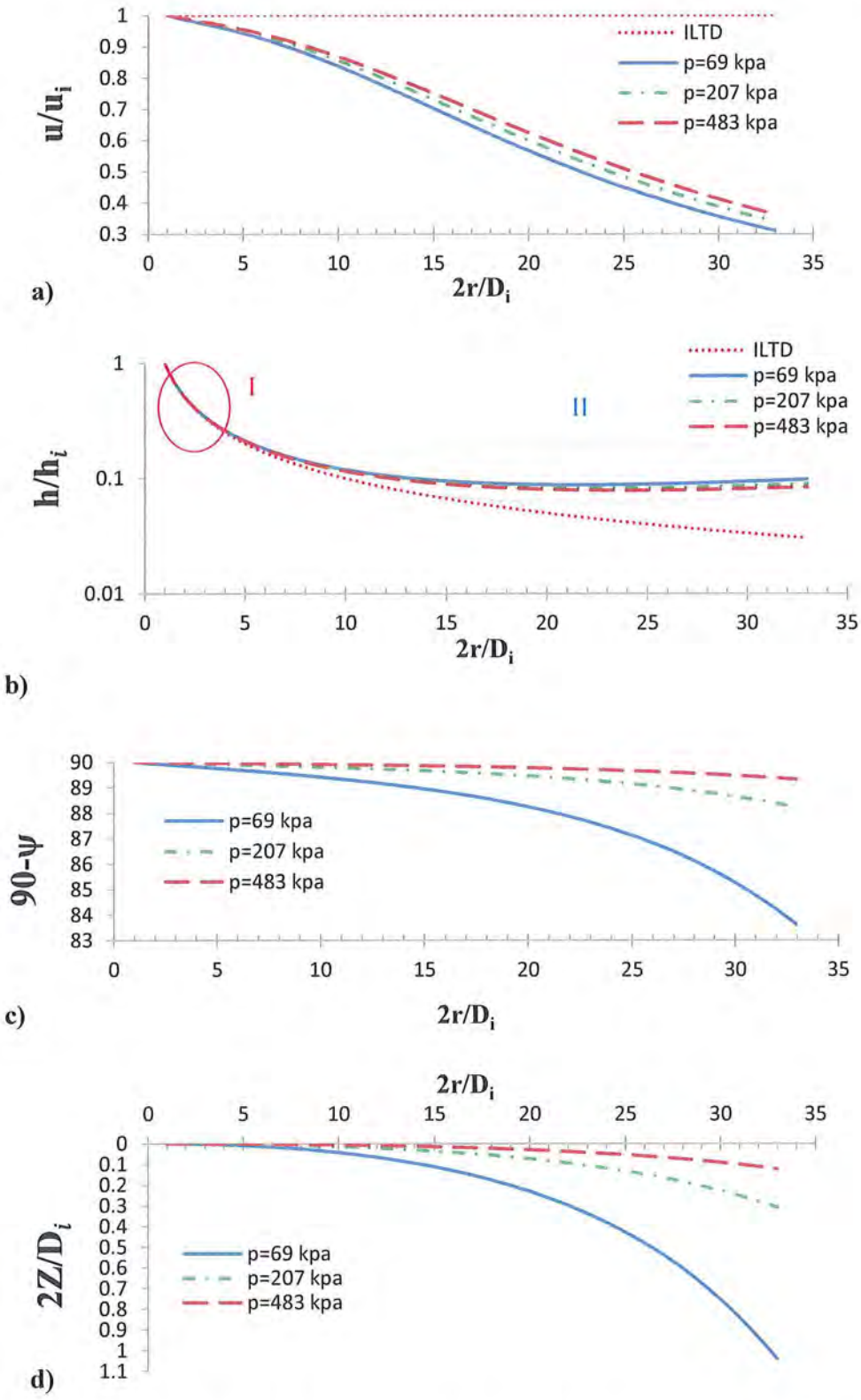

Figure 4-11: Effects of the change in injection pressure on dimensionless (a) velocity, (b) thickness, (c) deflection angle and (d) vertical displacement of the sheet upon an orthogonal impingement at 300 K.

As the release pressure changes, the predicted variation for dimensionless sheet thickness is not noticeable in the initial stage of sheet development as shown with "I" in Figure 4-11-(b). The variations become more apparent in distances after $2r/D_i=10$ as shown with "II". The droplet velocity (terminal velocity) in sprinkler applications can be between 70%-80% of the jet velocity at far fields, which also implies a sheet breakup prior the limit selected, $2r/D_d = 15$. However, extra care must be taken into account while comparing droplet velocity (at far distance) with the sheet velocity, as droplets may both speed up or decelerate while they are moving downward, until they reach the terminal velocity.

To sum up, the Figure 4-11 discloses that with an increase in the injection pressure the sheet speed is increased by 16.8%, Figure 4-11-(a), the sheet thickness is reduced by 14.4%, Figure 4-11-(b) and the radius of expanding sheet will amplify, hence smaller deflection angle by 89.2%, Figure 4-11-(c), and downward vertical displacement by 88.1%, Figure 4-11-(d), are obtained.

The streamwise speeds calculated from DTM is less than ILTD, by 63.8%-69%, Figure 4-11-(a), depending on jet release pressure. On the other hand the sheet thicknesses calculated from DTM is larger than ILTD, Figure 4-11-(b), which is calculated to be the same ratio as velocities. The error is defined as $err = \frac{|X_{predicted} - X_{measured}|}{X_{measured}} \times 100\%$, where X is any parameter of interest.

The results show that the ILTD approach could lead to important errors, compared to the more rigorous DTM approach.

Effects of Density of Surrounding Medium

In Figure 4-12 the ambient air temperatures are 300K, 500K and 900K, which correspond to dimensionless densities, $\tilde{\rho} = \rho_f/\rho_g$, of 787, 1412 and 2533, and depict conditions from cold flow to a typical fire scenario. The horizontal axis is investigated up to a length scale where the sheet is practically conformed to ligament or droplet. The water sheet leaves the disk with initial sheet deflection angle $\psi=0°$. The jet release pressure is assumed to be 69 kpa.

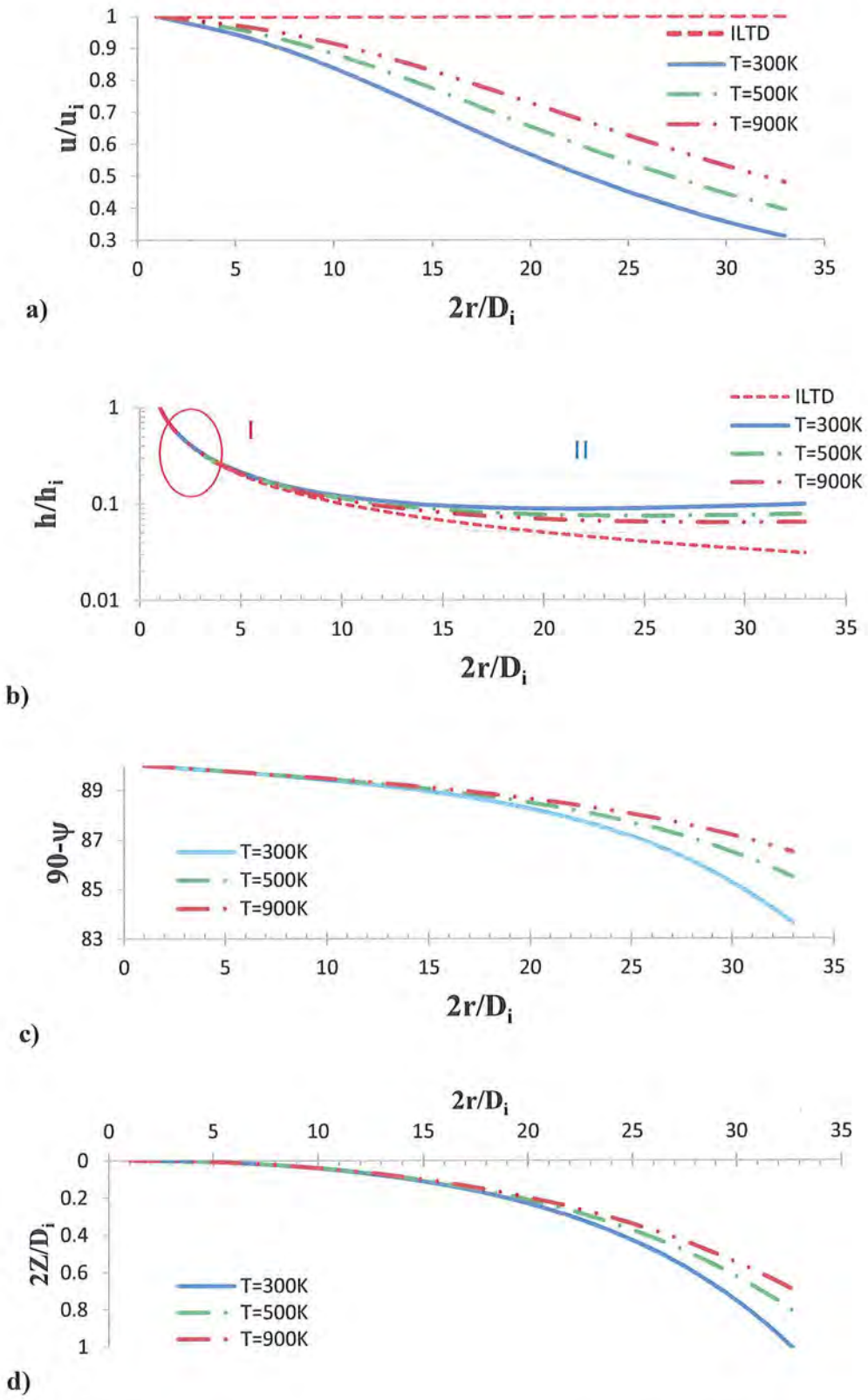

Figure 4-12: Effects of the change in ambient temperature on dimensionless (a) velocity,(b) thickness, (c) deflection angle and (d) vertical displacement of the sheet upon an orthogonal imping at 69 kPa

Figure 4-12 show that the sheet speed, thickness and elevation angle always decreases as the sheet moves away from impingement point. With an increase in the ambient gas temperature the sheet streamwise speed, Figure 4-12-(a) shows smooth and gradual decline in both their magnitude and rate. This could be explained by knowing that at lower ambient air temperatures, the density is higher and the drag force is more significant.

The sheet radial momentum will dissipate at a greater rate in denser medium. However while losing radial momentum; a vertical momentum will build up in the sheet due to gravitation force until the fluid reaches a terminal velocity. Figure 4-12-(b) shows more decrease in the sheet thickness with increase in the ambient air temperature. This complies with mass conservation law and discussion presented in §0.1. The increased radial momentum at the elevated ambient temperature tends to increase the sheet radius and less sheet deflection will be observed, Figure 4-12-(c & d). As the sheet expands, the sheet thickness becomes smaller and the surface tension force increases rapidly, causing the curvature to increase and sheet to bend.

Figure 4-12 discloses that with an increase in the ambient air temperature the sheet speed is reduced by 54.8%, Figure 4-12-(a), the sheet thickness is more reduced by 54.3%, Figure 4-12-(b) and the radius of expanding sheet will amplify, hence smaller deflection angle by 44.13%, Figure 4-12-(c), and downward vertical displacement by 31.45%, Figure 4-12-(d) are obtained. The change in temperature didn't affect the radial growth noticeably in the studied computational domain. The streamwise speeds calculated from DTM are less than ILTD, by 52%-69% Figure 4-12-(a), depending on the ambient gas temperature. On the other hand the sheet thicknesses calculated from DTM is larger than ILTD, by 52.2%-69% Figure 4-12-(b), which is the same percentage as velocities. These differences could result in a significant change in predicting spray characteristics of sprinklers.

Influence of ejection angle

Predictions presented in Figure 4-13 investigate the sheet characteristics as the sheet initial elevation angle changes. Three elevation angles $\theta = 0°, 30°, 45°$ have been chosen. Studying this change is quite important, as could mimic the situation

happening in the operating sprinklers, where water is directed in multiple elevation angles due to presence of the boss, tine/slit and yoke arms over the deflector or the inclined sheet which usually forms in upright and sidewall sprinklers.

As the sheet elevation angle is reduced, it is more released toward below the sprinkler or impingement point. Therefore the sheet would have momentums in both radial and vertical directions. The radial momentum loses its dominance as the elevation angle is reduced. With a decrease in the sheet initial elevation angle the streamwise speed, Figure 4-13-(a), is less reduced. This would be explained by reduced impact of the balance between capillary force and gravitational force due to their increased vertical momentum. The rate of change of non-dimensional thickness, h/h_i, Figure 4-13-(b), does not show noticeable change in the trend in near distances, however the variations become more apparent in radial distances after $2r/D_i=10$. The slightly less decrease in the sheet thickness with the decrease in the sheet initial elevation angle complies with mass conservation law and the above mentioned discussion for the streamwise speed trend change.

Figure 4-13-(c) shows less change in the deflection angle as the sheet is transformed towards lower elevation angles and Figure 4-13-(d) clearly shows amplified vertical displacement as of the initial vertical momentum that sheet has.

Figure 4-13 discloses that with a decrease in the sheet release angle the sheet speed is less reduced by 16.8%, Figure 4-13-(a), the sheet thickness is less reduced by 6.2%, Figure 4-13-(b) and the radius of expanding sheet will amplify, hence smaller deflection angle, Figure 4-13-(c), and 21 times larger downward vertical displacement, Figure 4-13-(d), are obtained. The streamwise speeds calculated from DTM is less than ILTD, by 59%-69%, Figure 4-13-(a), depending on the sheet initial elevation angle. On the other hand the sheet thicknesses calculated from DTM is larger than ILTD, Figure 4-13-(b), which is calculated to be the same ratio as velocities.

Later in this chapter the effects of these changes would be investigated and clarified in more depth.

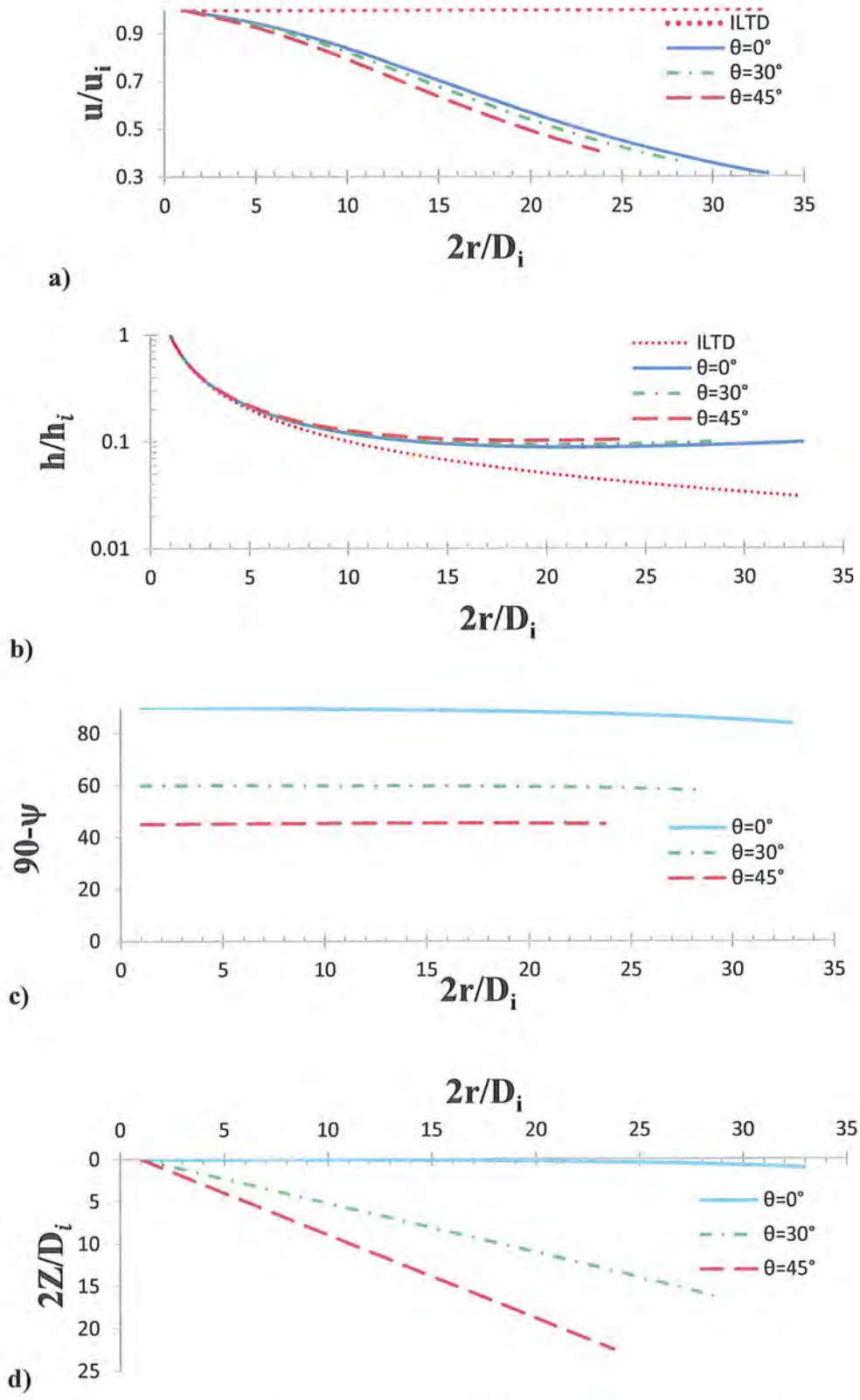

Figure 4-13: Effects of the change in injection angle on dimensionless (a) velocity, (b) thickness, (c) deflection angle and (d) vertical displacement of the sheet upon an impingement at 69 kPa and 300 K.

4.4 Deterministic Model Evaluation

Sheet breakup length, R_b, (distance that is taken to form ligaments or droplets) is one of the parameters that received attention in recent literature with advances in measurement techniques. Therefore, the calculation of sheet breakup distance is used as a method to verify some features of the developed methodologies in this dissertation. It has been achieved in two cases studies. In addition to this, part of the developed methodology is verified for droplet diameters. After that a qualitative study has been carried out to study the impact of change in sprinkler geometry (K-factor and deflector size) and fluid properties (pressure and temperature) on initial droplet formation radius and initial droplet size. A comparison between predictions of all four deterministic models has also been made.

4.4.1 Sheet Breakup Distance [case study-1]

Figure 4-14 below shows the trend of the ratio of normalized sheet breakup to $We_0^{-1/3}$ length as a function of ejection angles from jet. This trend has been computed from combination of BLM and DTM (Method-3). The breakup length corresponding to each ejection angle has been estimated by calculating radial and vertical position of breakup point in $r - z$ plane. The modeling being performed for a $\Delta p = 350000\, pa$, deflector size, $D_i = 47\, mm$, $K = 20.16\ lpm/kPa^{1/2}$ and $f = 12$.

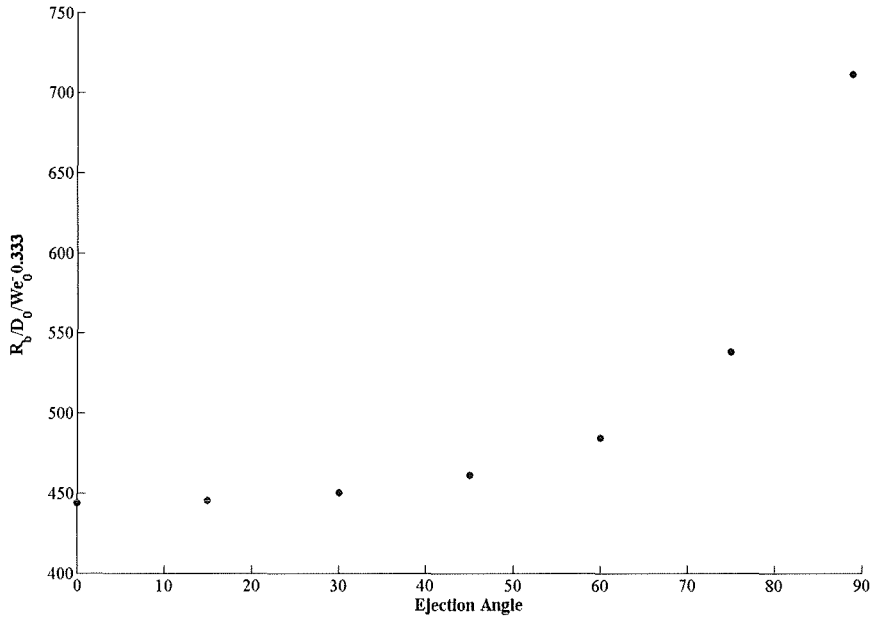

Figure 4-14: Correlation of sheet breakup distance with (-1/3) law for different release angles with ignoring viscous effects over deflector

The available validation for sheet breakup distance are those presented in §2.5.6. In Figure 4-14 for sheets released parallel to tine surface at $\theta = 0°$, Equation (4-1) has been obtained.

$$R_b/D_0 \cong 450\, We_0^{-1/3} \tag{4-1}$$

To account for the viscous effects at sprinkler orifice and also viscous interaction between the slit and deflector surfaces with flow, following dummy friction coefficients have been applied to modeling process $C_{c_1} = 0.9$, $C_{c_2} = 0.85$. They will modify to sprinkler nozzle velocity and sheet velocity at deflector edge, $U_0^* = C_{c_1} \times U_0$ and $u_i^* = C_{c_2} \times u_i$. To get more accurate and reliable values the friction coefficients should modeled numerically as the wetting surface in contact with water could considerably vary at different sprinkler configurations. If viscous effects being considered in the modeling process the dimensionless break up length would be given by

$$R_b/D_0 = 410\, We_0^{-1/3} \tag{4-2}$$

at $\theta = 0°$, as appears in Figure 4-15,

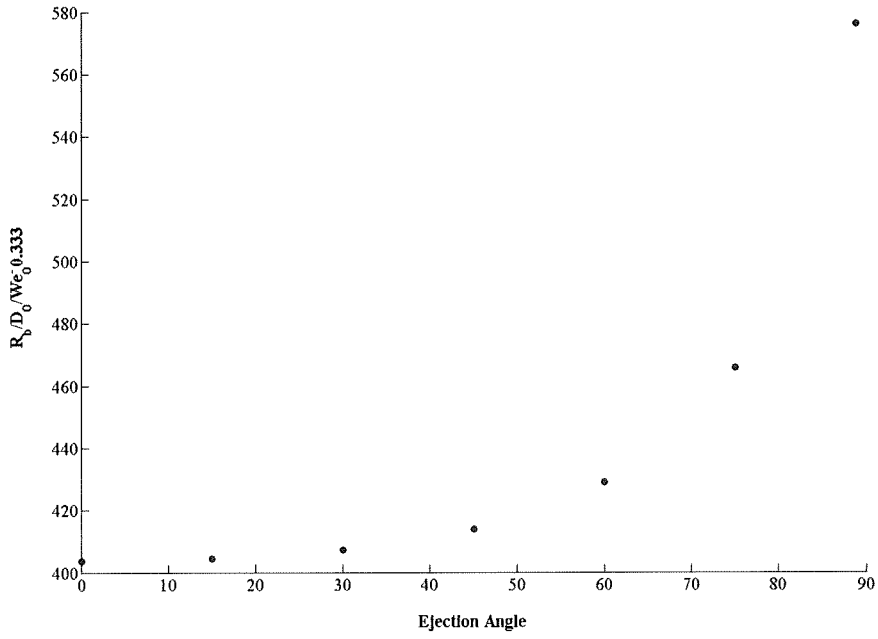

Figure 4-15: Correlation of sheet breakup distance with (-1/3) law for different release angles with the effect of friction coefficient in modeling

Equations (4-1), and (4-2) can be compared against correlations given in equation (2-12) of Huang [91] and (2-13) Ren [89] in Table 4-6:

Table 4-6: Comparison between some correlations for sheet breakup distance

Equation	Expression
(4-1)	$R_b/D_0 \cong 450\, We_0^{-1/3}$
(4-2)	$R_b/D_0 \cong 410\, We_0^{-1/3}$
(2-12)	$R_b/D_0 = 625\, We_0^{-1/3}$
(2-13)	$R_b/D_0 \cong 482\, We_0^{-1/3}$

The above highlighted discrepancies between sheet break-up distances could be due to the following reasons:

- The difference in method of creating the horizontal, axisymmetric sheets. Huang [91] used two opposed impinging jets to create his radially

expanding sheets, while a single impinging on a flat deflector surface was considered in studies of Ren et al., [90], [99]

- There is an uncertainty in the spatial locations of the measurements [91]. Subsequently the sheet formed may have not been exactly horizontal and parallel to the surface of deflector.
- Finally, it is not clear how the criteria for sheet breakup distances were implemented in different literatures. This is due the perforation formation.

The effect of film release angle is to increase the sheet breakup distance by a considerable amount. This is due to the dominance of gravity effect over inertial force for inclined sheets below the sprinkler's deflector surface.

In sprinklers due to the existence of slits in the structure the thinner sheet could form on the tine surface depending on sprinkler's operating pressure or ambient temperature conditions. This shall shorten the breakup distances from what Huang has measured to what Ren has reported for simplified nozzle configurations. Furthermore in real sprinklers the effect of viscous force is significant so that there would be more loss of inertial force, thus shorter sheet breakup distance is obtained.

Figure 4-16 compares the sheet breakup distance predicted by non-dimensional analysis, equation (3-112), against following:

- Available empirical correlations equations, (2-12) and (2-13)
- Expression derived by Marshall [125], equation (3-113)

The estimation of scaling laws has been obtained by neglecting deflection of the sheet. However in the experimental measurements the sheet would deflect and the deflection is more amplified at lower jet Weber numbers. This would result in shorter radial sheet breakup distances and this effect is implicitly reflected in the measurements without being reported most of times. However, as shown in Sheppard's measurements it is in a range of $15° - 40°$ depending the sprinkler configuration and the operating pressure.

This has been addressed in modeling with imposing a deflection angle of 30° and the results are being summarized in Figure 4-17. The discrepancy is improved by up to 32% at this deflection angle.

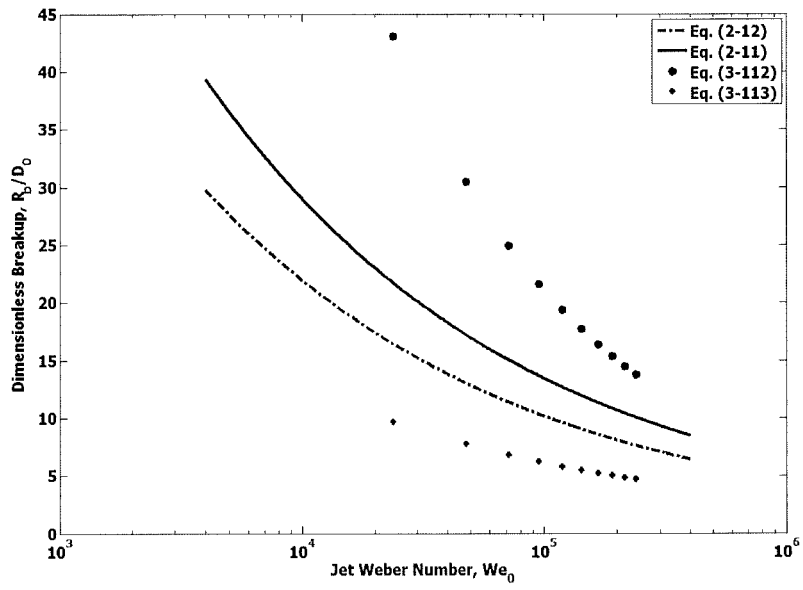

Figure 4-16: Sheet Breakup radial locations as a function of jet Weber number at 0° elevation angle release.

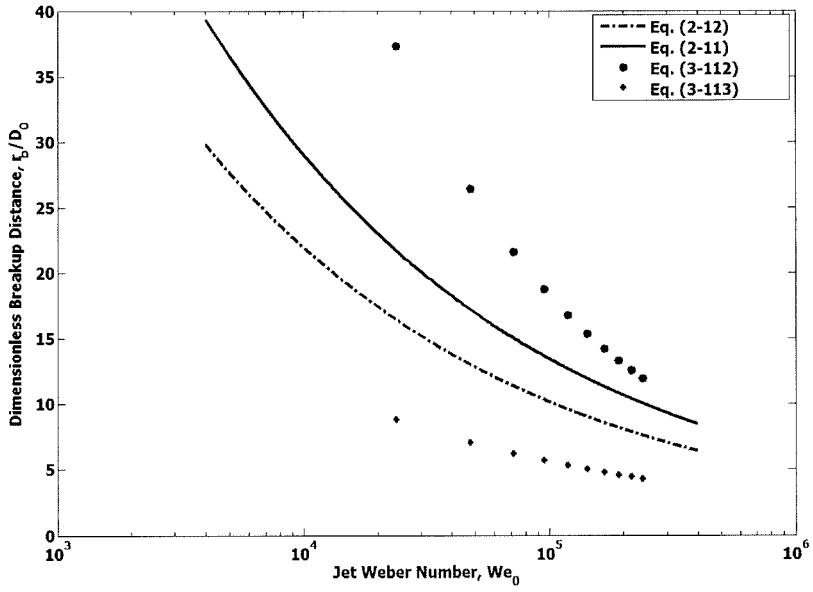

Figure 4-17: Sheet Breakup radial locations as a function of jet Weber number at 30° elevation angle release

It appears the formulation suggested by Marshall [125] is under-predicting the sheet breakup distance. In Figure 4-17 the differences between dimensionless sheet breakup radius of Marshall [125] and empirical correlation (2-13) is increased in average by further 7% as the sheet deflection approached to 30°.

On the other hand the discrepancy between presented scaling law and correlations became smaller. One realistic way to improve the predictions of dimensionless number is to introduce a hypothetical friction coefficient to equation (3-112)

which accounts for the viscous interaction between flat plate and the film flow implicitly. To get the precise and reliable values they should modeled numerically as the surface in contact with water could vary with the plate diameter.

In general the scaling law presented in this research over-predicts the correlations and Marshall's under-predicts the sheet breakup distance. Depending on the application, the dimensionless total growth of the wave could also be changed to tune the sheet breakup radial distance predictions from presented scaling law.

4.4.2 Sheet Breakup Distance [case study-2]

Table 4-7 shows the sheet break up distance over three deflector's plates of diameters 25.4, 38.1 and 50.8 mm. The measurements are carried out at four low pressures of 0.14, 0.28, 0.55 and 0.83 bar [95]. Figure 4-18 compares the predictions obtained for the sheet breakup distance by Methods 1-4, at the same range of pressure and for the three deflector diameters.

As a brief reminder the constituent sub-models of Methods 1 to 4 are as follow:

- Method-1, BLM-ILTD
- Method-2, AFM-ILTD
- Method-3, BLM-DTM
- Method-4, AFM-DTM

A tolerance is provided for all distances in the table. This gives an upper and lower limit for the range of the sheet breakup distances resulted in the experiment (shown with black solid lines in Figure 4-18 (a, b & c).

Table 4-7: Sheet breakup distance measured from three disk sprinklers [95]

	Disk (25.4 mm)	Disk (38.1 mm)	Disk (50.8 mm)
0.14 bar	233 ± 13	228 ± 18	235 ± 16
0.28 bar	198 ± 11	197 ± 16	207 ± 10
0.55 bar	166± 11	167 ± 12	173 ± 10
0.83 bar	153 ± 11	154 ± 10	152 ± 9

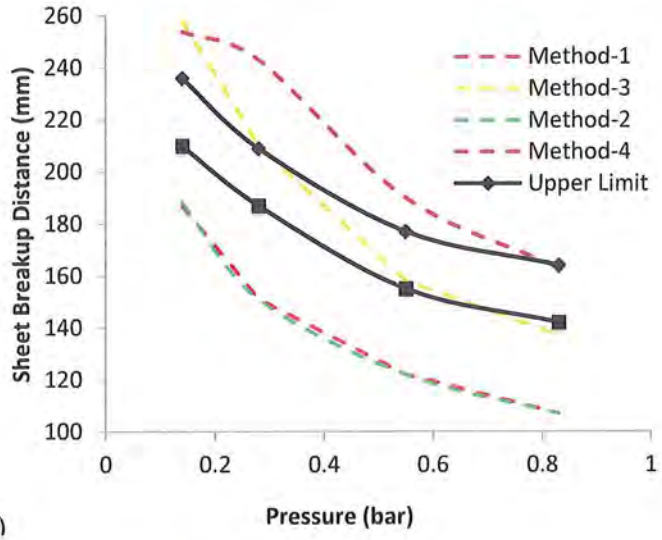

a)

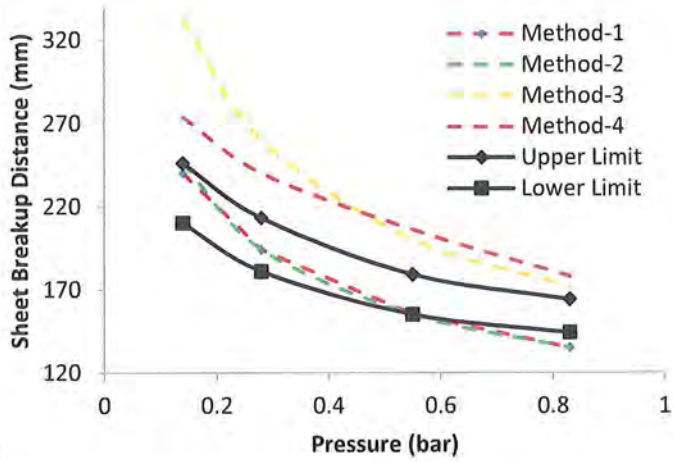

b)

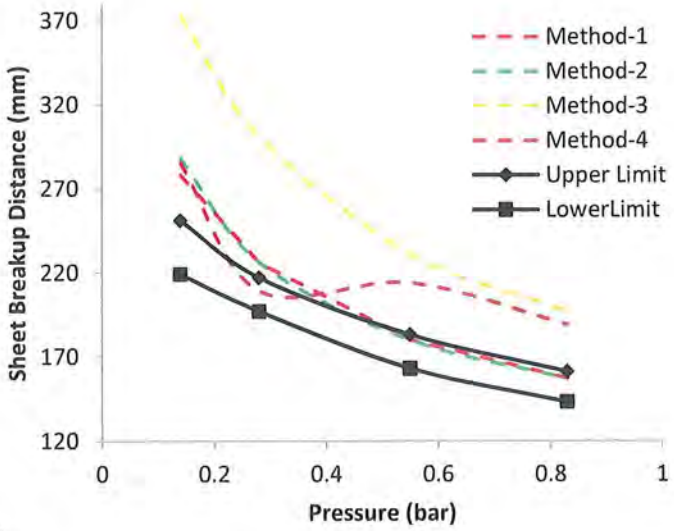

c)

Figure 4-18: Comparison of calculated sheet breakup distances at four pressures for deflectors of a) 25.4 mm, b) 38.1 mm and c) 50.8 mm in diameter

Overall, Methods-1&2 are predicted with higher degree of accuracy at the available range of low pressures (0.14bar–0.83bar). In all of the three cases which are studied here, the accuracy of the predicted sheet breakup distance by Methods-3&4 shows improvement as the pressure is increased. Method-4 gives better predictions as the size of the deflector increases. Methods-3&4 both tend to over-predict the sheet break up distances. The absolute mean error for Methods-1-4 has calculated to be 13.13%, 13.69%, 26.11% and 17.38% respectively.

4.4.3 Droplet Median Diameter

Figure 4-19 shows the predictions obtained from the proposed scaling law equation *(3-120)* and the comparison with equation *(3-121)* and the correlations suggested by Dundas.

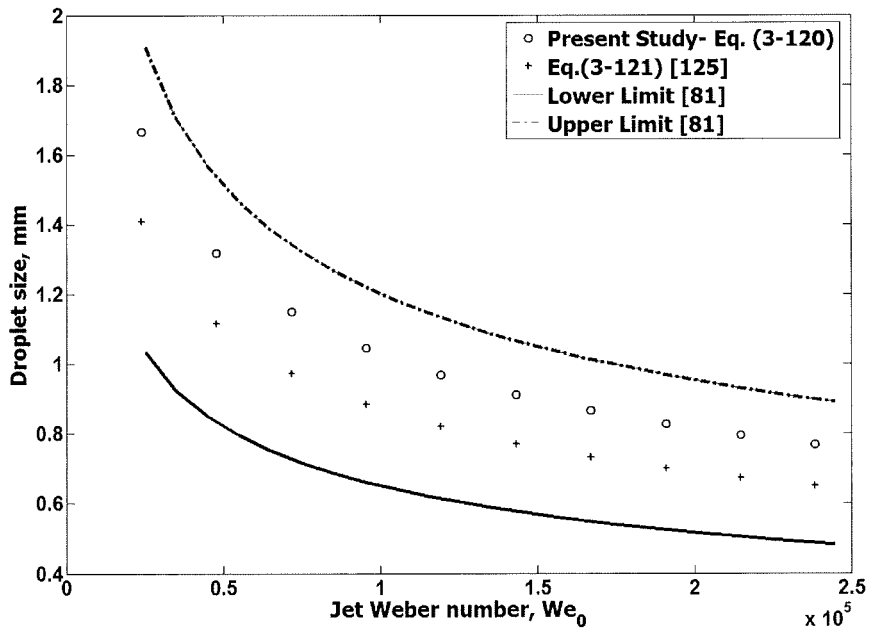

Figure 4-19: Droplet diameter as a function of jet Weber number

Dundas showed that the median droplet size from turbulent jet impingements could be correlated in the form $D_{v50}/D_0 = C.We_0^{-1/3}$. The constant C varied from 1.74 to 3.21. In Figure 4-16 the $D_{v_{50}} = 1.74We_0^{-1/3}D_0$ and $D_{v_{50}} = 3.21We_0^{-1/3}D_0$ has been considered as the lower (solid line) and upper (dashed line) droplet size range, respectively. It is clear that both equations *(3-120)* & *(3-121)* predict within the range provided from experiments. However equation *(3-120)* from the present work predicts slightly larger length scale for the droplets compared to equation

(3-121). The advantage of current formulation shall be explained through the consideration of configuration ratio X, better prediction of sheet breakup distance and more physical consistent nature of derivation.

One parameter which inevitably contributes to the modeling of sheet breakup distance and droplet length scale is the dimensionless total growth of the wave. There is an uncertainty in the considered value f=12, in the literature.

4.4.4 Qualitative Studies

4.4.4.1 Effects of K-factor and deflector size

Table 4-8 shows the effects of change in the K-factor and deflector size on initial droplet size (d_d) and initial droplet location (r_d). The K-factor is a measure of change the orifice, and the effects of changing the deflector size. The K-factor varied from 5×10^{-5} to 12×10^{-5} $m^3 s^{-1} kpa^{-1/2}$. This is range equivalent to 2-5 gal.min^{-1}.psi$^{-1/2}$in USA system. The presented data comes from modeling (Method-1), not experiments.

Table 4-8: Drop size and Initial drop location predictions of a sprinkler spray at standard atmospheric condition and $\Delta p = 138\ kPa$ while varying the diameter of the deflector and the sprinkler K-factor [$m^3 s^{-1} kpa^{-1/2}$.].

	K=5× 10^{-5}		K=7× 10^{-5}		K=10× 10^{-5}		K=12× 10^{-5}	
	d_d	r_d	d_d	r_d	d_d	r_d	d_d	r_d
D_i=12.5mm	*0.7082*	*237.6*	*0.7908*	*276.1*	*0.8898*	*324.4*	*0.9455*	*352.48*
D_i=25.0mm	*0.7158*	*240.7*	*0.7924*	*277.6*	*0.8864*	*324.3*	*0.9398*	*351.6*
D_i=37.5mm	*0.7391*	*247.8*	*0.8067*	*282.4*	*0.8931*	*327.1*	*0.433*	*353.4*

The drop size and breakup length are significantly increased with increasing of K-factor. These increases are due to the larger film and sheet thicknesses and are in compilation with mass conservation.

Increasing film and sheet thicknesses increases the sheet stiffness resulting in a slower wave growth rate (less amplification) for a given driving force for wave growth (pressure/surface tension force imbalance). The slower wave growth rate resulted in increased sheet thinning. On the other hand, the larger sheet thickness as a result of the larger K-factor has a dominant effect on the drop size causing λ_s^{cr} and corresponding droplet diameter to increase. In addition to this Table 4-8

shows minimum dependence of the initial droplet location and droplet diameter to the change in the deflector size. Increased deflector size results in reduced sheet speed and decreased sheet thickness.

4.4.4.2 Effects of injection pressure and density of surrounding medium

The results presented in Figure 4-20 show the predictions of initial drop size and initial droplet location in a sprinkler spray as a function of injection pressure and ambient temperature. The four methods described in §3.5 are compared against each other. The method-1 is considered as basis model. The spray characteristics is being studied over a range of injection pressures, 69, 207, 483 kPa, and ambient air temperatures, 300, 500, 1100 K.

The result shows strong coupling between the ambient and atomization process. These modeling results were obtained with the full deterministic viscous models. Equation (3-67) reveals that the wave growth rate varies linearly with ambient density. As the ambient temperature increases the d_d and R_b increase. Increases in ambient temperatures resulted in lower ambient density. These lower densities reduce the imbalance between critical aerodynamic pressure and surface tension forces, which is the driving force for wave amplification. The reduction in this driving force results in a slower wave growth rate and a corresponding longer breakup radius.

Decreasing ρ_g results in both longer R_b and longer sheet critical wavelength. These effects have opposing effects on d_d resulting in relatively small increases in d_d with increasing ambient temperature.

As a consequence of larger thickness film thickness predicted by the AFM (Figure 4-3 & Figure 4-4), Method-2 predicts larger spray characteristics. The predictions of initial droplet diameters and initial droplet locations from Method-2 are larger than Method-1 by approximately 15% and 10%, respectively. In Method-3 the DTM is used as sheet trajectory model in order to resolve the evolution of the liquid sheet trajectory with greater accuracy. The predicted initial droplet diameter and initial droplet location from Method-1 (solid line) and Method-3 (dashed line) are compared in Figure 4-20-(b) within the same range of operating pressures and ambient temperatures as Figure 4-20-(a). As can be seen in Figure 4-20-(b), the use of DTM in Method-3 influences the predictions

towards smaller droplet diameters and slightly larger initial droplet locations in most of operating conditions. The percentage of difference in initial droplet diameter and initial droplet location predictions is roughly 10% and 5%, respectively between Method-3 and Method-1. The discrepancy is due to the corrected radial variation of sheet thickness with Method-3, larger sheet breakup distance, smaller sheet breakup speed and smaller sheet thickness at breakup time. Method-4 which combines the IM and DTM is examined in Figure 4-20 (c) where its predictions (dashed lines) are compared to Method-1. The spray parameters predicted with Method-4 are slightly larger than those from Method-1. The difference in predictions of droplet diameter and initial formation radius is less than 9% and 15%, respectively between the two methods.

It might seem that as Method-3 is taking into account the air drag and predicts thicker sheet and lower velocity than Method-1, the drop size prediction of Method-2 should be larger than that of Method-1. This trend could be explained by taking into account the fact that droplet size is a direct function of ligament diameter and is not directly related to sheet breakup thickness and sheet breakup distance in the formulation. In addition to this, the ligament diameter has been calculated from equation *(3-84)* in the format of a polynomial where the sheet breakup thickness and sheet breakup distance appeared as part of the coefficients of that polynomial. Hence a clear conclusion could not be drawn, in which Method-3 necessarily led to a larger predicted droplet diameter in all situations.

On the modeling point of view, Methods-2, 3 and 4 could be considered as more accurate than Method-1, and Method-4 is accounted the most accurate of all four. However without detailed experimental data for droplet locations and diameter (unavailable) for comparisons, it is difficult to claim the superiority of a model. Nevertheless the results show that Methods-2, 3 and 4, which all offer more capabilities than Method-1, could be a good alternative for sprinkler spray modeling. Beside this, Methods 3 and 4 could be employed where the impingement of the jet and deflector is not orthogonal as the effect of tilting could be included in the DTM, by adjusting sheet deflection angle other than 90°.

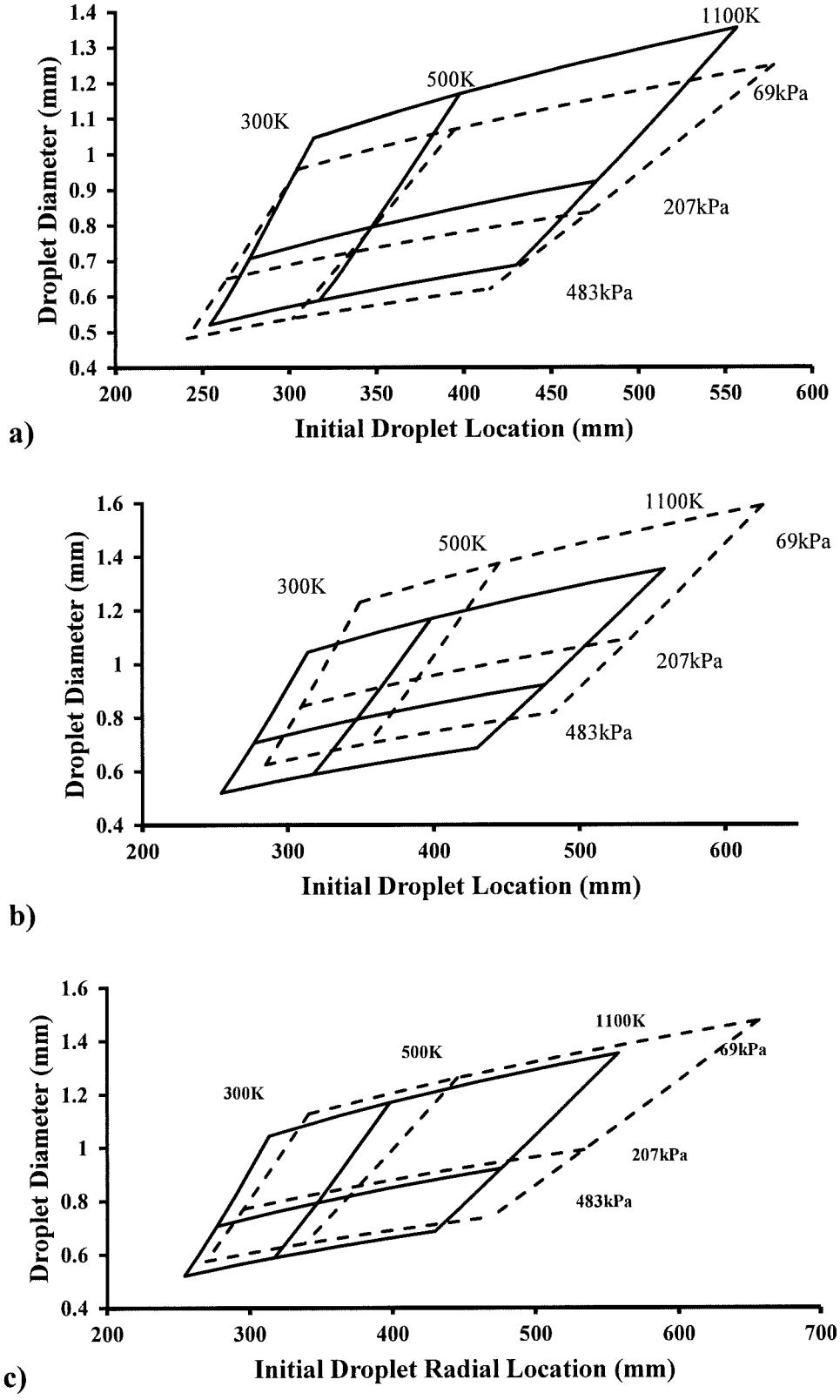

Figure 4-20: Comparison of predicted initial droplet location and diameter as a function of injection pressure and ambient temperature between Method-1(solid line) and (a) Method-2 (dashed line) (b) Method-3 (dashed line) (c) Method-4 (dashed line).

Summary

The deterministic initial single droplet size or location for a given pressure and temperature does not provide enough information on sprinkler atomization features. The single drop size prediction capability does not seem sufficient. To the best it might represent a characteristics size i.e., the volume median diameter or Sauter mean diameter, of whole spray. The stochastic approach is more realistic.

4.5 Stochastic Modeling:

As explained in the theory, the stochastic modeling has been adopted in the current dissertation to introduce a more realistic distribution to the spray characteristics. The stochastic distributions find significant importance where dispersion, vaporization, droplet penetration issues are of interest in suppression and extinguishment studies.

4.5.1 Qualitative Analysis

Figure 4-21 shows the stochastic distributions for initial droplet size for a sprinkler having $K = 7.7 \times 10^{-5} m^3 s^{-1} kpa^{-1/2}$, $D_i = 25mm$ and $\Delta p = 138kp$. [124]

Fluctuation intensities are specified in every single numerical iteration to describe the chaotic behavior of the spray process, including initial amplitude distribution ($0.15 \leq I_f \leq 0.25$), sheet fragmentation ($0.1 \leq I_l \leq 0.3$), ligament disintegration ($0.1 \leq I_d \leq 0.3$). In this case, n, p, and q are specified as 1000, 50 and 50.

Figure 4-21 shows that the droplet size distribution at these conditions is well presented by a normal distribution. For cases a) and b) the droplet sizes were as following accordingly, compared with characteristic size of 0.8161 mm predicted by Method-1.

1- The mean droplet size is 0.8117 and 0.8196 mm
2- minimum droplet size of 0.0414 and 0.2758 mm
3- maximum droplet size of 1.2357 and 1.3062 mm

The cumulative mass fraction (CMF) of the spray is drawn on figures.

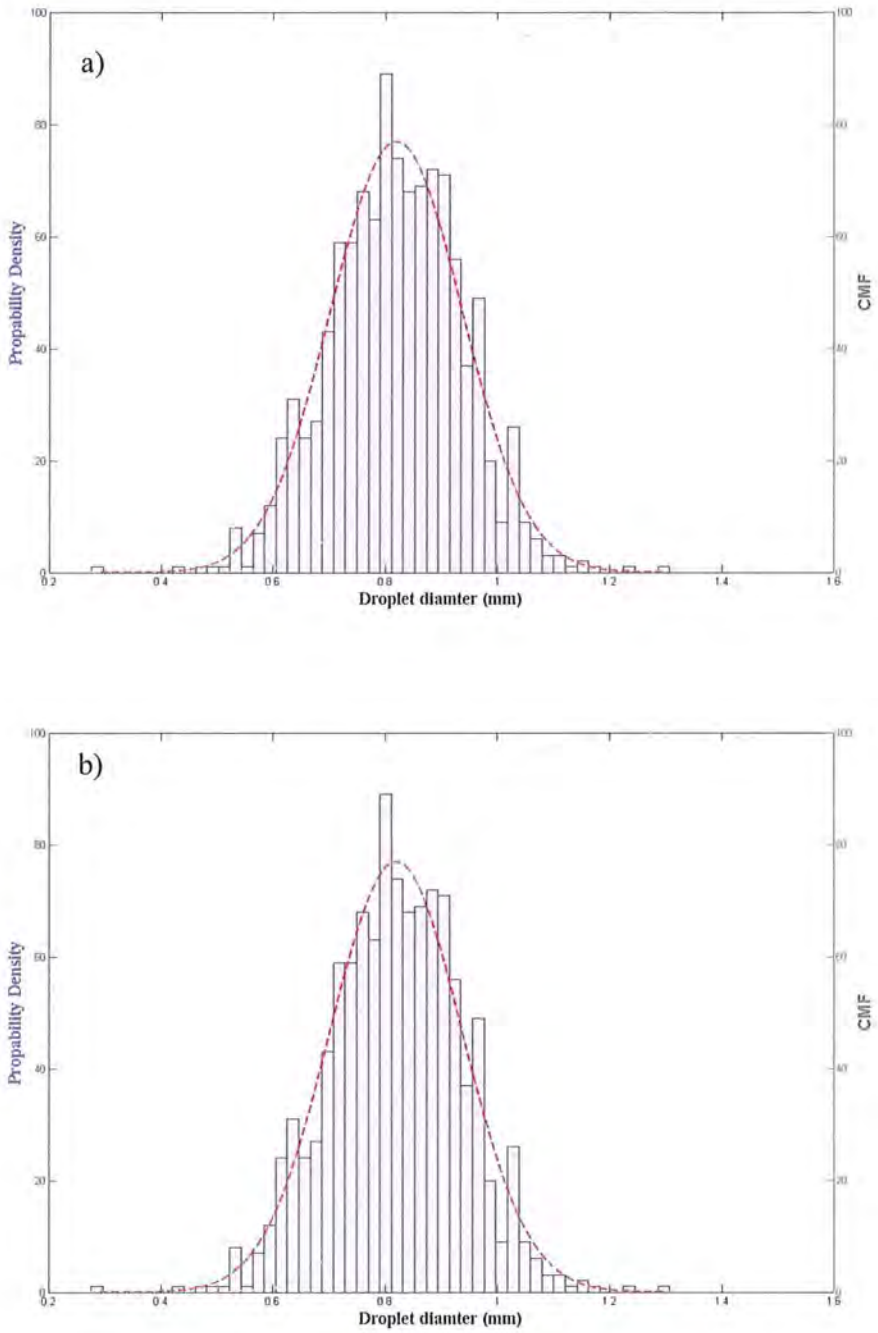

Figure 4-21: Two synopsis of Probability density function of initial drop size determined from stochastic model; $\Delta p = 138\ kpa$, $0.15 \leq l_f \leq 0.25$, $0.1 \leq l_l \leq 0.3$ and $0.1 \leq l_d \leq 0.3$.

4.5.2 Quantitative Analysis

A quantitative evaluation of the stochastic modeling was achieved by comparing the models predictions against the empirical correlations (obtained from actual sprinkler data). The stochastic behaviour of the physical processes governing the

sprinkler spray formation has been accounted with the four aforementioned atomization models combinations, Methods 1-4.

Figure 4-22 shows the stochastic modelling predictions from Method-1 to Method-4 compared with Dundas [85]. The sprinkler geometrical parameters are D_0=12.7 mm and D_i=31mm at ambient temperature of 300K. Method-1 is at the lower bound and Method-2 at the upper band. Method-3 and Method-4 which both utilize the DTM are the most closest to the experimental data. The mean errors between predictions and Dundas at the five jet Weber numbers are about 27%, 13%, 7% and 1% for Methods 1, 2, 3 and 4, respectively. The results confirm the improvements achieved with Methods-3&4.

The correlation in experiment [85] is reported to be $d_{V50}/D_0=3.1\times We_0^{-1/3}$. The predictions of the coefficient of proportionality by Method-3 and Method-4 are very close to 3.1. Having verified the methodology, Methods 3 and 4 have been verified for higher ambient temperatures and the coefficient of proportionality increases to 3.4 and 3.9 at 500K and 1100K respectively.

The methodologies have been further investigated by comparing their predictions of the droplet velocity with the formula of Sheppard [41] in Figure 4-23. The mean velocity is predicted by about 10% more accurately with Method-4 than Method-1 which brings the prediction closer to what has been estimated by empirical formulation of Sheppard [41]. It is noteworthy that the experimental data were not measured immediately after droplet formation, but a distance further away; hence the air drag force has effectively reduced the velocity by some extent. Procedure to calculate volume median diameters is explained in Appendix B.

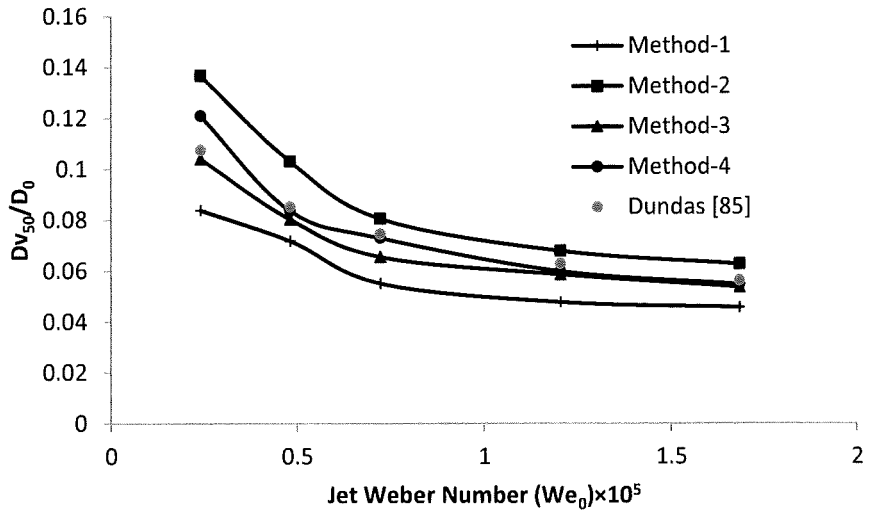

Figure 4-22: Comparison between stochastic model predictions and experimental data

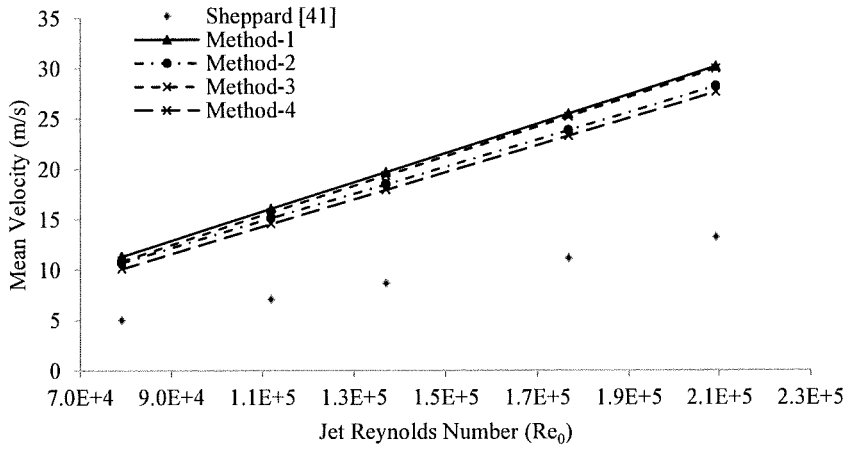

Figure 4-23: Stochastic predictions of mean velocity compared against empirical data

From the results obtained with the stochastic analysis, it can be concluded that Method-3 and Method-4 are in better agreement with the experimental data. This is thought to be due to more realistic treatment for underlying physics. However, they do suffer the drawback of higher computational cost as the number of stochastic space increases. For the generated 125000 (50×50×50) samples, CPU-time for Method-1 to Method-4 was about 1, 3, 10 and 40 minutes.

4.6 Semi-empirical Model Analysis-Pendant Sprinkler

The initial droplet sizes and spatial volume flux at seven elevation angles, $\theta° = 3$, 15, 30, 45, 60, 75, 90, for six azimuthal locations, $\phi°= 90$, 107, 123, 140, 157, 180

have been evaluated using the developed semi-empirical approach in §3.8 for a pendant sprinkler and the predictions are compared to the available experimental data (explained in §2.6.1).

4.6.1 Median Droplet Diameter

Figure 4-24 & 4.25 (a–g) show the spatial distribution of volume median diameter for a pendant sprinkler operating at *3.5 bar* and *5.2 bar*, respectively. The flow rates are equal to $6300\ cm^3/s$ and $7700\ cm^3/s$ and the jet Reynolds number is 5.75×10^{-5} and 7.04×10^{-5}. The change in pressure at the sprinkler head affected the droplet size and pattern.

Characterization of the near field sprinkler spray has been investigated by combination of the semi-empirical approach with Methods 1,2,3,4 for a pendant sprinkler at different elevation and azimuthal angles.

The absolute mean error resulting from each Method in either of release scenarios (*3.5 bar* and *5.2 bar*) have been calculated and are shown in Figure 4-26. The modeling approaches are able to give predictions at elevation angle below the sprinkler ($\theta = 90°$) where it is challenging to perform measurements due to high water fluxes. This can be seen in Figure 4-24& 4.25 (a-g) where no experimental data is reported for these angles for the presented azimuthal angles; however the models could predict the droplet diameters at 90^0 elevation angles. The flow through these angles represents either the slit flow or the yoke arm flow in the studied pendant type sprinkler. Overall very promising predictions were obtained, however Method-1 which under-predicts the droplet diameter for nearly all ranges of azimuthal locations shows the maximum error of *47%*, and Method-3 show the minimum error. The prediction accuracy of Method-4 is close to Method-3. The level of errors has increased as the release pressure increased from *3.5 bar* to *5.2 bar*. This could be explained through the increased jet Reynolds number. As being reviewed in chapter 2, additional shear instabilities are associated with impinging high Reynolds jets, producing mainly very small droplets.

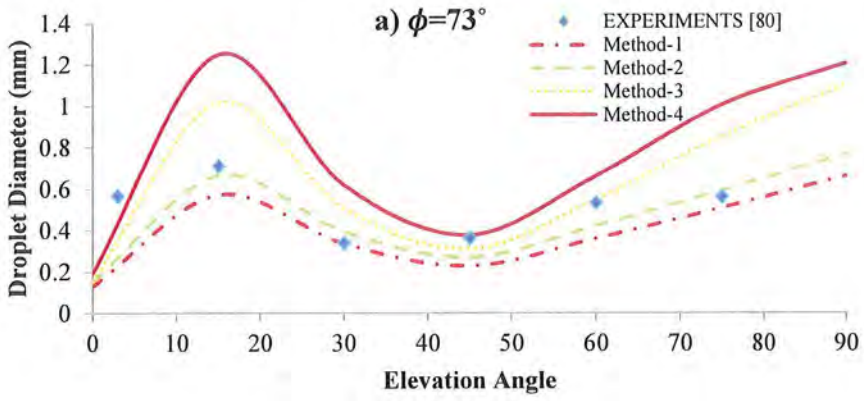
a) ϕ=73°
EXPERIMENTS [80]
Method-1
Method-2
Method-3
Method-4
Droplet Diameter (mm)
Elevation Angle

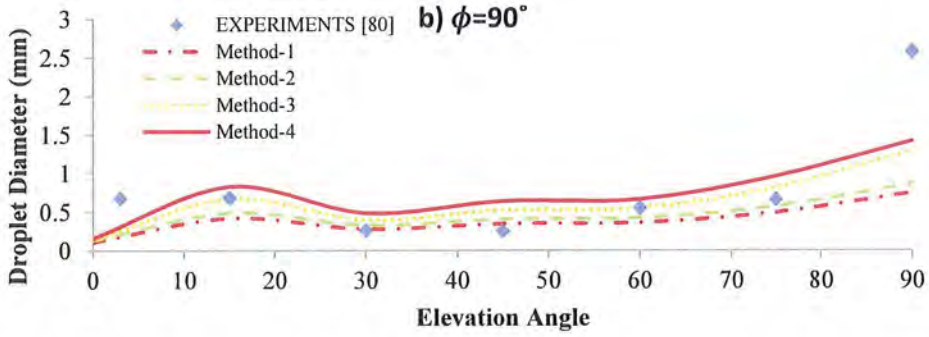
b) ϕ=90°
EXPERIMENTS [80]
Method-1
Method-2
Method-3
Method-4
Droplet Diameter (mm)
Elevation Angle

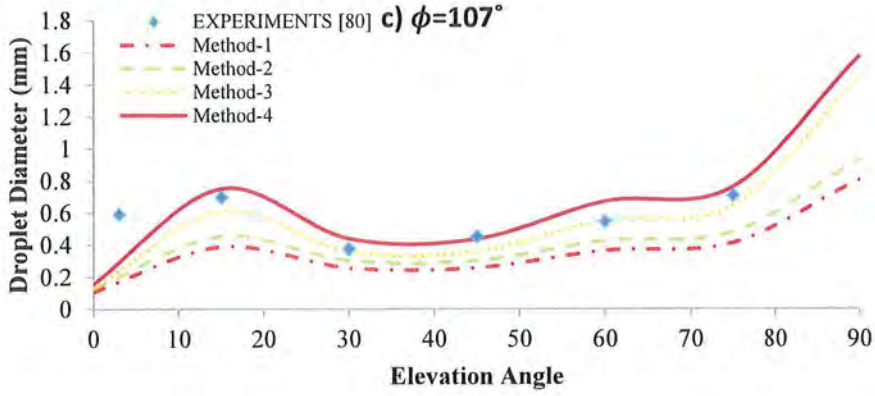
c) ϕ=107°
EXPERIMENTS [80]
Method-1
Method-2
Method-3
Method-4
Droplet Diameter (mm)
Elevation Angle

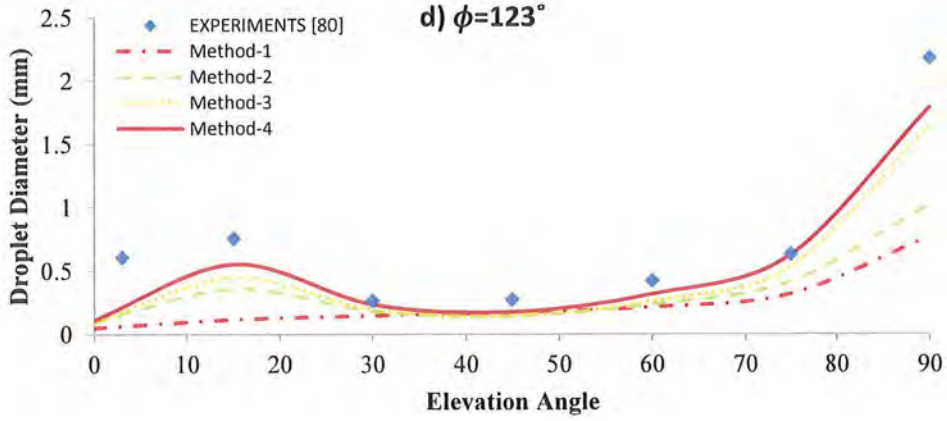
d) ϕ=123°
EXPERIMENTS [80]
Method-1
Method-2
Method-3
Method-4
Droplet Diameter (mm)
Elevation Angle

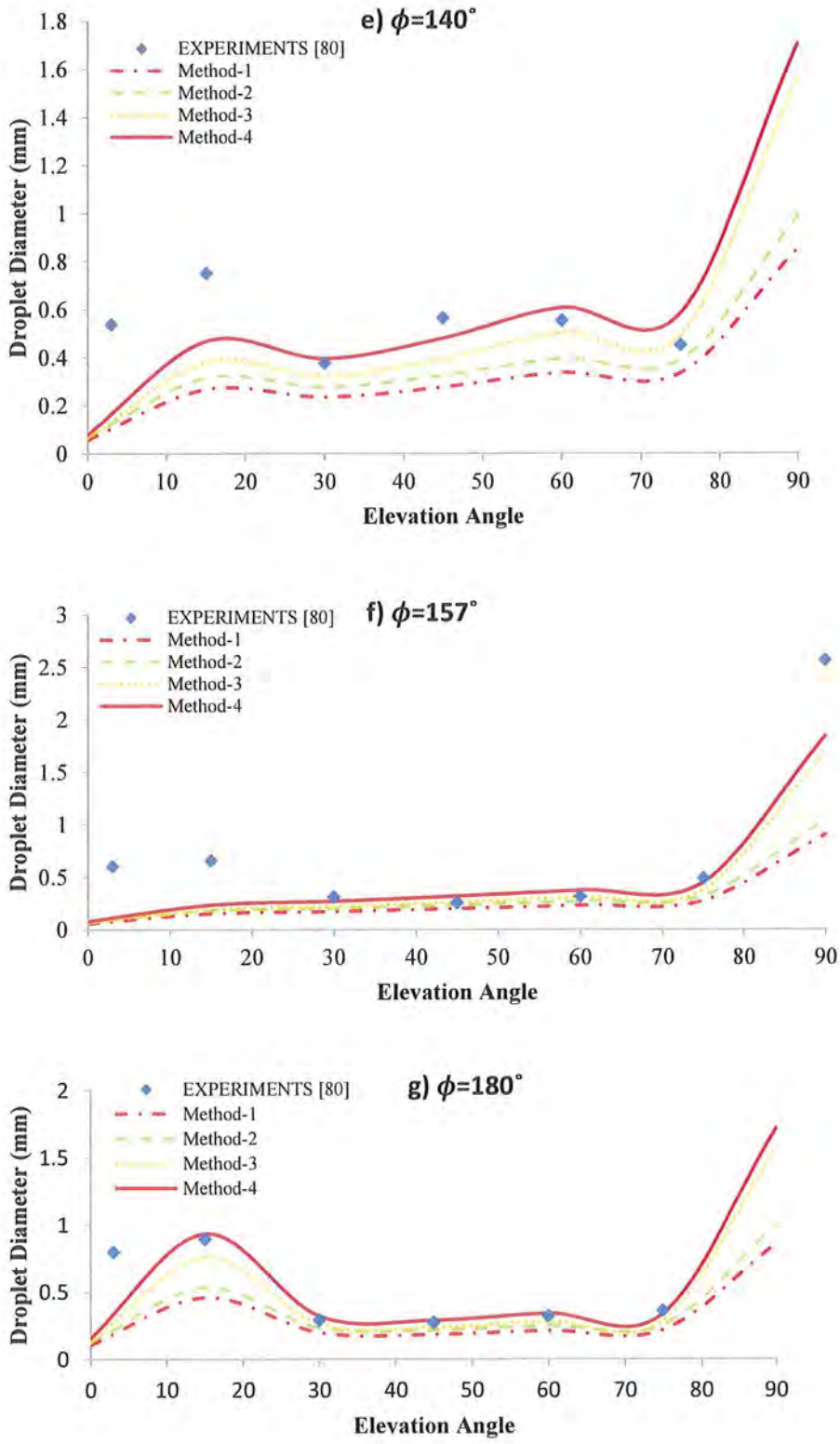

Figure 4-24: Volume-median-droplet-diameter (mm) measured and calculated in the near-field (0.76 m) for the K-205 sprinkler operating at 3.5 bar.

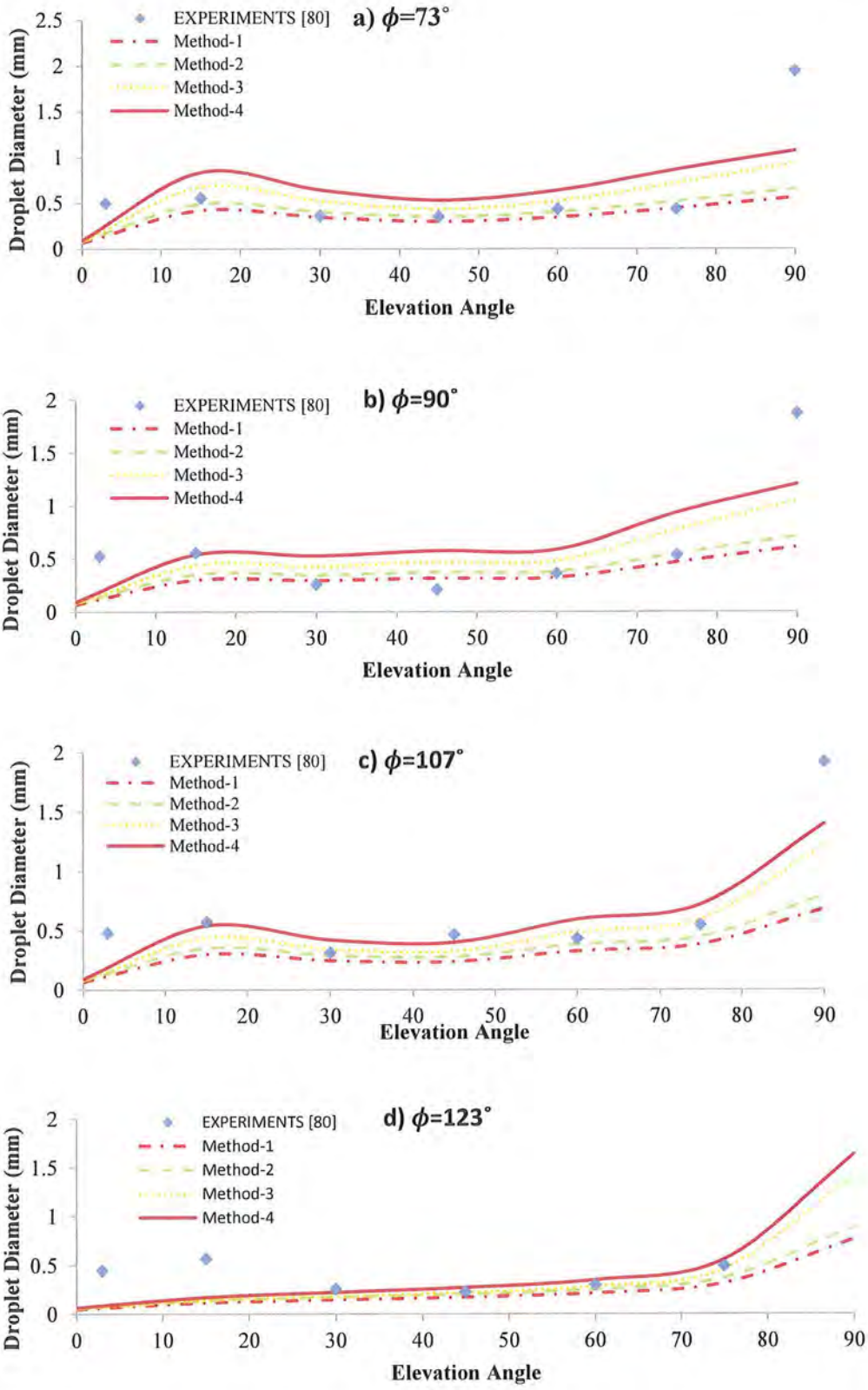
a) ϕ=73°
b) ϕ=90°
c) ϕ=107°
d) ϕ=123°
EXPERIMENTS [80]
Method-1
Method-2
Method-3
Method-4
Droplet Diameter (mm)
Elevation Angle
0
0.5
1
1.5
2
2.5
0
10
20
30
40
50
60
70
80
90

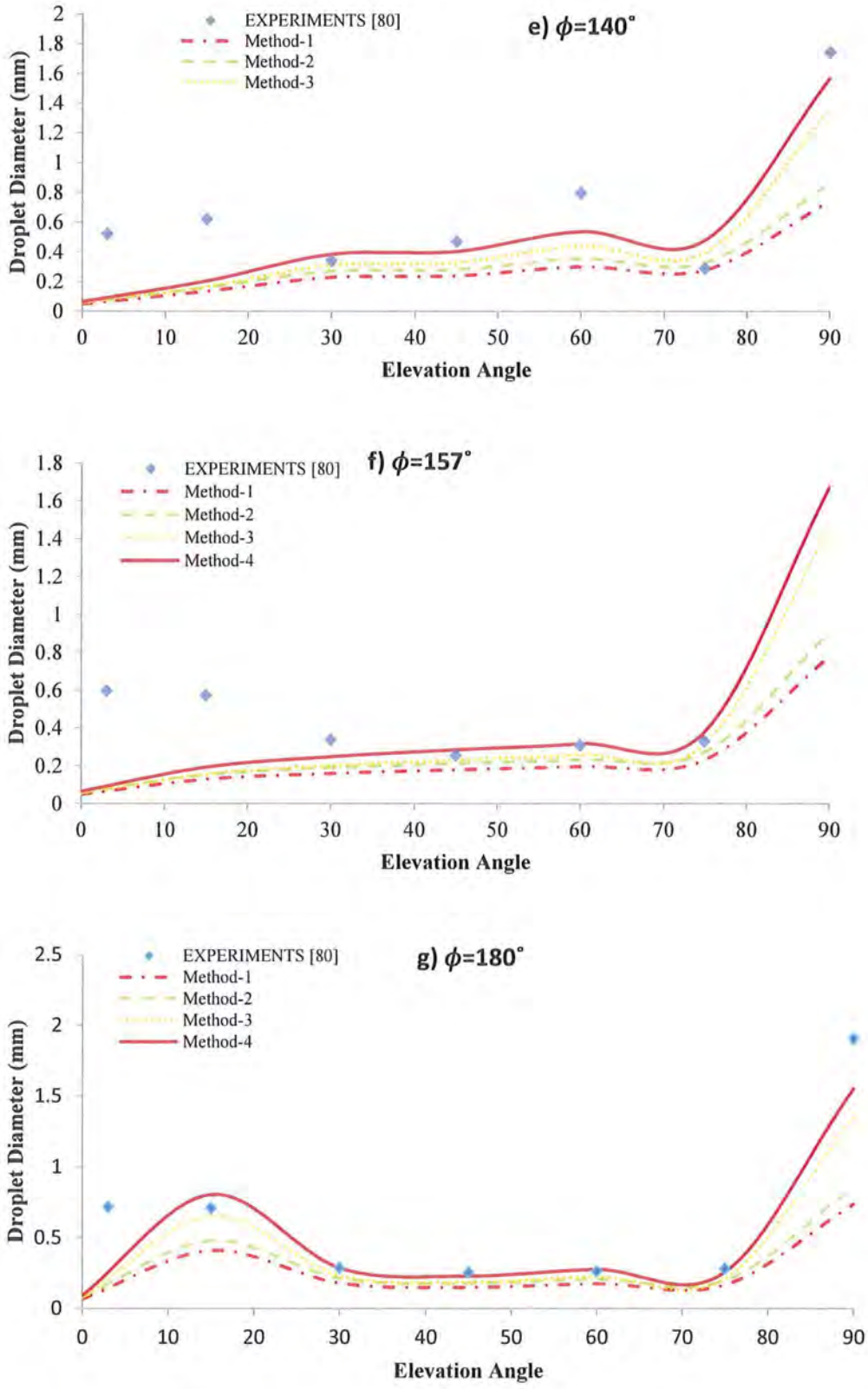

Figure 4-25: Volume-median-droplet-diameter (mm) measured and calculated in the near-field (0.76 m) for the K-205 sprinkler operating at 5.2 bar.

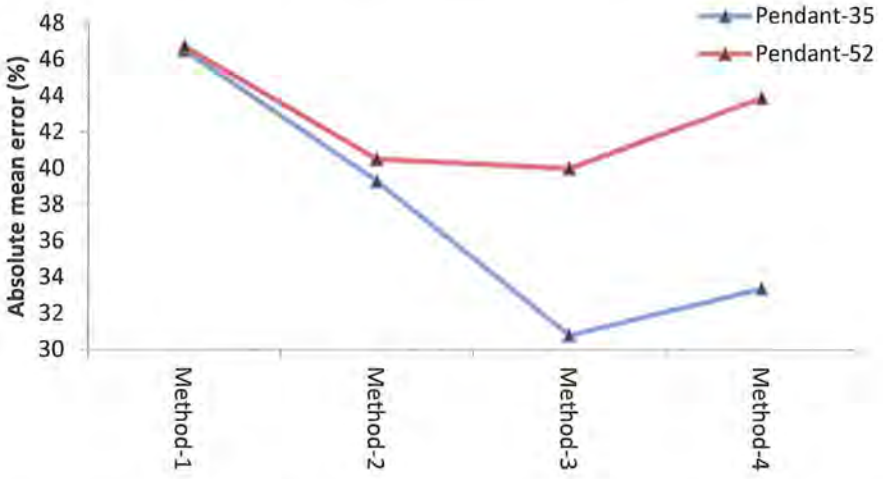

Figure 4-26: Comparison of absolute mean errors with experiment from four semi-empirical methods in predicting Volume-median-droplet-diameter of a pendant sprinkler operating at two pressures.

Since the errors of measurements have not been quantified in the experiments, extra care must also be taken in the interpretation of the differences provided here. The other sources of discrepancies in predictions/experimental should be attributed to:

- Partly due to the uncertainty in data acquisition measurements.
- Moreover in the models, a constant value of 12 is assumed for the dimensionless total growth of the wave. A variation of this constant affects the droplet size and may also explain the discrepancies. Further work may be needed to fully investigate the effect of this constant as well as the film model on the characteristics of real sprinklers.

On the other hand a locally evaluated volume fraction does not always reflect the measured volumetric median diameter, $d_{v_{50}}$. One of the contradictions is for elevation angles less than 20°. In this particular region, the droplets are not resulting from sheet break in directions pertinent to this region. The droplets are either originating from periodic shedding from sheet surface (mostly due to Kelvin-Helmholtz instability) or the turbulence driven (ambient air) force dispersed the droplets which are formed at lower elevation levels ($\theta > 15°$).

Nevertheless the results show relatively good predictions of Methods-3&4 which is due to their more rigorous sheet thickness evaluation at different sheet angles with the DTM approach.

4.6.2 Average Velocity

Predictions for average velocity of droplets at the probe position and at two sprinkler operating pressures, 3.5 bar and 5.2 bar, are presented in Figure 4-27.

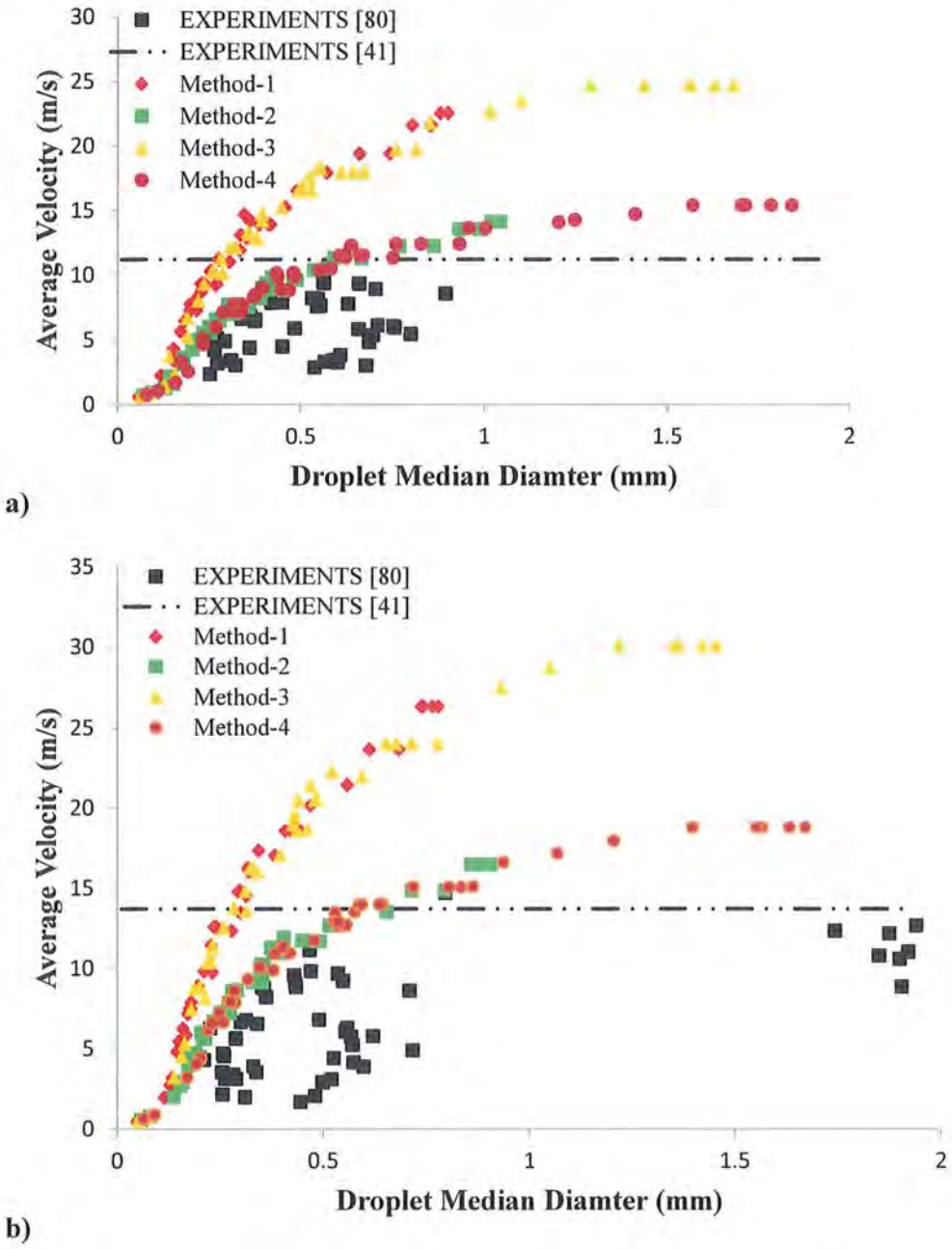

Figure 4-27: Comparing the average velocity predictions using the four methods, measurements and empirical correlation at different azimuthal angles for a pendant sprinkler operating pressure at a) 3.5 bar and b) 5.2 bar.

They are compared against experimental data and empirical correlation [41]. The predictions of droplet velocities show improvement at higher pressure of 5.2 bar when compared with the lower pressure of 3.5 bar.

The spray volume median diameters are usually between *0.9 mm* and *1.2 mm* in sprinkler applications. This means that the vast majority of the droplets in the spray have a corresponding diameter less than the spray volume median diameter. In Figure 4-27 the errors fall in an acceptable range for droplets with diameter less than *1.0 mm*. There are more disagreement model/experiments for larger droplets which could be explained by both un-quantified experimental errors and simplifications made in the model development.

Methods-1&2 predict narrower range of droplet sizes and Method-2 captures the velocity profile very well. Methods-3&4 predict broader range of droplet sizes and Method-4 is the most accurate method of all. Method-2 and Method-4 share AFM as their film model. This shows that the velocity profile predicted by AFM is closer to the reality and this could be one reason for superiority of AFM to BLM (in the aspect of velocity predictions). There is a lack of experimental measurements of film velocity and thickness at deflector edge.

Possible explanation of the available discrepancies can be listed as:

- Inaccuracies in the sheet breakup distance (longer theoretical droplet formation distance).
- Neglecting the effects of air turbulence (quiescent environment). In practical operation it cannot be assumed that the relative velocity between spray droplets and surrounding be negligible.
- Different level of viscous interaction faced by spray formed by slit flow, tine flow and arm flow. (Yet to be quantified)
- Uncertainties in the film velocity at deflector edge.
- Uncertainties in experimental data

4.6.3 Water Volume Fluxes

The predictions of spray volume flux for the pendant sprinkler operating at pressures of 3.5 bar and 5.2 bar are compared to the available experimental data for different azimuthal angles in Figure 4-28(a-g) and Figure 4-29(a-g), respectively. The spray modeling technique which has been employed for predictions of spray volume flux are Methods-1,2,3 & 4.

The quantified spray at azimuthal angles of $73°, 107°, 140°$ is mostly relevant to slit flow and the spray at $180°$ corresponds to flow affected by one of yoke arms, whereas most of the flow is in form of a jet. The spray quantified at azimuthal angle $90°, 123°, 157°$ is mostly related to the flow originated over tines.

In overall Methods-3&4 give better predictions again. The volume flux predictions could be categorized in three regions in terms of their accuracy:

- $0 \leq \theta \leq 15$: There is a considerable difference between theory and experiments:
- $15 \leq \theta \leq 75$: For the middle range elevation angles the predictions are very promising at both pressures and the maximum error model predictions/experiments is below 40%. In contrary to predictions obtained for droplet's volume median diameter, the level of discrepancy decreases as the sprinkler activation pressure increases from 3.5 bar to 5.2 bar.
- $75 \leq \theta \leq 90$: There is an over-prediction for elevation angles right below the sprinkler at all azimuthal angles, ϕ_i.

The main shortcoming in modeling approach which contributes the most to the discrepancies observed are:

- Uncertainties in sheet breakup distance evaluation, and the subsequent initial droplet formation radius
- Uncertainties in the number of droplets produced per unit volume and the frequency of its production per unit of time
- The available discrepancy in film thickness evaluation which had effects on droplet size
- The available discrepancies in droplet velocity

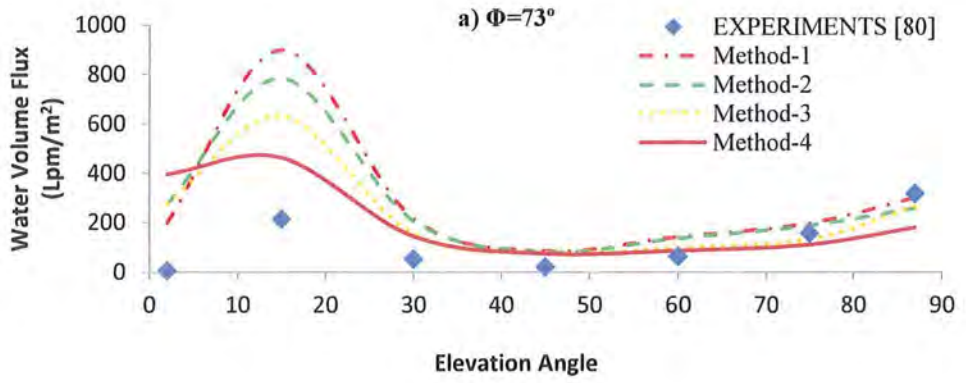
a) Φ=73°
EXPERIMENTS [80]
Method-1
Method-2
Method-3
Method-4
Water Volume Flux (Lpm/m²)
Elevation Angle

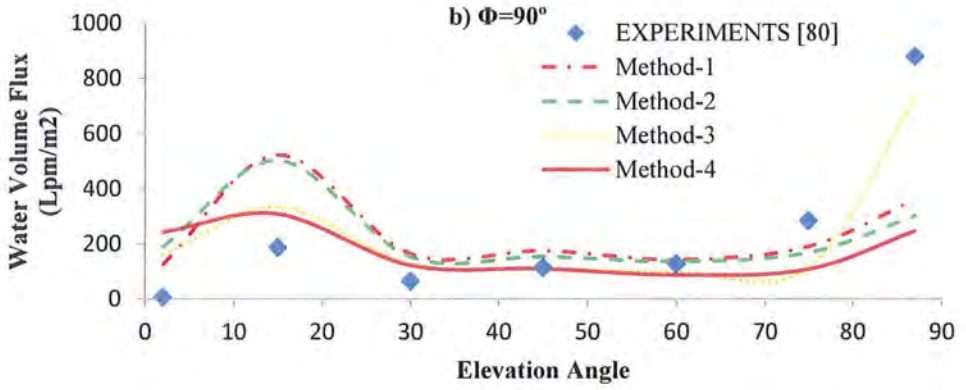
b) Φ=90°
EXPERIMENTS [80]
Method-1
Method-2
Method-3
Method-4
Water Volume Flux (Lpm/m2)
Elevation Angle

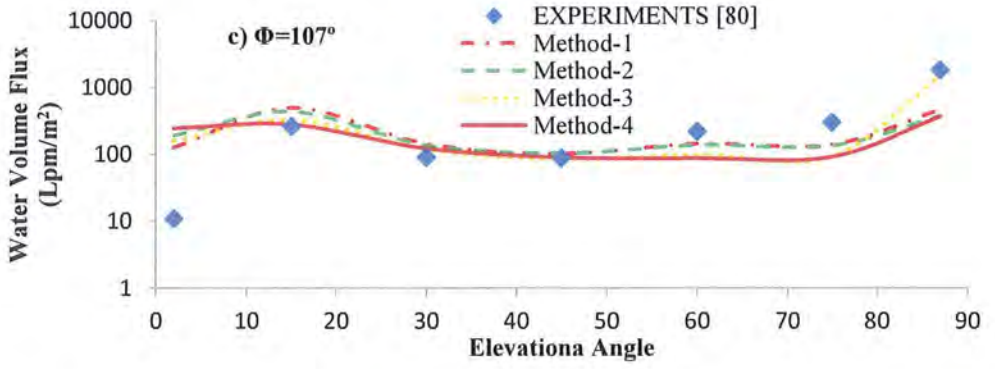
c) Φ=107°
EXPERIMENTS [80]
Method-1
Method-2
Method-3
Method-4
Water Volume Flux (Lpm/m²)
Elevationa Angle

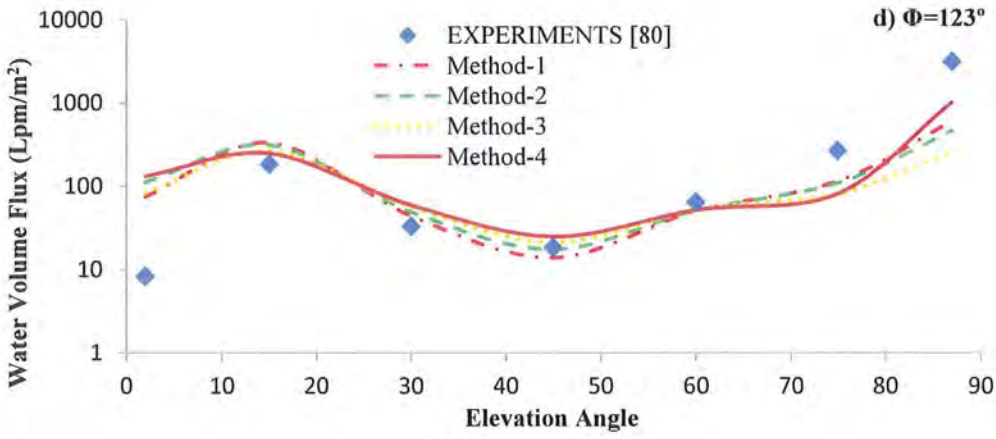
d) Φ=123°
EXPERIMENTS [80]
Method-1
Method-2
Method-3
Method-4
Water Volume Flux (Lpm/m²)
Elevation Angle

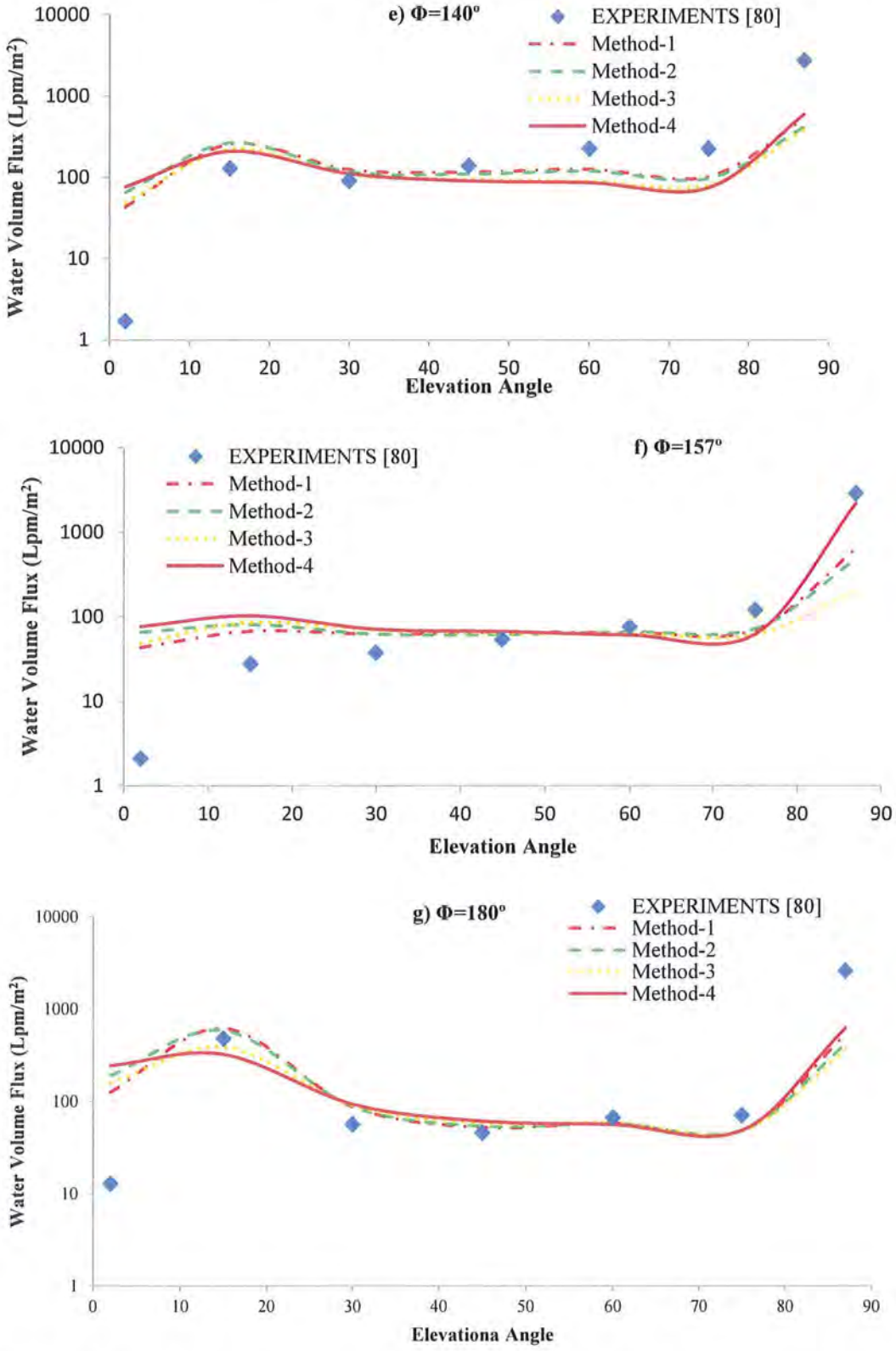

Figure 4-28: Water flux (lpm/m^2) measured and calculated in the near-field (0.76 m) for the K-205 sprinkler operating at 3.5 bar

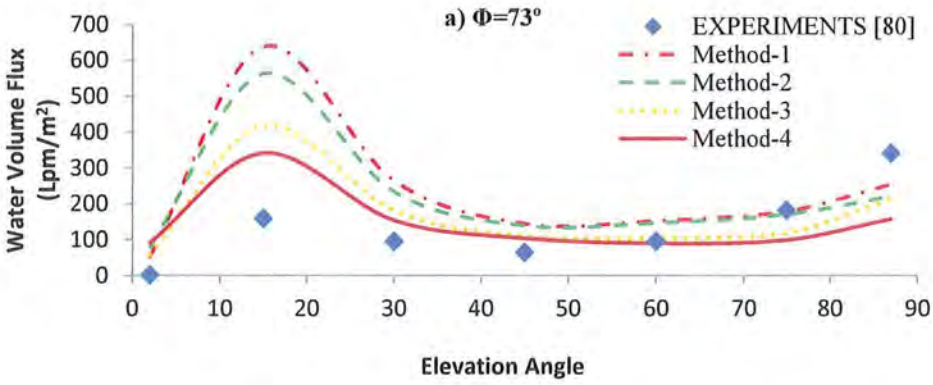
a) Φ=73°
EXPERIMENTS [80]
Method-1
Method-2
Method-3
Method-4
Water Volume Flux (Lpm/m²)
Elevation Angle

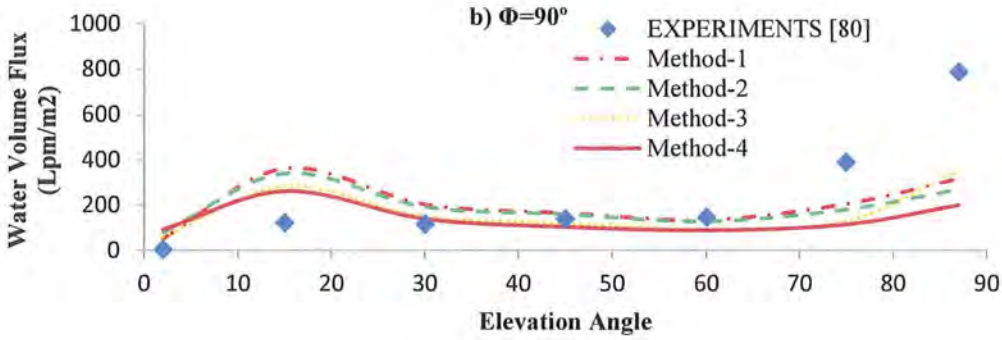
b) Φ=90°
EXPERIMENTS [80]
Method-1
Method-2
Method-3
Method-4
Water Volume Flux (Lpm/m2)
Elevation Angle

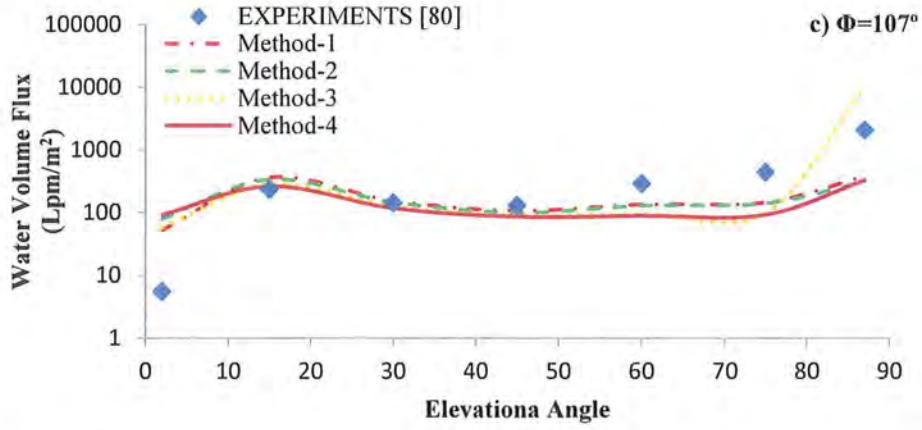
c) Φ=107°
EXPERIMENTS [80]
Method-1
Method-2
Method-3
Method-4
Water Volume Flux (Lpm/m²)
Elevationa Angle

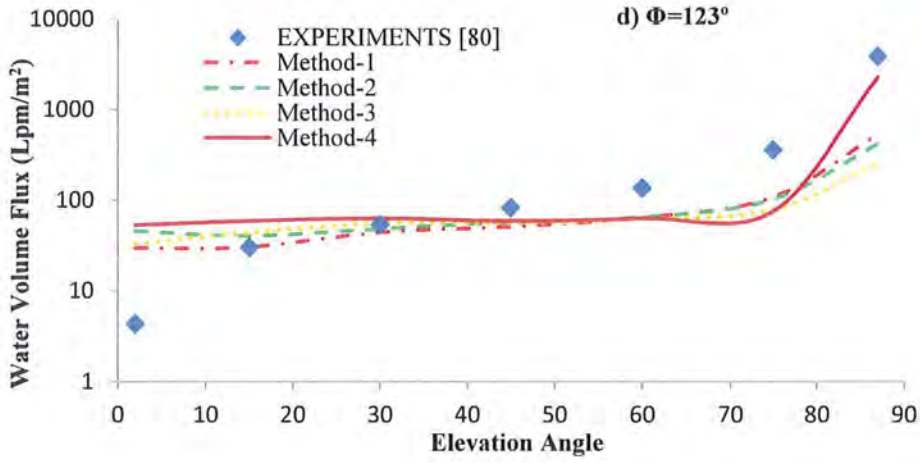
d) Φ=123°
EXPERIMENTS [80]
Method-1
Method-2
Method-3
Method-4
Water Volume Flux (Lpm/m²)
Elevation Angle

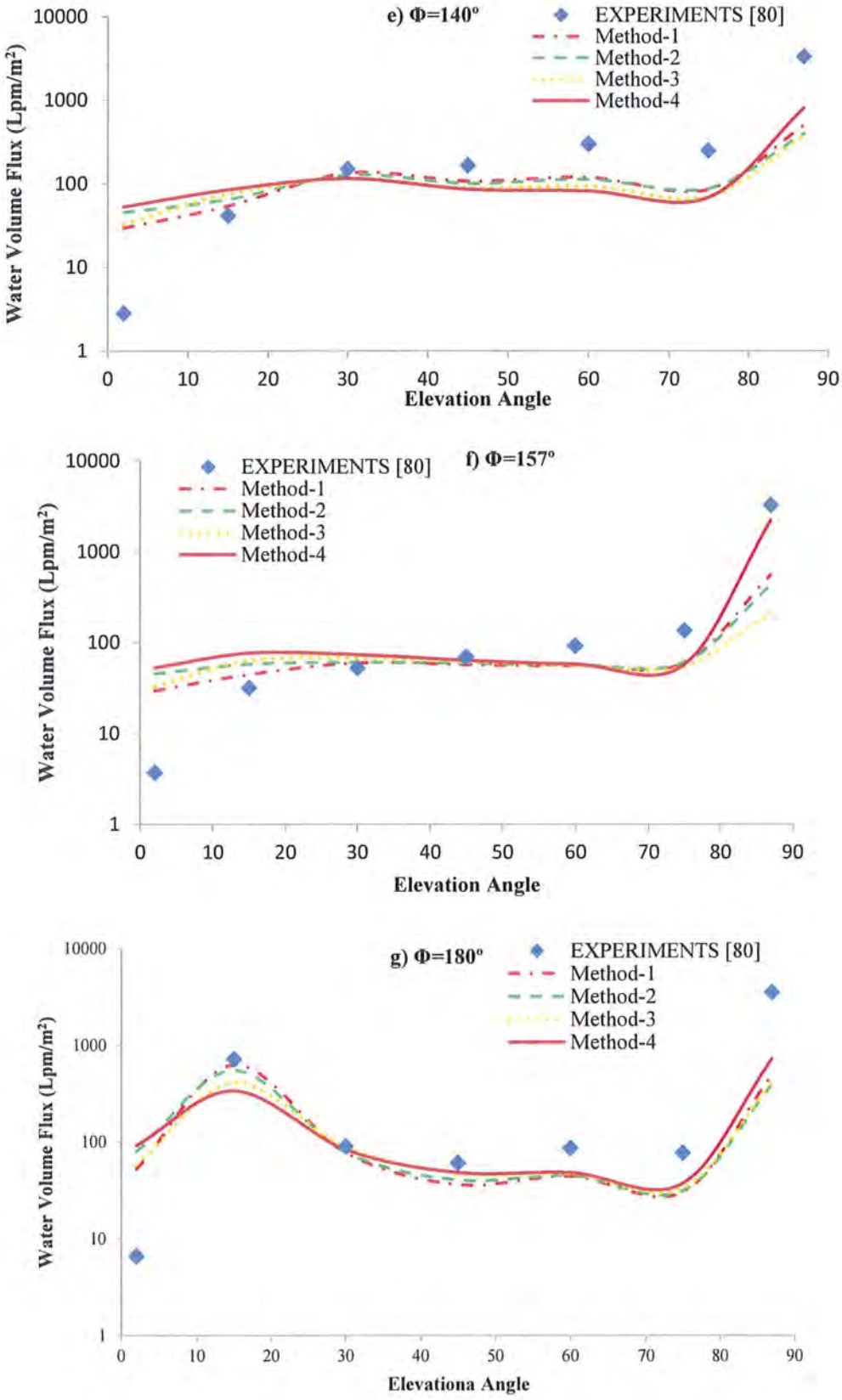

Figure 4-29: Water flux (lpm/m^2) measured and calculated in the near-field (0.76 m) for the K-205 sprinkler operating at 5.2 bar

4.7 Semi-empirical Analysis-Upright Sprinkler

This section investigates the characterization of the near field sprinkler spray by semi-empirical approach for an upright sprinkler. The experimental data for the K-162 upright sprinkler operating at 0.76 bar and 1.31 bar, Figure 4-30, shows the volume median diameter along the elevation angles in the near field at seven azimuthal angles.

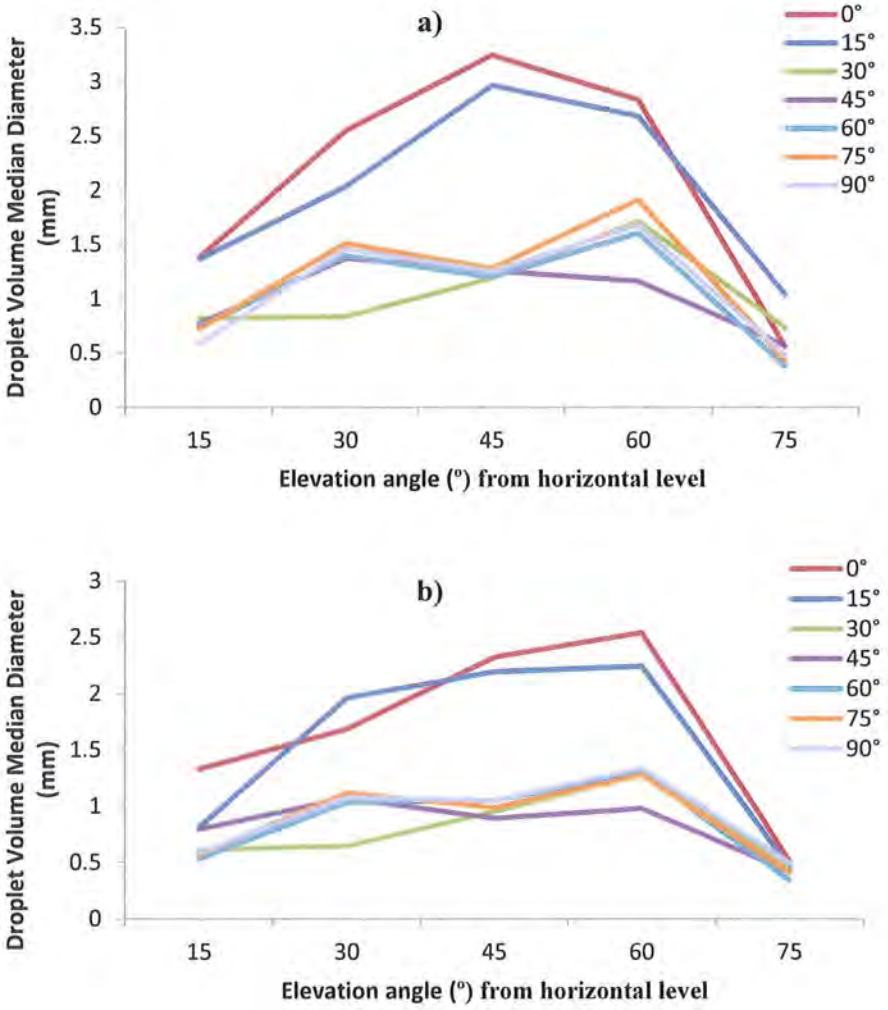

Figure 4-30: Volume median droplet diameter distribution along the elevation angle in the near field for the K-162 at a) 0.76 bar b) 1.31 bar and seven azimuthal angles [80]

Relatively large droplets appeared in the middle elevation range (30°-60°). In the region close to frame arms, i.e. at azimuthal angle of 0° and 15° the droplets are large because the spray atomization process was interrupted by the frame and the sprinkler pipeline system.

4.7.1 Median Droplet Diameter

The predicted spatial volume median diameters for an upright sprinkler K-162 (§2.6.1) at two pressures *0.76 bar* and *1.31 bar* are presented in Figure 4-31 and Figure 4-32, respectively. The flow rates are equal to $2300\ cm^3/s$ and $3100\ cm^3/s$ and the jet Reynolds number is 2.39×10^{-5} and 3.15×10^{-5}.

It should be reminded that the azimuthal angles $\phi = 0°\&180°$ are assigned to the two yoke arms in the sprinkler and the elevation angles are covered from 0° to 90°. A reasonably good agreement is found between predictions and experimental data for the droplet median diameter, Figure 8, in particular with Methods 3&4. The accuracy of predictions improves as the azimuthal angle approaches 90° which is the part of the flow field less affected by the sprinkler arms. The average mean differences between experiment/predictions as shown in Figure 4-33 change from 55%, 48%, 36% and 39% at 0.76 bar to 43%, 35%, 33% and 33% at 1.31 bar for Methods 1 to 4, respectively. It is found that Method-3 and Method-4 which both employ the DTM approach provide the same overall spatial prediction of droplet sizes.

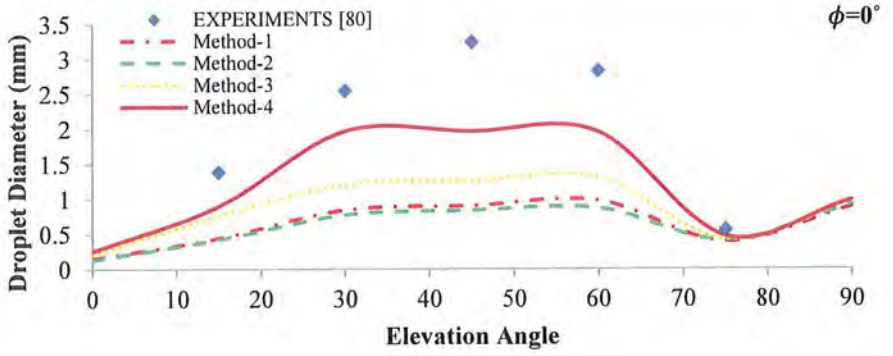
EXPERIMENTS [80]
Method-1
Method-2
Method-3
Method-4
ϕ=0°
Droplet Diameter (mm)
Elevation Angle

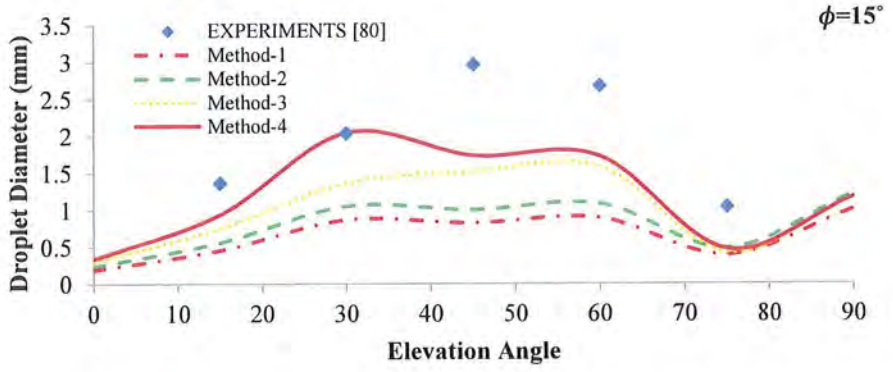
EXPERIMENTS [80]
Method-1
Method-2
Method-3
Method-4
ϕ=15°
Droplet Diameter (mm)
Elevation Angle

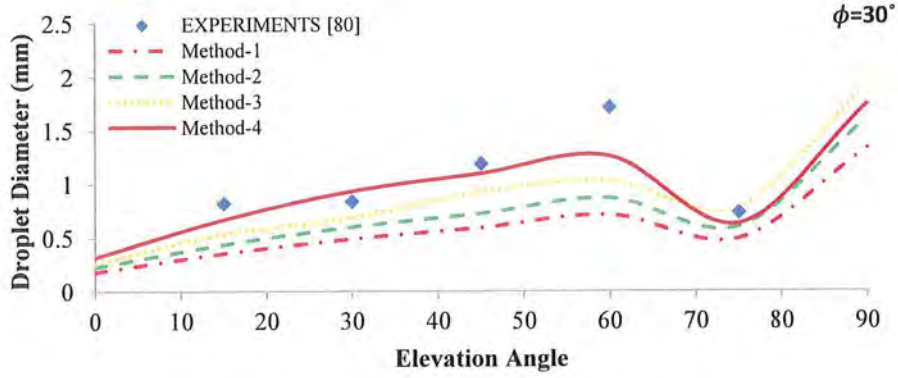
EXPERIMENTS [80]
Method-1
Method-2
Method-3
Method-4
ϕ=30°
Droplet Diameter (mm)
Elevation Angle

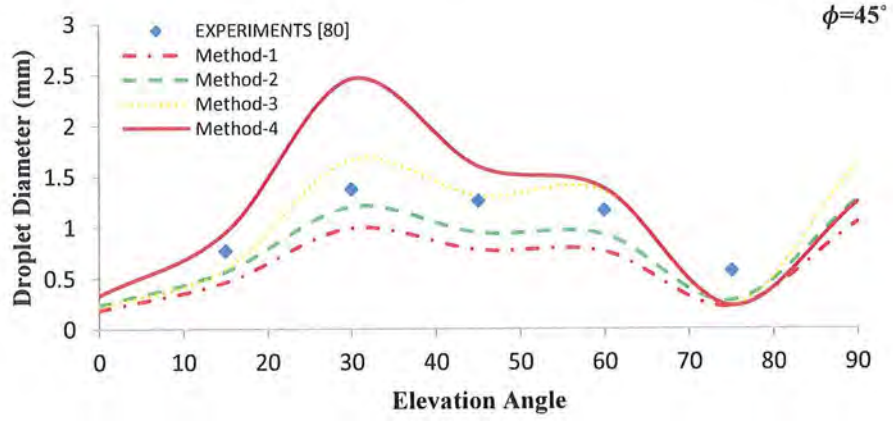
EXPERIMENTS [80]
Method-1
Method-2
Method-3
Method-4
ϕ=45°
Droplet Diameter (mm)
Elevation Angle

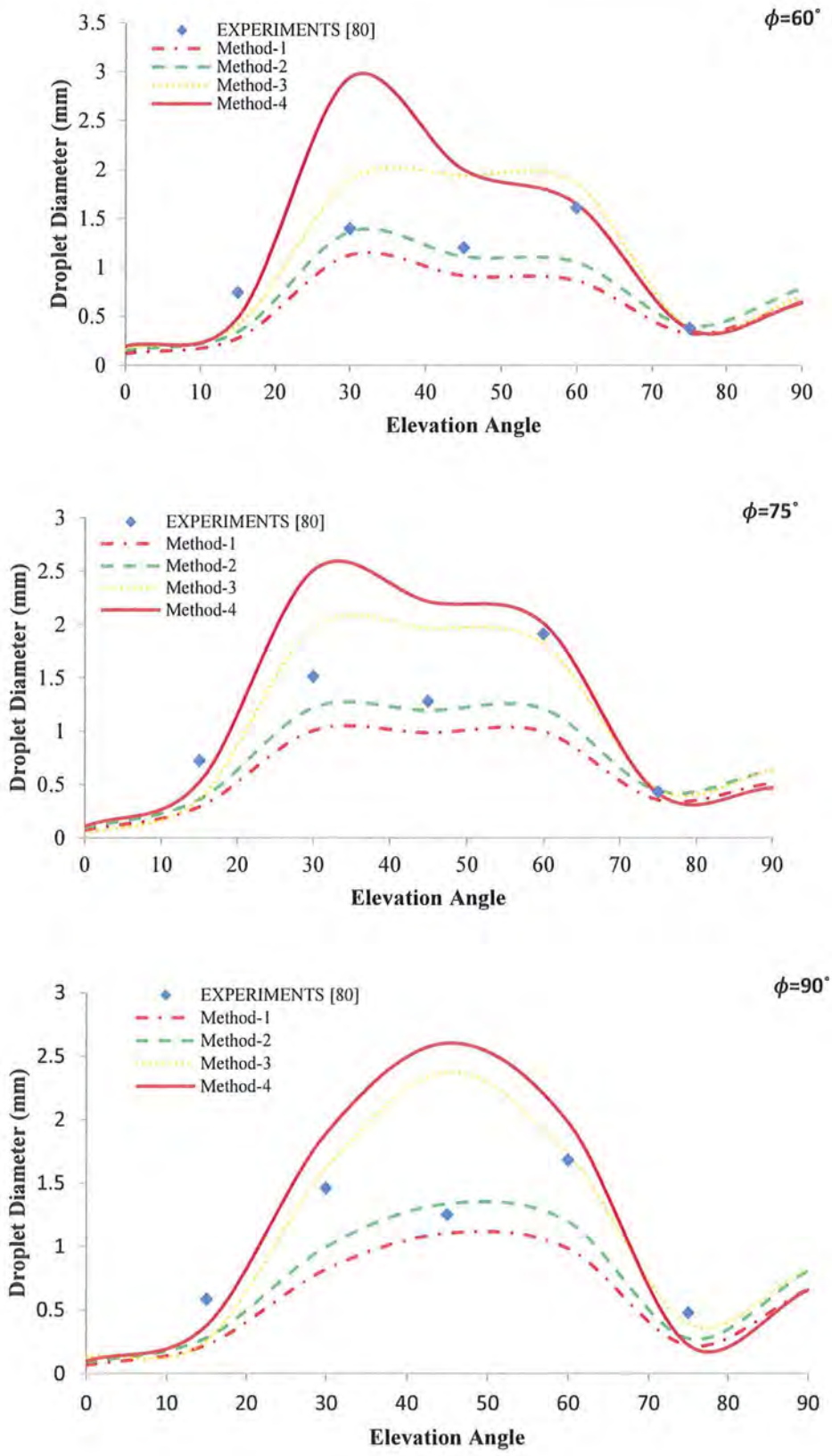

Figure 4-31: Volume-median-droplet-diameter (*mm*) measured and calculated in the near-field (0.76 *m*) for the K-162 sprinkler operating at 0.76 *bar*.

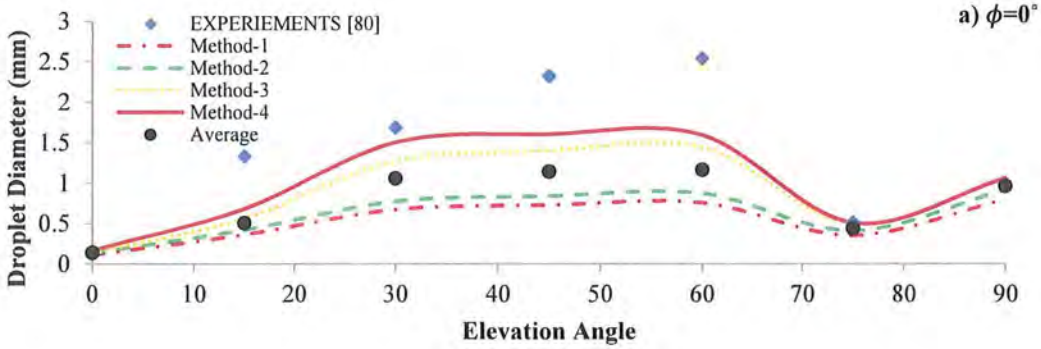
a) ϕ=0°
EXPERIEMENTS [80]
Method-1
Method-2
Method-3
Method-4
Average
Droplet Diameter (mm)
Elevation Angle

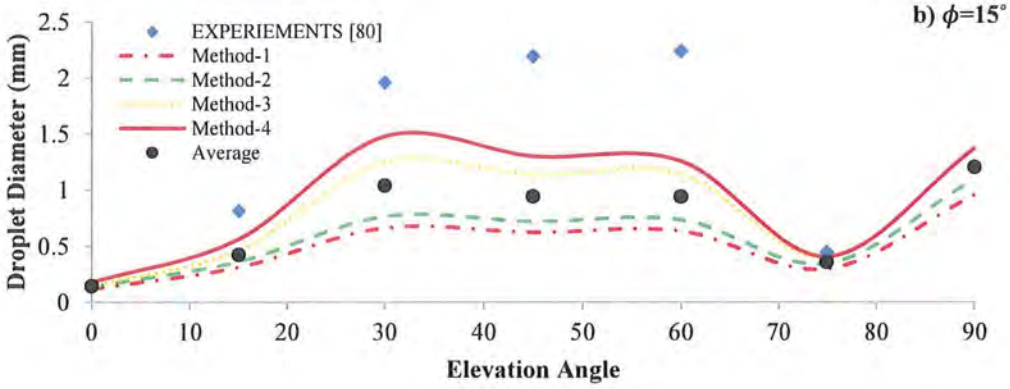
b) ϕ=15°
EXPERIEMENTS [80]
Method-1
Method-2
Method-3
Method-4
Average
Droplet Diameter (mm)
Elevation Angle

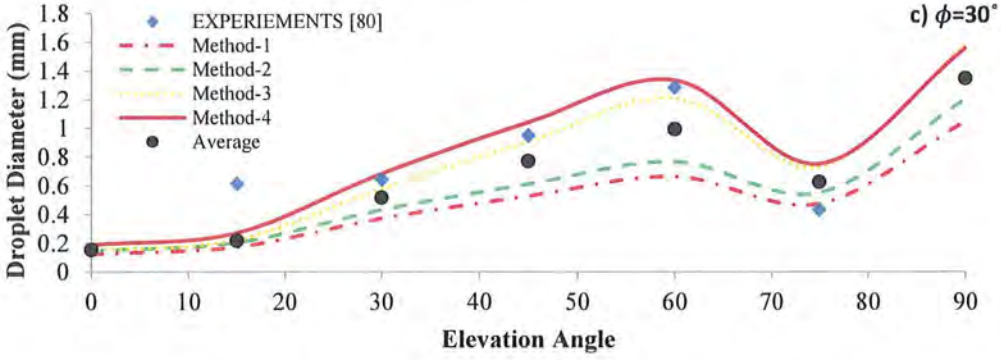
c) ϕ=30°
EXPERIEMENTS [80]
Method-1
Method-2
Method-3
Method-4
Average
Droplet Diameter (mm)
Elevation Angle

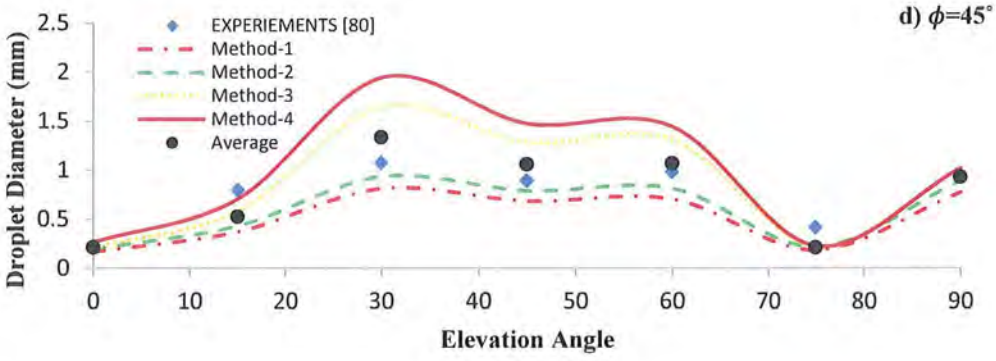
d) ϕ=45°
EXPERIEMENTS [80]
Method-1
Method-2
Method-3
Method-4
Average
Droplet Diameter (mm)
Elevation Angle

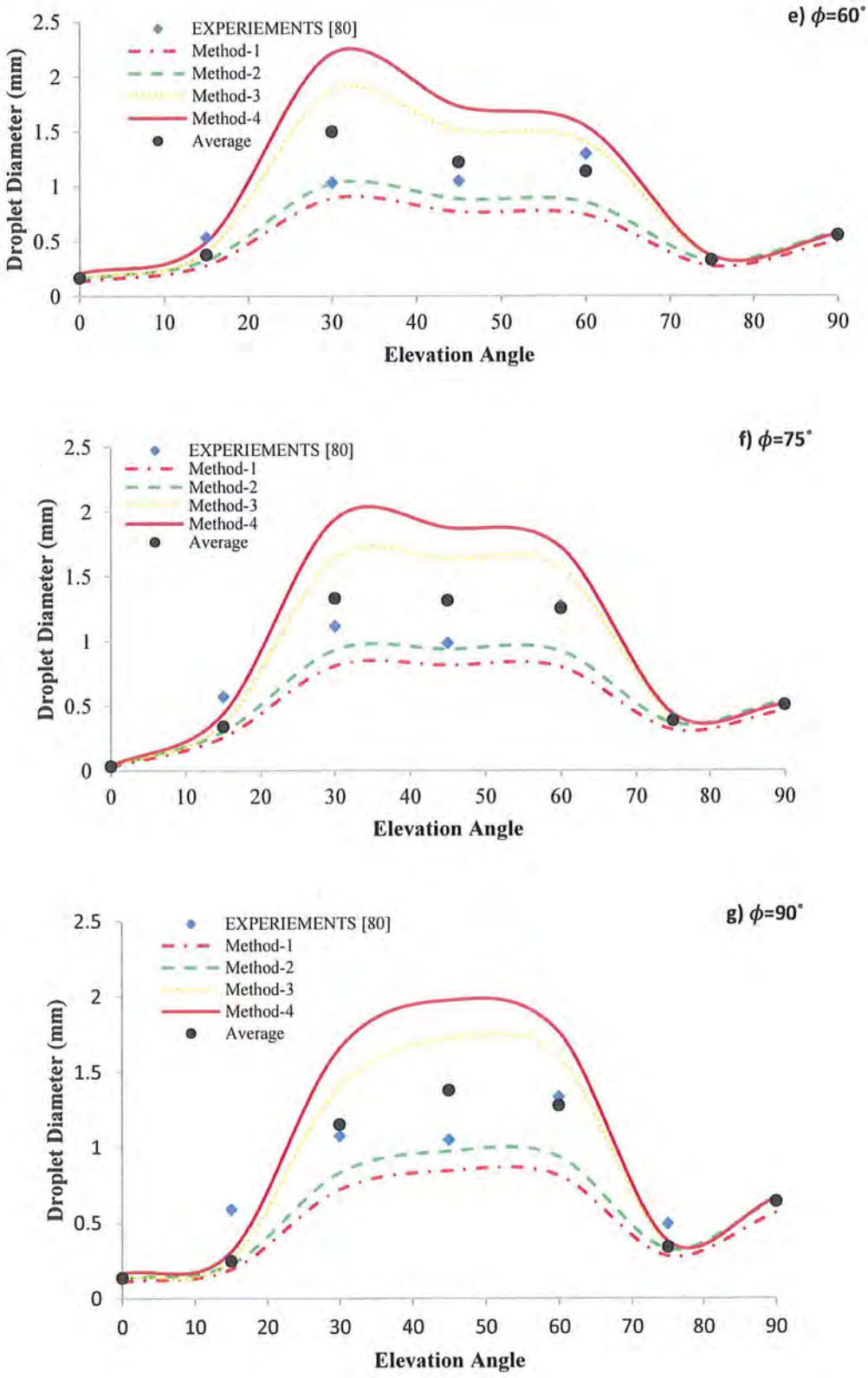

Figure 4-32: Volume-median-droplet-diameter (*mm*) measured and calculated in the near-field (0.76 *m*) for the K-162 sprinkler operating at 1.31 *bar*.

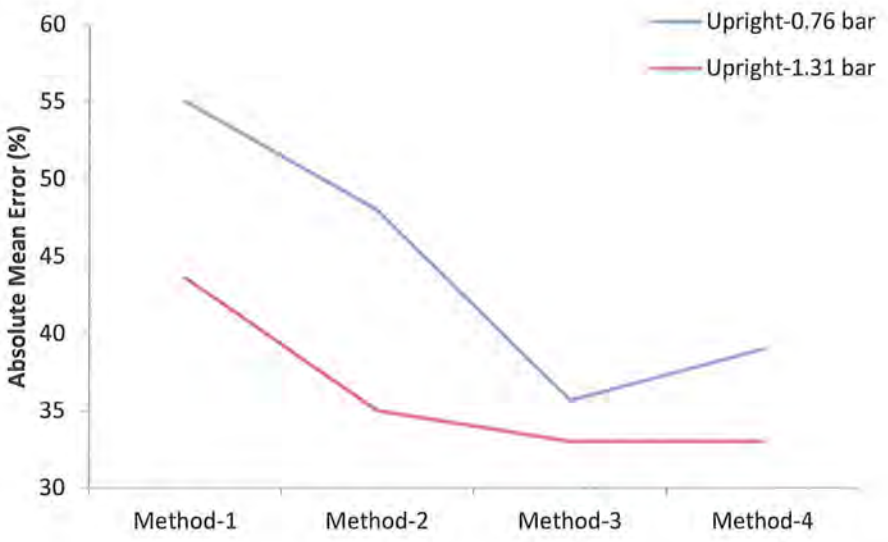

Figure 4-33: Absolute Mean Error (%) in predicting spray volume median diameter from Method 1,2,3 and 4 over seven elevation points at seven azimuthal positions.

4.7.2 Average Velocity

Predictions for average velocity of droplets at the probe position and at two sprinkler operating pressures, 0.76 bar and 1.31 bar, are presented in Figure 4-34. They are compared against experimental data and empirical correlation [41].

Similar to observation provided for the pendant sprinkler Methods-1&2 predict narrower range of droplet sizes and Mathod-2 captures the velocity profile very well. Methods-3&4 predict broader range of droplet sizes and Method-4 is the most accurate method of all. Method-2 and Method-4 which share AFM as their film model show that the velocity profile predicted by AFM is more accurate than BLM.

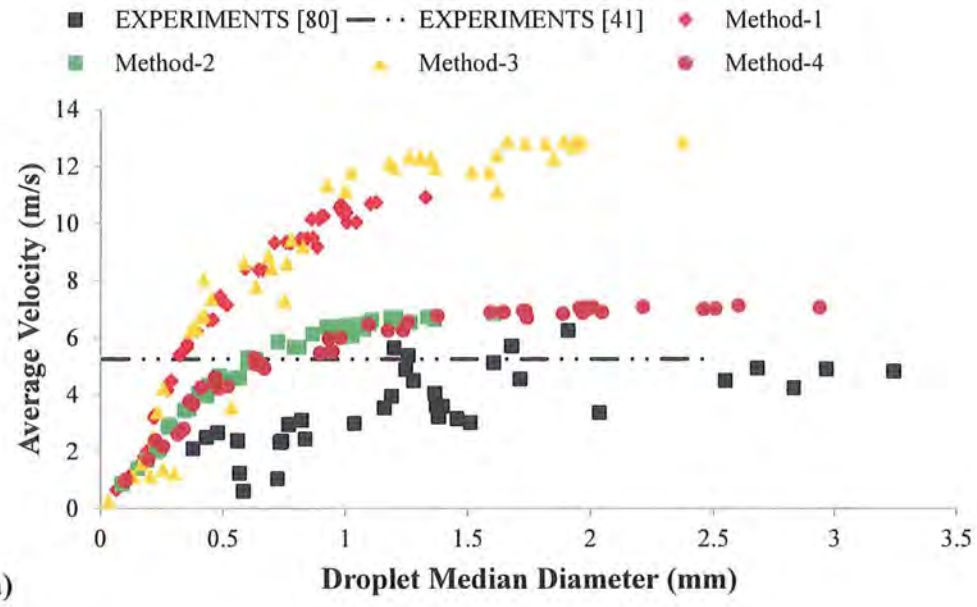

a)

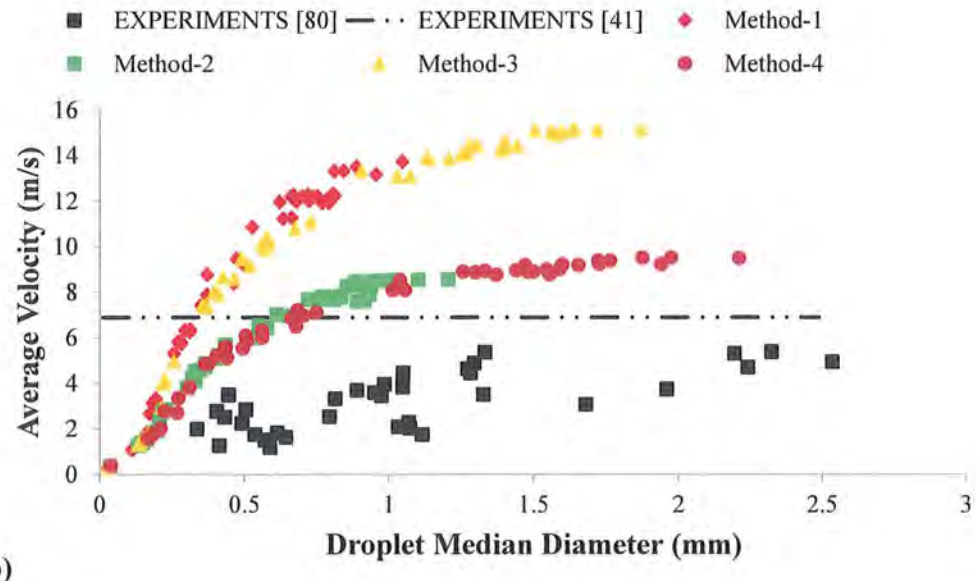

b)

Figure 4-34: Comparing the average velocity predictions using the four methods, measurements and empirical correlation at different azimuthal angles for an upright sprinkler operating pressure at a) 0.76 bar and b) 1.31 bar.

4.7.3 Water Volume Flux

Similar to predictions obtained for droplet size in previous section, the water volume fluxes in Figure 4-35 and Figure 4-36 are also better predicted with Method-3 and Method-4. In general all Methods over predict the water volume fluxes. The accuracy of predictions can be divided into two groups:

- $0 \leq \theta \leq 45$: The predictions are not acceptable.
- $45 \leq \theta \leq 90$: The predictions are improved as the azimuthal angle move away from yoke arms.

The discrepancies found in Figure 4-31, Figure 4-32, Figure 4-35 and Figure 4-36 could be explained by considering that the effect of initial perturbation on the film and sheet development is amplified in upright fire sprinklers compared to pendant sprinklers. There are strongly tilted tines in the configuration of the upright sprinkler, which makes the atomization process disobey from the simplifications made in deriving the formulation for an impinging atomizer. In general the type of disturbance would crucially affect the rate of instability growth and its modes.

In upright sprinklers yoke arms will disturb both sheet formation and breakup pattern to a considerable extent. The spray is affected by the interaction between jet flow and film flow around the sprinkler arms which has not been accounted for in the models. To understand the mechanisms through which the arms are contributing to the near field spray, first principle CFD analysis should be carried out. In the real operational condition, the pipe system which feeds the water to the upright sprinkler also affects the spray pattern in upright sprinklers. This leads to the droplets to agglomerate and increases the probability of formation of larger droplets. Part of the discrepancies for water volume flux is cascaded back from the over-predicted droplet velocity. In general it can be concluded the viscous effects are yet to be modeled properly. The last point to be mentioned here is that the experiments were carried out at quite low pressures. It is believed that the model should also be tested for higher pressures where less discrepancy is expected. The curvature of the sheet in the upright sprinkler can enhance the growth of waves on the sheets surface.

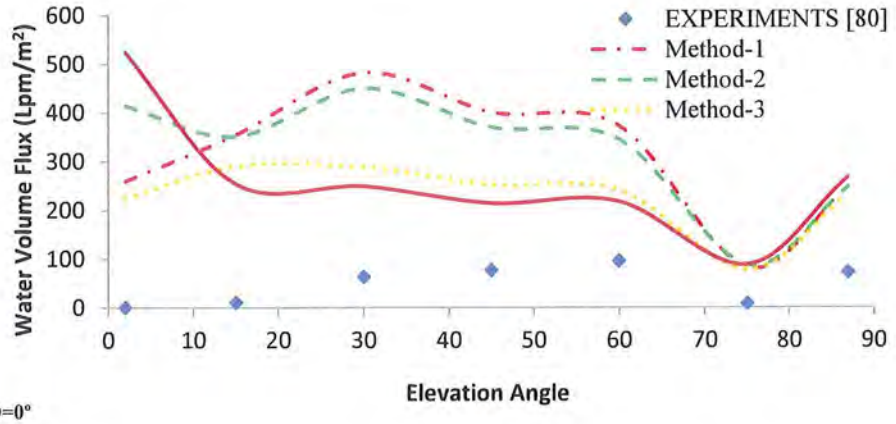

Φ=0°

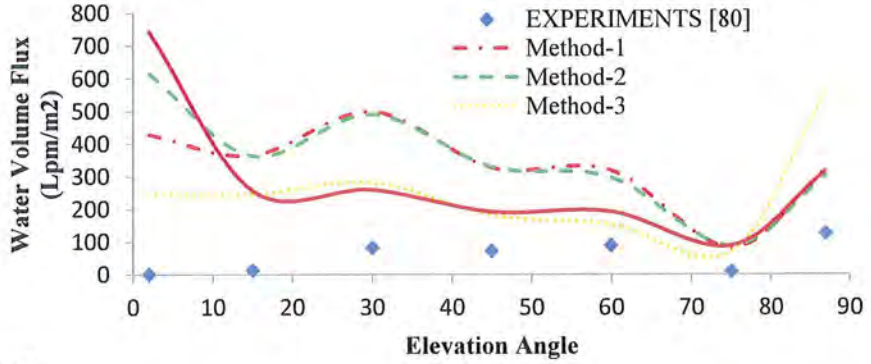

Φ=15°

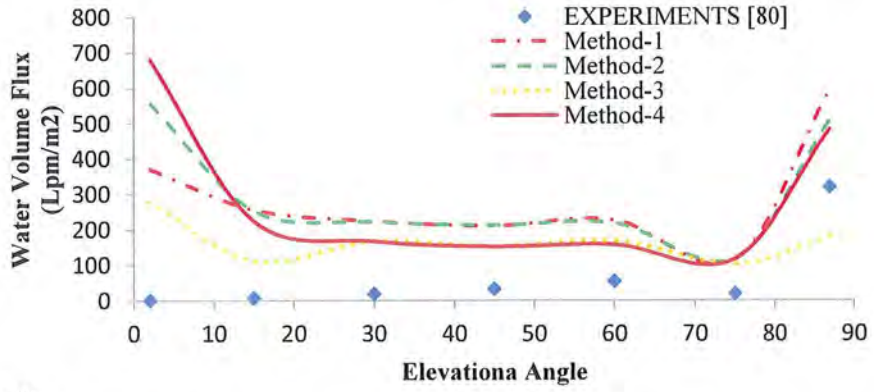

Φ=30°

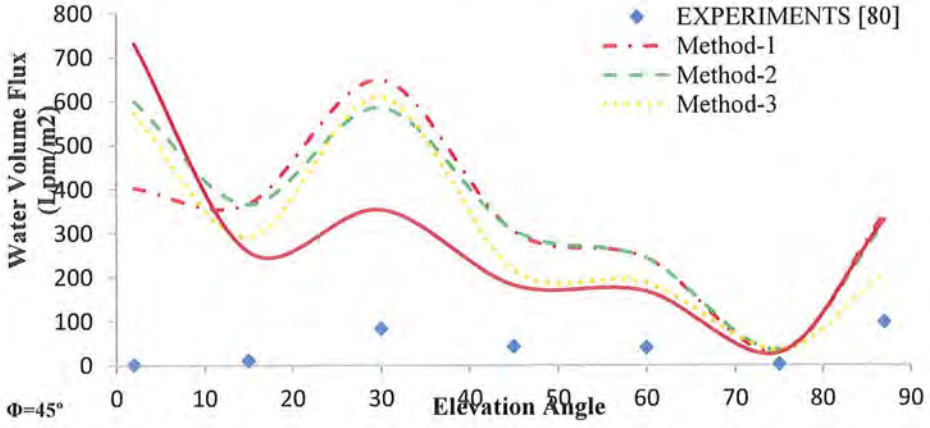

Φ=45°

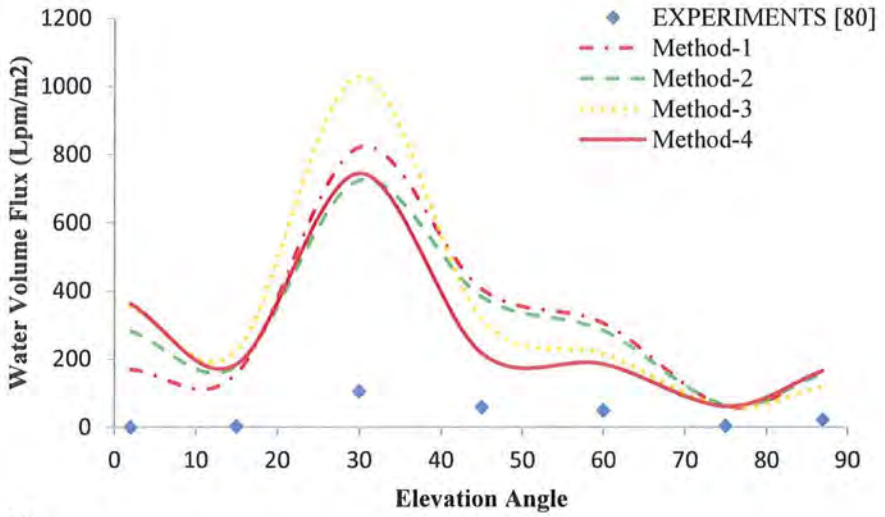

Φ=60°

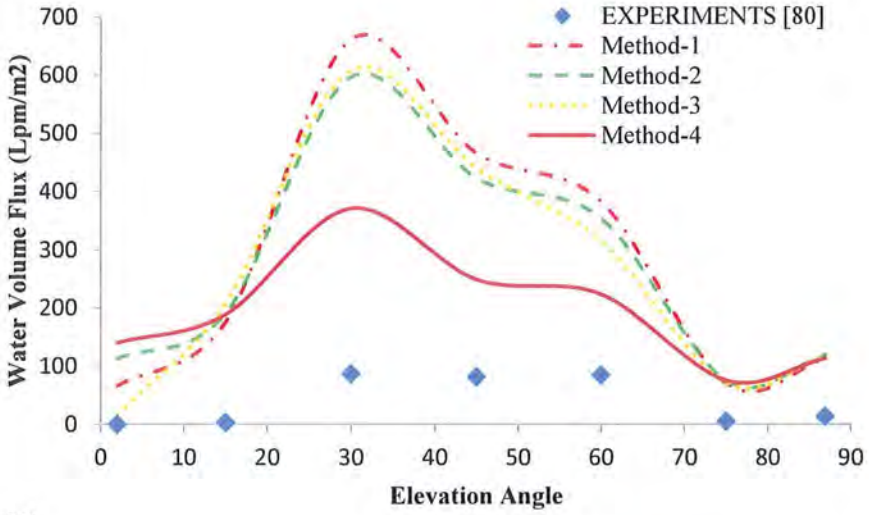

Φ=75°

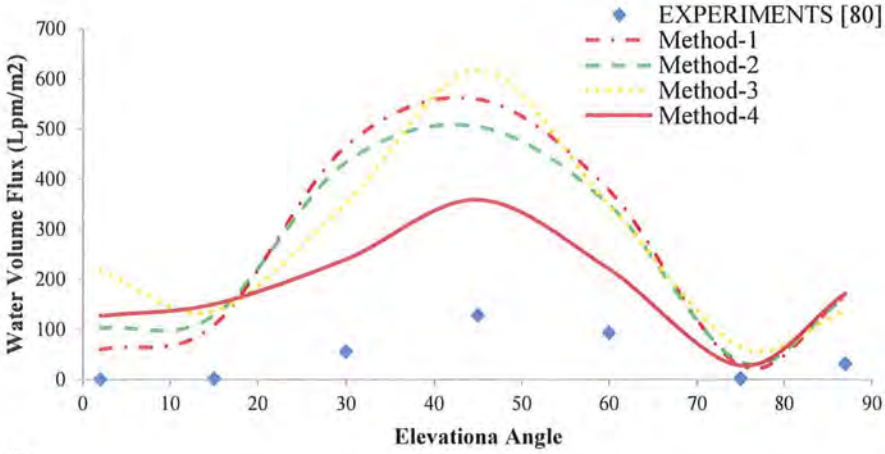

Φ=90°

Figure 4-35: water volume flux (lpm/m^2) measured in the near-field (0.76 *m*) for the K-162 sprinkler operating at 0.76 *bar*.

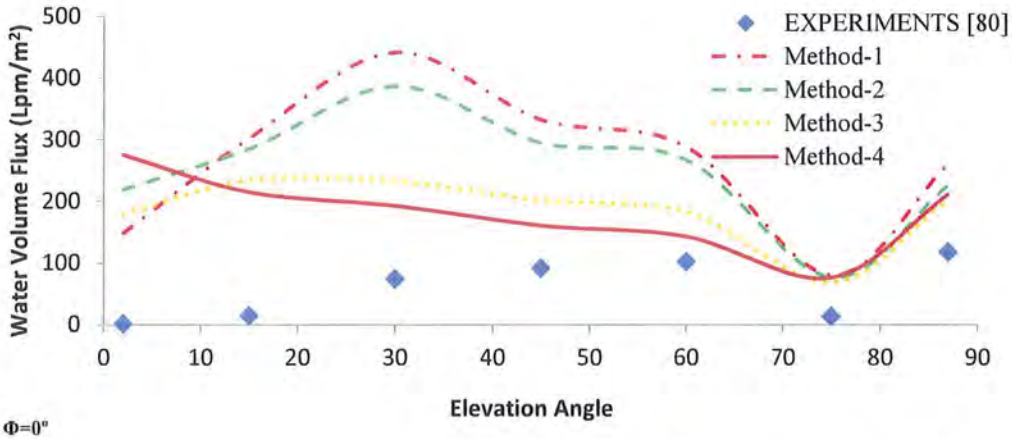

a) Φ=0°

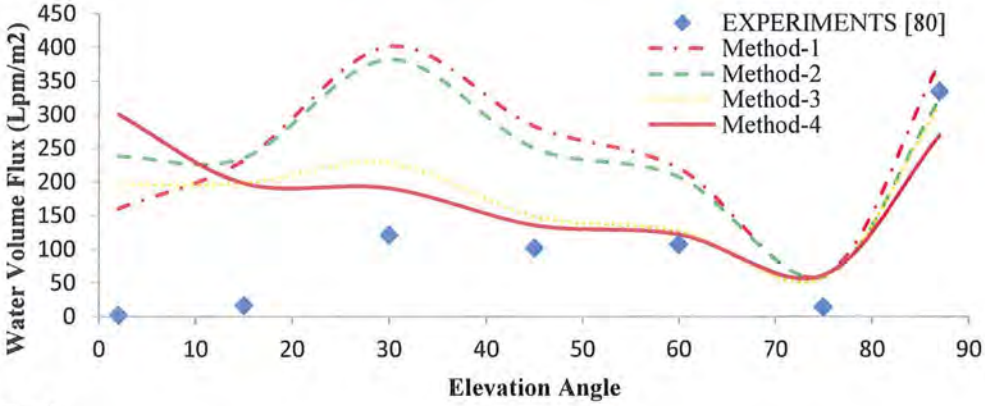

b) Φ=15°

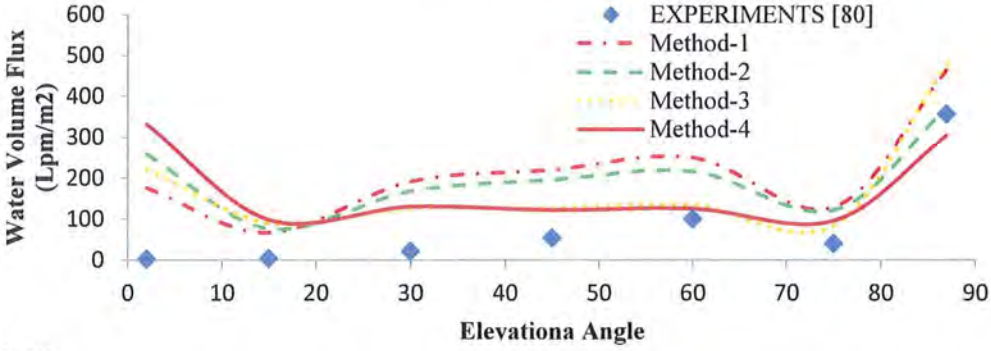

c) Φ=30°

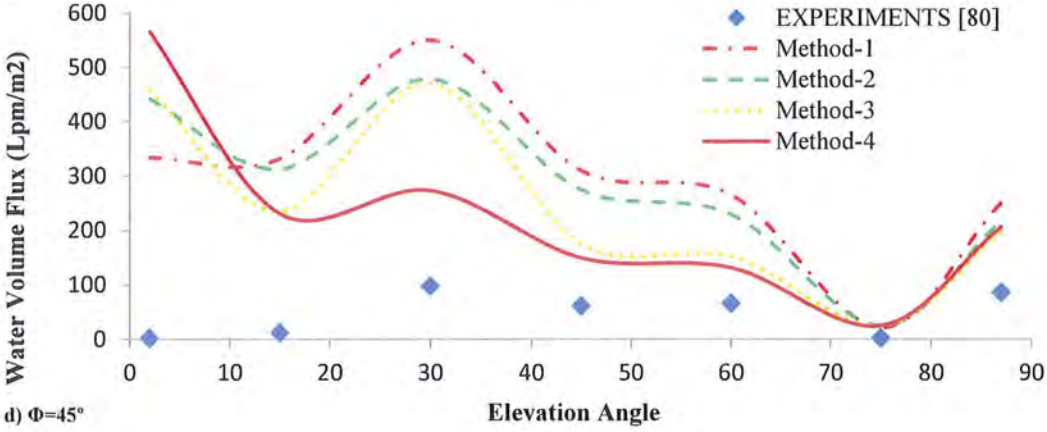

d) Φ=45°

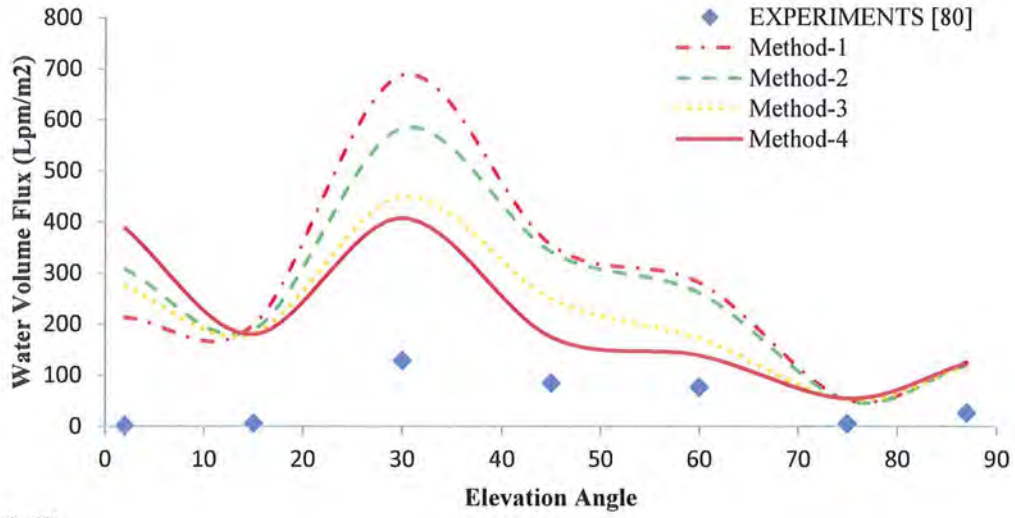

e) Φ=60°

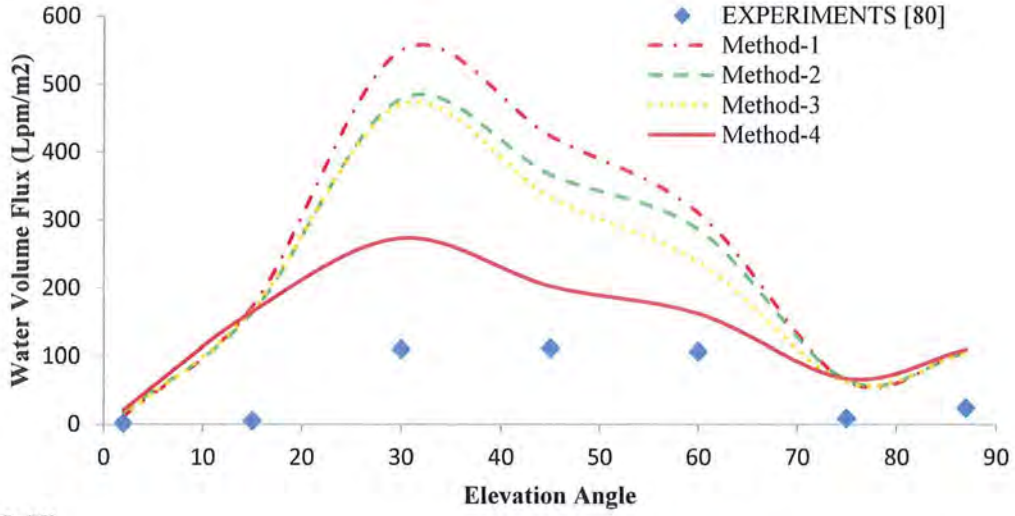

f) Φ=75°

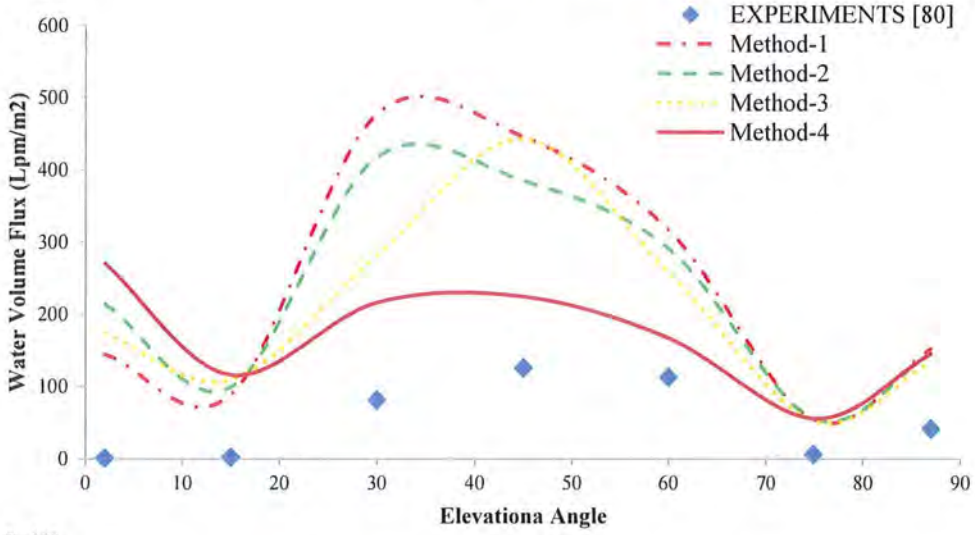

g) Φ=90°

Figure 4-36: water volume flux (lpm/m^2) measured in the near-field (0.76 *m*) for the K-162 sprinkler operating at 1.31 *bar*.

4.8 Sensitivity Analysis

In the previous sections (§4.6 and §4.7) the semi-empirical predictions of droplet initial diameter, droplet mean velocity and volume flux at its formation point has been presented. In this the sensitivity of predictions to the number of evaluated volume fraction will be investigated which may be available along a given azimuthal angle. In the previous set of predictions, the undertaken measurements were available at seven data points at seven equally distributed elevation angles between 0° to 90°.

With no doubt extracting volume fluxes or volume fractions at seven data points may not always be favorable due to technical complexity of running tests at multiple elevation angles and extra cost it would cause, hence economically disadvantageous.

The number of data points used in semi-empirical modeling has been artificially reduced to six and five data points from seven of original experimental data by neglecting the areas with less water volume densities. In the case of 6-points based estimates the contribution of volume flux corresponding to 3° elevation angle has been neglected in total volume flux. The volume flux at this location was the lowest compared to the other probe points for this particular pendant sprinkler. In the case of 5-points based estimates the contribution of volume flux corresponding to 3° and 45° elevation angles have been neglected due to the same reasoning. It could be realized from experimental data that this type of pendant sprinkler is directing most of the flow mainly toward two elevation angles of 15° and 90°.

4.8.1 Median Droplet Diameter

The median droplet diameter appraisal at six of the azimuthal angles – those which experimental data were available for- are presented in Figure 4-37 a – f. Method-3 has been chosen to obtain evaluations for the 7, 6 and 5 points based semi-empirical modeling, and the results are compared against experimental measurements at respective azimuthal angles.

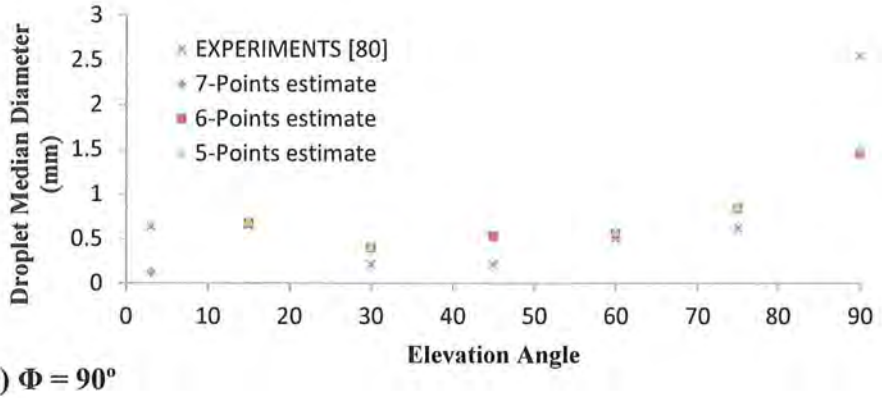

a) Φ = 90°

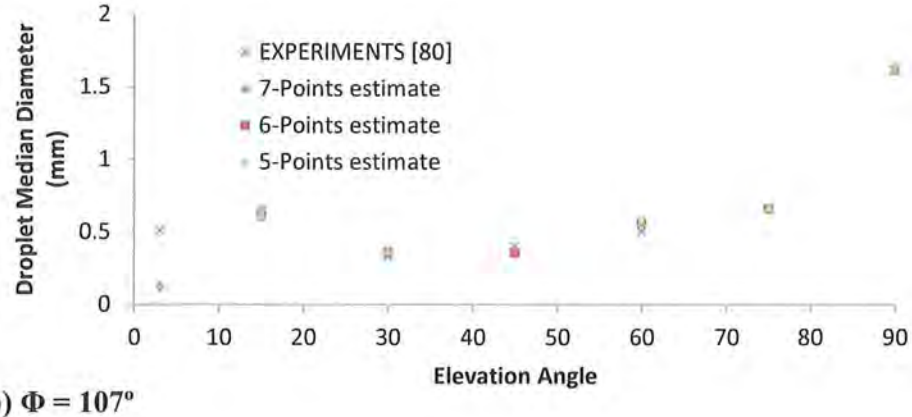

b) Φ = 107°

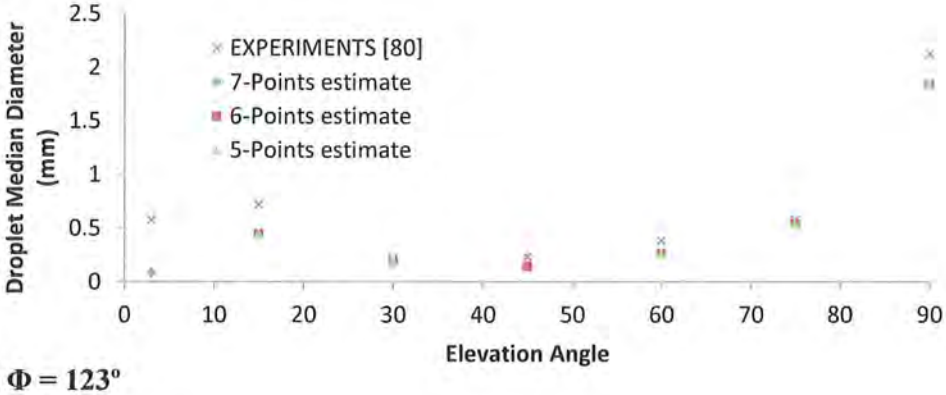

c) Φ = 123°

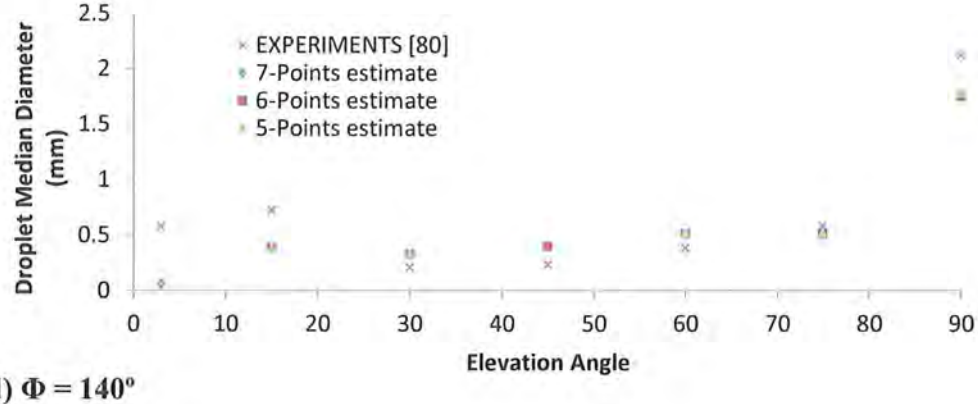

d) Φ = 140°

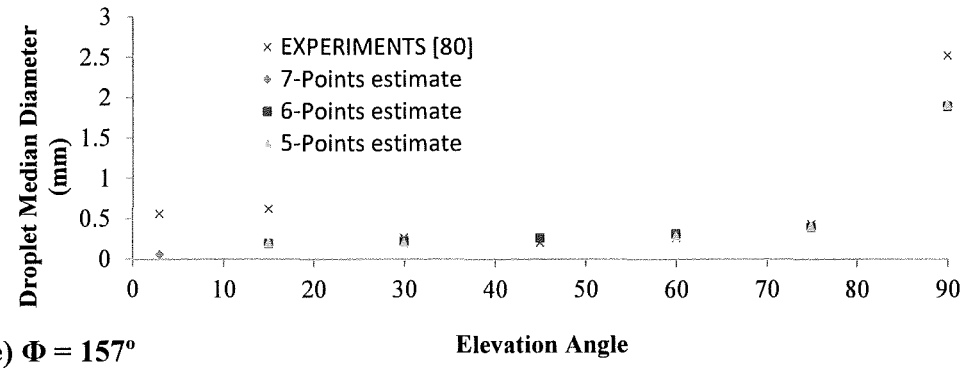

e) Φ = 157°

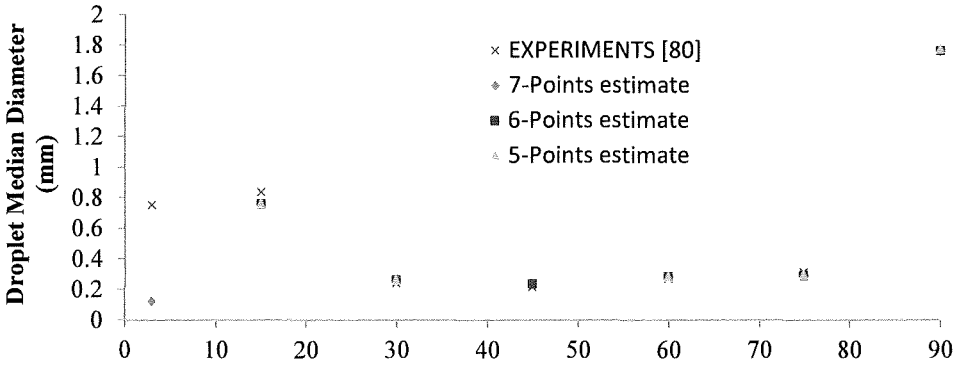

f) Φ = 180°

Figure 4-37: Investigating sensitivity of droplet median diameter estimations to the number of data points and comparison with experiments at different Azimuthal angles for pendant sprinkler at 5.2 bar

Neglecting the low density regions from semi-empirical calculation process had minor change in the evaluation of the median droplet diameter at the remaining elevation angles which are recognizable in the presented figures. The margin of changes remains within 1 percent.

4.8.2 Volume Flux

The volume flux appraisal at seven azimuthal angles is presented in Figure 4-38 a–g. In this figures evaluations obtained from the 7, 6 and 5 points based semi-empirical modeling are compared against experimental measurements at relevant azimuthal angles.

Similar to previous section, neglecting the low density volume fluxes out of semi-empirical calculation process did not bring about significant change in the evaluation of volume fluxes at the remaining elevation angles; hence they show an overlap in the figures demonstrated below and are not obvious as the results are presented in logarithmic scale. The margin of changes remains within 2 percent.

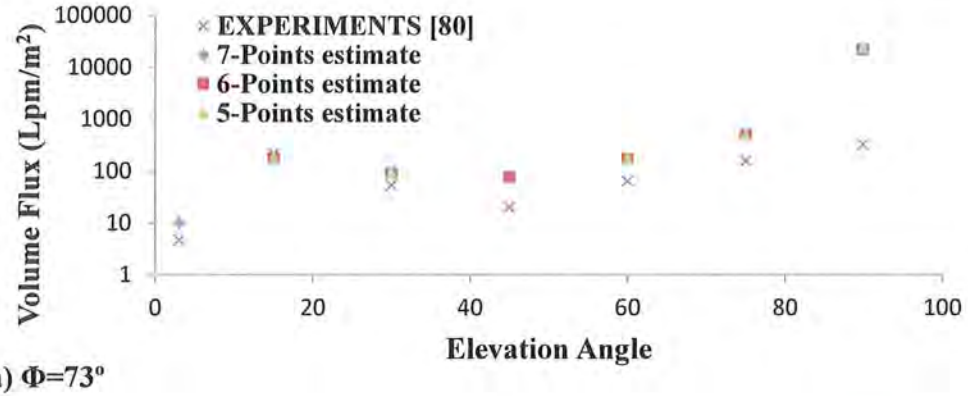

a) Φ=73°

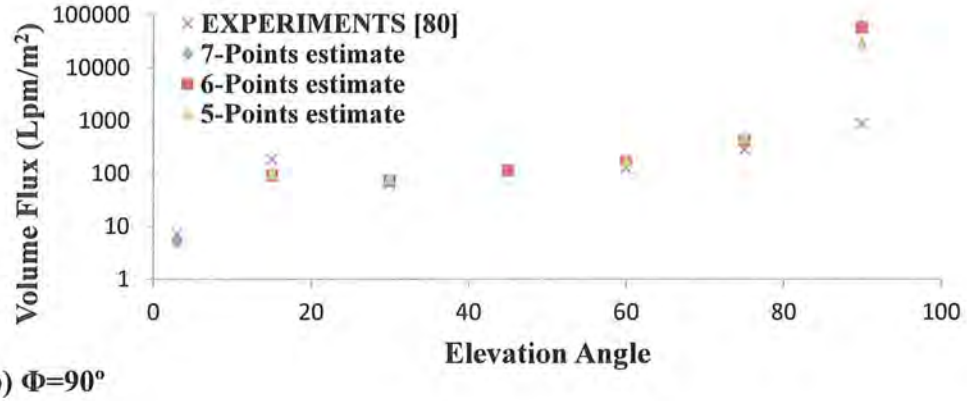

b) Φ=90°

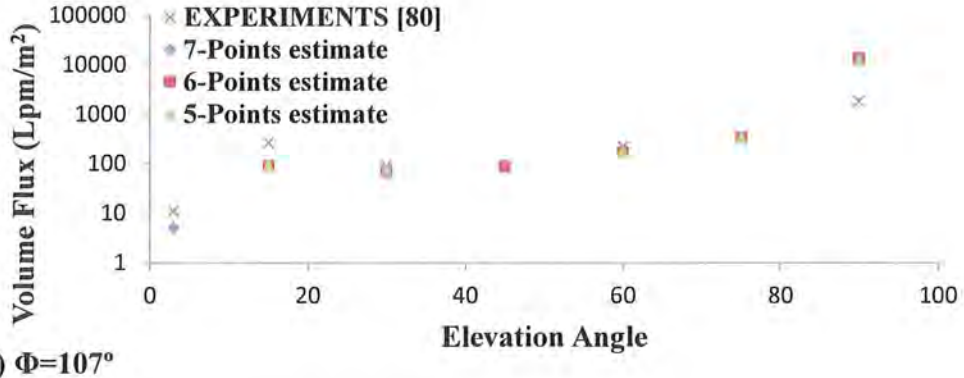

c) Φ=107°

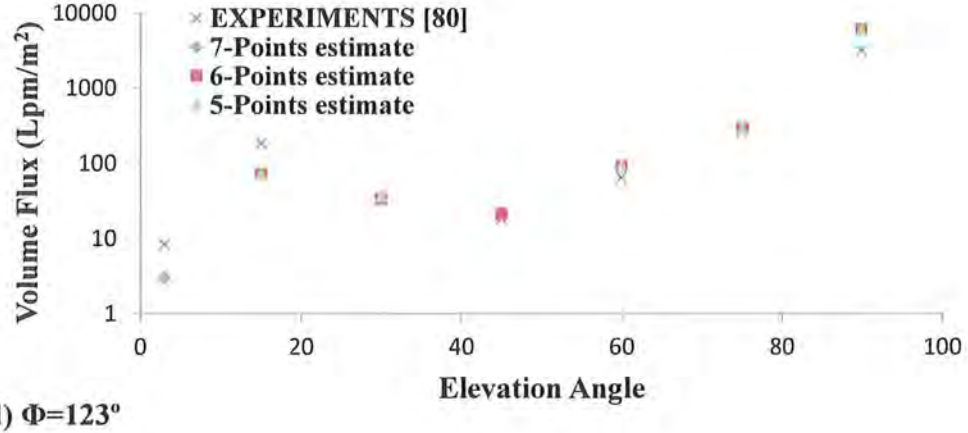

d) Φ=123°

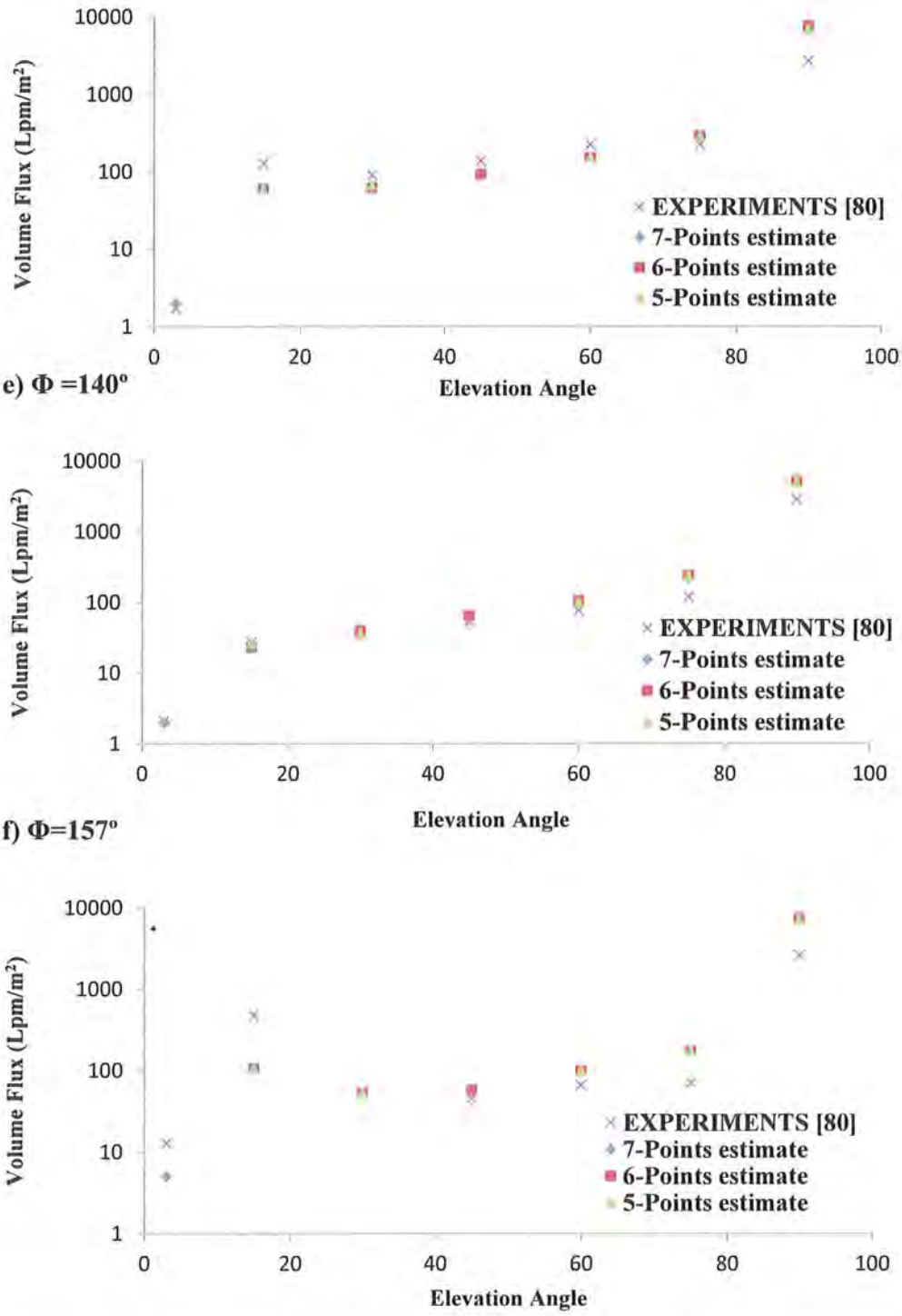

Figure 4-38: Investigating sensitivity of volume flux estimations to the number of data points and comparison with experiments at different Azimuthal angles for pendant sprinkler at 5.2 bar

As discussed before, the dominance of water flux occurs at segments corresponding to 15° and 90° elevation angles for the investigated pendant sprinkler. The maximum discrepancy is remains to the segment below the sprinkler, where the flow structure is still experimentally unresolved.

4.9 Uniform Distribution

To avoid the dependency of the semi-empirical modelling to the experimentally evaluated volume fractions, a uniform distribution assumption has been tested with developed methodologies in chapter three. In this scenario the volume fraction γ is taken to be the same for any studied elevation angle. This could be the first approach adopted when experimental data are not available for the volume fractions.

Two equally distributed spray calculations have been presented in this section. The number of studying point along $0° - 90°$ elevation angles were taken 7 ($\gamma = 1/7$) and 20 ($\gamma = 1/20$). Having γ less than *1/20* is numerically possible but results in physically meaningless sheet thicknesses and further resolution of the flow have been avoided.

Predicted characteristics (uniform distributions) of spray formed by pendant sprinkler at 3.5 and 5.2 bar are presented in Figure 4-39 and Figure 4-40, and the relevant predictions for upright sprinkler at 0.76 bar and 1.31 bar are given in Figure 4-41 and Figure 4-42, respectively. Method-4 has been preferred for doing theoretical calculation as it has shown higher overall performance in §4.7 & 4.8.

Considering the fact that no experimentally obtained volume fraction data been have been used in this section, relatively good predictions have been obtained for droplet size and velocity for both pendant and upright sprinklers using the uniform distribution. However care should be taken not to extrapolate this conclusion unless a wide range of sprinklers are tested experimentally and compared to the semi-empirical model for uniform distribution.

The spray volume flux predictions showed promising predictions for a uniform distribution with the semi-empirical approach in the following zones:

1- $15° \leq \theta \leq 90°$ for the pendant sprinkler
2- $15° \leq \theta \leq 75°$ and at the proximity of $\theta = 90°$.

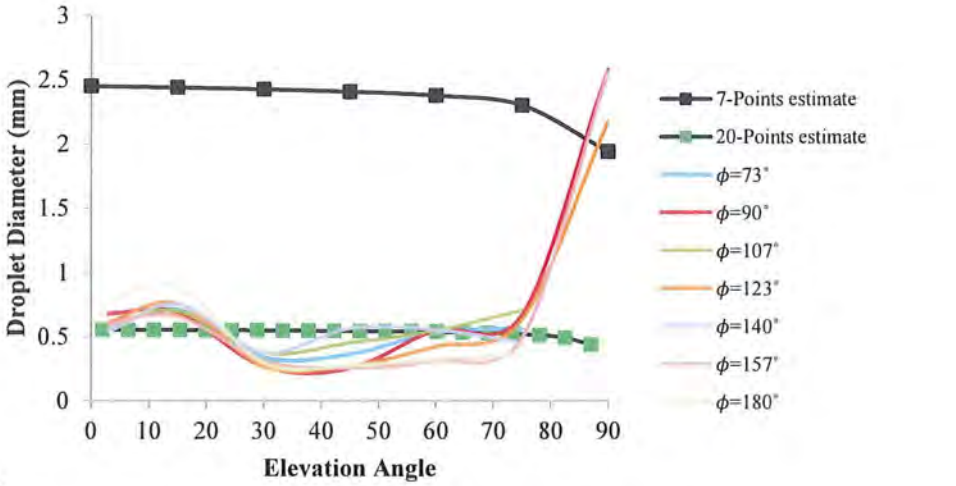

a)

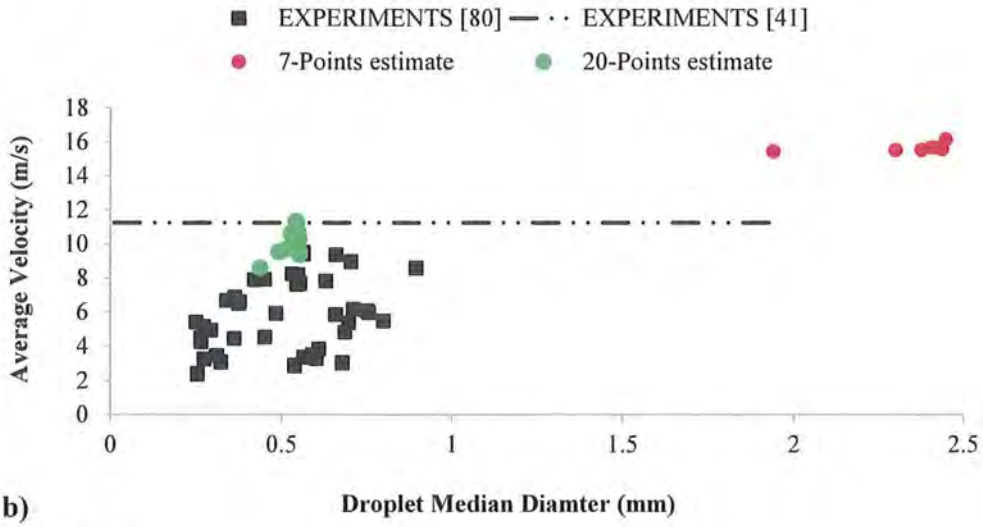

b)

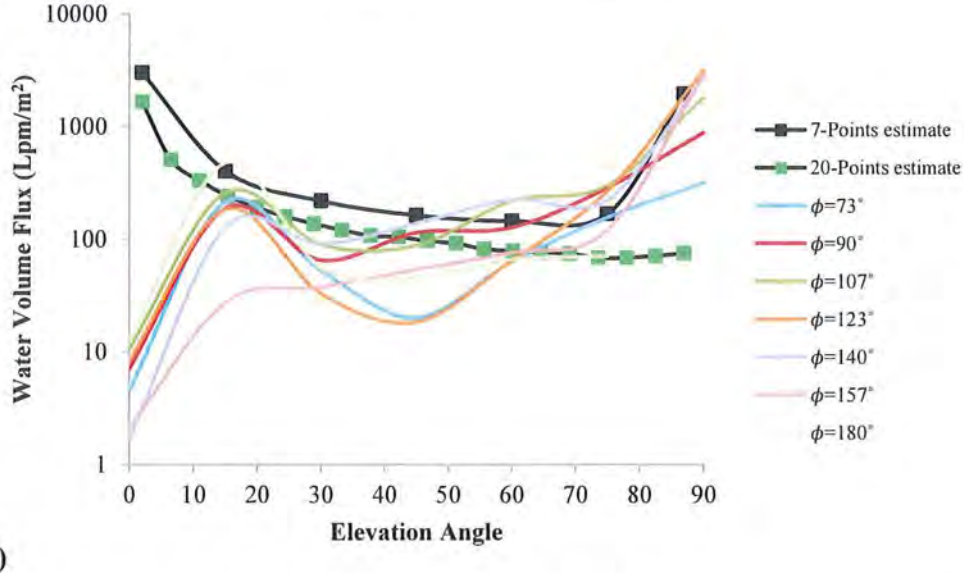

c)

Figure 4-39: Characteristics of pendant sprinkler at 3.5 bar a) Droplet Diameter b) velocity and c) volume flux

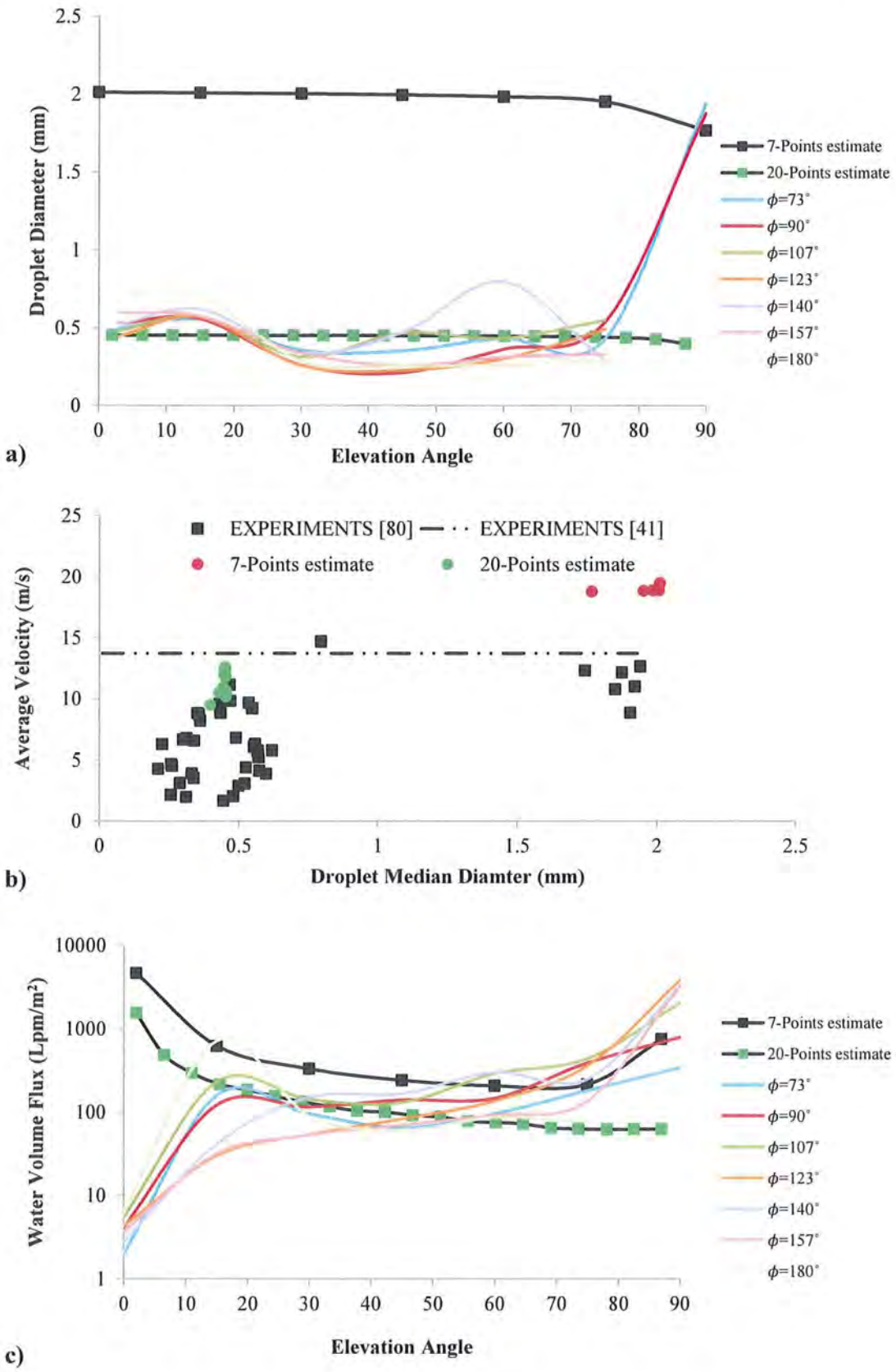

Figure 4-40: Characteristics of pendant sprinkler at 5.2 bar a) Droplet Diameter b) velocity and c) volume flux

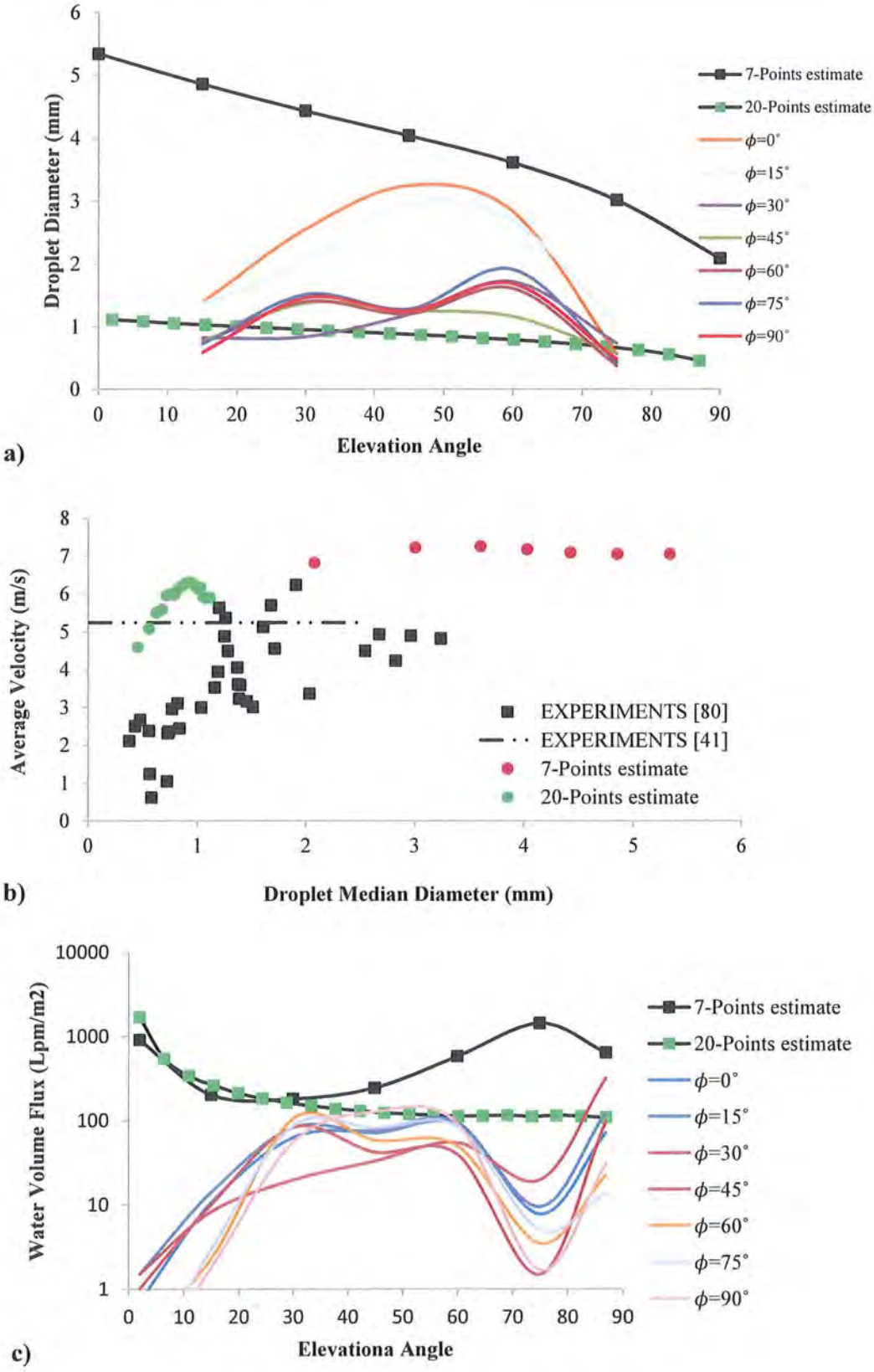

Figure 4-41: Characteristics of upright sprinkler at 0.76 bar a) Droplet Diameter b) velocity and c) volume flux

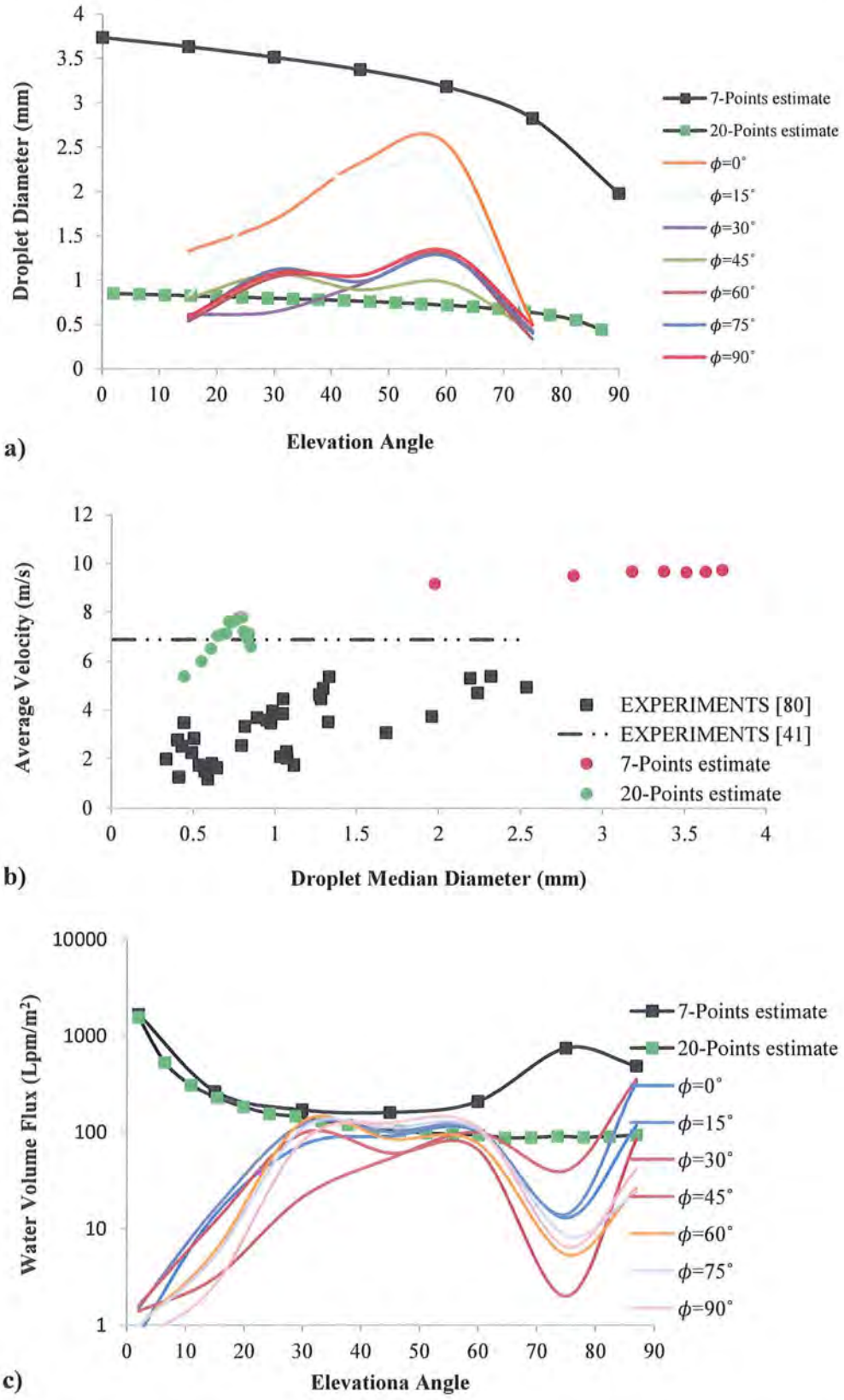

Figure 4-42: Characteristics of upright sprinkler at 1.31 bar a) Droplet Diameter b) velocity and c) volume flux

To close this section, deterministic analysis have been carried out and its overall spray predictions have been summarized for pendant sprinkler in, Table 4-9, and for upright sprinkler in, Table 4-10.

Table 4-9: Deterministic characteristics of the spray for the pendant sprinkler at 3.5bar and 5.2 bar

	3.5 bar			*5.2 bar*		
	d_d	u_d	$\dot{q}''$	d_d	u_d	$\dot{q}''$
Method-1	0.936	23.1	3994	0.813	27.6	3631
Method-2	1.084	14.4	2900	0.94	16.9	2542
Method-3	1.95	24.8	426	1.61	30.0	586
Method-4	2.38	15.4	819	1.99	18.8	951

Table 4-10: Deterministic characteristics of the spray for the upright sprinkler at 0.76 and 1.31 bar

	0.76 bar			*1.31 bar*		
	d_d	u_d	$\dot{q}''$	d_d	u_d	$\dot{q}''$
Method-1	1.51	11.33	4975	1.24	14.36	4043
Method-2	1.82	6.89	3676	1.48	8.74	312
Method-3	3.45	11.64	363	2.79	15.16	446
Method-4	3.91	7.10	600	3.30	9.27	507

The deterministic predictions are comparable with volumetric median droplet size of whole spray, while this is not available in the cited references and no clear conclusion could be drawn at this stage.

5 CONCLUSIONS AND FUTURE WORKS

5.1 Preamble

A comprehensive study of sprinkler sprays was carried out with emphasis on the initial spray characteristics (e.g. spatial distributions of drop size, drop velocity, mass flux). While fire suppression sprays control the fire through a number of mechanisms, including, cooling, blowing, oxygen depletion, radiation attenuation and wetting, the primarily suppression mechanism for fire sprinklers is wetting. Hence it is crucial to have accurate understanding of initial spray.

Water sprinkler has been extensively under interest due to the minimum protection they provide in residential applications and warehouses. As an overall overview the fire control and fire suppression sprinkler systems generation and development history are classified as the large drop sprinkler system to control high challenge storage fires, the Residential sprinkler system to maintain a survivable environment in residential areas, and the ESFR sprinkler system to suppress rather than control high challenge fires.

The effectiveness of the sprinkler spray at controlling a fire is governed by the spray characteristics. Large drops can penetrate a rising fire plume to reach the fire source and wet combustible material adjacent the burning commodity, whereas smaller drops will be entrained into the buoyant plum and carried away

from the fire. Furthermore, the evaporating smaller drops have a cooling effect on the hot gases, and in some cases will prevent additional fire sprinklers from activating. One of the main disadvantages of water sprinklers is the large quantity of water used. This can lead to extensive damage beyond that caused by the fire itself in some occasions.

It has been highlighted throughout the dissertation that detailed initial spray measurements revealed the strong relationship between the sprinkler configuration and geometry and the resulting spray pattern. In addition to this the spray formation in fire sprinklers is also affected by the operating pressure and ambient gas temperature. The performance of these suppression systems is primarily evaluated through very expensive full-scale spray dispersion tests and actual fire suppression tests. This is mainly due to challenges in developing comprehensive predictive models to estimate the spray characteristics based on the physics of atomization.

5.2 Original Contributions

The current dissertation targeted to build more theoretical basis for the described problem and achieved following contributions in that respect:

1- The BLM have been revised, and presented in new format to be incorporated with sprinkler applications.
2- The AFM have been introduced to estimate the film propagation over a flat disk.
3- A detailed sheet trajectory model has been implemented for sprinkler application to investigate the sheet radial thickness and velocity at different release angles and operational pressures. Inevitable change in the sheet characteristics has been observed as the release angle changes.
4- Three new deterministic models have been presented for prediction of the overall spray characteristics based on the physics observed in an impinging jet configuration (which is quite similar to the sprinklers).
5- The stochastic modeling has been applied to the presently developed models and one model from literature. This enables predicting a range of

values for the maximum and minimum values a parameter could take in spray conditions.

6- Droplet size, velocity and flux distribution are crucial in fire suppression studies. According to literature, the measured volume flux and droplet size distributions demonstrate strong directional dependence with azimuthal and elevation angles. In a move toward more realistic spray models, a Semi-empirical model has been developed using experimentally evaluated volume fractions and applied this to the four deterministic models. The developed semi-empirical model is capable of predicting the spatial distribution (at various local elevation and azimuthal angles) of the droplets volume median diameter, water volume flux and droplet average velocity in spherical coordinate system. This coordinate is consistent with the kinetics of the spray. This approach can implicitly mimic the combined effects of boss, arm and slits over the deflector.

7- A Non-dimensional analysis has been carried out for an impinging jet configuration. This is to evaluate the spray based on jet characteristics, geometrical specifications and ambient conditions. The accuracy of the developed dimensionless sheet breakup distance and dimensionless droplet diameter has been investigated for turbulent liquid jet impingement in the air, where the Weber numbers are in the range of 10^4-5×10^5 and geometrical ratio is larger than one. In general formulations derived in this research over-predicted the spray parameters, as the effect of viscosity has not been seen. The proposed correlations are powerful tools which reliably predict spray characteristics straightaway and serve as an additional method besides more sophisticated spray modeling approaches.

8- The developed methodologies can predict the near filed spray characteristics, originating from center of the deflector and do not require comprehensive. Only a few physically coherent parameters (K-factor, nozzle geometry, pressure and temperature) are required. Hence could be used as a reliable predictive tool to engineers and fire scientists.

5.3 Limitations and Assumptions

- Effect of initial perturbation in sprinklers is very different from the simplification made in driving the models.
- There are occasions in experiment where the vloume fraction is low but droplet sizes are large. In this methodology this characteritics could not been addressed.
- Bulk air movement has been neglected for near field spray evaluation. This may not have significant impact through atomization process, but will influence the spray characteristics, through the distance between initial formation locations and the measurement points. There are air movements arount sprinkler shifts away some droplets from spaces facing to slit flow toward spaces facing to tine flow. Hence volume flux is observable. (turbulence generated).
- Model gives promising predicitons for imping jets with Reynolds number of which the sheet falls in flappy regime.
- The photographic techniques include illuminating the drops using strobe lighting and pulsed lasers, and using still photographs and video cameras for image capture. Quantification of uncertainties in measurements has not been quantified.
- Droplet shedding from the edge of sheet has not been seen in this modeling. Predictions of droplet size distributions have been carried out based on ligament breakup.

5.4 Discussions and Conclusions

In the present study two physical sub-models have been used in order to improve the prediction accuracy of an existing model. The developed modeling approaches can quantify the near field sprinkler spray. The improvements in predicting spray characteristics have been presented and thoroughly discussed. The following conclusions can be drawn from the thesis:

Film Thickness and Velocity

The AFM didn't show significant superiority over BLM in predicting film thickness; however it contributes a lot in prediction of droplet velocities. Predictions obtained by the methods in which the AFM was incorporated (Method-2 and Method-4) showed enhanced velocity predications for both pendant and upright sprinklers.

Sheet Characteristics

Ambient temperature, sheet release angle and operating pressure found to have a significant effect on the rate of sheet propagation.

The streamwise speeds calculated from DTM are less than ILTD. The differences at different ambient gas temperature, sheet release angles and sprinkler operating pressure lies between 52%-69%, 59%-69%, and 63.8%-69%, respectively.

The sheet thickness decreased in downstream directions is owing to expansion and is in compliance with the requirements of conservation of mass. It is noteworthy that the trend of decrease in sheet thickness ratio from ILTD after $2r/D_i \cong 4$. Prior to this point the decline in streamwise speed lies less 5% of initial speed.

The sheet thicknesses calculated from DTM are larger than ILTD by the same ratios percentages as speeds, which complies with mass conservation law. These differences cascaded down and resulted in a significant change in predicting droplet size.

Sheet breakup distance

The dimensionless studies showed that the sheet breakup distance has a -1/3 power law relation with jet Weber number and -2/3 power law with density ratio. Weber number is affected by jet diameter and jet speed. Depending on the application, the dimensionless total growth of the wave could have been changed to tune the sheet breakup radial distance predictions from presented scaling law. The model follows the physical trend of jet flows with Weber number larger than 2000, since the sheet breakup distance decays as the jet turbulence is augmented.

Employing the more rigorous sheet trajectory model (DTM), improved the prediction of sheet break up distance.

Droplet size

The dimensionless formulation revealed that droplet diameter show a -1/3 power law relation with jet Weber number and -1/6 power law for density ratio. A decrease in ambient air density leads to larger median droplet diameters. An increase in jet speed, results in larger droplet median diameters. The droplet diameter has been predicted in the range mapped out by experiments.

Method-1 and Method-2 under predicted the droplet size, and Method-3 and Method-4 over-predicted this parameter. The sheet characteristics has more importance than the film characteristics.

Droplet Velocities

Droplet velocities have been predicted with very good degree of accuracy and the predictions of film has a great impact on this parameter. The available discrepancies could be mainly due to (i) longer theoretical droplet formation distance and (ii) neglecting the effects of air turbulence.

Water Volume Flux

The prediction of water volume flux has higher accuracy in pendant sprinkler compared to upright sprinkler. The pendant sprinklers have more similarity with impinging jet atomizers. The physics of spray formation in the studied upright sprinkler is quite different from the basis of developed methodology in current study. It has consisted of tilted tines, hence will affect the initiation and growth of perturbation over the sheet to a great pattern.

5.5 Suggestions and Recommendations for Future Work

Suggestions and recommendations for future developments of this work are proposed in the following.

- Fundamental numerical studies on flow around a flat plate over a broad range of mass flow rates, to study the formation of water bell and sheet and destruction mechanisms at different initial jet reynolds number. Beside this the effect of the deflector diameter size can be further investigated at

different geometrical ratios. This is due to the fact that the sprinkler configuration remains as the most influential property affecting characteristics like spatial volume flux.

- Extensive CFD studies to quantify the boundary layer development over sprinkler deflector at low, medium and high Reynolds number jet impigments, with/out presence of boss.
- Quantifying the effects of different tine/slit configuration in order to understand their effect on flow field splitting to tine and slit flows at a range of jet speeds. In addition to this the effects of tilted tines shall be investigated.
- More detailed ligament/droplet formation models should be developed, and incorporated to the rest of developed methodologies in the current dissertation.
- The detailed initial sprinkler spray could be integrated with CFD packages to investigated the interaction with fire plume and understand how would it resemble the performance of sprinklers.
- The effects of different distributions (spray volume flux) of different sprinklers on suppression capability. Hence the intereaction of fire plume to different droplet distributions can be studied.

REFERENCES:

[1] "Fire triangle," *Wikipeadia*. [Online]. Available: http://en.wikipedia.org/wiki/Fire_triangle. [Accessed: 24-Jan-2013].

[2] BS-EN:2-1992, "Classification of Fires." 1992.

[3] G. Grant, J. Brenton, and D. Drysdale, "Fire suppression by water sprays," *Progress in Energy and Combustion Science*, vol. 26, no. 2, pp. 79–130, Apr. 2000.

[4] International Chemical Safety Card-0635, "BROMOCHLORODIFLUOROMETHANE," *International Programme on Chemical Safety*, 2012. [Online]. Available: http://www.inchem.org/documents/icsc/icsc/eics0635.htm. [Accessed: 28-Jan-2013].

[5] International Chemical Safety Card-0837, "BROMOTRIFLUOROMETHANE," *International Programme on Chemical Safety*, 2012. [Online]. Available: http://www.inchem.org/documents/icsc/icsc/eics0837.htm. [Accessed: 28-Jan-2013].

[6] R. A. Hart, "Numerical Modelling of Tunnel Fires and Water Mist Suppression," The University of Nottingham, 2005.

[7] D. W. McCall, R. L. Alpert, J. G. Anderson, P. J. Dinennon, D. A. Dixon, R. E. Fernandez, R. H. Gormley, M. K. Ko, R. Pariser, A. R. Ravishankara, R. Rubenstein, G. M. Rusch, R. E. Tapscott, T. J. Wallington, D. J. Wuebbles, R. DeMarco, G. Sidney, J. Reed, and J. G. Wilson, "Fire Suppression Substitutes and Alternatives to Halon." U.S. Navy Applications. National Academy Press,, Washington, D.C., 1997.

[8] "The Montreal Protocol on Substances that Deplete the Ozone Layer," *United Nations Environment Program*, 2000. [Online]. Available: http://www.unep.org/ozone/Montreal-Protocol/Montreal-Protocol2000.shtml. [Accessed: 15-Jul-2012].

[9] BS 5306-4:2001, "Fire extinguishing installations and equipment on premises – Part 4: Specification for carbon dioxide systems," 2001.

[10] D. Drysdale, *An Introduction to Fire Dynamics*, 2nd Editio. Wiley, 1998.

[11] EPA-430-R-00-002, "Carbon Dioxide as a Fire Suppressant: Examining the Risks," *U.S. Environmental Protection Agency, Office of Air and Radiation, Stratospheric Proptection Division*, 2000. [Online]. Available: http://www.epa.gov/ozone/snap/fire/co2/co2report.pdf. [Accessed: 21-Dec-2012].

[12] "CO2 Fire Suppression Systems," *VFP Fire Systems*, 2013. [Online]. Available: http://www.vfpfire.com/systems-co2.php. [Accessed: 23-Jan-2013].

[13] BS-5306-6:1988, "Fire extinguishing installations and equipment on premises – Part 6: Foam Systems." British Standard Organisation, 1988.

[14] "Foam/Chemical Suppression," *VFP Fire Systems*, 2013. [Online]. Available: http://www.vfpfire.com/systems-foam.php. [Accessed: 23-Jan-213AD].

[15] "DuPont FM 200 Waterless Fire Suppression Systems," *DuPont*, 2012. [Online]. Available: http://www2.dupont.com/FE/en_US/products/FM200.html#.UP6smGeq090. [Accessed: 23-Jan-2013].

[16] "FM-200 Waterless Clean Agent," *Healeyfire*, 2013. [Online]. Available: http://www.healeyfire.com/index.php?option=com_content&view=article&id=56&Itemid=72. [Accessed: 23-Jan-2013].

[17] "FM 200 Fire Suppression Systems," *VFP Fire Systems*, 2013. [Online]. Available: http://www.vfpfire.com/systems-fm200.php. [Accessed: 23-Jan-2013].

[18] A. Jones and P. F. Nolan, "Discussions on the Use of Fine Water Sprays or Mists for Fire Suppression," *Journal of Loss Prevention in the Process Industries*, vol. 8, no. 1, pp. 17–22, Jan. 1995.

[19] G. G. Back III, C. L. Beyler, and R. Hansen, "A quasi-steady-state model for predicting " re suppression in spaces protected by water mist systems," *Fire Safety Journal*, vol. 35, pp. 327–362, 2000.

[20] R. G. Bill Jr, R. L. Hansen, and K. Richards, "Fine-Spray (Water Mist) Protection of Shipboard Engine Rooms," *Fire Safety Journal*, vol. 29, pp. 317–336, 1997.

[21] T. Log and P. C. Brookes, "'Water Mist' for Fire Protection of Historic Building and Museums," *Museum Management and Curatorship*, vol. 14, no. 3, pp. 283–298, 1995.

[22] Z. Liu, A. K. Kim, D. Carpenter, J. M. Kanabus-Kaminska, and P.-L. Yen, "Extinguishment of cooking oil fires by water mist fire suppression systems," *Fire Technology*, vol. 40, pp. 309–333, 2004.

[23] P. J. Disimile, J. R. Tucker, B. Croswell, and J. M. Davis, "The Transport of Water Sprays past Generic Clutter Elements found within Engine Nacelles," *Fire Safety Journal*, vol. 40, pp. 65–78, 2005.

[24] N. Ren and a. W. Marshall, "Characterizing the initial spray from large Weber number impinging jets," *International Journal of Multiphase Flow*, Aug. 2012.

[25] BS-ISO/TR-13387-7:1999, "Fire safety engineering – Part 7: Detection, activation and suppression," 1999.

[26] NFPA-750, "Standard on Water Mist Fire Protection Systems," Quincy, MA, USA, 2003.

[27] "Victaulic Vortex Fire Suppression System," *VFP Fire Systems*, 2013. [Online]. Available: http://www.vfpfire.com/systems-vortex.php. [Accessed: 23-Jan-2013].

[28] BS-5306-2:1990, "Fire Extinguishing Installations and Equipment on Premises – Part 2: Specification for Sprinkler Systems," 1990.

[29] BS-5306-8:2012, "Fire extinguishing installations and equipment on premises. Selection and positioning of portable fire extinguishers." British Standard Institution, 2012.

[30] BS-EN-12845:2004+A2:2009, "Fixed firefighting systems. Automatic sprinkler systems. Design, installation and maintenance." British Standard Institution, 2009.

[31] BS-9251:2005, "Sprinkler Systems for Residential and Domestic Occupancies," 2005.

[32] W. S. Beattie, "Evolution of the Fire Sprinkler," *The American Society of Safety Engineers*, 2010. [Online]. Available: http://waltbeattie.files.wordpress.com/2010/08/evolution-of-as-beattie.pdf. [Accessed: 13-Jul-2012].

[33] "How Fire Sprinklers Work," *Minnesota Department of Public Safety*, 2010. [Online]. Available: https://dps.mn.gov/divisions/sfm/programs-services/Documents/Sprinkler Applications/HowSprinklersWork.pdf. [Accessed: 28-Jan-2013].

[34] R. P. Fleming, "Quick Response Sprinklers: A Technical Analysis." National Fire Protection Research Fundation, Batterymarch Park, Quincy, MA 02269, 1986.

[35] W. D. Walton and E. K. Budnick, "Quick Response Sprinklres in Office Configurations: Fire Test Results.pdf." U.S. Department of Commerce, Gaithersburg, MD 20899 USA, 1988.

[36] S. Martorano, "Technical Article Automatic Sprinkler Thermal Sensitivity: Clarifying the Terms Fast Response and Quick Response." Vikingcorp, 2006.

[37] T.-S. Chan, "Measurements of Water Density and Drop Size Distributions of Selected ESFR Sprinklers," *Journal of Fire Protection Engineering*, vol. 6, no. 2, pp. 79–87, Jan. 1994.

[38] "ESFR-Early Suppression Fast Response Fire Sprinkler Systems," *VFP Fire Systems*, 2013. [Online]. Available: http://www.vfpfire.com/systems-esfr.php. [Accessed: 23-Jan-2013].

[39] "In-Rack FireSprinkler Systems," *VFP Fire Systems*, 2013. [Online]. Available: http://www.vfpfire.com/systems-in-rack.php. [Accessed: 23-Jan-2013].

[40] NFPA-13, "Standard for the Installation of Sprinkler Systems." National Fire Protection Research Assosiation, Quincy, MA, USA, 2013.

[41] D. T. Sheppard, "Spray Characteristics of Fire Sprinklers," North-western University, Evanston, IL, 2002.

[42] "Deluge Fire Sprinkler System," *VFP Fire Systems*, 2013. [Online]. Available: http://www.vfpfire.com/systems-deluge.php. [Accessed: 23-Jan-2013].

[43] "Quell Fire Sprinkler System," *VFP Fire Systems*, 2013. [Online]. Available: http://www.vfpfire.com/systems-quell.php. [Accessed: 23-Jan-2013].

[44] "Pre-action Fire Sprinkler System," *VFP Fire Systems*, 2013. [Online]. Available: http://www.vfpfire.com/systems-pre-action.php. [Accessed: 23-Jan-2013].

[45] "Wet Pipe Fire Sprinkler System," *VFP Fire Systems*, 2013. [Online]. Available: http://www.vfpfire.com/systems-wet-pipe.php. [Accessed: 23-Jan-2013].

[46] "Dry Pipe Fire Sprinkler System," *VFP Fire Systems*, 2013. [Online]. Available: http://www.vfpfire.com/systems-dry-pipe.php. [Accessed: 23-Jan-2013].

[47] A. H. Lefebvre, *Atomization and Sprays*. New York: Hemisphere Press, 1989.

[48] M. Lightfoot, "Fundamental Classification of Atomization Processes," *Atomization and Sprays*, vol. 19, no. 11, pp. 1065–1104, 2009.

[49] N. Chigier and R. D. Reitz, "Regimes of Jet Breakup and Breakup Mechanisms - Physical Aspects," *Progress in Astronautics and Aeronautics*, pp. 109–135, 1996.

[50] S. P. Lin and R. . Reitz, "Drop and Spray Formation from a Liquid Jet," *Annual Review of Fluid Mechanics*, vol. 30, pp. 85–105, 1998.

[51] J. C. Lasheras and E. J. Hopfinger, "Liquid Jet Instability and Atomization in a Coaxial Gas Stream," *Annual Review of Fluid Mechanics Rev Fluid Mech*, vol. 32, pp. 275–308, 2000.

[52] G. M. L. Faeth, "Atomization in Multiphase Flows: A Review," in *30th AIAA Fluid Dynamics Conference*, 1999.

[53] M. Birouk, T. Staebler, and B. J. Azzopardi, "An Experimental Study of Liquid Jets Interacting with Cross Airflows," *Particle & Particle Systems Characterization*, vol. 20, no. 1, pp. 39–47, 2003.

[54] P. K. Wu, K. A. Kirkendall, R. P. Fuller, and A. S. Nejad, "Breakup Processes of Liquid Jets in Subsonic Crossflows," *Journal of Propulsion and Power*, vol. 13, no. 1, pp. 64–73, 1997.

[55] A. BELLOFIORE, A. CAVALIERE, and R. RAGUCCI, "Air Density Effect on the Atomization of Liquid Jets in Crossflow," *Combustion Science and Technology*, vol. 179, no. 1–2, pp. 319–342, Jan. 2007.

[56] S. P. Lin and J. N. Chen, "Role Played by the Interfacial Shear in the Instability Mechanism of a Viscous Liquid Jet Surrounded by a Viscous Gas in a Pipe," *Journal of Fluid Mechanics*, vol. 376, pp. 37–51, 1998.

[57] J. Shen and X. Li, "Instability of an Annular Viscous Liquid Jet," *Acta Mechanica*, vol. 114, no. 1–4, pp. 167–183, 1996.

[58] H. Fu, X. Li, L. A. Prociw, and T. C. J. Hu, "Experimental Investigation on the Breakup of Annular Liquid Sheets in Two Co-Flowing Airstreams.," in *1st International Energy Conversion Engineering Conference*, p. AIAA 2003–5944.

[59] L. A. Jurman and M. J. Mccready, "Study of Waves on Thin Liquid-Films Sheared by Turbulent Gas-Flows," *Physics of Fluids A-Fluid Dynamics*, vol. 1, no. 3, pp. 522–536, 1989.

[60] R. D. Reitz and F. V. Bracco, "Mechanism of Atomization of a Liquid Jet," *Physics of Fluids*, vol. 25, pp. 1730–1742, 1982.

[61] J. Shen and X. Li, "Instability of an Annular Viscous Liquid Jet," *Acta Mechanica*, vol. 114, no. 1–4, pp. 167–183, 1996.

[62] H. Fu, X. Li, L. A. Prociw, and T. C. J. Hu, "Experimental Investigation on the Breakup of Annular Liquid Sheets in Two Co-Flowing Airstreams.," in *1st International Energy Conversion Engineering Conference*, p. AIAA 2003–5944.

[63] M. Adzic, I. S. Carvalho, and M. V. Heitoyr, "Visualization of the Disintegration of an Annular Liquid Sheet in a Coaxial Airblast Injector at Low Atomising Air Velocities," *Optical Diagnostics in Engineering*, vol. 5, no. 1, pp. 27–38, 2001.

[64] C. Clanet and E. Villermaux, "Life of a smooth liquid sheet," *Journal of Fluid Mechanics*, vol. 462, pp. 307–340, Aug. 2002.

[65] N. Chigier, "Breakup of Liquid Sheets and Jets," in *30th AIAA Fluid Dynamics Conference*, pp. AIAA–1999–3640.

[66] Y. Liao, A. T. Sakman, S. M. Jeng, and M. A. Benjamin, "A Comprehensive Model to Predict Simplex Atomizer Performance," *Journal of Engineering for Gas Turbines and Power*, vol. 121, no. 2, pp. 285–294, 1999.

[67] W. W. Hagerty and J. F. Shea, "A Study of the Stability of Plane Fluid Sheets," *Journal of Applied Mechanics*, vol. 22, no. 4, pp. 509–514, 1955.

[68] R. P. Fraser, P. Eisenklam, N. Dombrowski, and D. Hasson, "Drop Formation from Rapidly Moving Liquid Sheets," *AIChE Journal*, vol. 8, no. 5, pp. 672–680, Nov. 1962.

[69] T. Okawa, A. Kotani, and I. Kataoka, "Experiments for Liquid Phase Mass Transfer Rate in Annular Regime for a Small Vertical Tube," *International Journal of Heat and Mass Transfer*, vol. 48, pp. 585–598, 2005.

[70] F. Savarat, "Memoire sur le choc de deux veines liquides animees de mouvements directement opposes," *Ann. de Chim.*, vol. 55, pp. 257–310, 1833.

[71] F. Savarat, "Memoire sur la constitution des veines liquids lancees par des orifices circularizes en mince paroi," *Ann. de Chim.*, vol. 53, pp. 337–386, 1833.

[72] F. Savarat, "Memoire sur le choc d'une veine liquide lancee contre un plan circulaire," *Ann. de Chim.*, vol. 54, pp. 56–87, 1833.

[73] F. Savarat, "Suite de Memoire sur le choc d'une veine liqide lancee contre un plan circulaire," *Ann. de Chim.*, vol. 54, pp. 113–145, 1833.

[74] L. Rayleigh, "On the Instability of Jets," *Proceedings of the London Mathematical Society*, no. 1–10, pp. 4–13, 1878.

[75] C. Clanet, "Dynamics and Stability of Water Bells," *Journal of Fluid Mechanics*, vol. 430, pp. 111–147, 2001.

[76] N. Ren, "Advances in Characterizing Fire Sprinkler Sprays," University of Maryland, 2010.

[77] A. W. Marshall and M. Di Marzo, "Modelling Aspects of Sprinkler Spray Dynamics in Fires," *Process Safety and Environmental Protection*, vol. 82, no. March, pp. 97–104, 2004.

[78] N. Dombrowski and W. R. Johns, "The Aerodynamic Instability and Disintegration of Viscous Liquid Sheets," *Chemical Engineering Science*, vol. 18, no. 7, pp. 203–214, Jul. 1963.

[79] J. F. Widmann, D. T. Sheppard, and R. M. Lueptow, "Non-Intrusive Measurements in Fire Sprinkler Sprays," *Fire Technology*, vol. 37, pp. 297–315, 2001.

[80] X. Zhou, S. P. D'Aniello, and H.-Z. Yu, "Spray Pattern Measurements of Selected Fire Sprinklers," in *InterFLAM*, 2010, pp. 177–188.

[81] D. T. Sheppard, P. D. Gandhi, and R. M. Lueptow, "Understanding Sprinkler Spray: Trajectory Analysis," in *Fifteenth Meeting of the UJNR Panel on Fire Research and Safety*.

[82] N. Ren, H. R. Baum, and A. W. Marshall, "A Comprehensive Methodology for Characterizing Sprinkler Sprays," *Proceedings of the Combustion Institute*, vol. 33, no. 2, pp. 2547–2554, Jan. 2011.

[83] A. D. Putorti Jr., "Simultaneous Measurements of Drop Size and Velocity in Large-Scale Sprinkler Flows Using Particle Tracking and Laser-Induced Fluorescence," National Institute of Standards and Technology, Gaithersburg, MD 20899-8661, 2004.

[84] C. Yao and A. S. Kalelkar, "Effect of Drop Size on Sprinkler Performance," *Fire Technology*, vol. 6, no. 4, pp. 254–268, 1970.

[85] P. H. Dundas, "Optimization of Sprinkler Fire Protection The Scaling of Sprinkler Discharge: Prediction of Drop Size." Factory Mutual Research Corporation, Norwood, MA, USA, 1974.

[86] M. Pilch and C. A. Erdman, "Use of Breakup Time Data and Velocity History Data to Predict the Maximum Size of Stable Fragments for Acceleration-Induced Breakup of a Liquid Drop," *International Journal of Multiphase Flow*, vol. 13, no. 6, pp. 741–757, Nov. 1987.

[87] G. Heskestad, "Proposal for Studying Interaction of Water Sprays with Plume in Sprinkler Optimization Program: Memorandum to C. Yao." 1972.

[88] J. F. Widmann, "Characterization of a Residential Fire Sprinkler Using Phase Doppler Interferometry." National Institute of Standards and Technology, Gaithersburg, MD 20899 USA, 2000.

[89] N. Ren, "Analysis of the Initial Spray from Canonical Fire Suppression Nozzles," University of Maryland, 2007.

[90] N. Ren, a. Blum, C. Do, and a. W. Marshall, "Atomization and Dispersion Measurements in Fire Sprinkler Sprays," *Atomization and Sprays*, vol. 19, no. 12, pp. 1125–1136, 2009.

[91] J. C. P. Huang, "The Break-up of Axisymmetric Liquid Sheets," *Journal of Fluid Mechanics*, vol. 43, no. 2, pp. 305–319, 1970.

[92] A. F. Blum, "Discharge Characteristics of Canonical Sprinkler Spray," University of Maryland, College Park, 2007.

[93] J. F. Widmann, "Phase Doppler Interferometry Measurements in Water Sprays Produced by Residential Fire Sprinklers," *Fire Safety Journal*, vol. 36, no. 6, pp. 545–567, Sep. 2001.

[94] P. D. Gandhi and D. Steppan, "Using PDPA in Evaluation of Sprinklers," in *Fire Suppression and Detection Research Application Symposium, Research and Practice: Bridging the Gap*, 1999, pp. 65–78.

[95] X. Zhou and H.-Z. Yu, "Experimental investigation of spray formation as affected by sprinkler geometry," *Fire Safety Journal*, vol. 46, no. 3, pp. 140–150, Apr. 2011.

[96] H. Yu, "Investigation Of Spray Patterns Of Selected Sprinklers With The Fmrc Drop Size Measuring System," *Fire Safety Science*, vol. 1, pp. 1165–1176, 1986.

[97] S. J. Walmsley and A. J. Yule, "A Study of the Spray Produced by Fire Suppression Sprinkler Systems," in *8th International conference on liquid atomization and spray systems*, 2000.

[98] C. Presser, G. Papadopoulos, and J. F. Widmann, "PIV measurements of water mist transport in a homogeneous turbulent flow past an obstacle," *Fire Safety Journal*, vol. 41, no. 8, pp. 580–604, Nov. 2006.

[99] N. Ren, a. Blum, Y. Zheng, C. Do, and a. Marshall, "Quantifying the Initial Spray from Fire Sprinklers," *Fire Safety Science*, vol. 9, pp. 503–514, 2008.

[100] C. T. Do, "Stream-Wise Discharge Characteristics of Pendant Sprinkler Sprays," University of Maryland, College Park, 2009.

[101] G. Taylor, "Formation of Thin Flat Sheets of Water," *Proceedings of Royal Society. A*, vol. 259, pp. 1–17, 1960.

[102] E. Villermaux and C. Clanet, "Life of a flapping liquid sheet," *Journal of Fluid Mechanics*, vol. 462, pp. 341–363, Aug. 2002.

[103] TFP318, "Model ESFR-1 Early Suppression , Fast Response Pendent Sprinklers 14.0 K-Factor," *Tyco Fire Suppression and Building Products*, 2011. [Online]. Available: http://www.wormald.com.au/__data/assets/pdf_file/0003/313851/TFP318_03_2011.pdf. [Accessed: 28-Jan-2013].

[104] TF-2008009, "Storage Fire Protection Sprinklers." Tyco International Services GmbH, Lansdale, PA 19446 USA, 2008.

[105] R. L. Alpert, "Numerical Modeling of the Interaction between Automatic Sprinkler Sprays and Fire Plumes," *Fire Safety Journal*, vol. 9, pp. 157–163, 1985.

[106] R. G. Bill, "Numerical Simulation of Actual Delivered Density (ADD) Measurements," *Fire Safety Journal*, vol. 20, pp. 227–240, 1993.

[107] S. Nam and R. G. J. Bill, "Calculation of Actual Delivered Density using PHOENICS with GENTRA." Factory Mutual Research Corporation, Norwood, MA, USA, 1992.

[108] S. Nam, "Numerical Simulation of Actual Delivered Density of Sprinkler Spray Through Fire Plumes," *Atomization and Sprays*, vol. 4, pp. 385–404, 1994.

[109] S. Nam, "Development of a Computational Model Simulating the Interaction Between a Fire Plume and a Sprinkler Spray," *Fire Safety Journal*, vol. 26, pp. 1–33, 1996.

[110] S. Nam, "Numerical simulation of the penetration capability of sprinkler sprays," *Fire Safety Journal*, vol. 32, no. 4, pp. 307–329, Jun. 1999.

[111] K. McGrattan, A. Hamins, and G. P. Forney, "Modeling of sprinkler, vent and draft curtain interaction," Gaithersburg, MD 20899 USA.

[112] H. Jasak, H. G. Weller, and N. Nordin, "In-Cylinder CFD Simulation Using a C ++ Object-Oriented Toolkit," *SAE International Technical Papers*, vol. 2004–01–01, 2004.

[113] I. D. Chang and P. E. Russell, "Stability of a Liquid Layer Adjacent to a High-Speed Gas Stream," *The Physics of Fluids*, vol. 8, pp. 1018–1026, 1965.

[114] Z. W. Lian and S. P. Lin, "Breakup of a Liquid Jet in a Swirling Gas," *Physics of Fluids A 2: Fluid Dynamics*, vol. 2, no. 12, p. 2134, 1990.

[115] Y. Liao, S. M. Jeng, M. a. Jog, and M. a. Benjamin, "Advanced Sub-Model for Airblast Atomizers," *Journal of Propulsion and Power*, vol. 17, no. 2, pp. 411–417, Mar. 2001.

[116] E. J. Watson, "The Radial Spread of a Liquid Jet Over a Horizontal Plane," *Journal of Fluid Mechanics*, vol. 20, no. 03, pp. 481–499, Mar. 1964.

[117] E. A. Ibrahim and A. J. Przekwas, "Impinging Jets Atomization," *Physics of Fluids A 3*, p. 2981, 1991.

[118] C.-P. Mao, S. G. Chuech, and A. J. Przekwas, "An Analysis of Pressure Swirl and Pure Airblast Atomization," in *35th ASME International Gas Turbine and Aeroengine Congress and Exposition*, 1990, p. 9.

[119] N. K. Rizk and H. C. Mongia, "Model for Airblast Atomization," *Journal of Propulsion*, vol. 7, no. 3, pp. 305–311, 1991.

[120] J. H. Hilbing and S. D. Heister, "Droplet Size Control in Liquid Jet Breakup," *Physics of Fluids*, vol. 8, pp. 1574–1581, 1996.

[121] P. Y. Liang and R. J. Ungewittert, "Modeling of Atomization and Secondary Breakup from First Principles," *Progress in Astronautics and Aeronautics*, vol. 171, pp. 481–505, 1996.

[122] Y.-S. Chen, H.-M. Shang, C.-P. Chen, and T.-S. Wang, "General Numerical Model for Liquid Jet Atomization Applications," *Journal of Propulsion and Power*, vol. 14, no. 4, pp. 581–584, Jul. 1998.

[123] D. Wu, "Atomization Model Development for Fire Suppression Devices," University of Maryland, 2005.

[124] D. Wu, D. Guillemin, and A. W. Marshall, "A modeling basis for predicting the initial sprinkler spray," *Fire Safety Journal*, vol. 42, no. 4, pp. 283–294, Jun. 2007.

[125] A. W. Marshall, "Unraveling Fire Suppression Sprays," in *Proceedings of the Ninth International Symposium, IAFSS*, 2011.

[126] S. Gumkowski, "Modeling and Experimental Investigation of the Hydraulic Jump in Liquid Film Formed by an Impinging Two-Phase Air-Water Jet," *Heat Transfer Engineering*, vol. 29, no. 9, pp. 816–821, Sep. 2008.

[127] A. D. Young, *Boundary Layers*. BSP Proffional Books, 1989, pp. 32–36.

[128] F. M. White, *Viscous Fluid Flow*, 2nd ed. New York: Mc-Graw Hill, Inc., 1998.

[129] E. a Ibrahim and B. E. Outland, "A non-linear model for impinging jets atomization," *Proceedings of the Institution of Mechanical Engineers, Part C: Journal of Mechanical Engineering Science*, vol. 222, no. 2, pp. 213–224, Feb. 2008.

[130] T. M. Spielbauer and C. K. Aidun, "Mechanisms of Liquid Sheet Breakup and the Resulting Drop Size Distributioms; Part 1: types of spray nozzles and mechanisms of sheet disintegration," *Tappi Journal*, vol. 75, no. 2, pp. 136–142, 1992.

[131] T. M. Spielbauer and C. K. Aidun, "Mechanisms of Liquid Sheet Breakup and the Resulting Drop Size Distributioms; Part 2: strands breakup and experimental observations," *Tappi Journal*, vol. 75, no. 3, pp. 195–200, 1992.

[132] S. G. Chuech, "Numerical simulation of nonswirling and swirling annular liquid jets," *AIAA Journal*, vol. 31, no. 6, pp. 1022–1027, Jun. 1993.

[133] E. A. Ibrahim and T. R. McKinney, "Injection characteristics of non-swirling and swirling annular liquid sheets," *Proceedings of the Institution of Mechanical Engineers, Part C: Journal of Mechanical Engineering Science*, vol. 220, no. 2, pp. 203–214, Feb. 2006.

[134] S. G. Chuech, "Numerical Simulation of Nonswirling and Swirling Annular Liquid Jets.," *30th Aerospace Science Meeting, Reno, NV, AIAA paper 92-0464*, 1992. .

[135] Y. Liao, S. M. Jeng, M. A. Jog, and M. A. Benjamin, "Advanced Sub-model for Airblast Atomizers," *JOURNAL OF PROPULSION AND POWER*, vol. 17, no. 2, pp. 411 – 417, 2001.

[136] S. P. Lin and W. Y. Jiang, "Absolute and convective instability of a radially expanding liquid sheet," *Physics of Fluids*, vol. 15, no. 6, pp. 1745–1754, 2003.

[137] J. M. Prahl and B. Wendt, "Discharge Distribution Performance for an Axisymmetric Model of a Fire Sprinkler Head," *Fire Safety Journal*, vol. 14, no. 1–2, pp. 101–111, Jul. 1988.

[138] Weber Z., "Zum zerfall eines flussigkeitstrahles (on the disruption of liquid jets)," *Zeitschrift für Angewandte Mathematik und Mechanik*, vol. 11, pp. 136–54, 1931.

[139] R. P. Fraser, P. Eisenklam, N. Dombrowski, and D. Hasson, "Drop Formation from Rapidly Moving Liquid Sheets," *AIChE Journal*, vol. 8, no. 5, pp. 672–680, Nov. 1962.

[140] H.-F. Liu, X. Gong, W.-F. Li, F.-C. Wang, and Z.-H. Yu, "Prediction of droplet size distribution in sprays of prefilming air-blast atomizers," *Chemical Engineering Science*, vol. 61, no. 6, pp. 1741–1747, Mar. 2006.

[141] T. Boeck, J. Li, E. López-Pagés, P. Yecko, and S. Zaleski, "Ligament formation in sheared liquid–gas layers," *Theoretical and Computational Fluid Dynamics*, vol. 21, no. 1, pp. 59–76, Oct. 2006.

[142] K. Thooyamani and D. Norum, "Equations Describing Sprinkler Droplet Velocity," *Journal of Irrigation and Drainage Engineering*, vol. 115, no. 2, pp. 156–165, 1989.

[143] V. Novozhilov, D. J. E. Harvie, J. H. Kent, V. B. Apte, and D. Pearson, "A Computational Fluid Dynamics Study of Wood Fire Extinguishment by Water Sprinkler," *Fire Safety Journal*, vol. 29, pp. 259–282, 1997.

[144] K. B. McGrattan, H. R. Baum, and R. G. Rehm, "Large eddy simulations of smoke movement," *Fire Safety Journal*, vol. 30, no. 2, pp. 161–178, Mar. 1998.

[145] G. Marsaglia and W. W. Tsang, "A Simple Method for Generating Gamma Variables," *ACM Transactions on Mathematical Software*, vol. 26, no. 3, pp. 363–372, Sep. 2000.

[146] M. Olesen, "Prediction of drop-size distributions based on ligament breakup," Queen's University at Kingston, Kingston, Ontario, Canada, 1997.

APPENDICES:

Appendix A: Derivation of BLM

This sections normalization of the sheet thickness in region (iii) of §3.2.1

$$h_i = C_2 \left(\frac{\nu_f}{Q}\right)^{\frac{1}{4}} \frac{r_i^{\frac{9}{4}} + l^{\frac{9}{4}}}{r_i} \tag{A.1}$$

Where $C_2 = 0.0211$, and knowing that

$$l = C_3\, a\, (Q/\nu_f a)^{\frac{1}{9}} \tag{A.2}$$

where $C_3 = 4.126$. A.2 could be summarized in following form:

$$l = C_3 \frac{D_0}{2} \left(\frac{\frac{\pi}{4} D_0^2 U_0}{\nu_f \frac{D_0}{2}}\right)^{1/9} = C_3 \left(\frac{\pi}{2}\right)^{1/9} \frac{D_0}{2} \left(\frac{D_0 U_0}{\nu_f}\right)^{1/9} \tag{A.3}$$

Substituting Q in A.1 gives

$$h_i = C_2 \times \left(\frac{\nu_f}{\frac{\pi}{4} D_0^2 U_0}\right)^{1/4} \frac{r_i^{9/4} + l^{9/4}}{r_i}$$

$$= C_2 \times \left(\frac{4}{\pi}\right)^{1/4} \left(\frac{\nu_f}{D_0 U_0}\right)^{1/4} \left(\frac{1}{D_0}\right)^{1/4} \frac{r_i^{9/4} + l^{9/4}}{r_i} \tag{A.4}$$

The A.4 could be rearranged by introducing $C_4 = C_2 \times (4/\pi)^{1/4}$ and $Re_0 = D_0 U_0/\nu_f$

$$h_i = C_4 Re_0^{-1/4} D_0^{-1/4} \left[\frac{r_i^{9/4} + \left(C_3 \left(\frac{\pi}{2}\right)^{\frac{1}{9}} \frac{1}{2}\right)^{9/4} D_0^{9/4} Re_0^{1/4}}{r_i}\right] \tag{A.5}$$

Replacing $C_5 = \left(C_3 \left(\frac{\pi}{2}\right)^{\frac{1}{9}} \frac{1}{2}\right)^{9/4}$, A.5 would be further simplified to

$$h_i = C_4 Re_0^{-1/4} D_0^{-1/4} r_i^{5/4} + \frac{2 C_4 C_5 D_0^2}{D_i} \tag{A.6}$$

The normalizing then be identified

$$\frac{h_i}{\delta_0} = \frac{[A.6]}{D_0^2/4D_i} = 8 \times C_4 \times C_5 + \left[C_4\, Re_0^{-1/4}\, D_0{}^{-1/4}\, (D_i/2)^{5/4}\right] / \frac{D_0^2}{4D_i}$$

$$\frac{h_i}{\delta_0} = \tilde{\delta} = 8C_4C_5 + 4\, C_4\, (1/2)^{5/4}\, Re_0^{-1/4}\, D_i^{9/4}\, D_0^{-9/4} \qquad (A.7)$$

The A.7 could be expressed as A.8, by introducing $X \equiv D_i/D_0$ and $C_6 = 4\, C_4\, (1/2)^{5/4}$,

$$\tilde{\delta} = 8C_4C_5 + C_6\, Re_0^{-1/4}\, X^{9/4} \qquad (A.8)$$

Where C_4=0.0224, C_5=5.71 and C_6=0.0377.

$$\tilde{\delta} = 1.02327 + 0.03767\, Re_0^{-1/4}\, X^{9/4} \qquad (A.9)$$

Appendix B: Definition in Stochastic Analysis

Definitions

Mean:

$$\bar{x} = \frac{1}{N}\sum_{i=1}^{N} x_i$$

$$s = \sqrt{\frac{N\sum_{i=1}^{N} x_i^{\,2} - (\sum_{i=1}^{N} x_i)^2}{N\,(N-1)}}$$

Gaussian Normal Distribution

Many measurements tend to have probability distributions close to the curve of the normal distribution. In Sprinkler application bulk liquid disintegrates into ligaments which breakups into drops. In the absence of further information, one might assume that the distribution of ligament diameters is similar to the normal distribution. Thus, the size distribution can be modeled with the Gaussian normal distribution.

The curve of a normal distribution for ligaments is centered at the mean value $\bar{d}$ and has the standard derivation σ. These two parameters determine the shape and location of the normal probability density function, which has the symmetric "bell" shape. The function of the normal distribution is

$$f(x) = \frac{1}{\sigma\sqrt{2\pi}}\, exp\left(-\frac{(x-\bar{x})^2}{2\sigma^2}\right) \quad -\infty < x < \infty \qquad (B.1)$$

Gamma Distribution

As an alternative to the normal distribution, one can assume that the distribution of characteristic sizes could be modeled by using the gamma function. The gamma distribution family, presented in *(B.2),* is based on two parameters. The

chi-square and exponential distributions, which are special cases of the gamma distribution, are one-parameter distributions that fix one of the two gamma parameters.

$$f(x) = \frac{1}{\Gamma(\alpha)\,\beta^{\alpha}}\, x^{\alpha-1} \exp\left(-\frac{x}{\beta}\right) \quad x > 0 \qquad (B.2)$$

Where α and β are parameters that determine the specific shape of the curve and are called shape parameter and scale parameter, respectively. The parameters must be set positive [145]. When, $\alpha = 1$, the gamma density reduces to the exponential distribution. This option must be excluded, since an exponential distribution of characteristic sizes is physically not reasonable [146]. When, $\beta = 2$, the gamma density reduces to the exponential distribution.

The function $\Gamma(\alpha)$ is defined as

$$\Gamma(\alpha) = \int_0^{\infty} x^{\alpha-1}\, exp(-x)\; dx \;=\; (\alpha - 1)\,\Gamma(\alpha) \;=\; (\alpha - 1)! \qquad (B.3)$$

Chi-square Distribution

If v independent variables x_i are each normally distributed with mean μ_i and variance σ_i^2, then the quantity known as Chi-square is defined by

$$\chi^2 \equiv \frac{(x_1 - \mu_1)^2}{\sigma_1^2} + \frac{(x_2 - \mu_2)^2}{\sigma_2^2} + \cdots + \frac{(x_v - \mu_v)^2}{\sigma_v^2} = \sum_{i=1}^{v} \frac{(x_i - \mu_i)^2}{\sigma_i^2} \qquad (B.4)$$

Note that ideally, given the random fluctuations of the values of x_I about their mean values μ_I, each term in the sum will be of order unity. Hence, if we have chosen the μ_i and the σ_i correctly, we may expect that a calculated value of χ^2 will approximately be equal to v.

The quantity χ^2 defined in equation has the probability density function given by

$$f(\chi^2) = \frac{2^{-v/2}}{\Gamma\left(\frac{v}{2}\right)} (\chi^2)^{(v/2)-1} \exp(-\chi^2/2) \qquad (B.5)$$

This is known as the χ^2-distribution with v degree of freedom. V is a positive integer. The χ^2 ranges only over positive values: $0 < \chi^2 < \infty$. Therefore the chi-square distribution prevents the occurrence of negative ligaments at high fluctuation densities.

Here are graphs of $f(\chi^2)$ versus χ^2 for the three values of v is given in Figure B-1. The mean values of χ_v^2 is equal to v, and the variance of the χ_v^2 is equal to 2v.

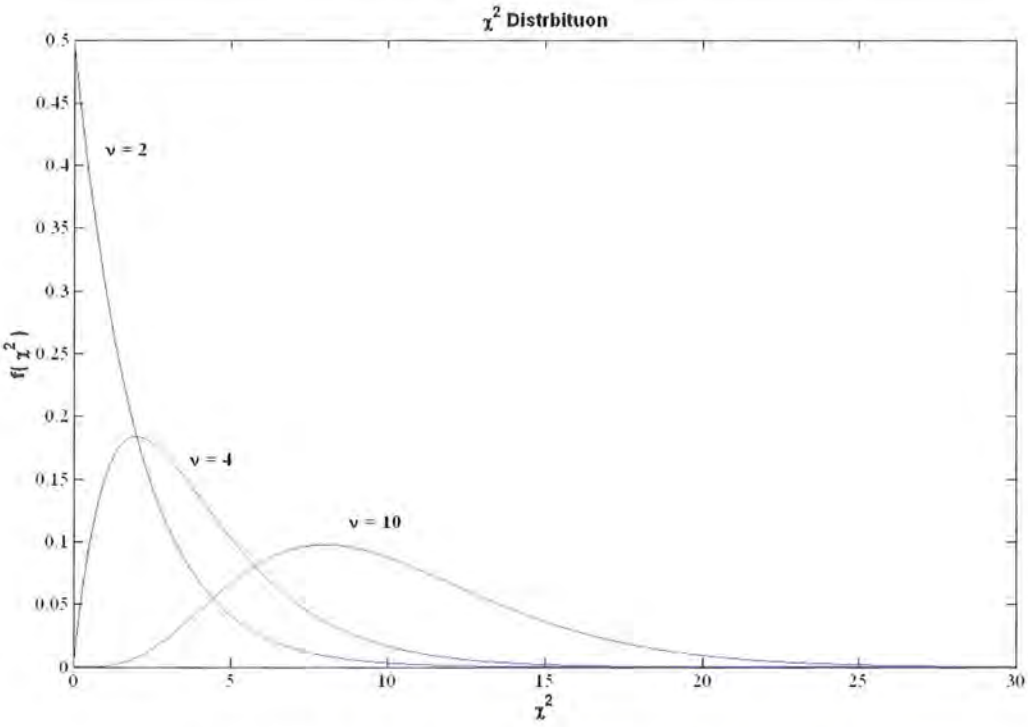

Figure B-1: The Chi-squared distribution for $v = 2, 4$, and 10.

Uniform Distribution

As a third modeling distribution for the characteristic diameters, the uniform distribution is tested. As known from statistics the function of the uniform distribution can be expressed as

$$f(d) = \frac{1}{d_{max} - d_{min}} \qquad (B.6)$$

Where d_{max} and d_{min} are the upper and lower limit of the uniform distribution. The mean characteristics sizes and the variance are

$$\bar{d} = \frac{d_{max} + d_{min}}{2}$$

$$\sigma^2 = \frac{(d_{max} - d_{min})^2}{12} \qquad (B.7)$$

Volume Median Diameter

By definition, half of a given volume of water is contained in droplets greater than this diameter and the other half in droplets smaller than this diameter. The volume median diameter, $D_{V_{50}}$, for a spray with different sized droplets is calculated by finding the droplet size below which half of the volume of water is contained. This is accomplished by first calculating total volume of water, V, contained in the droplets by summing the volumes of all droplets. The droplet diameters and their associated volumes are then sorted in ascending order. The cumulative volume by droplet size is then calculated for each droplet size. The $D_{V_{50}}$ diameter is chosen as the diameter at which the cumulative volume is one half of the total water volume. When one half of the total water volume is not located at a measured droplet diameter, linear interpolation is used to calculate $D_{V_{50}}$.

Appendix C: Experimental data.

Table C1 Water flux (lpm/m^2) measured in the near-field (0.76 *m*) for the K-205 sprinkler operating at 3.5 *bar*.

	Azimuthal angle						
Elevation angle	73°	90°	107°	123°	140°	157°	180°
3°	4.6	7.1	10.8	8.3	1.7	2.1	12.8
15°	214.1	187.5	259.4	183.9	128.6	27.6	475.8
30°	52.5	64.9	89.5	32.9	90.7	37.5	55.9
45°	20.0	113.9	87.7	18.3	138.7	53.7	45.6
60°	63.2	126.5	218.4	64.5	224.5	76.0	66.2
75°	155.9	284.1	299.1	266.6	223.0	119.8	70.5
90°	316.7	879.3	1819.7	3139.8	2718.4	2866.4	2570.7

Table C2 Water flux (lpm/m^2) measured in the near-field (0.76 *m*) for the K-205 sprinkler operating at 5.2 *bar*

	Azimuthal angle						
Elevation angle	73°	90°	107°	123°	140°	157°	180°
3°	2.0	4.1	5.5	4.3	2.8	3.7	6.6
15°	160.0	121.4	232.9	30.1	41.9	31.8	714.6
30°	95.2	114.9	141.8	53.7	150.6	52.7	89.8
45°	64.9	139.2	130.0	82.4	165.6	69.9	60.3
60°	95.1	145.9	289.6	135.5	300.3	92.3	86.0
75°	181.8	388.5	438.3	359.3	248.0	135.5	76.5
90°	341.3	787.1	2047.8	3845.5	3287.0	3236.8	3482.9

Table C3 Volume-median-droplet-diameter (*mm*) measured in the near-field (0.76 *m*) for the K-205 sprinkler operating at 3.5 *bar*.

	Azimuthal angle						
Elevation angle	73°	90°	107°	123°	140°	157°	180°
3°	0.566	0.678	0.591	0.609	0.538	0.602	0.799
15°	0.71	0.686	0.697	0.756	0.751	0.658	0.895
30°	0.339	0.265	0.375	0.264	0.377	0.311	0.293
45°	0.363	0.25	0.45	0.272	0.564	0.253	0.273
60°	0.532	0.548	0.545	0.42	0.554	0.309	0.322
75°	0.562	0.66	0.704	0.63	0.451	0.484	0.361
90°		2.576		2.178		2.564	

Table C4 Volume-median-droplet-diameter (*mm*) measured in the near-field (0.76 *m*) for the K-205 sprinkler operating at 5.2 *bar*.

	Azimuthal angle						
Elevation angle	73°	90°	107°	123°	140°	157°	180°
3°	0.499	0.526	0.48	0.445	0.521	0.598	0.716
15°	0.555	0.558	0.571	0.568	0.62	0.574	0.708
30°	0.357	0.26	0.313	0.257	0.34	0.338	0.288
45°	0.352	0.211	0.467	0.226	0.47	0.256	0.255
60°	0.434	0.362	0.433	0.3	0.796	0.311	0.263
75°	0.43	0.536	0.548	0.49	0.289	0.331	0.282
90°	1.941	1.875	1.921		1.744		1.905

Table C5 Average velocity magnitude (*m/s*) measured in the near-field (0.76 *m*) for the K-205 sprinkler operating at 3.5 *bar*.

	Azimuthal angle						
Elevation angle	73°	90°	107°	123°	140°	157°	180°
3°	3.310	3.000	3.463	3.796	2.848	3.245	5.439
15°	6.144	4.798	5.350	5.945	6.057	5.824	8.564
30°	6.640	4.218	6.461	4.475	6.576	3.420	4.896
45°	6.850	5.362	7.895	5.126	9.386	2.357	3.206
60°	8.216	8.181	7.579	7.872	7.659	3.398	3.048
75°	9.498	9.344	8.943	7.795	4.485	5.886	4.405
90°		10.510					

Table C6 Average velocity magnitude (*m/s*) measured in the near-field (0.76 *m*) for the K-205 sprinkler operating at 5.2 *bar*.

	Azimuthal angle						
Elevation angle	73°	90°	107°	123°	140°	157°	180°
3°	2.896	4.411	2.059	1.682	3.085	3.876	4.884
15°	6.079	6.296	5.223	5.745	5.780	4.130	8.599
30°	8.741	4.531	6.773	4.674	6.556	3.533	5.637
45°	8.811	4.295	11.151	6.280	9.817	2.144	3.522
60°	8.839	8.199	9.092	6.648	14.696	1.976	3.119
75°	9.553	9.664	9.203	6.783	3.125	3.897	3.400
90°	12.647	12.157	11.006		8.856		10.547

Appendix D: Demonstration of volume fractions

Table D-1: Spray volume flux (Lpm/m^2) along the elevation angle in the near field for the K-205 Sprinkler operating at 3.5 bar at seven azimuthal angles [4]

Azimuthal angle			
Elevation angle	140°	157°	180°
3°	1.7	2.1	12.8
15°	128.6	27.6	475.8
30°	90.7	37.5	55.9
45°	138.7	53.7	45.6
60°	224.5	76	66.2
75°	223	119.8	70.5
90°	2718.4	2866.4	2570.7
SUM	3525.6	3183.1	3297.5

Table D-2: Volume fractions along the elevation angle in the near field for the K-205 Sprinkler operating at 3.5 bar at seven azimuthal angles

Volume Fraction			
Elevation angle	Azimuthal angle		
	140°	157°	180°
3°	0.00048	0.00066	0.00388
15°	0.03648	0.008671	0.14429
30°	0.02573	0.011781	0.01695
45°	0.03934	0.01687	0.01383
60°	0.06368	0.023876	0.02008
75°	0.06325	0.037636	0.02138
90°	0.77105	0.900506	0.77959
SUM	1	1	1